TRC0304

ACHM Mix Stiffness and Static Creep Behavior

Nam H. Tran, Kevin D. Hall

Final Report

2005

FINAL REPORT

TRC-0304

ACHM Mix Stiffness and Static Creep Behavior

by

Nam H. Tran and Kevin D. Hall

Conducted by

Department of Civil Engineering
University of Arkansas

In cooperation with

Arkansas State Highway and Transportation Department

U.S. Department of Transportation
Federal Highway Administration

University of Arkansas
Fayetteville, Arkansas 72701

SEPTEMBER 2005

TRC-0304

ACHM Mix Stiffness and Static Creep Behavior

EXECUTIVE SUMMARY

Flexible pavement design procedures proposed for use within the Mechanistic-Empirical Pavement Design Guide (MEPDG) require the input of the dynamic modulus (E*) of hot-mix asphalt concrete. In addition, the E* test has been proposed as a "simple performance test" for use in mixture design and construction quality control. Objectives of this study included conducting the dynamic modulus test, evaluating the accuracy/variability of test results, constructing master curves for the mixtures tested, and evaluating the Witczak predictive equation contained in the MEPDG for determining E*. Three replicate test specimens were prepared for this study for each of two aggregate types, two binder grades, three nominal maximum aggregate sizes, and two air voids levels. The analysis showed that the variability of the average dynamic modulus for each set of four replicates was acceptable. Since the dynamic modulus tests were run at intermediate temperatures in this study, a modified procedure, using Arrhenius and power functions, was employed to construct the master curves. Based on the master curves, the effects of aggregate size, binder content, and air voids on the tested asphalt mixtures were evaluated and determined to be consistent and reasonable. The correlation of measured and predicted values (from the Witczak equation) was then assessed using the goodness-of-fit statistics. The measured and predicted values were also compared by matching the two values and master curve comparison. The goodness-of-fit statistics showed that the performance of the Witczak equation in predicting the dynamic moduli of the mixtures used in this study was very good to excellent, and the Witczak predictive equation had good correlation to the measured dynamic modulus values. The master curve comparison of measured and predicted values also confirmed that the Witczak predictive equation fitted the test data in this study very well. The testing procedure and results of this study are recommended for preparing input data for the MEPDG.

TABLE OF CONTENTS

LIST OF FIGURES

x

LIST OF TABLES

CHAPTER 1: INTRODUCTION

1.1 Problem Statement

The *AASHTO Guide for Design of Pavement Structures* has served well as a design guide for many state highway agencies to design new and rehabilitated highway pavements for several decades. In the 1995-97 National Pavement Design Review, the Federal Highway Administration (FHWA) stated that about 80 percent of the States make use of either the 1972, 1986, or 1993 AASHTO Guide (*1*). The Arkansas State Highway and Transportation Department (AHTD) currently uses the 1993 AASHTO Guide for new pavement design.

More recently, the AASHTO Joint Task Force on Pavements (JTFP), which has responsibility for the development and implementation of pavement design technologies, has recognized the limitations of the earlier Guides in the areas of traffic loading, foundations, drainage, climate effects, pavement performance, and pavement rehabilitation. The JTFP initiated an effort to develop a new Guide under National Cooperative Highway Research Program (NCHRP) Project 1-37A: "*Development of the 2002 Guide for the Design of New and Rehabilitated Pavement Structures*".

The overall objectives of NCHRP Project 1-37A were (1) to develop a new pavement design guide based on existing mechanistic-empirical (M-E) design concepts; and (2) to develop rudimentary computational software based on the Design Guide.

One advanced feature of the NCHRP 1-37a mechanistic-empirical pavement design guide (MEPDG) which was not found in previous versions of the AASHTO Guide is the hierarchical approach to design inputs (*1*). The hierarchical approach includes three levels of inputs. For a given flexible pavement design project, inputs may

be provided using a mix of levels, and the variability associated with each input level is directly applied in the design reliability simulation. Therefore, a design using lower levels of input accuracy may result in a more conservative design because the design must consider the uncertainties of design inputs when establishing reliability.

The hierarchical approach is used with regard to traffic, materials, and environmental inputs (*1*):

- Level 1 inputs provide the highest level of accuracy of inputs and the lowest level of uncertainty. Level 1 material inputs require laboratory or field testing. They would typically be used for designing heavily trafficked pavements.

- Level 2 inputs provide an intermediate level of accuracy, which is typically selected from an agency database, derived from a limited testing program, or estimated through correlations. This input level is closest to the typical procedures used with earlier editions of the AASHTO Guide and can be used when level 1 inputs are not available.

- Level 3 inputs provide the lowest level of accuracy. Inputs typically would be user selected default values or typical averages for the region. This input level is intended for designing low volume roads.

In the MEPDG, level 1 material characterization inputs for hot-mix asphalt (HMA) require a dynamic modulus (E*) value from laboratory tests while level 2 and 3 HMA inputs are estimated using Witczak's predictive model (*2*). However, level 2 dynamic modulus predictions require laboratory measured binder viscosity whereas level 3 $|E^*|$ predictions use the default binder properties established for all binder grades in the MEPDG.

However, the dynamic modulus of HMA has never been routinely measured and reported in Arkansas because current flexible pavement design procedures used in Arkansas, based on the 1993 *AASHTO Guide for the Design of Pavement Structures*, do not require input values related to the dynamic modulus of the HMA mixture. The general approach in the 1993 AASHTO Design Guide uses a "structural coefficient" to describe the structural capacity of the asphalt layer, and this coefficient is not varied for different types of hot mix asphalt (HMA) used in a given pavement. Therefore, it is necessary to determine the dynamic modulus of all typical mixtures used in Arkansas for future implementation of the MEPDG.

The application of the dynamic modulus is not limited to the pavement design, but it is also used for quality control/quality assurance research purposes. In 1993, the Strategic Highway Research Program (SHRP) developed a new HMA mixture design procedure called "Superpave". The Superpave system included the Superpave gyratory compactor (SGC) that better simulates the field compaction of HMA mixtures. The Superpave gyratory compactor uses a combination of pressure and a gyratory angle to compact an HMA specimen. The angle of gyration is an important factor affecting the compaction effort. A current standard (AASHTO T312) allows two different methods of gyratory angle calibration: external and internal. The internal calibration method uses the Dynamic Angle Validation (DAV) kit. Recent studies demonstrated the DAV ability to calibrate the internal angle of different SGCs to produce HMA specimens having similar densities (*3,4*), which is crucial to both HMA mix design and quality control/quality assurance purposes.

However, researchers generally agree that the magnitude of the internal angle of gyration measured by the DAV is a function of the stiffness (dynamic modulus) or shear resistance of the particular HMA mixture used in the determination (*5*). Therefore, it is necessary to determine whether the impact of HMA stiffness on the associated internal angle of gyration measured by the DAV is significant.

1.2 Objectives of Project

The overall objective of this research was to support the implementation of the MEPDG in Arkansas by establishing HMA material inputs – namely, the dynamic modulus. Specific objectives include:

1. developing a dynamic modulus database and determining the data variability for level 1 $|E*|$ inputs;

2. evaluating the $|E*|$ predictions for level 2 and 3 inputs using Witczak's predictive model;

3. identifying the appropriate $|E*|$ input level for the future applications in the MEPDG;

4. investigating the effects of dynamic modulus on the associated internal angles of gyration measured by the DAV;

5. studying the potential of using the simulated loading devices for the internal gyration angle calibration of SGCs.

1.3 Scope of Work

In order to successfully complete the objectives of this study, the following research tasks were accomplished:

The first research effort reviewed updated literature regarding HMA volumetric properties, performance-related tests, and pavement distresses. The review focused on current test methods to evaluate the stiffness of HMA mixtures, especially dynamic modulus test and prediction techniques. In addition, the development and application of the DAV was reviewed.

All typical mixtures used in Arkansas were identified and verified in the laboratory. The experimental plan included four aggregate sources, three nominal maximum aggregate sizes, two binder grades, and two air void levels. After the dynamic modulus of HMA mixtures was determined, the test variability was evaluated, and the subsequent master curves were constructed. The dynamic modulus test results were then used to assess available predictive models for the dynamic modulus of HMA mixtures.

The DAV procedure was tested on three HMA mixtures with significantly different stiffness values. The results were used to investigate effects of the stiffness of the mixtures on the internal angle of gyration.

A final task related to the project was an investigation of the concept of 'static creep' in hot-mix asphalt. A 'white paper' was prepared detailing the findings of the literature review performed regarding static creep.

CHAPTER 2: DESIGN OF HOT-MIX ASPHALT

HMA pavement design consists of two parts: mix design and structural design, which determine the pavement's resistance to common distresses. This chapter covers the primary stresses in flexible pavements followed by the fundamentals of mix design.

2.1 Flexible Pavement Distresses

When a wheel load is applied on a pavement, stresses are transmitted to the pavement structure. The pavement structure must be strong enough to resist the accumulation of damage as function of time and traffic. The primary flexible pavement distresses that engineers try to avoid are permanent deformation, fatigue cracking, and low temperature cracking. Permanent deformation and fatigue cracking are load-associated distresses. Low temperature cracking is caused by the pavement shrinkage in cold weather.

2.1.1 Permanent Deformation

Permanent deformation is an accumulation of small amounts of unrecoverable deformation occurring each time a load is applied. Wheel path rutting is a common form of permanent deformation. Two types of permanent deformation are normally addressed in literature.

One type of rutting is caused by the weak support below the asphalt layer(s), as illustrated in Figure 2.1(a). It is considered as a structural problem rather than a materials problem. The deformation occurs in the underlying layers rather than in the asphalt layer(s).

(a)   (b)
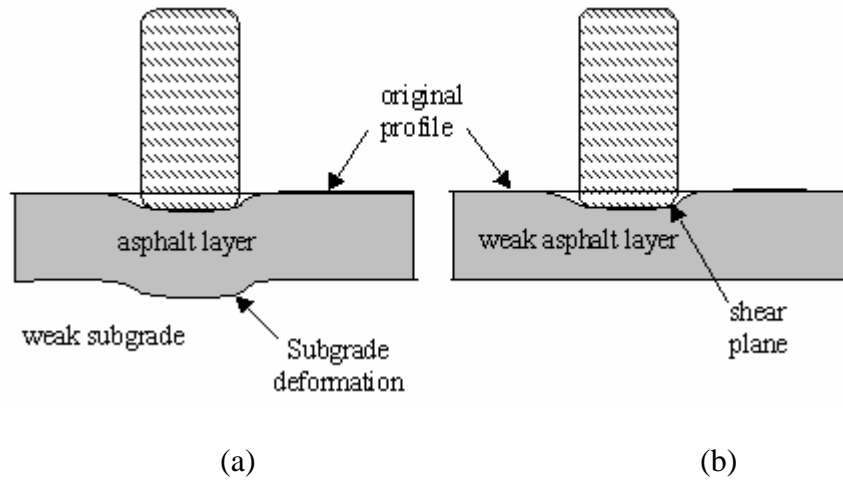
Figure 2.1. Permanent Deformation Phenomena

The other type of rutting is deformation in the asphalt layer(s), as illustrated in Figure 2.1(b). The asphalt mixture is not strong enough to resist the shear occurred in the asphalt layer(s) under repeated heavy loads. As a result, the asphalt mixture under the wheel path is pushed downward and laterally. Deformation of a weak mixture typically occurs under high pavement temperatures. It is not solely an asphalt binder problem but a combined problem of mineral aggregate and asphalt binder (*6*).

Permanent deformation changes drainage characteristics, decreases runoff capability, which reduces skid resistance of the surface course, increases hydroplaning conditions and impedes the removal of snow and ice in cold weather. In addition, rutting increases roughness and reduces the overall serviceability of the pavement.

Studies conducted by National Center for Asphalt Technology (NCAT) showed that permanent deformation generally occurred in the top 75 to 100 mm (3 to 4 in.) of flexible pavements (*7,8*).

2.1.2 Fatigue Cracking

Fatigue cracking is initiated at points where the critical tensile strains and stresses occur under repeated traffic loads. Once the cracking initiates at the critical location, the continued traffic loads eventually causes the cracks to propagate through the entire bound layer. An early sign of fatigue cracking is longitudinal hair cracks in the wheel path. When transverse cracks join the longitudinal cracks, this state of fatigue cracking is called alligator cracking. Severe alligator cracking may lead to potholes.

Fatigue cracking is usually caused by large deflections under repeated heavy wheel loads. Large deflections lead to increased horizontal tensile stresses at the bottom

of the bound layer. That results in fatigue cracking to initiate at the bottom of the bound layer and propagate to the surface (bottom-up cracking). If the phenomenon of cracking initiation and propagation occurs in an underlaying stabilized layer, cracking reduces the overall structural capacity of the layer and then pavement, and it induces reflective cracking in the upper bound layers.

The other type of fatigue cracking is initiated from the top and propagates down (top-down cracking). Top-down fatigue cracking of a highly aged thin surface layer may be due to critical tensile and/or shear stresses developed at the surface and caused by extremely high contact pressure at the tire edge-pavement interface (*1*).

Fatigue cracking propagating throughout the bound layer thickness allows water to seep into the underneath unbound layers. It weakens the pavement structure, increases roughness, and reduces overall pavement serviceability.

2.1.2 Low Temperature Cracking

Low temperature cracking is caused by cold weather rather than by traffic loads. It is described by transverse cracks occurring at nearly equal spacing (*6*). The pavement shrinkage in cold weather causes tensile stress building within the layer. At some critical locations, the tensile stress exceeding the tensile strength of the bound layer causes low temperature cracks.

2.2 Asphalt Mixture Design Procedures

Asphalt mixture design procedures typically include the steps used to select asphalt binder and mineral aggregates and subsequently combine them together. HMA

mixtures are designed to resist to the pavement distresses such as permanent deformation, fatigue cracking, and low temperature cracking. In addition, HMA mixtures must meet requirements for workability, durability, and skid resistance.

2.2.1 Marshall and Hveem Methods

The Marshall mixture design method was developed in 1939 by Bruce Marshall, an engineer working for the Mississippi State Highway Department. The method was then refined by the U.S. Army Corps of Engineers to standardize as ASTM D 1559 and AASHTO T 245 (*6*).

One advantage of the Marhsall method is that it designs an asphalt mixture using stability and void analyses. In addition, it requires inexpensive and portable equipment. However, the impact compaction may not simulate field densification of the mixture. Additionally, the Marshall stability test does not adequately measure the shear strength of the mixture in question, making it difficult to characterize the mixture rutting resistance (*6*).

The final form of Hveem mixture design method was introduced in 1959 by Francis Hveem of the California Department of Transportation. The procedure was standardized as ASTM D 1560 and ASTM D 1561. The method was normally employed in the western states.

The Hveem method is like the Marshall method in that it requires a density and stability analysis. In addition, it measures the mixture's resistance to swell in the presence of water. It is felt that the kneading compaction better simulate the field densification characteristics of HMA. The Hveem stability test directly measures the

internal friction angle of shear strength, which determines the mixture resistance to lateral displacement under a vertical load. However, the test equipment for the Hveem method is expensive and not portable. It is thought that the Hveem method is too subjective and probably creates non-durable HMA with too little asphalt binder (*6*).

2.2.2 Superpave Asphalt Mixture Design Procedure

In 1987, the United States Congress established a five-year fund for the Strategic Highway Research Program (SHRP). The research efforts were to improve durability and performance of asphalt materials and mixtures used for roadways in the U.S. The principal product of the SHRP was Superpave (Superior Performing Asphalt Pavements). Superpave consists of two major parts, the Superpave asphalt binder analysis and the Superpave asphalt mixture design and analysis. Superpave is considered as a superior system for grading asphalt binders, selecting aggregate materials, conducting asphalt mixture design, and predicting mixture performance.

In the Superpave performance graded asphalt binder specification (*9*), asphalt binders are selected based on the climate and traffic conditions at the site of the paving project. The Superpave asphalt binder specification classifies binder grades according to the high and low temperatures between which the binder possesses adequate physical properties in pavements.

The minimum required PG binder is chosen to satisfy the pavement temperatures and the design reliability. The pavement temperatures for determining the binder grade include the yearly, 7-day-average, maximum pavement temperature measured 20 mm below the pavement surface and the yearly, 1-day-minimum pavement

11

temperature measured at the pavement surface. The above temperatures can be obtained from actual site data or using LTPPBind software (*10*). The design reliability is chosen based on road classification, traffic level, cost, and other factors.

If traffic speed or the design equivalent single loads (ESAL) warrant, the binder grade selection should be adjusted (*10*). The binder grades for slow and standing traffic load rate would be increased by one and two grade equivalents, respectively. If the design traffic is expected to be between 10 million and 30 million ESALs, the binder grade is considered increasing by one grade equivalent. If the design traffic is expected to exceed 30 million ESALs, the binder grade is required to increase by one grade equivalent.

In the Superpave system, a Superpave design aggregate gradation developed on a 0.45 power gradation chart must pass between gradation control points. The combined aggregate gradation is classified as coarse graded when it passes below the Primary Control Sieve (PCS) control point. All other gradations are classified as fine graded. The aggregates must meet the requirements for coarse aggregate angularity, fine aggregate angularity, flat and elongated particles, and clay content (*10*). The Superpave system ensures that the design aggregate structure has a strong stone skeleton to enhance resistance to rutting while maintaining enough voids to enhance mixture durability (*6*).

Two new key features in the Superpave system comparing to other mix design methods are laboratory compaction and performance testing. Laboratory compaction is performed using a Superpave gyratory compactor (SGC). The SGC is designed to better simulate the field compaction of HMA. Performance testing includes two new

performance based testing procedures: the Superpave Shear Test (SST) and the Indirect

Tensile Test (IDT). The data from the tests are used in the performance prediction

models included in the Superpave system to estimate the mixture performance (*6*).

However, the Superpave performance testing has never been implemented by the

asphalt paving community.

2.3 Asphalt Mixture Volumetric Properties

An asphalt mixture is designed based on the volumetric properties and their

requirements specified in the Superpave system. This section reviews only the

volumetric properties that are important to characterize the HMA later in this study

(*11*). The volumetric properties of an asphalt mixture can be presented in a multiphase

diagram, as shown in Figure 2.2.

Air voids (V_a) are the percent by volume of air between the coated aggregate

particles of a compacted paving mixture and calculated using Equation 2.1.

$$V_a = 100 \times \left(1 - \frac{G_{mb}}{G_{mm}}\right) \tag{2.1}$$

where:

G_{mm} = maximum specific gravity of the mixture

G_{mb} = bulk specific gravity of the compacted specimen

Voids in mineral aggregate (*VMA*) are the volume of the void space between the

aggregate particles of a compacted mixture. VMA includes the air voids and the

effective binder content, and it is calculated using Equation 2.2.
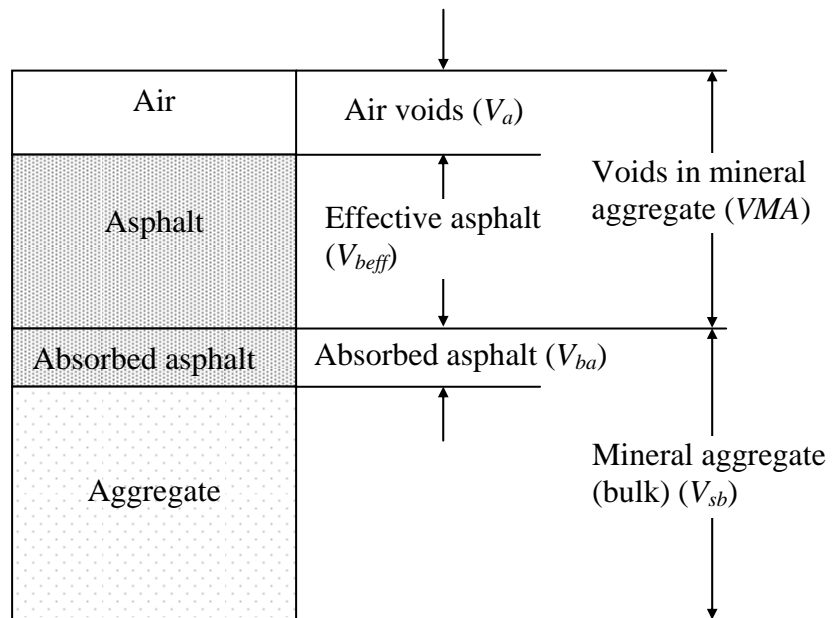
Figure 2.2. Volumetric Properties of HMA

$$VMA = 100 \times \left(1 - \frac{G_{mb}P_s}{G_{sb}}\right) \qquad (2.2)$$

where:

G_{mb} = bulk specific gravity of the compacted specimen

P_s = percent of aggregate in the total weight of mixture

G_{sb} = bulk specific gravity of aggregate

Binder content (P_b) is the percent by mass of binder in the total mixture including binder and aggregate. The binder content is optimum when the compacted HMA mixture has the required air void level at N_d. In Arkansas, the required air void levels are 4.5 percent for binder grade PG70-22 and 4.0 percent for binder grade PG76-22 (*12*).

Effective binder volume (V_{beff}) is the volume of binder that is not absorbed into the aggregate, and it is determined using Equation 2.3.

$$V_{beff} = VMA - V_a \qquad (2.3)$$

Voids filled with asphalt (*VFA*) are the percent of the VMA filled with binder and calculated using Equation 2.4.

$$VFA = 100 \times \left(\frac{VMA - V_a}{VMA}\right) \qquad (2.4)$$

2.4 Superpave Hot-Mix Asphalt Design Requirements in Arkansas

This section summarizes the requirements for the Superpave HMA design used in Arkansas (*12*). The combined aggregate shall pass between the gradation control points specified in Table 2.1. The HMA design shall meet the V_a, *VMA*, *VFA*, and dust-to-effective binder ratio requirements presented in Table 2.2.

15

Table 2.1. Superpave Gradation Control Points Used in Arkansas (*12*)

Sieve Size (mm)	Nominal Maximum Aggregate Size-Control Points (% Passing)					
	37.5 mm		25.0 mm		12.5 mm	
	Min	Max	Min	Max	Min	Max
50.0	100	-	-	-	-	-
37.5	90	100	100	-	-	-
25.0	-	90	90	100	-	-
19.0	-	-	-	90	100	-
12.5	-	-	-	-	90	100
9.5	-	-	-	-	-	90
4.75	-	-	-	-	-	-
2.36	15	41	19	45	28	58
1.18	-	-	-	-	-	-
0.075	0	6	1	7	2	10

Table 2.2. Superpave HMA Design Requirements Used in Arkansas (*12*)

V_a *at* N_{design} (%)		VMA (% Minimum)			VFA (%)	Dust-to-Binder Ratio
Binder Grade		Nominal Max Aggregate (mm)				
PG70-22	PG76-22	37.5	25.0	12.5		
4.5	4.0	11.5-13.0	12.5-14.0	14.5-16.0	65-75	0.7-1.4

2.5 Effects of Mixture Properties on HMA Performance

Performance of an HMA mixture is influenced by the aggregate properties, binder properties, and volumetric properties of the HMA mixture. Aggregate properties that relate to HMA performance are gradation and size, aggregate particle shape and angularity, and properties of minus 200 material.

Gradation of the combined aggregate in an HMA mixture significantly affects the HMA pavement performance, especially rutting resistance (*13-15*). A reasonably dense gradation with adequate VMA helps to improve resistance to degradation during construction and under traffic, and it also increases resistance to fatigue cracking when used in thick pavements (*13*). In general, HMA mixtures with large maximum size resist permanent deformation better than those with small maximum size (*13*).

Aggregate particle shape and angularity of an HMA mixture plays an important role in the mixture performance. The angularity factor of an aggregate used in HMA includes the angularity of coarse aggregate and the angularity of fine aggregate. In general, the aggregate angularity has a major effect on mix stability (*16*), and high angularity provides better resistance to permanent deformation (*17,18*). However, the angularity of the fine aggregate is a more important factor to rutting resistance than the angularity of coarse aggregate (*19*). Another study finds a stronger relationship between the fine aggregate angularity and rutting than between the coarse aggregate angularity and rutting (*20*). Higher fine aggregate angularity results in greater VMA and smaller permanent deformation (*21*). Mixtures containing manufactured sand (that normally has a higher angularity) show less rutting than mixtures with natural sand (that typically has a lower angularity) (*17, 22-24*).

17

The aggregate particle shape affects the coarse aggregate breakdown, the rutting susceptibility, and volumetric properties of compacted HMA mixtures (*25*). Flat and elongated particles are undesirable in HMA mixtures due to their tendency to breakdown during construction and operation. Thin aggregates may decrease the fatigue life of HMA mixtures (*13*).

In addition, the HMA mixture performance is influenced by the properties of minus 200 material (the material passing No. 200 sieve). Fines sometimes can act as an extender of asphalt cement binder, which may result in an over-rich HMA mixture, leading to rutting (*26*). Some fines affect the asphalt binder to act stiffer than its grade, influencing the HMA fracture behavior (*27,28*).

Binder properties affecting performance of asphalt pavements include binder content and performance grade. The binder content in an HMA mixture should not be 0.5 percent above or below an optimum level (*29*). Excessive binder contents, may lead to rutting in the HMA mixture (*30*). However, asphalt contents below the optimum may affect the long-term durability of the mixture and produce dry mixtures that complicate lay-down and compaction (*31*).

When polymer modifiers are added to conventional or unmodified asphalts, the modified asphalts have higher performance grades. The use of modified asphalt in an HMA mixture significantly improves the rutting resistance of the mixture (*32*). In a case, when the modified asphalt was used, rutting was reduced up to 50 percent, and pavement load-carrying capacity was increased more than 300 percent (*31*).

The amount of air voids in the HMA mixture is one of the volumetric properties, which affects the HMA stability and durability (*30*). When the air voids are higher than

8 percent, the mixture is permeable to air and water, which fastens the oxidation of the asphalt binder, causing premature cracking (*33,34*). However, when the air voids are lower than 3 percent, the pavement may show permanent deformation due to plastic flow (*35,36*).

The minimum VMA requirement in the Superpave system was to specify the minimum permissible asphalt content in the mixture to ensure its durability (*37*). Recently, the effects of VMA, an important mix design parameter, on the asphalt mixture performance have been studied in several projects. One such study (*37*) stated that the VMA criteria should be different for coarse and fine asphalt mixtures. In contrast, another study by Anderson and Bentsen (*38*) reported that no statistically significant difference was found between the fatigue cracking parameters of a coarse mix and a fine mix with the same VMA. In addition, the fatigue properties of a mix with 13 percent VMA and a mix with 15 percent VMA were not significantly different. However, increasing the VMA from 13 percent to 15 percent in coarse mixtures can lead to poor performance. Some researchers (*39,40*) questioned the suitability of the VMA criteria in the Superpave system.

There is increasing interest in using asphalt film thickness either to supplement or to replace the VMA requirements in the Superpave system (*37,41-43*). Stiady et al. (*43*) proposed that the film thickness included in mixture design procedures would have an acceptable range of 7 to 9 microns.

2.6 Relationship of SGC Properties to HMA Performance

One of key features in the Superpave system is laboratory compaction using the SGC. The SGC can simulate the field compaction of HMA mixtures, and it is thought that the SGC data collected during gyratory compaction of an HMA mixture can be used to assess the HMA pavement performance.

A study under NCHRP Project 9-16 (*44*), "Relationship Between Superpave Gyratory Compactor Properties and Permanent Deformation of Pavements in Service," showed that the product of compaction slope and air voids, $k \times AV$, was not related to estimated rut depth. The study reported that the best parameter was the number of gyrations at which the peak shear stress occurs during compaction, *N-SR_{max}*. This parameter can be determined using an AFG1 SGC from Pine Instruments or a Gyratory Load Cell Plate Assembly (GLPA) developed at the University of Wisconsin – Madison. However, the biggest limitation of the *N-SR_{max}* parameter is that it is sensitive to the aggregate structure and asphalt binder volume but insensitive to the stiffness of the asphalt binder in an asphalt mixture. Therefore, this parameter may serve as a rapid indicator of HMA rutting potential but not a replacement for performance-related testing.

Another study by D'Angelo et.al. (*45*) did not find a relationship of the compaction slope to the asphalt pavement performance. The research team concluded that the slope of the compaction curve should not be a good indicator for the HMA mixture performance. However, in recent research conducted by the Pennsylvania Transportation Institute (PTI) and Advanced Asphalt Technologies (AAT) (*46*), the compaction slope together with indirect tensile (IDT) strength and VMA were used to

develop a good, simple and rational model ($R^2 = 0.82$, unadjusted) that can predict laboratory rutting potential.

2.7 Summary

This chapter introduced the primary flexible pavement distresses: permanent deformation, fatigue cracking, and low temperature cracking. The pavement distresses are not only considered in the structural design of flexible pavements but also in the design of HMA mixtures. The HMA mixture design methods, such as Marshall method, Hveem method, and Superpave mixture design procedure, were developed to design the mixtures that can resist to the primary pavement distresses. Among the mix design methods, the Superpave system is the most comprehensive mix design procedure up to date. In the Superpave system, the binder and aggregates used in the mix design are chosen carefully based on their properties, and the subsequent HMA mixture is designed based on its volumetric properties.

The effects of the mixture properties, such as aggregate, binder and volumetric properties, on performance of asphalt pavements were also reviewed in this chapter. Among the important volumetric properties that affect the HMA mixture stability and durability, the VMA requirements in the Superpave system were questioned. There is growing interest in using asphalt film thickness either to supplement or to replace the VMA requirements in the Superpave design procedure.

The SGC is a key feature in the Superpave system. It can simulate the field compaction of HMA mixtures. Research is ongoing to investigate the use of SGC data in the evaluation of performance of HMA mixtures. One promising approach is to use

the compaction slope together with the indirect tensile strength and VMA in model that

can predict laboratory rutting potential.

CHAPTER 3: CHARACTERIZATION OF ASPHALT MIXTURES

3.1 Mechanical Behavior of Asphalt Binder

Since asphalt binders are characterized as viscoelastic materials, their behavior is dependent on both temperature and rate of loading. At high temperatures, such as 135C (275F), or under sustained loads (e.g., slow moving or stopped vehicles), asphalt cements typically behave as simple Newtonian or non-Newtonian fluids (*9*). The Newtonian fluids have (1) a constant ratio of shear stress to shear strain rate and (2) a constant viscosity regardless of shear strain rate, as shown in Figure 3.1. For non-Newtonian liquids, the ratio of shear stress to shear strain rate is not constant. Most modified binders are non-Newtonian liquids at mixing and compaction temperatures in the field (*47*). At cold temperatures or under fast moving loads, asphalt binders behave as elastic solids. Asphalt binders may be too brittle and initiate low temperature cracking at very low temperatures. At intermediate temperatures, asphalt binders act as viscoelastic materials exhibiting both viscous and elastic characteristics (*9*).

Asphalt binders also react with oxygen, and this reaction is called oxidation. Oxidation changes the structure and composition of asphalt molecules, making asphalt binders more brittle. Therefore, old asphalt pavement is more susceptible to cracking. Oxidation occurs faster in warm climates (*9*) or when the HMA mixtures have more than 8 percent air voids (*33,34*).

Shear stress

μ

Rate of Shear Strain

Viscosity

Rate of Shear Strain
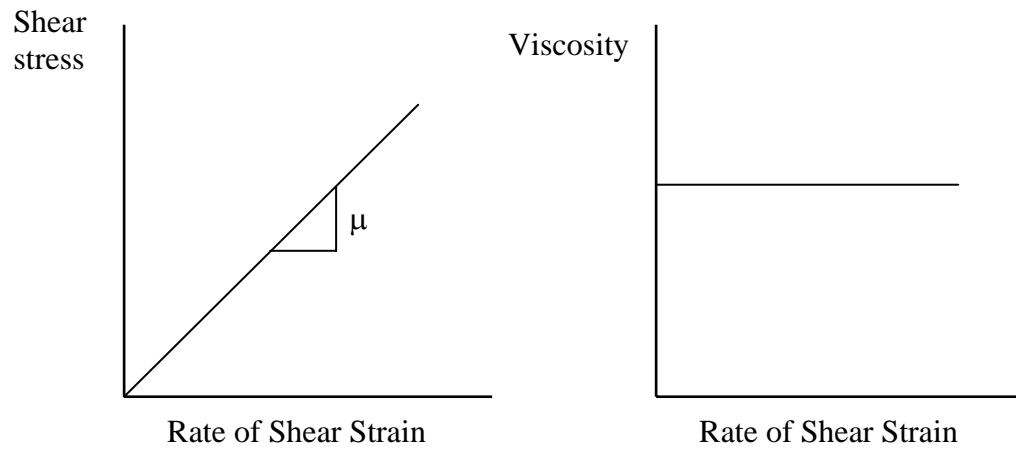
Figure 3.1. Newtonian Liquid Behavior (9)

3.2 Superpave Asphalt Binder Tests

The Superpave binder tests are designed to evaluate the binder performance at three states of its life: in its original state, after mixing and compaction, and after in-service aging (*9*). Table 3.1 shows a list of the Superpave binder testing equipment that conduct various Superpave binder tests to determine the physical properties of asphalt binders, which affect the HMA performance. Table 3.2 shows the binder aging conditions for Superpave binder tests.

Tests performed on original asphalt binders determine the binder properties for transport, storage, and handling. The binders are then aged using the rolling thin film oven (RTFO) procedure, which simulates the aging condition of the binders during mix production and construction. In this form of aging, asphalt binders are aged by two mechanisms: volatilization of light oils in the binders and oxidation by reacting with the oxygen in the environment. In-service aging of RTFO-aged binders in the laboratory is performed using the pressure aging vessel (PAV) procedure, which simulates the oxidation of asphalt binder as part of the HMA layer in an asphalt pavement (*9*).

This section summarizes the dynamic shear rheometer (DSR) and rotational viscometer (RV) test procedures. The test parameters, such as complex shear modulus and viscosity, obtained from these tests are used for predictive equations for the dynamic modulus of HMA later in this study. Detailed procedures for the binder tests listed in Table 3.2 can be found in the appropriate AASHTO test methods (*48-51*).

Table 3.1. Superpave Asphalt Binder Testing Equipment (*30*)

Binder Test Equipment	PURPOSE	Performance Parameter
Rolling Thin Film Oven (RTFO)	Simulate binder aging (hardening) during HMA production and construction	Resistance to aging (durability) during construction
Pressure Aging Vessel (PAV)	Simulate binder aging (hardening) during HMA service life	Resistance to aging (durability) during service life
Rotational Viscometer (RV)	Measure binder properties at high construction temperatures	Handling and pumping
Dynamic Shear Rheometer (DSR)	Measure binder properties at high and intermediate service temperatures	Resistance to rutting and fatigue cracking
Bending Beam Rheometer (BBR)	Measure binder properties at low service temperatures	Resistance to low temperature cracking
Direct Tension Tester (DTT)	Measure binder properties at low service temperatures	Resistance to low temperature cracking

Table 3.2. Aging Conditions for Superpave Binder Tests (*9*)

Superpave Binder Test	BINDER CONDITION
Dynamic Shear Rheometer (DSR)	Original binder
	RTFO-aged binder
	PAV-aged binder
Rotational Viscometer (RV)	Original binder
Bending Beam Rheometer (BBR)	PAV-aged binder
Direct Tension Tester (DTT)	PAV-aged binder

3.2.1 Dynamic Shear Rheometer

The dynamic shear rheometer (DSR) characterizes the viscous and elastic properties of asphalt binders at intermediate and high temperatures. This test measures the dynamic (complex) shear modulus ($|G^*|$), and phase angle (δ) of asphalt binders. A schematic of the DSR is illustrated in Figure 3.2.

All Superpave DSR tests are conducted on unaged, RTFO-aged, or PAV-aged binders at an angular frequency of 10 radians per second, which is equal to approximately 1.59 Hz. A constant stress is applied as the loading mode. Original and RTFO-aged binders are tested at strain values of 10 to 12 percent, and PAV-aged binders are tested at strain values of about one percent (*52*). These strain limits keep the binder behavior in the linear viscoelastic range. During each cycle, both stress and strain are measured. At the end of the test, the $|G^*|$ and δ are reported.

The complex shear modulus (G^*), which is a complex number, consists of two components: the storage modulus (G'), which represents the elastic (recoverable) response, and the loss modulus (G''), which represents the viscous (non-recoverable) response. The phase angle (δ) represents the relationship between G^*, G', and G'', as shown in Figure 3.3.

The relationship between the applied stress and resulting strain, as shown in Figure 3.4, is used to calculate the dynamic (complex) shear modulus ($|G^*|$), which is the ratio of total shear stress (τ_{max} - τ_{min}) to total shear strain (γ_{max} - γ_{min}) (*30*):

$$|G^*| = \frac{\tau_{max} - \tau_{min}}{\gamma_{max} - \gamma_{min}} \tag{3.1}$$
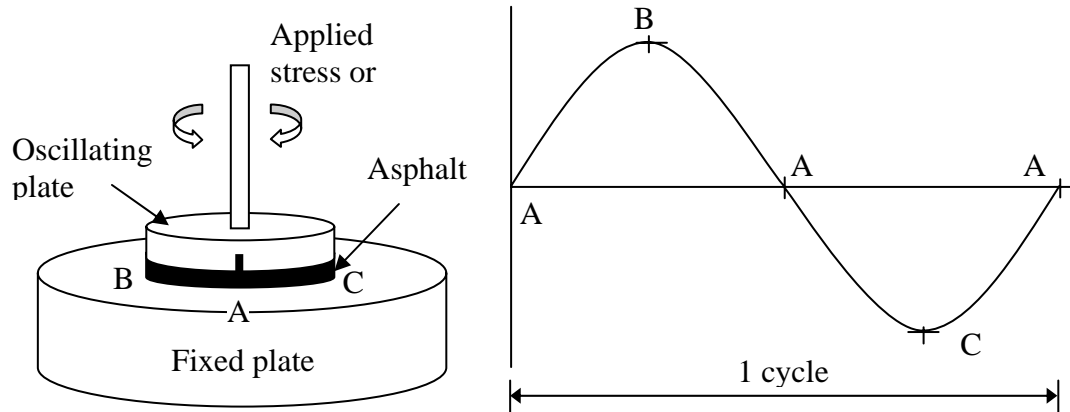
Figure 3.2. Schematic of Dynamic Shear Rheometer (*30*)
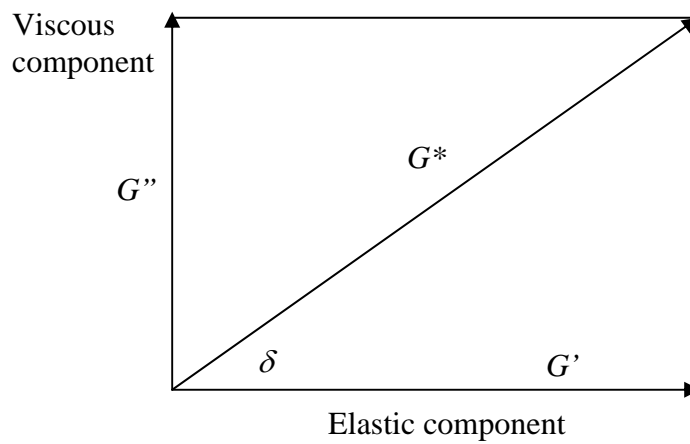
Figure 3.3. Components of Complex Shear Modulus (*30*)

The figure shows two stacked plots. The upper plot is labeled "Applied shear stress" with a sinusoidal curve. Its peak is marked τ_{max} and its trough is marked τ_{min}. The lower plot is labeled "Resulting shear strain" with a sinusoidal curve. Its peak is marked γ_{max} and its trough is marked γ_{min}. Between the two curves a horizontal measurement shows $\Delta t =$ time lag, and δ, phase angle.

Figure 3.4. Stress-Strain Response of a Viscoelastic Material (*30*)

The storage modulus (G') and loss modulus (G'') are computed from the dynamic (complex) modulus ($|G*|$) and the phase angle (δ) between the peak stress and the peak strain in Equations 3.2 and 3.3, respectively.

$$G' = |G*|\cos\delta \tag{3.2}$$

$$G'' = |G*|\sin\delta \tag{3.3}$$

The ratio of the loss modulus (G'') to the storage modulus (G') is the loss tangent.

$$\text{Loss tangent} = \tan\delta = \frac{G''}{G'} \tag{3.4}$$

The asphalt binder is tested in the DSR in its original and RTFO-aged conditions at the maximum design temperature to determine the binder's ability to resist rutting. PAV-aged binders are tested at the intermediate design temperature to evaluate the binder's resistance to fatigue cracking (*30*).

Permanent deformation is governed by limiting $G*/\sin\delta$, determined at the maximum design temperature, to values greater than 1.00 kPa for original binders and 2.20 kPa for RTFO-aged binders. Fatigue cracking is governed by limiting $G*\sin\delta$, determined at the intermediate temperature, to values less than 5,000 kPa after PAV aging (*9*).

3.2.2 Rotational Viscometer

A rotational viscometer test (Figure 3.5) is used to determine the binder viscosity, which assures that the binder is fluid enough at normal operating temperature to pump and handle at the hot mix facility.
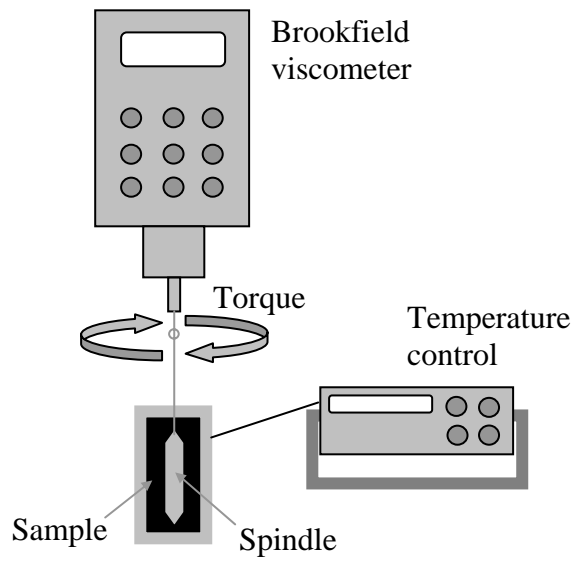
Figure 3.5. Schematic of Brookfield Viscometer (*9*)

The rotational viscosity is determined by measuring the torque required to maintain a constant rotational speed (20 rpm) of a cylindrical spindle while submerged in an asphalt binder sample at a constant temperature (*9*).

The Superpave binder specification limits the viscosity to 3 Pa·s at 135C (*30*). The viscometer test data can also be used to develop temperature-viscosity charts for estimating mixing and compaction temperatures for use in mixture design. An example of the temperature-viscosity chart is shown in Figure 3.6. The relationship between temperature and binder viscosity in Figure 3.6 is linear after log-log transformation of the viscosity data and log transformation of the temperature data (*53*).

$$\log \log \eta = A + VTS \log T_R \tag{3.5}$$

where:

η = viscosity, cP

T_R = temperature, Rankine

A = regression intercept

VTS = regression slope of Viscosity-Temperature Susceptibility

For conventional asphalt binders, mixing and compaction temperatures are determined by selecting temperatures corresponding to the viscosity value of 0.17 ± 0.02 Pa·s for mixing and 0.28 ± 0.03 Pa·s for compaction (*9*). For modified binders, a study by Bahia et al. (*47*) proposed to use the viscosity values of 0.75 ± 0.05 Pa·s for mixing and 1.40 ± 1.00 Pa·s for compaction measured at 20 rpm with Brookfield viscometer.
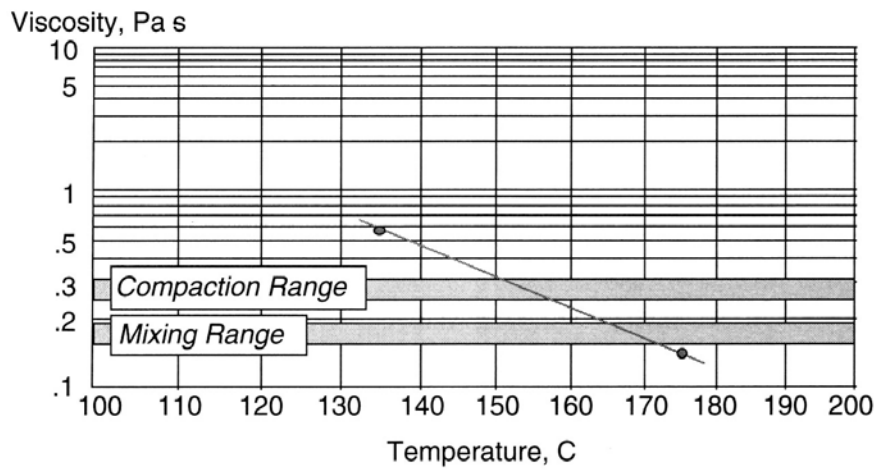
Figure 3.6. Temperature-Viscosity Relationship (*9*)

The binder viscosity can be estimated from the complex shear modulus data using Equation 3.6 (*1*).

$$\eta = \frac{G*}{10}\left(\frac{1}{\sin \delta}\right)^{4.8628}$$ (3.6)

where:

η = viscosity, Pa·s

$G*$ = complex shear modulus of binder, Pa

δ = phase angle, degree

3.3 Mechanical Behavior of HMA Mixture

Hot-mix asphalt is a composite material, which is composed of aggregates, asphalt binder and perhaps other additives. Therefore, according to Uzan (*54*), it is more complicated to characterize the asphalt mixture behavior than to characterize the asphalt binder alone because HMA properties vary with composition, temperature, loading frequency, and stress level. An HMA mixture can change its properties from linear viscoelasticity at low temperatures, high frequencies, and low load levels to nonlinear viscoelastoplastic at high temperatures, low frequencies, and high load levels (*54,55*).

The HMA mechanical behavior at cold temperatures (lower than 10C) is governed by the viscoelastic behavior of the asphalt binder (*54,56*), and the maximum stiffness of the mix is dependent on the limiting binder stiffness (*57*). According to Christensen (*58*), asphalt binders have been characterized as linear viscoelastic materials, so HMA mixture can also be approximated as a linear viscoelastic material at cold temperatures lower than 0C (32F).

A study by Goodrich (*56*) showed that at intermediate temperatures (between 10C and 50C), HMA rheology was sensitive to unique properties of the binders, and modified asphalt binders were expected to improve the performance of HMA mixtures at medium temperatures.

At high temperatures (above 50C), the aggregate structure influences the compressive strength of the mix more than the viscous behavior of the asphalt binder (*54*). The differences in the binders are not apparent in the dynamic mechanical properties of the mixes (*56*). The compressive strength reaches a limiting equilibrium value, which is dependent on the aggregate gradation (*57*).

3.4 HMA Stiffness

HMA stiffness is used in pavement engineering to evaluate the relative quality of mixtures and to predict the response of pavements subjected to wheel loads. HMA stiffness parameters often used are resilient, dynamic, and relaxation moduli.

3.4.1 Resilient Modulus

The resilient modulus is defined as the elastic modulus that is applied in the elastic theory (*59*). Pavement materials are not elastic because they experience some permanent deformation after each load application. However, if the load is small compared to the strength of the material, the deformation under each load repetition after a large number of load repetitions is nearly completely recoverable, and the materials can be considered elastic.

The elastic modulus based on the recoverable strain under repeated loads is called the resilient modulus (M_R), which is the ratio of the deviator stress (σ_d) to the recoverable strain (ε_r).

$$M_R = \frac{\sigma_d}{\varepsilon_r} \tag{3.7}$$

3.4.2 Dynamic (Complex) Modulus

Hot mix asphalt is a composite material, whose mechanical behavior is primarily governed by the viscoelastic nature of the asphalt binder. The fundamental problem in the investigation of HMA viscoelastic property is the determination of the functional relationship between the kinematic quantity (strain) and the dynamic quantity (stress).

The complex modulus is one of many methods available for describing the stress-strain relationship of linear viscoelastic materials. Huang (*59*) presents the theory of complex modulus using the Kevin model, shown in Figure 3.7-a, using a sinusoidal loading.

The sinusoidal loading can be represented by a complex number:

$$\sigma = \sigma_0 \cos(\omega t) + i\sigma_0 \sin(\omega t) = \sigma_0 e^{i\omega t} \tag{3.8}$$

in which σ_0 is the stress amplitude and ω is the angular velocity, which is related to the frequency f by:

$$\omega = 2\pi f \tag{3.9}$$

By assuming that the inertia effect is negligible, the governing differential equation for the Kevin model can be written as:

$$\lambda_1 \frac{\partial \varepsilon}{\partial t} + E_1 \varepsilon = \sigma_0 e^{i\omega t} \tag{3.10}$$

$\sigma_0 \sin(\omega t)$

E_1

λ_1

(a)

Imaginary

E^*

$|E^*|$

E_2

ϕ

E_1

Real

(b)

σ, ε

Stress $\sigma_0 \sin(\omega t)$

Strain $\varepsilon_0 \sin(\omega t - \phi)$

σ_0

ε_0

ϕ/ω

t

(c)
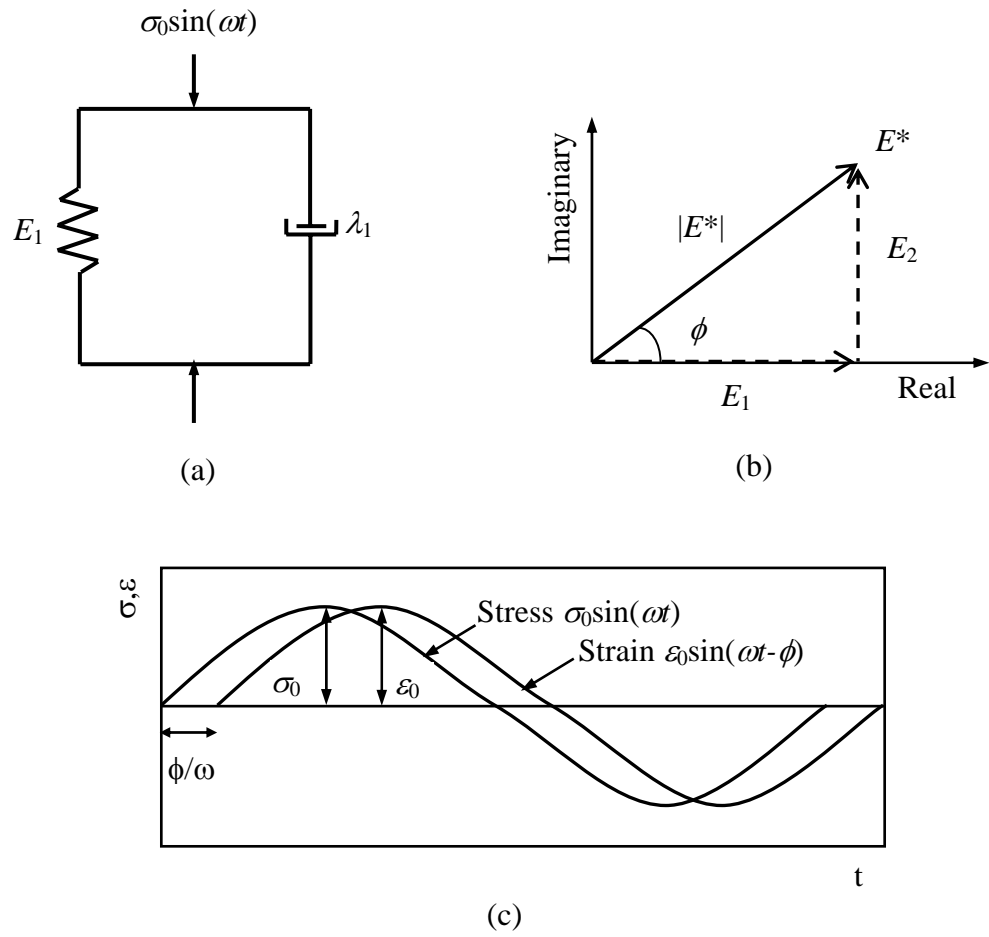
Figure 3.7. Dynamic (Complex) Modulus

Referring to Equation 3.8, the strain due to sinusoidal loading can be expressed as:

$$\varepsilon = \varepsilon_0 e^{i(\omega t - \phi)} \tag{3.11}$$

in which ε_0 is the strain amplitude and ϕ is the phase angle by which the strain lags behind the stress, as shown in Figure 3.7-c. Substituting Equation 3.11 into Equation 3.10 gives:

$$i\lambda_1 \varepsilon_0 \omega e^{i(\omega t - \phi)} + E_1 \varepsilon_0 e^{i(\omega t - \phi)} = \sigma_0 e^{i\omega t} \tag{3.12}$$

After canceling $e^{i\omega t}$ on both side of Equation 3.12 and equaling the real terms to σ_0 and the imaginary terms to zero, the following two equations are obtained to solve ε_0 and ϕ:

$$\lambda_1 \omega \varepsilon_0 \sin \phi + E_1 \varepsilon_0 \cos \phi = \sigma_0 \tag{3.13a}$$

$$\lambda_1 \omega \varepsilon_0 \cos \phi - E_1 \varepsilon_0 \sin \phi = 0 \tag{3.13b}$$

The solutions for Equation 3.13 are:

$$\varepsilon_0 = \frac{\sigma_0}{\sqrt{E_1^2 + (\lambda_1 \omega)^2}} \tag{3.14a}$$

$$\tan \phi = \frac{\lambda_1 \omega}{E_1} \tag{3.14b}$$

For elastic materials, $\lambda_1 = 0$, so $\phi = 0$; for viscous materials, $E_1 = 0$, so $\phi = 90^\circ$. The complex modulus (E^*) is then defined as the ratio of the applied stress $\sigma = \sigma_0 \sin(\omega t)$ to the strain $\varepsilon = \varepsilon_0 \sin(\omega t - \phi)$ that results in a steady state:

$$E^* = \frac{\sigma}{\varepsilon} = \frac{\sigma_0 e^{i\omega t}}{\varepsilon_0 e^{i(\omega t - \phi)}} \tag{3.15a}$$

or $$E^* = \frac{\sigma_0}{\varepsilon_0} \cos\phi + i \frac{\sigma_0}{\varepsilon_0} \sin\phi \qquad (3.15b)$$

The real part of the modulus is called the storage or elastic modulus E_1, while the imaginary part is the loss or viscous modulus $E_2 = \lambda_1 \omega$, shown in Figure 3.7-b:

$$E^* = E_1 + iE_2 \qquad (3.16)$$

Equation 3.14b is the ratio of the energy lost to the energy stored in a cyclic deformation:

$$\tan\phi = \frac{E_2}{E_1} \qquad (3.17)$$

The dynamic modulus is the absolute value of the complex modulus, which is the ratio of the amplitude of the stress to that of the steady-state strain:

$$|E^*| = \sqrt{\left(\frac{\sigma_0}{\varepsilon_0}\cos\phi\right)^2 + \left(\frac{\sigma_0}{\varepsilon_0}\sin\phi\right)^2} = \frac{\sigma_0}{\varepsilon_0} \qquad (3.18)$$

The dynamic compliance ($|D^*|$) is defined as:

$$|D^*| = \frac{1}{|E^*|} = \frac{\varepsilon_0}{\sigma_0} \qquad (3.19)$$

3.4.3 Creep and Relaxation Modulus

Asphalt concrete is characterized as a linear viscoelastic material at low temperatures and as a viscoelastoplastic material at intermediate and high temperatures. Various test procedures have been developed to characterize the viscoelastic behavior of asphalt concrete at low and intermediate temperatures (*55,60*). The mechanical behavior of material is considered to be linear viscoelastic if (1) the proportional change in input causes the same proportional change in response and (2) the response due to

independent inputs acting simultaneously is equal to the sum of the responses due to each input acting separately, which is the superposition principle (*61*).

A linear viscoelastic material is tested at low to intermediate temperatures using creep or relaxation tests. In creep tests, a constant stress (σ_0) is applied on a viscoelastic sample, and the associate strain ($\varepsilon(t)$), as a function of time, is measured. The creep modulus ($S(t)$) and creep compliance ($D(t)$) are defined as follows:

$$D(t) = \frac{1}{S(t)} = \frac{\varepsilon(t)}{\sigma_0} \tag{3.20}$$

In relaxation tests, an instantaneous strain (ε_0) is maintained on a specimen while measuring the stress ($\sigma(t)$) as a function of time. The relaxation modulus is:

$$E(t) = \frac{\sigma(t)}{\varepsilon_0} \tag{3.21}$$

Several methods for estimating the relationship between relaxation modulus and creep modulus are available in the literature (*62,63*).

3.5 History of Dynamic (Complex) Modulus Testing

In 1962, Papazian (*64*) defined the general stress-strain equations of linear, viscoelastic materials as the frequency domain in terms of algebraic coefficients, which were functions of frequency. These coefficients were complex numbers whose magnitude and phase, at any given frequency, depend on the properties of the material. He also described viscoelastic tests performed on asphalt mixtures. A sinusoidal stress was applied on a cylindrical specimen at a given frequency, and a sinusoidal strain response was measured. Tests were conducted under controlled temperature conditions

at different frequencies and loading magnitudes. He concluded that viscoelastic concepts could be applied to asphalt pavement design and performance studies.

In the 1970s, the Asphalt Institute, along with other research agencies, devoted considerable time and effort toward the development of the complex modulus laboratory test procedure. Witczak and Root (*65*) summarized the research findings, including the effect of testing variables, material and test variability on asphalt mixtures, as well as predictive techniques for the complex modulus. They indicated that the tension-compression test was more representative to field loading conditions than the tension loading test and compression loading test. They also reported that the complex modulus test, which measures both elastic and viscous properties of asphalt mixtures, was one of the several fundamental tests available for use in new pavement design procedures. Bonnaure et al. (*66*) set up an experimental program using a bending test to determine the factors that have the greatest influence on the complex modulus of asphalt mixes. The program was in line with work done by other Shell laboratories for more than twenty years in order to predict the stiffness modulus of asphalt mixes using either two nomographs or a computer program.

In 1990, the International Union of Testing and Research Laboratories for Materials and Structures (RILEM) Technical committee on Bitumen and Asphalt Testing initiated an interlaboratory testing program to promote and develop mix design methodologies and associated significant measuring methods (*67*). There were fifteen laboratories in Europe and the US participating in the dynamic modulus testing program. Each laboratory used different facilities and sample geometries to measure the complex moduli at various temperatures and frequencies. Based on the results presented

by the laboratories, the conclusions were that the bending test yielded a better agreement than all others under certain conditions. In addition, the phase angle was easier to reproduce than the stiffness modulus for all the testing procedures and testing conditions.

In the 1990s, complex modulus tests were performed over a range of frequencies and temperatures on both tall cylindrical specimens and indirect tensile specimens of materials used in the Minnesota Road Research Project (Mn/ROAD) (*68-70*). The study showed that the results of dynamic modulus and phase angle obtained from two different setups were different.

The most comprehensive research effort related to complex modulus started in the mid-1990s as part of NCHRP Project 9-19 (*60*). The research proposed a new testing protocol for determining dynamic modulus of hot-mix asphalt concrete mixtures. The protocol specified the specimen geometry and size, and it provided the procedures for specimen preparation, testing, and loading pattern. The protocol also included a brief guideline for constructing a master curve from the dynamic modulus test data.

Based on the NCHRP Project 9-19 research team's recommendation, NCHRP Project 9-29 was initiated to design, procure, and evaluate first-article simple performance testers (SPTs), which would be used in the Superpave mix design and in HMA materials characterization for pavement structural design (*71*). The research team concluded that the Interlaken Simple Performance Test System was not acceptable. The Shedworks Simple Performance Test System was conditionally approved and required minor improvements in several functional areas.

3.6 Factors Affecting Dynamic (Complex) Modulus of Asphalt Mixtures

Previous studies show that the stress-strain response of asphalt mixtures is influenced by several important factors. Witczak et al. (*72*) summarized five major groups of factors that influence the value of the dynamic modulus of bituminous mixes as follows:

(a) Temperature

(b) Time and type of applied load

(c) Mix properties (including those influenced by traffic)

(d) Type of test

(e) Type of specimens

3.6.1 Temperature

Since asphalt binder is a viscous material, its behavior is significantly affected by the test temperature. At extremely cold temperatures of -10°C (14°F) or lower, the dynamic moduli may be greater than 6900 MPa (1x10^{6} psi), which are approaching those presented by PCC-pozzolanic materials. In contrast, at high temperatures of 37.8^{o}C (100 ^{o}F) or more, asphalt binders become less viscous, and modulus values may be lower than 690 MPa (1x10^{5} psi), which are approaching those of dense graded crushed stone base course materials. Therefore, the test temperature is the most significant variable influencing the dynamic modulus of asphalt mixtures. Both dynamic modulus and phase angle are a function of temperature (*65*).

The temperature influence is more complicated when the asphalt layers in service are subjected to local changes of temperature over a year and to a temperature

gradient across the layer depth that may vary in a wide range in a single day. Hence, temperature must be a factor presented in any system for predicting the dynamic modulus.

3.6.2 Time and Type of Applied Load

The time for dynamic stress build-up in the pavement due to a moving wheel also affects the value of dynamic modulus. For a given axle group at a constant mix-environmental condition, as the vehicle velocity increases, the stress load (pulse) time decreases, and the dynamic modulus increases. Therefore, the dynamic response of an asphalt mixture is a function of the vehicle speed or the rate of loading (frequency).

Additionally, since the stress is overlapped between adjacent axle groups, the stress state of an in-service asphalt layer may not go back to a "pure zero" condition before stresses due to the next axle group start increasing again. As such, the length of time on which the material is subjected to a finite induced stress state increases as the number of axle groups increases. Hence, the dynamic response of bituminous materials is also a function of the axle configuration. Generally, the larger the axle configuration, the lower the dynamic modulus response of the material at the same temperature since this corresponds to an increased loading time.

Temperature adds another dimension to the problem here. As temperature decreases, the stiffness of the asphalt layer increases, so the stress is distributed over a larger area of the pavement system. This, in turn, causes a longer stress period, resulting in a reduction of the dynamic modulus. Conversely, during warm conditions, the asphalt mix stiffness is low, and the stress build-up due to a passing axle approaches a series of

applied load repetitions. Hence, the loading time is smaller, and the modulus is larger. Therefore, the dynamic behavior of a bituminous material is also a function of the time of the year.

In order to simulate dynamic stress build-ups on laboratory specimens, two types of laboratory waveform loads normally used are continuous wave (e.g., sinusoidal) and pulse load (e.g., haversine).

The load time (t) for the continuous (sinusoidal) wave pattern is associated with the time for one complete cycle, and frequency (f) is defined as:

$$f = t^{-1} \tag{3.22}$$

Therefore, for a wave load time of 0.1 sec, $f = 10$ Hz.

Pulse load pattern is characterized by two time variables: time of load (t_p) and rest time (t_r). The pulse frequency f' associated with the pulse load is defined as:

$$f' = (t_p + t_r)^{-1} \tag{3.23}$$

However, the true rate of load application (time rate of stress build-up) is:

$$f = t_p^{-1} \tag{3.24}$$

Therefore, for $t_p = 0.1$ sec and $t_r = 0.9$ sec, $f' = 1$ Hz, but $f = 10$ Hz.

Thus, it is important to recognize the type of dynamic load applied when interpreting dynamic response behavior of asphalt materials.

3.6.3 Mix Properties

The dynamic modulus of asphalt mixture is also influenced by the physical and chemical properties of:

(a) asphalt binder (type and aging)

(b) aggregate characteristics (type and gradation)

(c) compacted mix characteristics (gravimetric components and volumetric
components)

Different types of asphalt binder have different viscosity ranges, which relate to the stiffness of asphalt binder. As the stiffness of the asphalt binder increases, the dynamic modulus increases. When field cores are used for testing, there is an increased state of hardness due to additional viscosity increase caused by hardening/aging effects on the material in service.

Aggregate gradation also has an effect on the dynamic modulus. Well-graded aggregates allow more stable mixes and higher dynamic modulus as compared to poorly graded aggregate mixes. Furthermore, as the maximum aggregate size of the mix increases, the dynamic modulus will increase.

The most important mix properties are the amount of effective bitumen and the air voids. The dynamic modulus increases as asphalt content decreases and/or air voids decrease.

3.6.4 Type of Test

Ideally, different types of tests should yield similar modulus values, but several studies have clearly shown that different test procedures do not yield precisely the same results. Therefore, the dynamic modulus is a function of the test method (procedure) used and the way in which dynamic (and/or static) stress states are applied.

The major approaches available to characterize the dynamic modulus of asphalt mixtures are:

(a) Direct Compression

(b) Direct Tension

(c) Indirect Tension

(d) Flexural

Of these, the most widely used is the direct compression test.

3.6.5 Size and Type of Specimen

The specimen geometry and compaction method also affect the dynamic modulus. Generally, the dynamic modulus tests use specimens 4 inches in diameter by 6 inches in height to reduce the effects of specimen geometry on the modulus values (*73*).

Modulus values associated with laboratory compacted specimens and cored specimens from in-service pavements may be different even though gyratory compacted specimens best simulate the in-situ field structure of rolled compacted paving mixtures.

3.7 Dynamic (Complex) Modulus Test

The dynamic modulus test was originally developed in the early 1960s by Ohio State University researchers. In 1979, the test procedure was originally adopted by the American Society for Testing and Materials (ASTM) as a Standard Test Method for Dynamic Modulus of Asphaltic Mixtures (ASTM D 3497-79). The test procedure was refined under NCHRP Project 1-19 (*60*). The new procedure was adopted by AASHTO

as a Standard Method of Test for Determining Dynamic Modulus of Hot-Mix Asphalt Concrete Mixtures (AASHTO TP 62-03) (*74*).

The test method covers procedures for preparing and testing asphalt concrete mixtures to determine the dynamic modulus and phase angle over a range of temperatures and loading frequencies.

First, the test specimen (101.6 mm (4 in.) diameter and 152.4 mm (6 in.) high) is prepared from a gyratory compacted sample (152.4 mm (6 in.) diameter and 170 mm (6.7 in.) high). The unconfined test sample is then subjected to sinusoidal (i.e., haversine) axial compressive stresses at different temperatures and loading frequencies, as shown in Figure 3.8. Each test specimen is tested from low to high temperatures. For each temperature, the specimen is tested from high to low frequencies. This temperature-frequency sequence is specified to minimize damage to the specimen before the next sequential test.

At a given combination of temperature and frequency, the applied stress, which is measured using a load cell, and the resulting recoverable axial strain response of the specimen, which is measured using linear variable displacement transducers (LVDTs), are recorded and used to calculate the dynamic modulus and phase angle.

A basic assumption in the development of the theory for the dynamic (complex) modulus test is that the asphalt mixture behaves as a linear viscoelastic material (*65*). However, it is well known that an asphalt mixture do not always act as a linear material. In order to characterize an asphalt mixture approximately as a linear material, the applied stress must be controlled to maintain axial strains in the range of 50 to 150 microstrain (*74*).
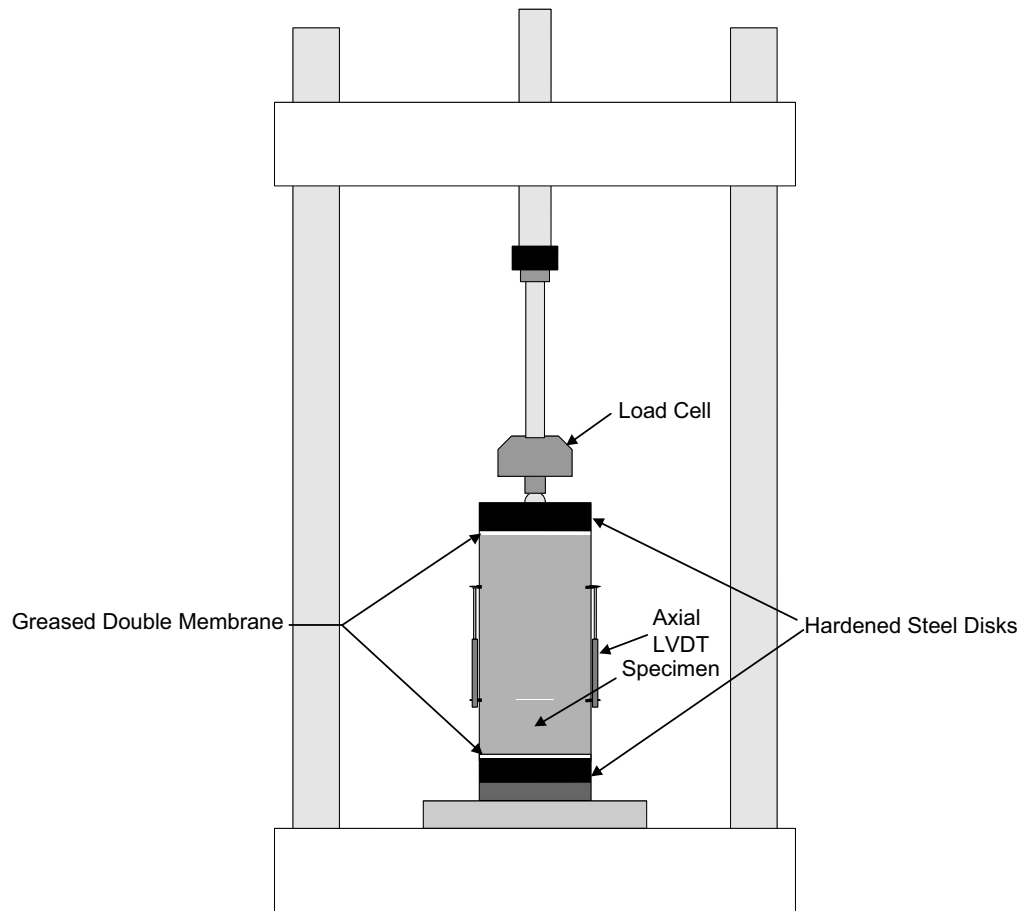
Figure 3.8. Schematic of Dynamic (Complex) Modulus Test (*74*)

Load Cell

Greased Double Membrane

Axial
LVDT
Specimen

Hardened Steel Disks

Dynamic modulus values measured over a range of temperatures and frequencies of loading can be shifted into a smooth master curve for characterizing asphalt concrete for pavement thickness design and performance analysis. The values of dynamic modulus and phase angle can also be used as performance criteria for asphalt concrete mixture design (*60,71*).

3.8 Variability of Dynamic (Complex) Modulus Test Results

Recent studies under NCHRP Projects 9-19 and 9-29 (*71,73,75*) evaluated the testing variability associated with the dynamic (complex) modulus test using variances related to the measurements within and between specimens. In these studies, displacements were measured using two LVDTs placed on either side of the specimen. Each measured displacement was analyzed to determine the component of variance "within" a specimen. Since two replicates were used, the component of variance "between" specimens was also estimated.

Equation 3.25 is used to calculate the "within" specimen variance between the parameters determined from the individual LVDTs in a specimen. A pooled variance for the two replicates is the average of the "within" specimen variances calculated from the two specimens. Then, Equation 3.26 is used to calculate the "between" specimen variance between the average parameters determined for the two specimens.

$$S_w^2 = \frac{1}{n-1} \sum_{i=1}^{n} \left(x_i - \overline{X}_s \right)^2 \tag{3.25}$$

where:

S_w^2 = "within" specimen variance

x_i = parameter from individual LVDT measurements

$\overline{X}_s$ = specimen average parameter

n = number of LVDTs per specimen

$$S_b^2 = \frac{1}{m-1}\sum_{j=1}^{m}\left(\overline{X}_{sj} - \overline{X}\right)^2 \tag{3.26}$$

where:

S_b^2 = "between" specimen variance

$\overline{X}_{sj}$ = specimen average parameter

$\overline{X}$ = grand average

m = number of specimens

Since the dynamic (complex) modulus of asphalt mixtures changes dramatically across affecting factors, such as temperature and frequency, the coefficient of variation (*CV*) is a better choice to evaluate the test variability than the variance. The coefficient of variation, as presented in Equation 3.27, is found to have a normalizing effect allowing data to be combined across temperatures (*73*). In addition to the variance, the coefficient of variation was also investigated as a measure of test variability.

$$CV = \frac{s}{\overline{X}}\times 100 \tag{3.27}$$

where:

CV = "within" or "between" coefficient of variation

s = "within" or "between" standard deviation

$\overline{X}$ = grand average

Table 3.3 summarizes the analysis of test variability from three studies under

NCHRP Projects 9-19 and 9-29. The coefficient of variation was used to evaluate the

variability of the dynamic modulus and phase angle measurements, and the standard

deviation was used to assess the variability of the phase angle. The values reported in

Table 3.3 shows that the test variability is similar in these three studies.

Witczak et al. (*73*) reported that the variances of the parameters in the dynamic

(complex) modulus test were not affected by aggregate size. In addition, the "within"

specimen variability was higher than the "between". This suggested that additional

instrumentation on the specimens would result in greater test reliability.

For a known population variance, the width of the confidence interval is

calculated by Equation 3.28.

$$\pm R = z_{\alpha/2}\left(\frac{\sigma}{\sqrt{n}}\right) \qquad (3.28)$$

where:

R = width of confidence interval

σ = population standard deviation

$z_{\alpha/2}$ = standard normal deviate for selected level of significance

α = level of significance

n = number of samples

Table 3.3. Analysis of Test Variability

Study	Coefficient of Variation for $|E^*|$ (%)		Coefficient of Variation for ϕ (%)		Std. Deviation for ϕ (degree)
	Within	Between	Within	Between	Between
Witczak (*73*)	26.2	15.2	11.0	8.7	2.3
Pellinen (*75*)	39.0	13.0	17.0	10.0	2.3
Bonaquist (*71*)		13.0			1.8

The last term in Equation 3.28 is the standard error of the mean, which is a measure of the dispersion of the data. The standard error is calculated based on the "within" and "between" variances in Equation 3.29 (*73*) for "*i*" LVDTs and "*j*" replicate specimens.

$$\left(\frac{\sigma}{\sqrt{n}}\right) = \sqrt{\frac{\sigma_w^2}{ij} + \frac{\sigma_b^2}{j}}$$ (3.29)

where:

σ_b = "between" specimen standard deviation

σ_w = "within" specimen standard deviation

i = number of LVDTs per specimen

j = number of specimens

According to Witczak et al. (*73*), the coefficient of variation is a more relevant variability indicator for asphalt material tests across different temperatures, and it may be substituted for the standard deviation in Equations 3.28 and 3.29 to calculate the width of the confidence interval.

$$\pm R = z_{\alpha/2}\sqrt{\frac{CV_w^2}{ij} + \frac{CV_b^2}{j}}$$ (3.30)

where:

$z_{\alpha/2}$ = standard normal deviate for selected level of significance

CV_w = "within" specimen coefficient of variation

CV_b = "between" specimen coefficient of variation

i = number of LVDTs per specimen

j = number of specimens

The confidence interval, which was set to a limit of less than ± 15 percent (*74*),

can be used to estimate the number of specimens and the number of LVDTs used per

specimen for the dynamic (complex) modulus test if the test variance is known. Based

the test variability shown in Table 3.3, Witczak et al. (*73*) recommended an optimum

testing program for the dynamic (complex) modulus that used three replicate specimens

instrumented with four LVDTs per specimen. For this testing program, the estimated

standard error of the mean for critical dynamic modulus parameter would be less than

10 percent for mixtures with nominal aggregate sizes of 25 mm or less, and less than 15

percent for 37.5 mm nominal aggregate size.

3.9 Time Temperature Superposition Principle and Shift Factors

Asphalt mixtures in a linear viscoelastic state can be characterized in term of a

common time/frequency and temperature parameter. In other words, the effects of

time/frequency and temperature can be expressed through one joint parameter, reduced

time/frequency at a reference temperature (*76*). This time-temperature superposition

principle allows data from the dynamic (complex) modulus testing conducted within

linear viscoelastic limits at different frequencies and temperatures to form a single

continuous master curve. The master curves for the dynamic modulus ($|E^*|$) and the

phase angle (ϕ) are constructed at a given reference temperature by horizontally shifting

individual curves at other testing temperatures along the time/frequency axis.

Figure 3.9 shows how the curves at other testing temperatures are aligned to

form a single master curve at the reference temperature of 20C (70F). The dynamic

modulus values determined at the temperatures lower than 20C (70F) are shifted to the

right, and those determined at the temperatures higher than the reference temperature are shifted to the left. A fitting model is then used to fit the shifted data, forming a single master curve. The master curve of the modulus, as a function of time, describes the time dependency of the asphalt materials.

The magnitude of shift for each curve at a given temperature is quantified by shift factors, $a(T)$. The testing frequency (f) at a given temperature is divided by a shift factor to get a reduced frequency (f_r) for the master curve, as shown in Equation 3.31 (*57*).

$$f_r = \frac{f}{a(T)} \quad \text{or} \quad \log(f_r) = \log f - \log a(T) \tag{3.31}$$

The shift factor can also be expressed in term of loading time in Equation 3.32.

$$a(T) = \frac{t_r}{t} \quad \text{or} \quad \log(t_r) = \log a(T) + \log(t) \tag{3.32}$$

A master curve can be constructed using an arbitrarily selected reference temperature, T_r, to which all data are shifted. At the reference temperature, the shift factor, $a(T)$, equals to 1. There are several different models used to obtain shift factors of viscoelastic materials, and the most common one is the Williams-Landel-Ferry (WLF) equation (*77*):

$$\log a(T) = \frac{-C_1(T - T_r)}{C_2 + T - T_r} \tag{3.33}$$

where:

$a(T)$ = horizontal shift factor

T = temperature, $^\circ$C

T_r = reference temperature, $^\circ$C

C_1, C_2 = empirical constants

Figure 3.9. Constructing a Dynamic (Complex) Modulus Master Curve

Pellinen (*75*) proposed a new method in which master curves were constructed by fitting a sigmoidal function to the measured dynamic modulus test data using non-linear least square regression. The shifting is done by solving shift factors simultaneously with the coefficients of the sigmoidal function, without assuming any functional form for the relationship of *a(T)* versus temperature. The sigmoidal fitting function is defined in Equation 3.34.

$$\log\left(|E*|\right) = \delta + \frac{\alpha}{1 + e^{\beta - \gamma \log f_r}} \tag{3.34}$$

where:

|E*| = predicted dynamic modulus

δ = minimum value of |E*|

α = span between maximum and minimum value of |E*|

β, γ = parameters describing the shape of the sigmoidal function

f_r = reduced frequency at T_r

The logarithm of the shift factors (i.e. log [$a(T_i)$]) obtained after the development of the dynamic modulus master curve of an asphalt mixture has a second order polynomial relationship with the temperatures in Fahrenheit (*78*).

$$\log\left[a(T_i)\right] = bT_i^2 + cT_i + d \tag{3.35}$$

where:

$a(T_i)$ = shift factor as a function of temperature T_i

T_i = temperature of interest, Fahrenheit

b, c, d = coefficients of the second order polynomial

3.10 Predictive Models for Dynamic (Complex) Modulus

The Mechanistic-Empirical (M-E) Design Guide recommends the dynamic (complex) modulus as a design parameter in the M-E design procedure for flexible pavements (*1*). Currently, there are two models considered reasonably predict the dynamic modulus of HMA mixtures: the Witczak and Hirsch models.

3.10.1 Witczak Model for Estimating Dynamic Modulus

The M-E design procedure proposes three levels of analysis. Level 1 analysis requires actual dynamic modulus test data to characterize properties of the asphalt layers. The test data is used to develop master curves and shift factors based on Equations 3.32 and 3.34. Level 2 and 3 analyses generate master curves using the Witczak's predictive equation, as shown in Equation 3.36 (*2*).

$$\log E = -1.249937 + 0.02932\rho_{200} - 0.001767\rho_{200}^2$$

$$- 0.002841\rho_4 - 0.058097V_a - 0.802208\left(\frac{V_{b0eff}}{V_{beff} + V_a}\right)$$

$$+ \frac{3.871977 - 0.0021\rho_4 + 0.003958\rho_{38} - 0.000017\rho_{38}^2 + 0.005470\rho_{34}}{1 + e^{(-0.603313 - 0.313351\log(f) - 0.393532\log(\eta))}} \quad (3.36)$$

where:

E = dynamic modulus, 10^5 psi

η = bitumen viscosity, 10^6 Poise

f = loading frequency, Hz

V_a = air void content, %

V_{beff} = effective bitumen content, % by volume

ρ_{34} = cumulative % retained on the 19-mm sieve

ρ_{38} = cumulative % retained on the 9.5-mm sieve

ρ_4 = cumulative % retained on the 4.76-mm sieve

ρ_{200} = % passing the 0.075-mm sieve

However, in the Level 2 analysis, the binder viscosity term (η) is determined from the relationship between binder viscosity and temperature, as shown in Equation 3.5. The relationship is established as described in section 3.2.2 based on the Superpave binder tests, such as rotational viscometer (RV) and dynamic shear rheometer (DSR). Level 3 analysis requires no laboratory test data, and the modulus is predicted using the Witczak predictive model, which requires volumetric mix properties from the HMA mixture design and binder viscocity recommended in the M-E Design Guide.

The Witczak's predictive model, as shown in Equation 3.36, has a capability to predict the dynamic modulus of asphalt mixtures over a range of temperatures, rates of loading, and aging conditions from information that is readily available from material specifications or volumetric design of the mixture. Based on the first predictive equation introduced by Shook and Kallas of the Asphalt Institute in 1969, Witczak and his colleagues at the University of Maryland developed and enhanced the model as additional data became available. In 1996, Fonseca and Witczak expanded the model to include the effects of mixture aging caused by both plant mixing and in-service aging (*79*). The final form of the predictive equation, as illustrated in Equation 3.36, is based on 2750 dynamic modulus measurements from 205 different asphalt mixtures tested over the last 30 years in the laboratories of the Asphalt Institute, the University of Maryland, and the Federal Highway Administration (*1*).

Andrei et al. (*2*) claimed that the final of the Witczak equation considered any degree of aging and did not lose accuracy at extreme temperature/frequency conditions. The goodness of fit statistics of the final model are as follows:

- $R^2 = 0.941$ in log space (0.886 in arithmetic space)

- $S_e/S_y = 0.244$ in log space (0.338 in arithmetic space)

3.10.2 Hirsch Model for Estimating Dynamic Modulus

The Hirsch model was originally developed to calculate the modulus of elasticity of cement concrete or mortar based on the assumption that the responses of cement matrix, aggregate and the composite concrete behave in a linear elastic region (*80*). Based on the original model, Christensen (*81*) developed the Hirsch model for HMA during the initial phases of NCHRP Projects 9-25 and 9-31. The model served as a tool for analyzing the effect of changes in air voids, voids in mineral aggregate, and other volumetric mix factors on the modulus of HMA and related mechanical properties.

There are two versions of the Hirsch model for HMA (*81*): one for estimating the dynamic (complex) shear modulus ($|G^*|$), and the other for estimating the dynamic (complex) modulus ($|E^*|$). The Hirsch models for estimating the dynamic (complex) modulus ($|E^*|$) and phase angle (ϕ) of HMA was refined using the dynamic modulus and phase angle data tested at Arizona State University as part of NCHRP Project 9-19. The model for estimating the dynamic modulus was then verified by Christensen using the measured dynamic modulus reported by Alavi and Monismith (*82*).

The mathematical form of the Hirsch model for predicting the dynamic modulus ($|E*|$) is presented in Equation 3.37 (*81*). The Hirsch model is simpler than the Witczak model in that it requires fewer constituent mix properties.

$$|E*| = P_c \left[4{,}200{,}000 \left(1 - \frac{VMA}{100} \right) + 3 \, |G*|_{binder} \left(\frac{VFA \times VMA}{10{,}000} \right) \right]$$

$$+ \left(1 - P_c \right) \left[\frac{1 - \dfrac{VMA}{100}}{4{,}200{,}000} + \frac{VMA}{3VFA \, |G*|_{binder}} \right]^{-1} \tag{3.37}$$

where:

$$P_c = \frac{\left(20 + \dfrac{VFA \times 3 \, |G*|_{binder}}{VMA} \right)^{0.58}}{650 + \left(\dfrac{VFA \times 3 \, |G*|_{binder}}{VMA} \right)^{0.58}}$$

$|E*|$ = dynamic (complex) modulus of HMA, psi

$|G*|_{binder}$ = dynamic (complex) shear modulus of asphalt binder, psi

VMA = voids in mineral aggregates, percent

VFA = voids filled with asphalt, percent

The Hirsch model for estimating phase angle (ϕ) of the dynamic (complex) modulus of HMA is given in Equation 3.38. This model may not be highly accurate but is useful for predicting the phase angle of the dynamic modulus of HMA (*81*).

$$\phi = -21 \left(\log P_c \right)^2 - 55 \log P_c \tag{3.38}$$

The reported correlation coefficient (R^2), a measure of model accuracy, is 0.98 for the Hirsch model for estimating the dynamic modulus of HMA and 0.89 for the Hirsch model for predicting the phase angle (*81*).

3.10.3 Evaluation of Models for Estimating Dynamic Modulus

The final form of the Witczak predictive equation was first evaluated by Pellinen (*75*) using the dynamic modulus test data obtained during NCHRP Project 9-19. The HMA mixtures used to determine the dynamic modulus in NCHRP Project 9-19 were from three experiment sites: MnROAD in Minnesota, FHWA-accelerated loading facility (ALF) in Virginia, and Westrack in Nevada. First, the evaluation was done by matching the predictive stiffness to measured stiffness, as shown in Figure 3.10. The matching showed that the predictive stiffness estimated by the Witczak equation was favorably comparable to the measured values over the entire temperature range of 40 to 100F (*75*). The goodness of fit statistics were also determined for each data set based on the test temperatures to evaluate the correlation between the predicted and measured stiffness, as presented in Table 3.4.

Pellinen (*75*) concluded that the Witczak predictive equation predicted the dynamic modulus of HMA very well. However, the model did not accurately capture the true effect of the mixture volumetric properties (V_a, *VMA* and *VFA*) (*75*).

In another study by Clyne et al. (*83*), the dynamic modulus test was performed on four different asphalt mixtures from the MnRoad experiment site. The test was conducted at six temperatures and five frequencies. The test data was used to generate the master curves of the dynamic modulus. These master curves were compared to those generated from the Witczak predictive equation. For all mixtures, the Witczak predictive equation slightly underpredicted the dynamic modulus of HMA (*83*).
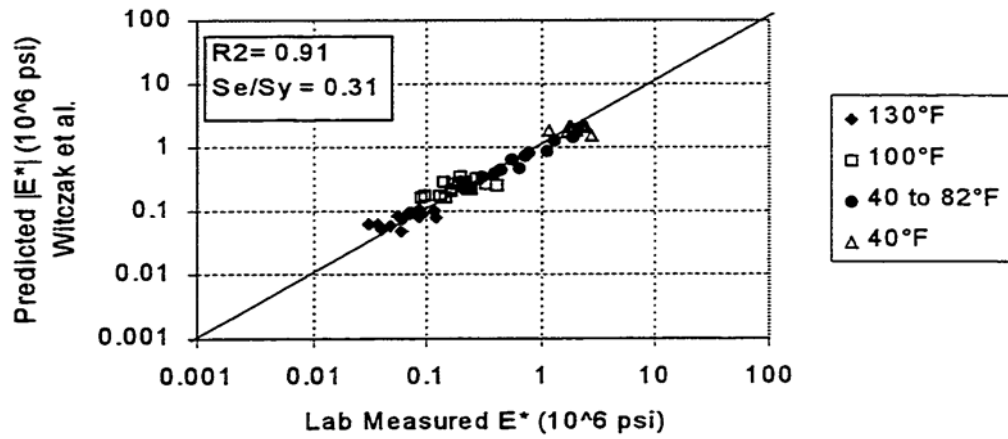
Figure 3.10. Comparing Predictive to Measured Stiffness by Pellinen (*75*)

Table 3.4. Goodness of Fit Statistics for Witczak Model Reported by Pellinen (*75*)

Temperature (F)	R^2	S_e/S_y
130	0.38	0.81
100	0.19	0.93
50-82	0.93	0.28
40	1.06	0.001
40-130	0.91	0.31
100-130	0.66	0.58

In a recent study by Dongre et al. (*84*), dynamic modulus values for asphalt mixtures from five construction sites in the U.S. were estimated using the Witczak and Hirsch predictive models. The predictive dynamic modulus values were then compared to the values measured in the laboratory based on both laboratory-blended (design) mix and plant-produced (sampled) mix. The Superpave binder $|G^*|$ and phase angle data used in the Hirsch model was measured for original, RTFO, and PAV aged asphalt binders used at the construction sites. The binder data was then used to determine the viscosity parameters *A* and *VTS* for the Witczak equation. The NCHRP 1-37A design software was also utilized to predict rutting and International Roughness Index (IRI) using measured and predicted $|E^*|$ data from each construction sites.

The study found that both models reasonably predicted the dynamic modulus of HMA. However, in the statistical evaluation, the Hirsch model ($R^2 = 0.96$, $S_e/S_y = 0.19$) was slightly better than the Witczak model ($R^2 = 0.92$, $S_e/S_y = 0.28$) (*84*). In addition, the Hirsch model was easier to use, required less constituent mix properties, and used Superpave G^* data directly in calculation that reduced a conversion step causing one more source of error.

One problem with both Witczak and Hirsch models was that they lost accuracy when predicting $|E^*|$ values for production samples (*84*). Both models underpredicted $|E^*|$ values when production samples had higher binder content or air voids than the mix design samples. Two equations overpredicted $|E^*|$ values when production sampled had binder content and air voids lower than the values specified in the mix design.

In general, the asphalt concrete rutting predicted by the design software was inconsistent at any Level analysis with different binder grades (from PG 58-28 to PG

70-22) (*84*). In the Level 3 analysis, even though the authors found some trend between rutting and the high temperature PG grades, the differences were not significant. The default *A* and *VTS* values recommended in Level 3 analysis were reported to be significantly different to the values determined in the study (*84*).

In summary, both predictive equations can reasonably predict the dynamic (complex) modulus of HMA. However, both models need some improvements to capture the true effects of mixture properties, which allows accurate predictions of $|E^*|$ in case where the mix properties of production samples deviate from the mix design values.

3.11   Applications of Dynamic (Complex) Modulus

The research team of NCHRP Project 9-19 reported that the dynamic modulus test $|E^*|$ had potential to be a unique Simple Performance Test (SPT) test that would predict asphalt concrete rutting, fatigue cracking (top-down and bottom-up) and thermal fracture distresses from mixture properties (*85*). The dynamic modulus $|E^*|$ can tie the Superpave volumetric mix design directly to the structural field performance through the M-E Design Guide (*85*).

The dynamic modulus is used as the material characterization input in the M-E Design Guide through the master curve development. The master curve incorporates time and temperature dependent material behaviors to the pavement response models, which predict stresses, strains, and deflections in the pavement system. The distress models that incorporate the dynamic modulus test in the design system will address

rutting and fatigue cracking (*1*). Currently, the dynamic modulus of asphalt mixtures is not a performance indicator for thermal cracking (*86*).

3.11.1 Use of Dynamic (Complex) Modulus as An Indicator for HMA Performance

The correlation between the dynamic modulus test data and field performance of HMA was investigated in NCHRP Project 9-19. The correlation of the laboratory measured data and field performance values was assessed using goodness-of-fit statistics. The statistics include S_e/S_y (the standard error of estimate/standard deviation) and correlation coefficient, R^2. Subjective criteria, which were used in NCHRP project 9-19 Task C (*87*), are presented in Table 3.5.

The mixture responses, including $|E^*|$ and $|E^*|/\sin\phi$ measured at 100 and 130F at 5 Hz in unconfined-linear, unconfined-nonlinear and confined-nonlinear conditions, were correlated to rutting (*87*). It was found that the unconfined tests in the linear range had the best correlation to rutting. The best weighted average correlation between rutting and the dynamic modulus test data is presented in Table 3.6. The correlation between the mixture responses and rutting was rated good to excellent. Figure 3.11 presents typical plots and analyses of the test results obtained from ALF site using a power model. Overall, the response parameter $|E^*|/\sin\phi$ of HMA mixture had the best statistical correlation ($S_e/S_y = 0.35$ and $R^2 = 0.90$) with permanent deformation for all experiment sites (MnROAD, ALF, and WesTrack) (*87*).

Table 3.5. Criteria for Goodness of Fit Statistical Parameters (*87*)

Criteria	R^2	S_e/S_y
Excellent	≥ 0.90	≤ 0.35
Good	0.70 – 0.89	0.36 – 0.55
Fair	0.40 – 0.69	0.56 – 0.75
Poor	0.20 – 0.39	0.76 – 0.89
Very Poor	≤ 0.19	≥ 0.90

Table 3.6. Weighted Average Correlation for All Experimental Sites (*87*)

Test Parameter	Stress/Strain Level	130F			
		R^2	S_e/S_y	Rational	Rating
$|E^*|$	UnC-Linear	0.789	0.519	Yes	Good
$|E^*|/\sin\phi$	UnC-Linear	0.914	0.305	Yes	Excellent
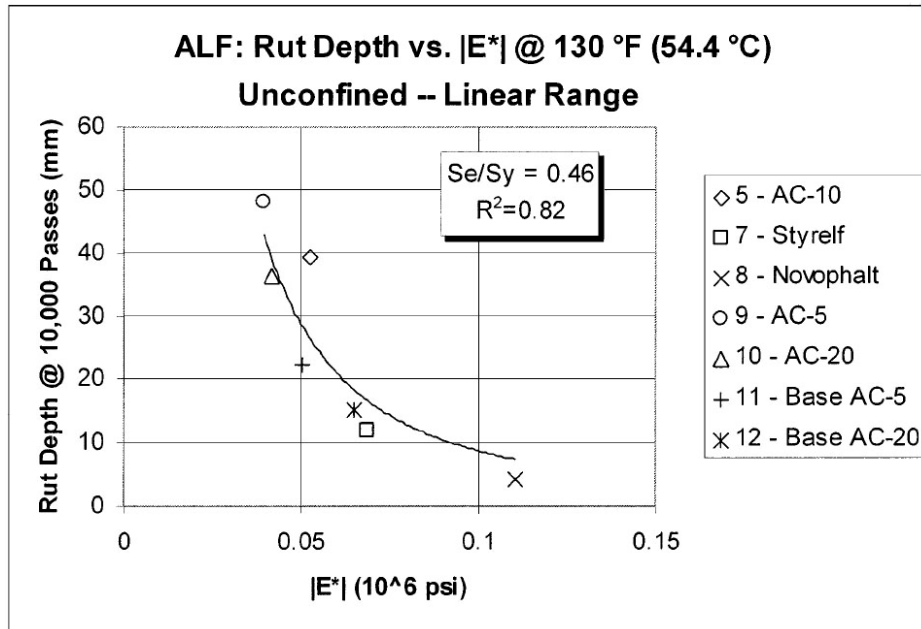
(A)
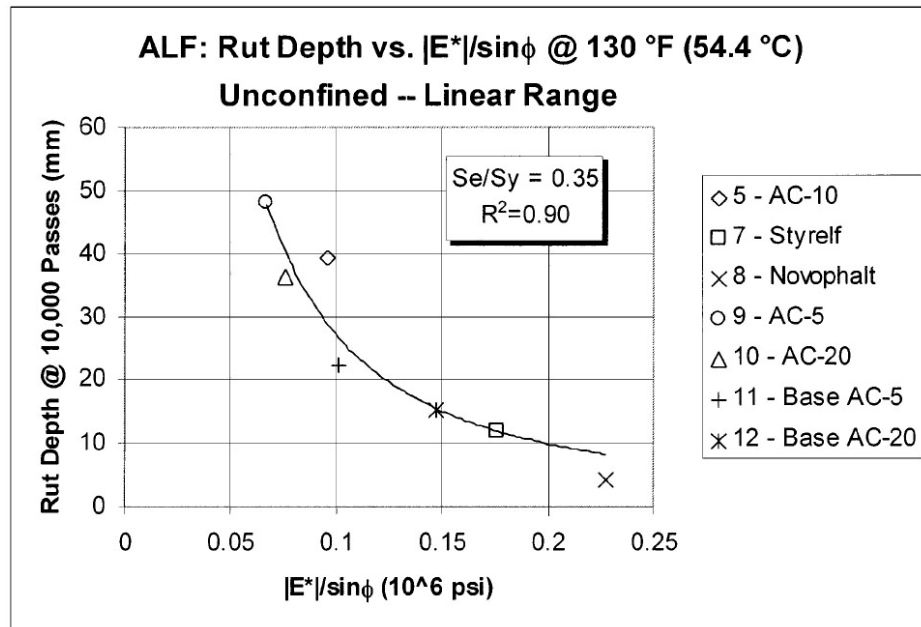
(B)

Figure 3.11. (a) Rut Depth vs. |*E**| and (b) Rut Depth vs. |*E**|/sinϕ (*87*)

In another study under NCHRP Project 9-19, the dynamic modulus test data, including $|E^*|$ and $|E^*|\sin\phi$, was compared to fatigue cracking at ALF and Westrack sites and thermal cracking at MnROAD test. The dynamic modulus $|E^*|$ had a poor relationship ($S_e/S_y = 0.79$ and $R^2 = 0.53$) with thermal cracking at MnROAD test, as shown in Figure 3.12 (*85,86*). The research team recommended further verification of the correlation between $|E^*|$ and thermal cracking. It was found that the stiffness factor $|E^*|\sin\phi$ did not correlate with fatigue cracking, which agreed with findings that the binder stiffness factor $|G^*|\sin\delta$ did not correlate with fatigue cracking (*86*). The only dynamic modulus value measured at 4.4C and 10 Hz under the 206-kPa confined condition had a good and rational correlation ($S_e/S_y = 0.45$ and $R^2 = 0.87$) with fatigue cracking at WetTrack site, as shown in Figure 3.13. Since the effect of confinement on the dynamic modulus test values is very small at the test temperatures below 21C, the dynamic modulus test at the same temperature and frequency under unconfined-linear condition should have similar correlation with fatigue cracking at WestTrack (*85,86*). Therefore, the unconfined dynamic modulus $|E^*|$ was recommended for predicting fatigue cracking in the field.

After the Simple Performance Test (SPT) used with the Superpave mixture design procedure had been recommended by NCHRP Project 9-19, a preliminary field validation of the SPT for permanent deformation was implemented in Texas (*88*). The data used in the study included (1) rut depth measured on Special Pavement Studies-1 (SPS-1) sections on US-281 in Texas, and (2) the calculated parameter $|E^*|/\sin\phi$ obtained from the dynamic modulus test at 40C at 5 and 10 Hz.

MnROAD:Cracking vs |*E*| @ 4.4C 10 Hz
Unconfined – Linear Range
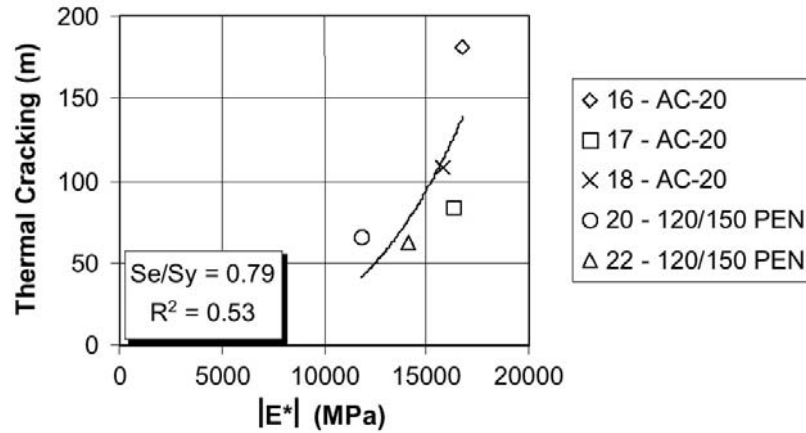
Figure 3.12. Thermal Cracking vs. Dynamic Modulus |*E*| (*86*)

WesTrack:Cracking vs |*E*| @ 4.4C 10 Hz
Confined 207 kPa – Linear Range
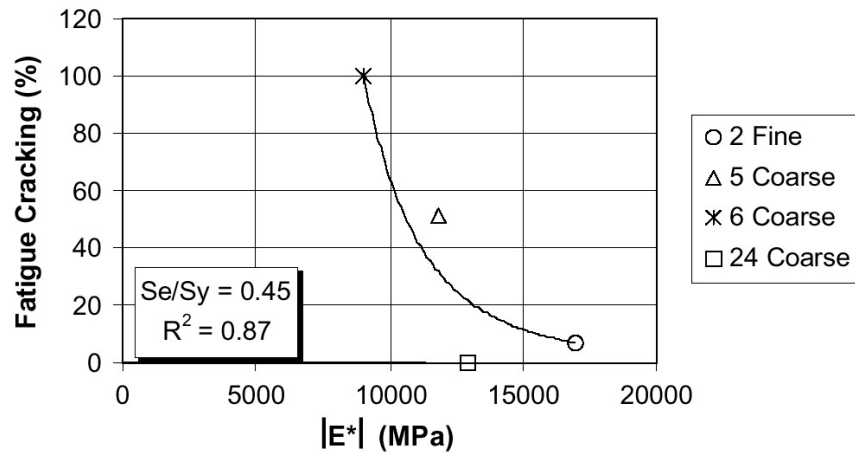
Figure 3.13. Fatigue Cracking vs. Dynamic Modulus |*E*| (*86*)

Both frequencies of 5 Hz and 10 Hz were used in this field evaluation because the frequency of 5 Hz was recommended by Project NCHRP 9-19 teams (*87*) and the frequency of 10 Hz represented actual loading time in the field.

Field rut depth was plotted versus the dynamic modulus |E*| and the calculated parameter $|E^*|/\sin\phi$ at the frequency of 5 Hz, as shown in Figure 3.14. It appeared that both parameters could effectively distinguish the good mixtures from the bad. However, there was a case where S164R, which had a higher modulus than that of S162 and S161, performed the worst in the field. The plots of field rut depth versus the dynamic modulus parameters at 10 Hz had similar trend with those at 5 Hz. Therefore, the dynamic modulus measured at either 5 or 10 Hz could be used to differentiate the good mixtures from the bad.

3.11.2 Use of |E| as An Input for HMA in the M-E Design Procedure*

Asphalt as a viscoelastic-plastic material is sensitive to temperature and the rate of loading. At high temperatures and long rates of loading, the modulus of an asphalt mixture may approach that of an unbound material (*1*). In contrast, the modulus of HMA may approach that of cement concrete at cold temperatures and short loading rates.
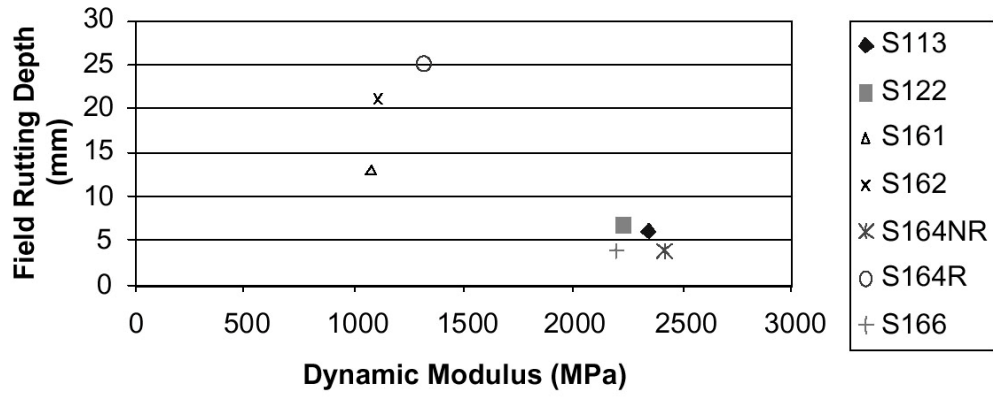
(A)
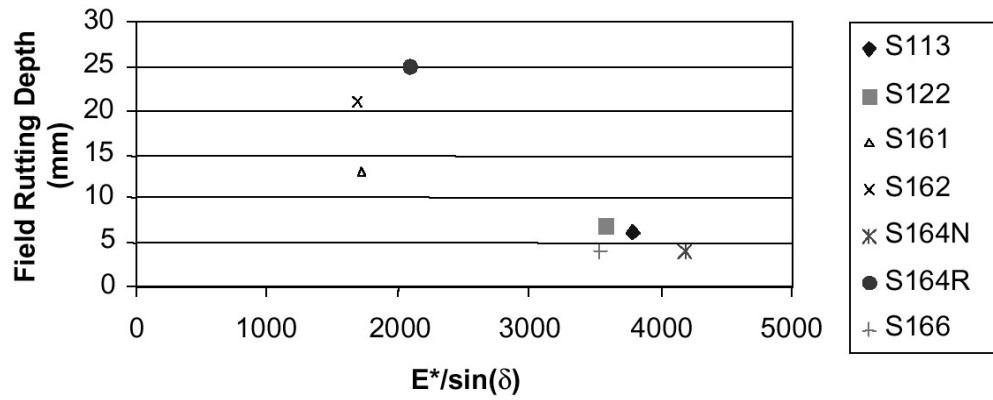
(B)

Figure 3.14. (a) |*E**| and (b) |*E**|/sinϕ at 5 Hz vs. Field Rut Depth (*88*)

74

The use of the dynamic modulus of HMA via a master curve allows the engineer to account for the effects of temperatures and the loading rates in the design methodology (*1*). The effects of temperatures are considered across the range of temperatures expected in the design period. The rate of load effect on material response is a function of the vehicular speed and the location of material within the pavement structure. In general, as loading proceeds deeper into the pavement, the length of the stress pulse acting on a given material increases, suggesting that the time of the load pulse also increases. The design flow chart in Figure 3.15 and the following detailed step-by-step procedure presents the methods of incorporating the effects of temperature and the rate of loading via the use of the dynamic modulus in the M-E Design Guide.

Step 1: Input Data

The detailed input data required for the M-E design procedure is presented in (*1,89*). The general approach for selecting design inputs is based on a hierarchical system, which provides greater flexibility for the engineer in obtaining and selecting design inputs.

Level 1 inputs provide the highest level of accuracy, which is applied for designing heavily trafficked pavements. Level 1 input data requires laboratory or field testing.

Level 2 inputs provide an intermediate level of accuracy, which is closest to the typical procedure used in earlier editions of the AASHTO Guide (*1*). Level 2 design inputs are selected from an agency database or estimated through correlations.
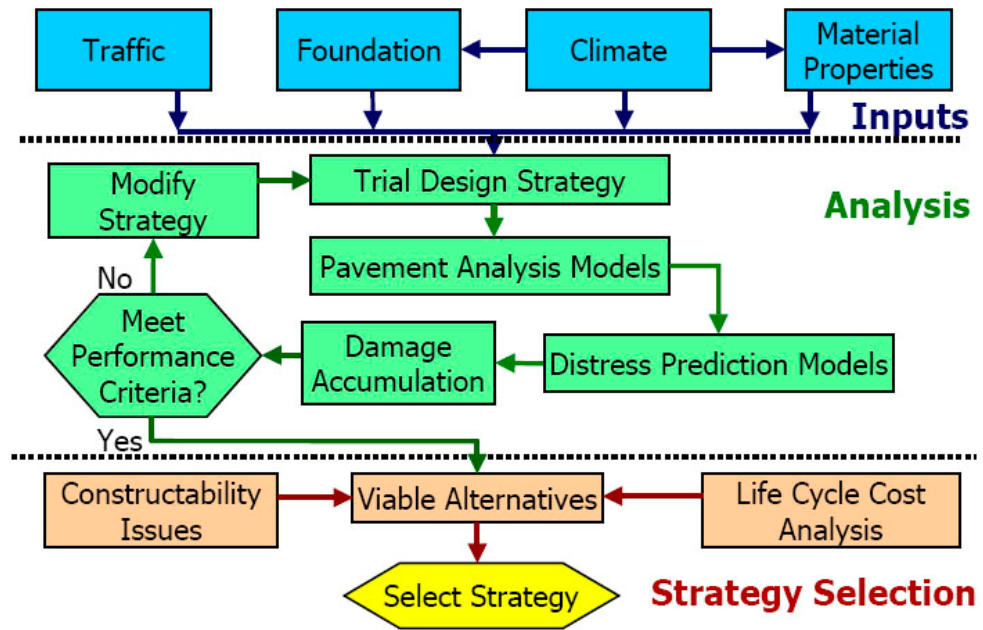
Figure 3.15. Overall Design Process for Flexible Pavement (*1*)

Level 3 inputs provide the lowest level of accuracy. Inputs typically are default

values for the region. For a given design project, inputs may be obtained using a mix of

levels for traffic, climate, and material properties.

Table 3.7 presents a list of required input data for asphalt materials in the

hierarchical system for designing a new flexible pavement.

Step 2: Process Traffic Data

The traffic data needs to be processed to determine the equivalent number of

single axles produced by each pass of tandem, tridem, and quad axles (*90*). In addition,

in order to determine the dynamic (complex) modulus ($|E*|$) of the asphalt layers within

a pavement system, the frequency of loading needs to be determined at all depths. In

general, the stress pulse at a point within a pavement system under a wheel load can be

assumed to be haversine, the relationship relating the time of load to the vehicle speed

and the effective length of the pulse can be expressed in Equation 3.39 (*90*).

$$t = \frac{L_{eff}}{17.6v_s} \tag{3.39}$$

where:

t = time of load, sec

L_{eff} = effective length, in

v_s = velocity, mph

Table 3.7. Hierarchical Approach for Asphalt Materials (*1*)

Design	Input Level	Description
New	1	• Conduct dynamic (complex) modulus ($|E^*|$) test • Conduct G-δ on binder at $\omega = 10$ rad/sec • Simulate short term aging for mix and RTFO for binder • Develop A-VTS for viscosity-temperature relationship • Develop master curve for AC mixture
	2	• No E^* laboratory test required • Use E* prediction equation • Conduct G-δ on binder at $\omega = 10$ rad/sec • Develop A-VTS for viscosity-temperature relationship • Develop master curve for AC mixture
	3	• No E^* laboratory test required • Use E* prediction equation • Use typical A-VTS recommended in the Guide for viscosity-temperature relationship • Develop master curve for AC mixture

The effective length (L_{eff}) at a given point, as illustrated in Figure 3.16, is dependent on the specified depth within the pavement system, the layer properties and the loading configuration (axle spacing and the radius of contact). The procedure for calculating the effective length is detailed in (*90*). Knowing the time of loading pulse, the loading frequency can be calculated using Equation 3.22. When the loading goes to greater depths, the loading frequency decreases. Since asphalt layers are close to the surface, the depth of layer may not be a significant factor, but speed of the vehicle may result in different frequency of load, resulting in different dynamic (complex) modulus of asphalt in the analysis (*90*).

Step 3: Process Climatic Profile Data

The climatic profile data used in the design process is generated using the Enhanced Integrated Climatic Model (EICM) software. The Version 2.6 EICM program is linked to the design software as an independent module. For a flexible pavement, three major climate data files are necessary for the overall design process: (1) temperature frequency distribution for asphalt layers, (2) hourly temperature distribution for thermal fracture, and (3) environment and moisture prediction for unbound material (*1*).
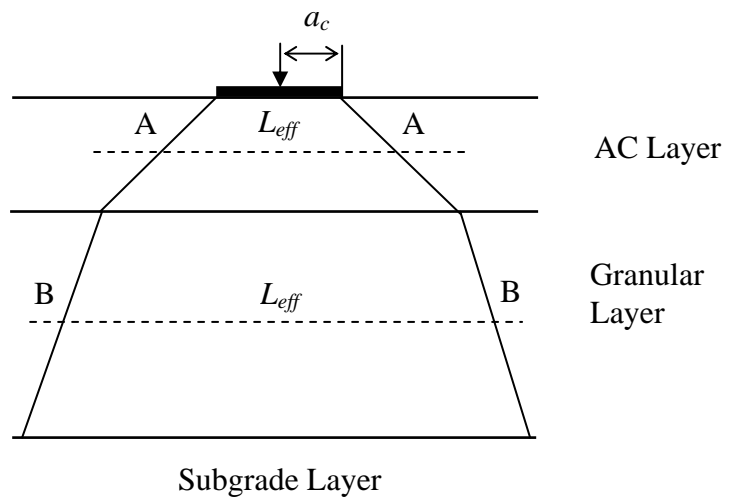
Figure 3.16. Effective Length Concept Within Pavement System (*90*)

Temperature data for a flexible pavement design is computed in a computational analysis period of one month. In case where the pavement is exposed to freezing and thawing cycles, the base unit of 15-day period is used to account for rapid changes in the pavement materials properties during frost/thaw period. Using the average temperature value within a given analysis period will not be able to account for rutting and fractural damage caused by extreme temperatures. Therefore, the frequency distribution of temperature data obtained using EICM program in an analysis period is used to capture the effects of extreme temperatures (*1*).

The EICM program is able to estimate temperature data at intervals of 0.1 hours (six minutes) over an analysis period at a specific depth. The temperature data for a given analysis period of a month or 15 days can be represented by a normal distribution $N(\mu,\sigma)$ (*1*), as shown in Figure 3.17. In order to account for extreme temperatures during the analysis period, the temperature data is divided into five different sub-seasons. For each sub-season, the temperature at the point of interest is defined by a temperature that represents 20 percent of the frequency distribution of the pavement temperature. In this sub-season, only 20 percent of traffic volume during the analysis period is accounted. The sub-season temperatures are computed corresponding to standard normal deviates of –1.2816, -0.5244, 0, 0.5244, and 1.2816, which represent accumulated frequencies of 10, 30, 50, 70 and 90 percent, as illustrated in Figure 3.17 (*89*).

The detailed environment and moisture prediction for unbound material is well explained in (*1,89*).

f(x)

20% 20% 20%

20%　　　　　　　　20%

z = -1.28　z = -0.52　z = 0　z = 0.52　z = 1.28
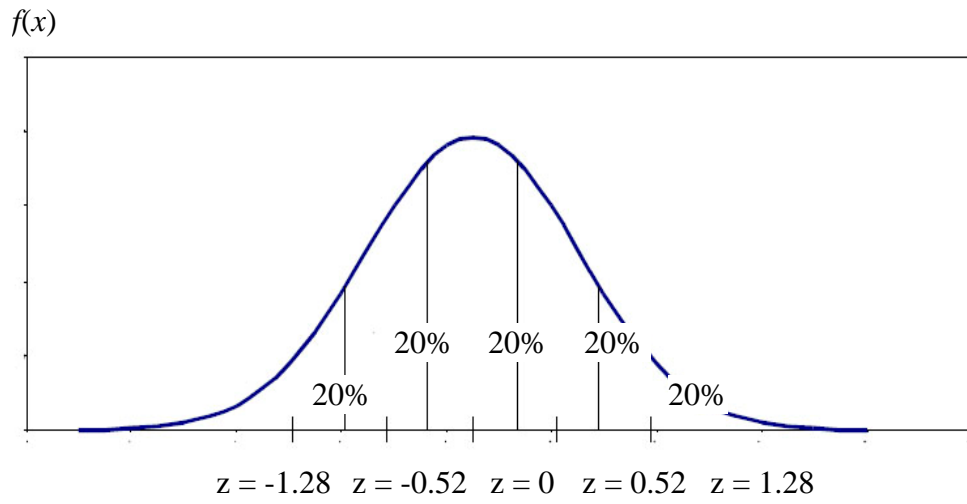
Figure 3.17. Temperature Distribution for an Analysis Period (*89*)

Two pavement structural analysis methods, linear elastic analysis (LEA) and finite element method (FEM), are used in the Design Guide to determine stresses, strains and deformations in flexible pavement systems. The design method that utilizes LEA uses the JULEA multilayer elastic theory program to compute the pavement responses. FEM is used to simulate both linear and nonlinear material behavior. However, the FEM is mainly used for research purposes, and it is not ready for routinely designing of pavements (*1*).

Some critical pavement responses computed in the structural analysis are (*1*):

- Horizontal tensile strain at the surface of the pavement (for HMA fatigue cracking)

- Horizontal tensile strain at the bottom of the HMA layer (for HMA fatigue cracking)

- Horizontal tensile strain at the bottom of the bound or stabilized layers (for fatigue cracking of bound layers)

- Compressive vertical stresses/strains within the HMA layer (for HMA rutting)

- Compressive vertical stresses/strains within the base/subbase layers (for rutting of unbound layers)

- Compressive vertical stresses/strains at the top of the subgrade (for rutting of subgrade)

For permanent deformation analysis, the vertical elastic (resilient) strain at the critical depths (along a vertical axis, defined in the x, y plane) is computed in Equation

3.40 using the three-dimensional stresses and the material properties (modulus and Poisson's ratio) of the HMA layer (*1*).

$$\varepsilon_{rz} = \frac{1}{|E*|}\left(\sigma_z - \mu\sigma_x - \mu\sigma_y\right) \tag{3.40}$$

where:

ε_{rz} = vertical elastic (resilient) strain at the critical depth, in/in

$|E*|$ = dynamic (complex) modulus, psi

μ = Poisson's ratio

σ_z = vertical stress at the critical depth, psi

σ_x, σ_y = horizontal stress at the critical depth, psi

For fatigue cracking analysis, the horizontal elastic (resilient) strain at the critical depths in a layered pavement cross section is computed in Equation 3.41 using the three-dimensional stresses and the material properties (modulus and Poisson's ratio) of the HMA layer (*1*).

$$\varepsilon_{rx,y} = \frac{1}{|E*|}\left(\sigma_{x,y} - \mu\sigma_{y,x} - \mu\sigma_z\right) \tag{3.41}$$

The dynamic (complex) modulus ($|E*|$) of HMA is incorporated in the Design Guide via a master curve. $|E*|$ is a function of the mix properties, temperature, and rate of loading.

Step 5: Predict Pavement Performance

The performance analysis of a pavement structure is based on the accumulation of damage as a function of time and traffic. Damage is estimated and accumulated for

each analysis interval of one month or 15 days. The primary pavement distresses considered in the analysis include (*1*):

- Permanent deformation

- Fatigue cracking (bottom-up and top-down)

- Thermal cracking

- Pavement smoothness (IRI) based on the above primary distresses

In this report, only rutting and fatigue cracking prediction for HMA layers is discussed to demonstrate the use of the dynamic modulus ($|E^*|$) in designing a new flexible pavement. Other important distress prediction procedures, such as rutting in unbound materials layers, fatigue cracking in chemically stabilized layers, thermal cracking, and pavement smoothness, can be found in (*1*)

Permanent Deformation in Asphalt Layers. Total permanent deformation is a product of accumulative ruts occurring in all layers of a pavement system as expressed mathematically in Equation 3.42. However, it is assumed that no permanent deformation occurs in chemically stabilized layers, bedrock, and concrete fractured slabs.

$$RD = \sum_{i=1}^{n} \varepsilon_p^i h^i \tag{3.42}$$

where:

RD = total permanent deformation

n = number of sublayers

ε_p^i = total plastic strain in sublayer i

$$h_i \quad = \text{thickness of layer } i$$

The final model to estimate the plastic strain in the asphalt layers is shown in Equation 3.43. The rutting model is partially calibrated using 387 field rutting observations obtained from 88 new Long-Term Pavement Performance (LTPP) sections in 28 states (*1*).

$$\frac{\varepsilon_p}{\varepsilon_r} = k_1 * 10^{-3.4488} T^{1.5606} N^{0.479244} \tag{3.43}$$

where:

ε_p = accumulated plastic strain at N repetitions of load, in/in

ε_r = resilient strain of the asphalt material, as determined in

       Equation 3.40, in/in

T = temperature, deg F

N = number of load repetitions

k_1 = depth parameter

The depth parameter (k_1) is introduced to correct the confining pressure at different depths, which improves the rut depth prediction. The depth parameter is a function of total asphalt layers thickness (h_{ac}, in) and depth (*depth*, in) to computational point, as shown in Equation 3.44a.

$$k_1 = (C_1 + C_2 * depth) * 0.328196^{depth} \tag{3.44a}$$

$$C_1 = -0.1039 * h_{ac}^2 + 2.4868 * h_{ac} - 17.342 \tag{3.44b}$$

$$C_2 = 0.0172 * h_{ac}^2 - 1.7331 * h_{ac} + 27.428 \tag{3.44c}$$

Fatigue Cracking in Asphalt Layers. The M-E Design Guide provides models to estimate both top-down and bottom-up fatigue damage. The top-down fatigue damage is calculated at the surface of the pavement, and the bottom-up fatigue damage is computed at the bottom of each asphalt layer. The fatigue damage is estimated based on Miner's Law, as shown in Equation 3.45. The fatigue damage is then used to calculate the fatigue cracking (*1*).

$$D = \sum_{i=1}^{T} \frac{n_i}{N_{fi}}$$ (3.45)

where:

        D = fatigue damage

        T = total number of periods

        n_i = actual traffic for period *i*

        N_{fi} = traffic allowed under conditions prevailing in period *i*

In the M-E Design Guide, the number of repetitions to fatigue cracking (N_f) is estimated in Equation 3.46. The model is calibrated based on the data from 82 LTPP sections located in 24 states. The data includes 441 data points for alligator cracking and 408 observations for longitudinal cracking (*1*).

$$N_f = 0.0432 * k_1' * C * \left(\frac{1}{\varepsilon_t}\right)^{3.9492} \left(\frac{1}{|E^*|}\right)^{1.281}$$ (3.46)

where:

        N_f = number of repetitions to fatigue cracking

        k_1' = correction factor

        C = laboratory to field adjustment factor

ε_t = tensile strain at the critical location

$|E^*|$ = dynamic (complex) modulus of the material

The laboratory to field adjustment factor for HMA mixtures is estimated in Equation 3.47a (*1*).

$$C = 10^M \tag{3.47a}$$

$$M = 4.84\left(\frac{V_{beff}}{V_a + V_b} - 0.69\right) \tag{3.47b}$$

where:

V_{beff} = effective binder content, percent

V_a = air void content, percent

The correction parameter ($k_1^{'}$) is introduced in the Design Guide to account for different asphalt layer thickness effects. The parameter can be computed differently for bottom-up and top-down damage as shown in Equations 3.48a and 3.48b, respectively (*1*).

a. For bottom-up fatigue damage

$$k_1^{'} = \frac{1}{0.000398 + \dfrac{0.003602}{1 + e^{(11.02 - 3.49 h_{ac})}}} \tag{3.48a}$$

b. For top-down fatigue damage

$$k_1^{'} = \frac{1}{0.01 + \dfrac{12}{1 + e^{(15.676 - 2.8186 h_{ac})}}} \tag{3.48b}$$

where:

h_{ac} = total thickness of the asphalt layers, in

The fatigue damage computed in Equation 3.45 is utilized to calculate the fatigue cracking using transfer functions as expressed in Equations 3.49a and 3.49b for bottom-up and top-down fatigue cracking, respectively.

a. For bottom-up fatigue cracking

$$FC_{bottom} = \frac{1}{60}\left(\frac{6000}{1 + e^{C_1 + C_2 * \log(D*100)}}\right) \qquad (3.49a)$$

where:

FC_{bott} = bottom-up fatigue cracking, percent lane area

D = bottom-up fatigue damage

C_1 = $-2C_2$

C_2 = $-2.40874 - 39.748 * (1 + h_{ac})^{-2.856}$

b. For top-down fatigue cracking

$$FC_{bottom} = \frac{1}{60}\left(\frac{6000}{1 + e^{C_1 + C_2 * \log(D*100)}}\right) \qquad (3.49b)$$

where:

FC_{top} = top-down fatigue cracking, ft/mile

D = top-down fatigue damage

The reliability design for rutting and fatigue cracking can be found in the M-E Design Guide (*1*).

3.11.3 Effects of HMA Stiffness on Gyratory Compaction Effort

Gyratory compactors are an important part of Superpave mix design system. The ability of different Superpave gyratory compactors (SGCs) to produce similar mix densities is critical. Research has shown that different types of compactor could produce

89

different compaction results. These differences can cause up to 1 percent change in air voids (*4*). The problem is that mixture stiffness causes different frame reactions for each type of gyratory compactor, resulting in different internal gyration angles that affect the gyratory compaction efforts.

In order to solve the above problem, the Dynamic Angle Validation (DAV) was designed to fit inside a SGC mold. The DAV is used with the HMA mixture to measure the internal angle of gyration. During compaction, the DAV is resting on top or bottom of the mix within the mold, as shown in Figure 3.18. The DAV uses two probes connected to a single LVDT to measure the movement between the mold wall and the end plates. The DAV contains a data acquisition, storage and power source. The data is then downloaded onto the computer using the software provided by the manufacturer. The internal angle of gyration is the average of the "top" and "bottom" measured angles.

The DAV is designed to measure the internal angle of gyration during compaction of a full height (115±5 mm) tall HMA mixture. However, some SGC molds are not tall enough for the 81 mm tall DAV and the HMA mixture for a 115 mm tall specimen. In those cases, the DAV procedure is handled using an extrapolation method (*91*).

For extrapolation method, the internal angles of gyration for at least two lesser specimen heights are measured. The internal angle of a full height specimen is then extrapolated using a linear relationship between sample height and internal angle of gyration. The extrapolation method was verified and used in several research projects (*4,5*).
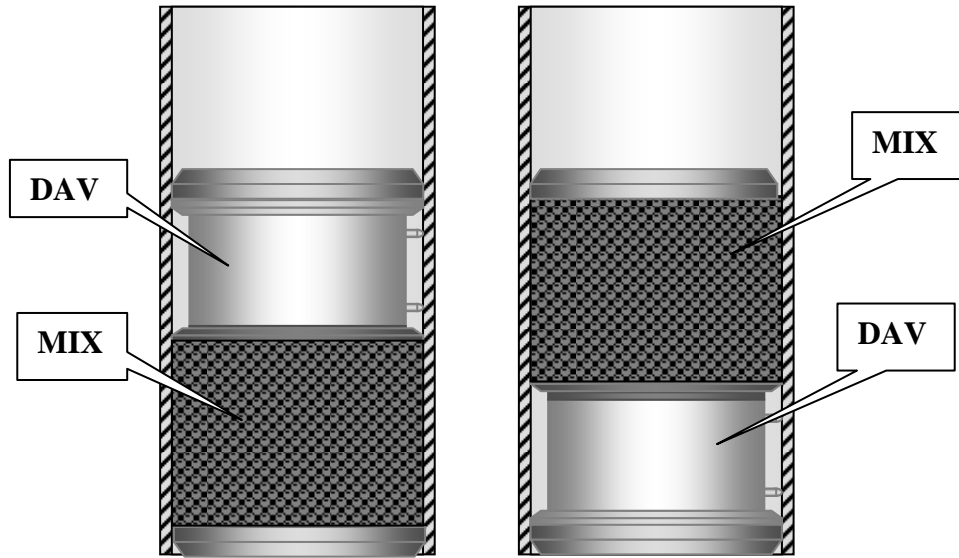
Figure 3.18. Schematic of Internal Angle Measurements Using DAV with Mix (5)

The angle of gyration is influenced by the resistance of the HMA mixture to compaction effort due to the SGC frame reactions. This mixture resistance can be represented by the tilting moment induced during compaction. The tilting moment is a function of the gyratory force, which is a single force representing a compaction load gradient applied on the surface of the HMA specimen, and an eccentricity, which is the distance between the loading point and the centerline, as presented in Figure 3.19.

$$M = F \times e \tag{3.50}$$

where:

M = tilting moment, N-mm

F = gyratory force, approximately 10602 N

e = eccentricity, mm

The compaction force and eccentricity in Equation 3.50 can be measured using the Pressure Distribution Analyzer, as presented in Figure 3.20. The device can fit in the mold of a SGC and measure the gyratory load at three points. The three-point loads are used to determine the gyratory force and eccentricity from the center of the specimen.

Mixtures with a higher resistance to compaction create a steeper gradient shown in Figure 3.19, resulting in a higher eccentricity. An increase in the eccentricity causes an increase in the associated tilting moment, resulting in a lower internal angle due to SGC frame stiffness problem (*92,93*). Research has shown that the internal gyration angle is dependent on the HMA mix characteristics and the type of compactor, and the change can be substantial with some compactors (*94,95*). Various studies have shown that the eccentricity measured by PDA for several mixtures is between 15 and 35 mm (*93,96*).
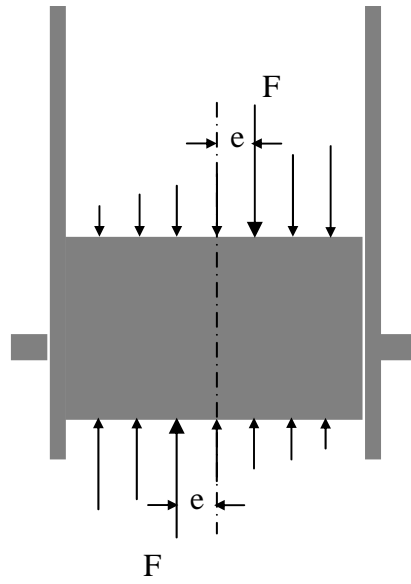
Figure 3.19. Compaction Force and Eccentricity
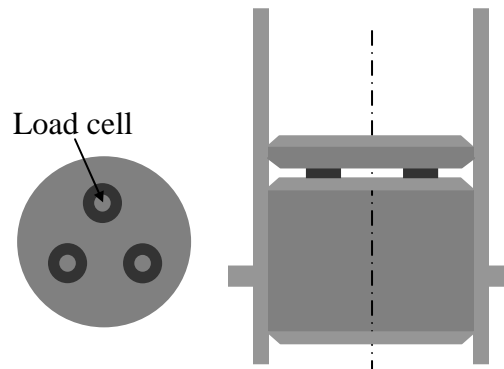
Figure 3.20. Pressure Distribution Analyzer

The above concept of eccentricity is used to develop the simulated loading devices, which are mechanical systems used to measure the internal gyration angle without using HMA mixtures. Two simulated loading devices are currently available: (1) the Hot-Mix Simulator (HMS) working with the DAV to simulate mixture resistance during angle measurement; and (2) the Rapid Angle Measurement (RAM) simultaneously inducing a load on the SGC while measuring the internal angle of gyration.

The HMS simulates the eccentricity concept by transmitting gyratory force through a point of contact between the surface of an upper dome and the inside of a cone-shaped depression, as shown in Figure 3.21. The eccentricity produced by the HMS can be determined using Equation 3.51 presented by the manufacturer (*97*).

$$e = \frac{115 \times \tan \varepsilon}{2} \qquad (3.51)$$

where:

e = eccentricity, mm

ε = angle of depression in upper HMS plate, rad

The RAM uses two raised contact rings to simulate the above eccentricity concept. The radius of these rings provides a known eccentricity for the gyratory force, as presented in Figure 3.22.
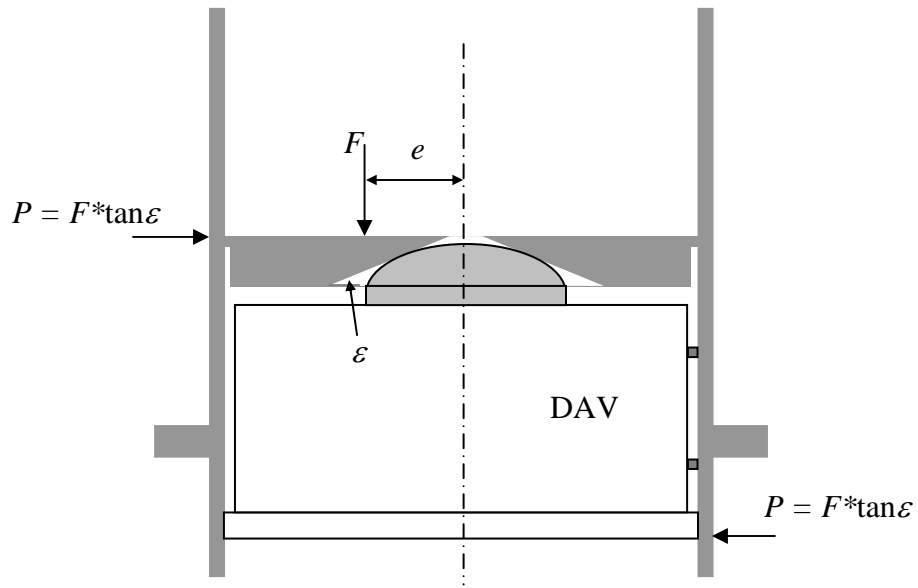
Figure 3.21. Schematic of DAV with HMS
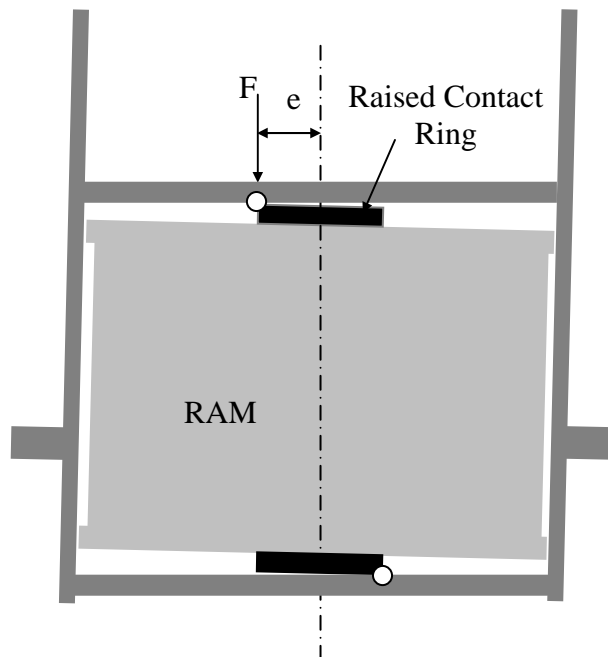
Figure 3.22. Schematic of RAM

Many studies have shown that the DAV procedure, as detailed in AASHTO PP-48, could be used to adjust SGC units to the target dynamic internal angle of 1.16 ± 0.03^o to produce HMA specimens having similar densities (*3*, *4*, *98*). However, the DAV procedure requires the use of HMA with the DAV device, which is considered labor intensive and time consuming. Therefore, it is desired to have a mechanical system that can produce similar results with the DAV procedure, and the HMS with DAV and the RAM are promising candidates for this mechanical system.

Harman et al. (*93*) compared the dynamic internal angles measured by the DAV with HMS and those measured by the DAV with mix. The conclusion was that the differences between the internal angles measured by two devices were not significant. However, the testing plan was limited to one gyratory compactor and two mixtures.

The results measured by the RAM were also compared to those measured by the DAV with mix. Dalton (*92*) reported that the RAM and DAV devices could agree within 0.01^o with a confidence of 90 percent. The precision for the test method for the internal angle using the RAM has been established for various compactors by Hall and Easley (*5*).

In summary, many studies have shown the ability of the DAV to calibrate SGCs to produce similar density samples. However, the current test method requires the DAV to use with HMA mixture. Based on the eccentricity measured by the PDA compacted in the SGC mold with HMA mixture, two simulated loading devices, the HMS and RAM, have been developed. Studies have shown that the HMS with DAV and the RAM were promising alternatives to the DAV with mix. However, since the eccentricity of

the gyratory force is different for each HMA mixture and type of gyratory compactor, more research effort is still needed.

3.12 Summary

Mechanical behaviors of asphalt binders and HMA mixtures were reviewed in this chapter. At mixing and compaction temperatures in the field, asphalt binders typically behave as simple Newtonian or non-Newtonian fluids. However, at low temperatures (under 0C) asphalt binders behave as elastic solids. At intermediate temperatures, asphalt binders act as viscoelastic materials.

To characterize the mechanical behaviors of asphalt binders, the physical properties of asphalt binders must be determined using the Superpave asphalt binder tests. Two asphalt binder tests were reviewed in this chapter: the dynamic shear rheometer (DSR) and rotational viscometer (RV). The DSR test procedure is used to determine the dynamic shear modulus ($|G^*|$) and phase angle (δ) of original, RTFO-aged, and PAV-aged asphalt binders. The RV test provides the viscosity of original binder. The Superpave binder specification uses the DSR test data to determine the binder grade and the binder susceptibility to rutting and fatigue cracking. The RV test data is used to make sure the binder can be pumped and handled at the hot mix facility. In this study, the DSR and RV test data are used as an input to predict the dynamic modulus of HMA.

Mechanical behaviors of HMA are more complicated to characterize than those of asphalt binders. At cold temperatures, HMA mixtures performance is influenced by the viscoelastic behaviors of asphalt binders. At high temperatures (above 50C), the

mixture behavior is dependent on the aggregate structure. At intermediate temperatures, HMA rheology is sensitive to unique properties of the binders.

The mechanical behaviors of HMA can be characterized using HMA stiffness parameters. The HMA stiffness parameters often used are resilient, dynamic, and relaxation moduli. Since it was first introduced in the 1960s, the dynamic (complex) modulus ($|E*|$) of HMA has been refined and developed as standardized ASTM and AASHTO test procedures. The dynamic (complex) modulus of HMA can be measured in the laboratory or predicted from HMA mixture properties using the Witczak or Hirsch predictive model at the temperatures and frequencies that represent the field conditions. The dynamic moduli determined at different temperatures and frequencies are then shifted horizontally along the frequency axis to form a single master curve at a reference temperature.

The dynamic modulus is used as an indicator for rutting and fatigue cracking of HMA mixtures. In addition, it is used via master curves to incorporate time and temperature dependent material behaviors in the M-E Design Guide. The dynamic modulus is used in the pavement response models to predict stresses, strains, and deflections in the pavement system. The pavement responses are then used in the pavement distress models to address rutting and fatigue cracking.

The HMA mixture resistance to compaction was an important factor that affects the consistency of SGCs. Different types of gyratory compactor having different frame stiffness produce different internal gyration angles, resulting in different mixture densities. In order to address this issue, the DAV with mix can be used to calibrate the SGCs in question. Two alternatives, which are considered cheaper and less time

consuming than the DAV with mix, are the HMS with DAV and the RAM. Research

efforts still continue to refine the test methods and implement the internal angle

calibration.

CHAPTER 4: EXPERIMENTAL PLAN

4.1 Dynamic (Complex) Modulus Test

4.1.1 Materials and Mixtures

This section describes the materials and mixtures used in the laboratory test

program. Four aggregate sources were used in the dynamic (complex) modulus study,

including limestone from McClinton Anchor, Inc. (MCA), sandstone from Arkhola, Inc.

(ARK), syenite from Granite Mountain, Inc. (GMQ), and gravel from Jet Asphalt

Company (JET), as shown in Table 4.1. These sources reasonably bracket an expected

range of mixes encountered in Arkansas. HMA mixtures were collected from the

Arkansas State Highway and Transportation Department (AHTD) and then verified in

the asphalt laboratory at the University of Arkansas.

For each aggregate source, a surface mix (12.5 mm), a binder mix (25.0 mm),

and a base mix (37.5 mm) was prepared. The mixes were designed using both binder

grades PG 70-22 and PG 76-22. Design gyration levels and design air voids were

selected corresponding to the type of binder used for the mixtures, as specified in (*99*).

All mix designs, including material gradations and volumetric properties, used in this

study were summarized in Appendix B.

4.1.2 Test Specimen Preparation

The HMA mixtures were prepared at optimum binder contents and compacted at

two air void levels. The HMA mixtures used binder grade PG 70-22 were compacted at

4.5 percent and 7.0 percent air voids, and the mixtures used binder grade PG 76-22 were

compacted at 4.0 percent and 7.0 percent air voids.

Table 4.1. Experimental Matrix

Source	Agg. Size (mm)	Binder Grade and Content	Gyrations	Air Voids (%)
Limestone (MCA)	12.5 25.0 37.5	PG 70-22 Design	100	4.5 7.0
		PG 76-22 Design	125	4.0 7.0
Syenite (GMQ)	12.5 25.0 37.5	PG 70-22 Design	100	4.5 7.0
		PG 76-22 Design	125	4.0 7.0
Sandstone (ARK)	12.5 25.0 37.5	PG 70-22 Design	100	4.5 7.0
		PG 76-22 Design	125	4.0 7.0
Gravel (JET)	12.5 25.0 37.5	PG 70-22 Design	100	4.5 7.0

For each combination of individual parameters shown in Table 4.1, three replicate specimens were prepared. The number of replicates was chosen as recommended by Witczak et al. (*73*). As a result, the experimental plan required 126 specimens to be tested.

Each mixture was mixed and compacted at the temperatures specified in the mix design. All mixtures were conditioned in the oven for four (4) hours before compaction at the compaction temperatures for short-term mixture conditioning for mechanical property testing, as specified in (*100*).

The samples were compacted with a Pine gyratory compactor in a 150 mm diameter mold to 170 mm height. The quantity of mixture for each specimen to meet the target air voids was determined from a trial compaction program. For each testing combination, three gyratory compacted specimens were compacted using 6400, 6600, and 6800 gram of asphalt mixture. Then, three trial test specimens, 150 mm high and 100 mm diameter, were cored and end-cut from the gyratory compacted specimens. Finally, the air voids of the trial specimens were determined. It was found that the relationship between the mixture quantity used for gyratory compacted specimens and the air voids of the associated trial test specimens could be estimated using a linear regression model. Therefore, a linear regression representing the relationship between the mixture quantity for gyratory compacted specimens and the air voids of the trial test specimens was determined for each testing combination. Based on the linear regression, the quantities of HMA mixture used to produce specimens at the target air voids were determined. Figure 4.1 presents an example of the trial procedure to determine the mix quantities for test specimens that meet the target air voids.

MCA-25, PG 70-22

Trial Results:

A.void (%)	7.3	5.0	2.5
Mix Quantity (g)	6400	6600	6800

MCA-25, PG 70-22

$y = -83.285x + 7010.9$

$R^2 = 0.9994$
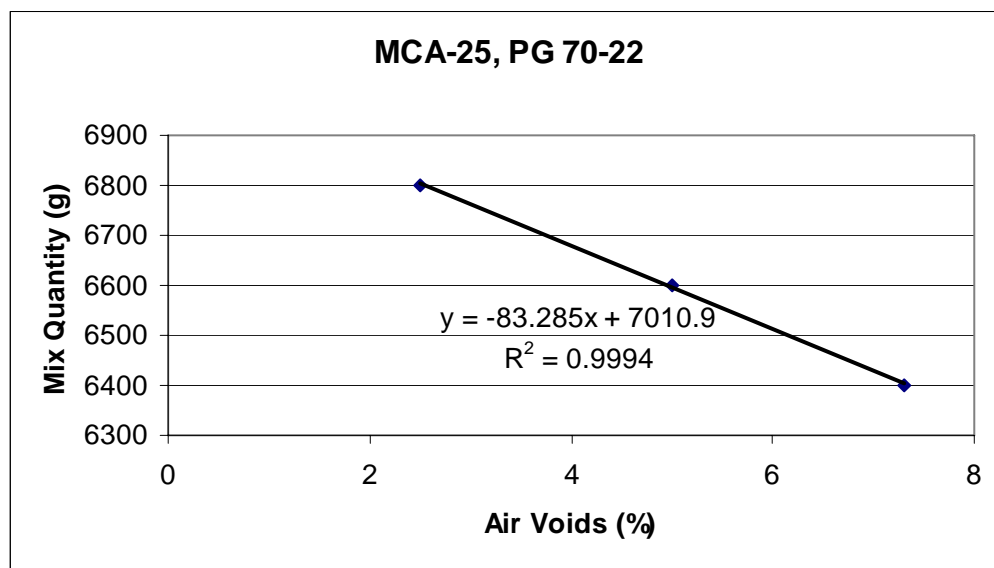
Targeted Mix Quantities:

A.void (%)	7.0	4.5
Mix Quantity (g)	6428	6636
Rounded (g)	**6430**	**6640**

Figure 4.1. Mix Quantities to Meet Target Air Voids

Tables 4.2, 4.3, and 4.4 summarize the mix quantities used to produce the test specimens that had the target air voids of 4.0, 4.5, and 7.0 percent. The data provided in these tables would be useful for future studies. For the same mix designs used in this study, the quantity of HMA mixture required to produce a sample at the target air voids of 4.0, 4.5, or 7.0 percent can be obtained directly from the tables. For those samples compacted at other target air voids, the quantity of HMA mixture can be linearly interpolated/extrapolated from the appropriate data presented in the tables.

After the trial compaction program, three gyratory compacted specimens were prepared for each testing combination. Then, the test specimens, 100 mm diameter and 150 mm height, were cored and end-cut from the gyratory compacted specimens. Figure 4.2 shows a test specimen of 100 mm diameter and 150 mm height next to a gyratory compacted specimen of 150 mm diameter and 170 mm height.

Finally, the air voids and geometric properties of each specimen were determined for acceptance. Table 4.5 provides the criteria for acceptance and rejection of test specimens. A step-by-step diagram, as illustrated in Figure 4.3, summarizes the procedure for preparing test specimens.

4.1.3 Selection of Test Parameters

In order to develop of master curves for all mixtures to use in the M-E Design Guide, each specimen was tested at 5 different temperatures and at 6 different frequencies for each test temperature, as shown in Table 4.6. The other parameters, such as dynamic stresses and cycles, were selected corresponding to the test temperatures and frequencies, respectively.

Table 4.2. MCA Mixture Quantities for Test Specimens

Aggregate Source	Aggregate Size (mm)	Binder Grade	Air Voids (percent)	Mix Quantity (g)
MCA	12.5	PG 70-22	4.5 %	6660
			7.0 %	6470
		PG 76-22	4.0 %	6690
			7.0 %	6450
	25.0	PG 70-22	4.5 %	6640
			7.0 %	6430
		PG 76-22	4.0 %	6580
			7.0 %	6290
	37.5	PG 70-22	4.5 %	6590
			7.0 %	6320
		PG 76-22	4.0 %	6580
			7.0 %	6330

Table 4.3. GMQ Mixture Quantities for Test Specimens

Aggregate Source	Aggregate Size (mm)	Binder Grade	Air Voids (percent)	Mix Quantity (g)
GMQ	12.5	PG 70-22	4.5 %	6770
			7.0 %	6570
		PG 76-22	4.0 %	6800
			7.0 %	6560
	25.0	PG 70-22	4.5 %	6740
			7.0 %	6450
		PG 76-22	4.0 %	6680
			7.0 %	6380
	37.5	PG 70-22	4.5 %	6870
			7.0 %	6640
		PG 76-22	4.0 %	6860
			7.0 %	6600

Table 4.4. ARK and JET Mixture Quantities for Test Specimens

Aggregate Source	Aggregate Size (mm)	Binder Grade	Air Voids (percent)	Mix Quantity (g)
ARK	12.5	PG 70-22	4.5 %	6560
			7.0 %	6360
		PG 76-22	4.0 %	6590
			7.0 %	6340
	25.0	PG 70-22	4.5 %	6520
			7.0 %	6300
		PG 76-22	4.0 %	6560
			7.0 %	6300
	37.5	PG 70-22	4.5 %	6440
			7.0 %	6140
		PG 76-22	4.0 %	6500
			7.0 %	6210
JET	12.5	PG 70-22	4.5 %	6680
			7.0 %	6490
	25.0	PG 70-22	4.5 %	6570
			7.0 %	6310
	37.5	PG 70-22	4.5 %	6640
			7.0 %	6430

Figure 4.2. Gyratory-Compacted and Cored Specimens

Table 4.5. Criteria for Acceptance of Test Specimens (*74*)

Criterion Items	Requirements
Size	Size of sample: 100 mm in diameter by 150 mm in height
Coring	Nominal diameter of sample after coring: 100 mm
	Side of sample after coring: smooth, parallel, and free from steps, ridges, and grooves
Diameter (*)	Standard deviation of six measurements: not greater than 2.5 mm
Ends	Ends of sample after sawing: smooth and perpendicular to the axis
	Tolerance of a cut surface waviness height: ± 0.05 mm across any diameter
	Angle departing from perpendicular to axis of specimen: not more than 0.5 degrees
Air Void Content	Air Void Content of test Specimen: within 0.5 percent from the target air void content

Notes: (*) The diameters of a test specimen were measured at the mid height and third points along axes that are 90 degrees apart.

```
┌─────────────────────────────────────────────┐
│ **Aggregate Preparation:**                   │
│                                              │
│ Dry Aggregate                                │
│                                              │
│ Fractioning                                  │
│                                              │
│ Batching                                     │
└─────────────────────────────────────────────┘
                        │
                        ▼
┌─────────────────────────────────────────────┐
│ **Mixing and Compaction:**                   │
│                                              │
│ Mixing                                       │
│                                              │
│ Aging (4 hours)                              │
│                                              │
│ Compaction (H170 * D150)                     │
└─────────────────────────────────────────────┘
                        │
                        ▼
┌─────────────────────────────────────────────┐
│ **Gmb Test for Compacted Specimens:**        │
│                                              │
│ Gmb Test (SSD Test)                          │
└─────────────────────────────────────────────┘
                        │
                        ▼
┌─────────────────────────────────────────────┐
│ **Coring and Sawing:**                       │
│                                              │
│ Coring (H170 * D100)                         │
│                                              │
│ Sawing (H150 * D100)                         │
└─────────────────────────────────────────────┘
                        │
                        ▼
┌─────────────────────────────────────────────┐
│ **Gmb Test for Test Specimens:**             │
│                                              │
│ Drying Core                                  │
│                                              │
│ Gmb Test (SSD Test)                          │
└─────────────────────────────────────────────┘
                        │
                        ▼
┌─────────────────────────────────────────────┐
│ **Acceptance of Test Specimens:**            │
│                                              │
│ Diameter, Ends                               │
│                                              │
│ Air Void Content                             │
└─────────────────────────────────────────────┘
```
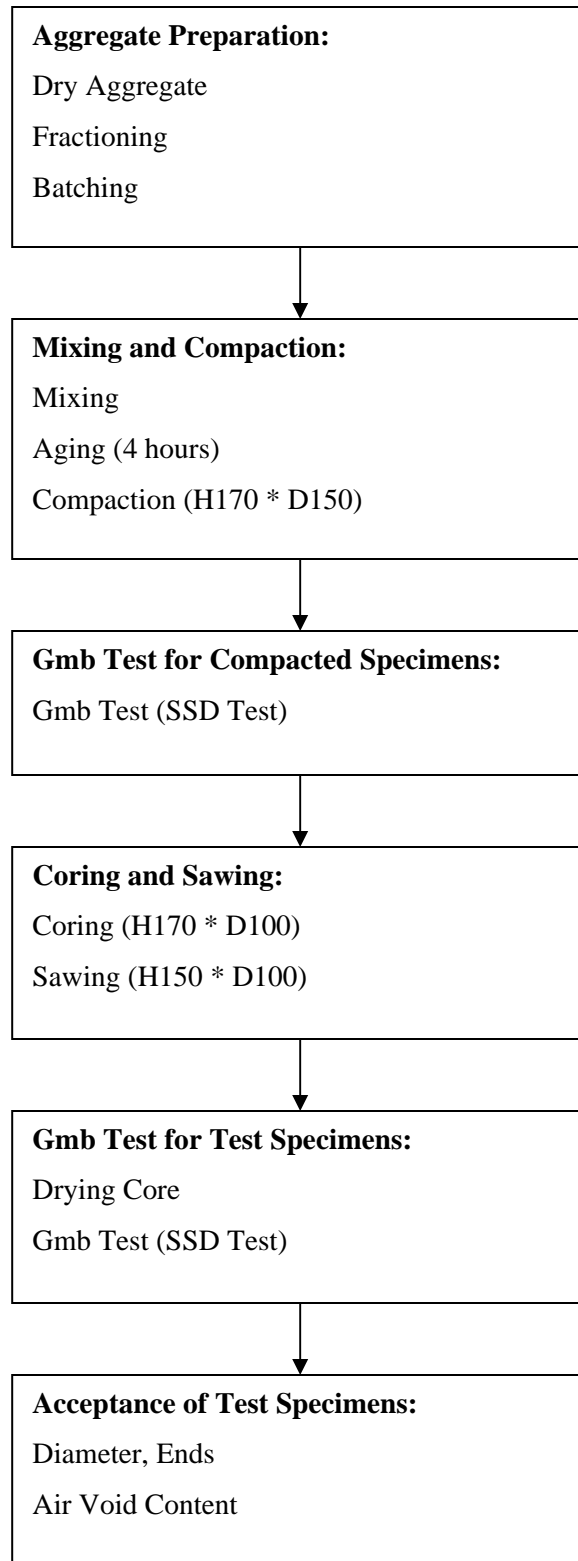
Figure 4.3. Procedure for Preparing Test Specimens

Table 4.6. Test Parameters (*74*)

Parameters	Values
Temperature	At –10, 4.4, 21.1, 37.8, and 54.4^{o}C (14, 40, 70, 100, and 130°F)
Frequency	At 25, 10, 5, 1, 0.5, 0.1 Hz
Contact Load	5 percent of the dynamic load
Preconditioning	With 200 cycles at 25 Hz
Axial Strains	Between 50 and 150 microstrain
Dynamic Stress (*)	At -10 ^{o}C (14°F): 1400 to 2800 kPa (200 to 400 psi)
	At 4.4^{o}C (40°F): 700 to 1400 kPa (100 to 200 psi)
	At 21.1^{o}C (70°F): 350 to 700 kPa (50 to 100 psi)
	At 37.8^{o}C (100°F): 140 to 250 kPa (20 to 50 psi)
	At 54.4 ^{o}C (130°F): 35 to 70 kPa (5 to 10 psi)
Cycles	At 25 Hz: 200 cycles
	At 10 Hz: 200 cycles
	At 5 Hz: 100 cycles
	At 1 Hz: 20 cycles
	At 0.5 Hz: 15 cycles
	At 0.1Hz: 15 cycles

(*) The dynamic load should be adjusted to obtain axial strains between 50 and 150 microstrain.

4.1.4 Dynamic (Complex) Modulus Test Procedure

The test was run on each test specimen at five different temperatures, including -10, 4.4, 21.1, 37.8, and 54.4C (14, 40, 70, 100, and 130F), and the test started from the lowest temperature to the highest temperature. For each test temperature level, the test was run at six different frequencies from the highest to the lowest, including 25, 10, 5, 1, 0.5, 0.1 Hz. All testing was conducted in an unconfined condition.

At each temperature, the specimen was placed in the environmental chamber and allowed to equilibrate to the specified testing temperature ± 0.5C (1F). The specimen temperature was monitored using a dummy specimen with a thermocouple mounted at the center. Once the specimen reaches the specified test temperature, four LVDTs were mounted on the specimen using two aluminum rings, as shown in Figure 4.4, and they were adjusted to near the end of their linear range to allow the full range to be available for the accumulation of compressive permanent deformation. As for the number of replicates, the number of LVDTs used in this testing plan was chosen as recommended by Witczak et al. (*73*). A testing program used three replicated specimens instrumented with four LVDTs was optimum for dynamic (complex) modulus testing (*73*).

Two 0.5 mm (0.02 in.) thick latex membranes separated with silicone grease were placed between the specimen and the hardened steel disks at the top and bottom. The test specimen was centered with the hydraulic actuator in order to avoid eccentric loading. The specimen was allowed to equilibrate in the environmental chamber for another one hour.
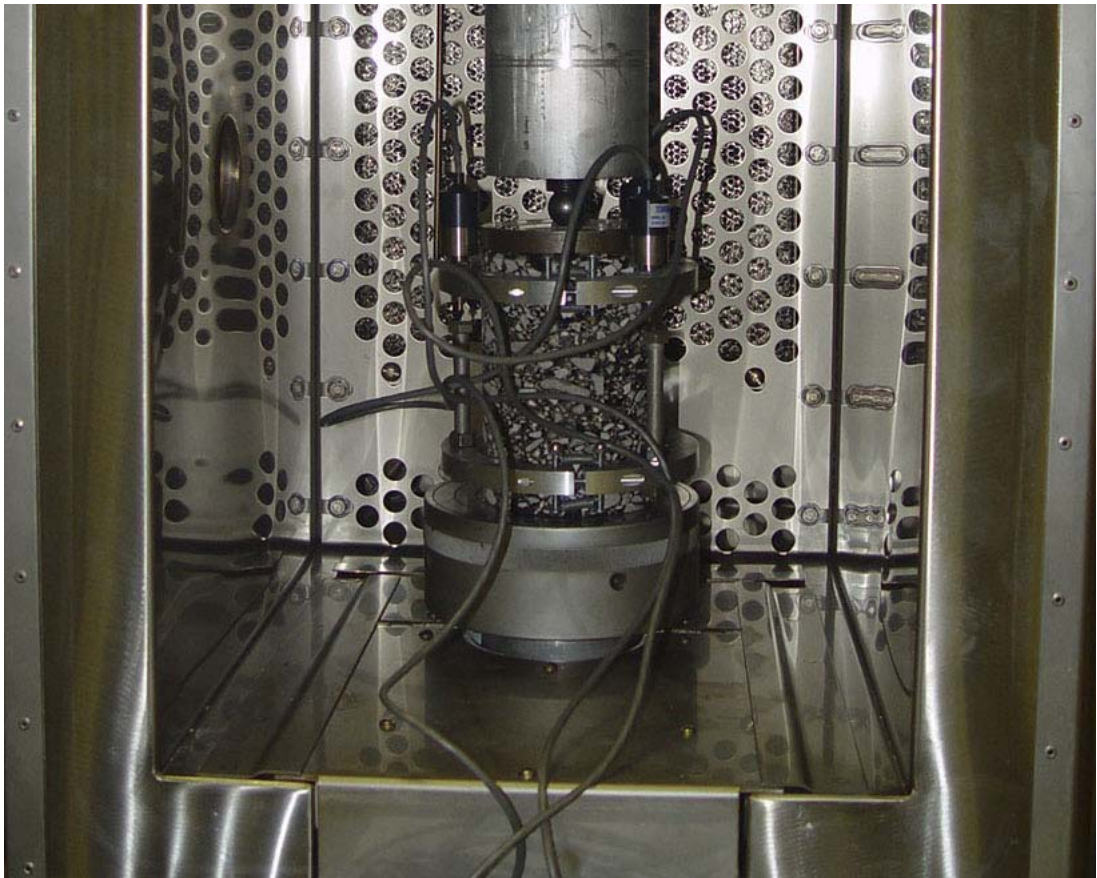
Figure 4.4. Dynamic Modulus Test Setup

To begin testing, the LVDTs were zeroed, and a minimal contact load was applied to the specimen. A sinusoidal axial compressive load was applied on the specimen in a cyclic manner. The specimens were preconditioned using 200 cycles at 25 Hz. The load was then adjusted to keep the axial strains between 50 and 150 microstrain (*74*). Testing was continued from 25 Hz through 0.1 Hz. The number of test cycles for each frequency was shown in Table 4.6.

It was required to keep the axial strain between 50 and 150 microstrain at the end of each frequency testing period and the cumulative un-recovered permanent strain under 1500 microstrain at the end of any testing series for each temperature. This requirement was to ensure the testing was performed in the linear viscoelastic range of the HMA mixtures. To meet this requirement, the dynamic stress at each testing temperature was determined using a trial and error procedure. The minimum recommended dynamic stress at each temperature, as shown in Table 4.6 was first applied. Then, it was increased in an increment of 20 percent of the minimum recommended dynamic stress to meet the axial strain requirement.

Finally, the data acquisition system was setup to record the last six cycles at each frequency with about 200 points per cycle. The test data, including loading time, loading magnitude, and vertical deformation measured by LVDTs, were then stored for latter analyses.

4.2 Internal Gyration Angle Study

The objectives of the internal angle study are (1) to determine if siffness (in form of the dynamic modulus) of HMA mixtures significantly affects the internal angle

measurements; and (2) to evaluate if the simulated loading devices (the HMS with DAV and the RAM) can replace the DAV with mix to calibrate the internal angle of different SGCs. In order to accomplish the aforesaid objectives, the internal angle study was performed as follows:

- Study 1 was to determine the internal angles of different SGCs using the DAV with mix

- Study 2 was to have the internal angles of SGCs using the simulated loading devices, Hot-Mix Simulator (HMS) with DAV and Rapid Angle Measurment (RAM)

- Study 3 was to obtain the eccentricities induced during compacting the HMA mixtures or the simulated loading devices

The detailed testing programs for the above studies are presented in the following sections.

4.2.1 Study 1

Two aggregate sources were used for Study 1, including limestone from McClinton Anchor, Inc. (MCA) and sandstone from Arkhola, Inc. (ARK). For each aggregate source, a surface mix (12.5 mm) and a binder mix (25.0 mm) were prepared. The mixes were designed using both binder grades PG 70-22 and PG 76-22. All mix designs, including material gradations and volumetric properties, were summarized in Appendix B.

Two gyratory compactors (Pine Model AFGC125 and Troxler Model 4141) were used in this study. The Pine SGC has an internal angle of 1.17^{o}, which is in the

target internal angle range of 1.16 ± 0.03^o (*3*). The Troxler SGC has an angle of 1.07^o, which is out of the above target internal angle range. By choosing these SGCs for this study, it was expected that the study results would be good for different SGCs whose internal angles were in or out of the aforesaid target range.

The testing matrix for Study 1 is presented in Table 4.7. For the Pine SGC, the test specimens were compacted to 115 mm high using 4,500 g of mix. However, since the molds for the Troxler SGC are not tall enough for the 81 mm tall DAV and the HMA mixture for a 115 mm tall specimen, the DAV procedure is handled using the extrapolation method, and the internal angles corresponding to the 115 mm specimens were linearly extrapolated using the angles measured using 35 and 65 mm high specimens. The HMA mixtures used for 35 and 65 mm specimens were 1,250 and 2,450 g, respectively. For each testing combination presented in Table 4.7, three replicates were used to measure the top internal angles, and three were used for the bottom angles.

A DAV unit, as shown in Figure 4.5, was placed on top or bottom of the mix within the mold to measure the movement between the mold wall and the top and bottom plates during the compaction of the mix. The movement data were stored in the DAV unit and downloaded onto the computer using TestQuip software provided by the manufacturer. Figure 4.6 shows the movement data acquired from the DAV using the TestQuip Software. The data file was then saved as a .cvs file that was used to determine the internal gyration angle using a spreadsheet provided by the manufacturer.

Table 4.7. Testing Plan for Internal Angle Study 1

SGC	Agg.	Size	Binder	Est. Ht. (mm)	Mix Qt. (g)	No. of Replicate
PINE 125X	MCA	12.5	70-22	115	4500	3 Top & 3 Bott.
			76-22	115	4500	3 Top & 3 Bott.
		25	70-22	115	4500	3 Top & 3 Bott.
			76-22	115	4500	3 Top & 3 Bott.
	ARK	12.5	70-22	115	4500	3 Top & 3 Bott.
			76-22	115	4500	3 Top & 3 Bott.
		25	70-22	115	4500	3 Top & 3 Bott.
			76-22	115	4500	3 Top & 3 Bott.
BABY TROXLER 4141	MCA	12.5	70-22	35	1250	3 Top & 3 Bott.
				65	2450	3 Top & 3 Bott.
			76-22	35	1250	3 Top & 3 Bott.
				65	2450	3 Top & 3 Bott.
		25	70-22	35	1250	3 Top & 3 Bott.
				65	2450	3 Top & 3 Bott.
			76-22	35	1250	3 Top & 3 Bott.
				65	2450	3 Top & 3 Bott.
	ARK	12.5	70-22	35	1250	3 Top & 3 Bott.
				65	2450	3 Top & 3 Bott.
			76-22	35	1250	3 Top & 3 Bott.
				65	2450	3 Top & 3 Bott.
		25	70-22	35	1250	3 Top & 3 Bott.
				65	2450	3 Top & 3 Bott.
			76-22	35	1250	3 Top & 3 Bott.
				65	2450	3 Top & 3 Bott.

Figure 4.5. Dynamic Angle Validation (DAV)

Figure 4.6. Raw Data Acquired from DAV using TestQuip Software

4.2.2 Study 2

Two simulated loading devices, the HMS with DAV and the RAM were used to measure the internal gyration angles of two gyratory compactors, Pine Model AFGC125 and Troxler Model 4141. The internal angles of the SGCs were set the same as for Study 1.

The HMS with DAV, as shown in Figure 4.7, was used to measure the internal angles of the Pine and Troxler SGCs using three cone-shaped depressions machined at 18, 21 and 24°. The RAM, as shown in Figure 4.8, was used to measure the internal angles of the SGCs using 44 and 64 mm diameter rings.

The test matrix for Study 2 is presented in Table 4.8. For each testing combination in Table 4.8, three replicates were measured for the top angles, and three were for bottom angles. Since both HMS and RAM devices can fit in the SGC molds, no extrapolation method was used in this study.

4.2.3 Study 3

In Study 1, the internal angles of gyration measured using the DAV with mix were affected by the resistance of the HMA mixture to compaction effort due to the SGC frame stiffness. In study 2, the internal gyration angles measured using the HMS and RAM were influenced by the degree of cone-shaped depression and the diameter of the ring, respectively.

Figure 4.7. Hot Mix Simulator (HMS) with Dynamic Angle Validation (DAV)

Figure 4.8. Rapid Angle Measurement (RAM)

Table 4.8. Testing Plan for Internal Angle Study 2

SGC	Device	Angle/Dia	Height (mm)	Replicate
PINE 125X	DAV 106	18 Deg	115.0	3 Top & 3 Bott
		21 Deg	115.0	3 Top & 3 Bott
		24 Deg	115.0	3 Top & 3 Bott
	DAV 110	18 Deg	115.0	3 Top & 3 Bott
		21 Deg	115.0	3 Top & 3 Bott
		24 Deg	115.0	3 Top & 3 Bott
	RAM 29	44 mm	125.0	3 Top & 3 Bott
		64 mm	125.0	3 Top & 3 Bott
	RAM 12	44 mm	125.0	3 Top & 3 Bott
		64 mm	125.0	3 Top & 3 Bott
TROXLER 4141	DAV 106	18 Deg	115.0	3 Top & 3 Bott
		21 Deg	115.0	3 Top & 3 Bott
		24 Deg	115.0	3 Top & 3 Bott
	DAV 110	18 Deg	115.0	3 Top & 3 Bott
		21 Deg	115.0	3 Top & 3 Bott
		24 Deg	115.0	3 Top & 3 Bott
	RAM 29	44 mm	125.0	3 Top & 3 Bott
		64 mm	125.0	3 Top & 3 Bott
	RAM 12	44 mm	125.0	3 Top & 3 Bott
		64 mm	125.0	3 Top & 3 Bott

At this point, it felt that the resistance of HMA mixtures and the influences of the cone degree and the ring diameter could be represented by the eccentricity of the compaction force. It was also thought that the internal gyration angles of a gyratory compactor measured using different methods should be similar if the corresponding eccentricities induced using all methods were similar. Therefore, in order to match the internal gyration angles measured in Study 1 and Study 2, Study 3 was designed to measure the eccentricities induced during compaction of the HMA mixtures, HMS and RAM.

For Study 3, the testing matrix for the simulated loading devices is presented in Table 4.9. The eccentricities induced by the simulated loading devices were measured using the PDA, as shown in Figure 4.9. The PDA was placed on the top or bottom of the simulated devices to measure the top and bottom eccentricities.

Based on the eccentricity measurements using the RAM, as presented in Chapter 7, it was observed that the top and bottom eccentricities were very similar. To investigate if the top and bottom eccentricities were still similar when mixtures were used, two HMA mixtures, including 12.5 mm MCA mixture using PG 70-22 and 25 mm MCA mixture using PG 76-22, were tested, and the test results are presented in Table 4.10. The test results showed that the top eccentricities were about 1 mm farther from the centerline than the bottom ones, so the average eccentricities were about 0.5 mm higher and lower than the bottom and top values, respectively. Therefore, it was decided that the eccentricities be measured with the PDA placed on top and bottom of the HMA mixtures.

Table 4.9. Testing Plan for PDA with Simulated Loading Devices

SGC	Device	Angle/Dia	Height (mm)	Replicate
PINE 125X	DAV 106	21 Deg	115.0	3 Top & 3 Bott
		24 Deg	115.0	3 Top & 3 Bott
	DAV 110	21 Deg	115.0	3 Top & 3 Bott
		24 Deg	115.0	3 Top & 3 Bott
	RAM 29	44 mm	125.0	3 Top & 3 Bott
		64 mm	125.0	3 Top & 3 Bott
	RAM 12	44 mm	125.0	3 Top & 3 Bott
		64 mm	125.0	3 Top & 3 Bott
TROXLER 4141	DAV 106	21 Deg	115.0	3 Top & 3 Bott
		24 Deg	115.0	3 Top & 3 Bott
	DAV 110	21 Deg	115.0	3 Top & 3 Bott
		24 Deg	115.0	3 Top & 3 Bott
	RAM 29	44 mm	125.0	3 Top & 3 Bott
		64 mm	125.0	3 Top & 3 Bott
	RAM 12	44 mm	125.0	3 Top & 3 Bott
		64 mm	125.0	3 Top & 3 Bott

Figure 4.9. Pressure Distribution Analyzer (PDA)

Table 4.10. Top and Bottom Eccentricities Measured using PDA with Mix

SGC	Mix	Rep.	Load (N)			e (mm)			T. Mom. (N-m)		
			Top	Bott	Avg	Top	Bott	Avg	Top	Bott	Avg
PINE 125X	12.5 mm	1	10720	11094		29.39	28.91		315	321	
	PG 70-22	2	10413	11218		31.29	29.58		326	332	
		3	11095	11714		30.40	29.20		337	342	
		Avg	10743	11342	11042	30.36	29.23	29.80	326	332	329
	25 mm	1	10935	11194		28.89	28.01		316	314	
	PG 76-22	2	10424	11211		31.01	29.98		323	336	
		3	10901	11614		30.56	29.80		333	346	
		Avg	10753	11340	11047	30.15	29.26	29.71	324	332	328
TROXLER	12.5 mm	1	9995	10840		30.79	29.01		308	314	
4141	PG 70-22	2	10182	10400		30.57	29.86		311	311	
		3	10593	11151		30.70	29.40		325	328	
		Avg	10257	10797	10527	30.69	29.42	30.06	315	318	316
	25 mm	1	10282	11054		28.13	27.13		289	300	
	PG 76-22	2	10192	11094		29.20	28.40		298	315	
		3	10382	10871		29.88	28.78		310	313	
		Avg	10285	11006	10646	29.07	28.10	28.59	299	309	304

To determine the eccentricities induced during compaction of HMA mixtures, eight HMA mixtures and two gyratory compactors used in Study 1 were employed. The testing plan for the PDA with mix is presented in Table 4.11.

The PDA unit, as shown in Figure 4.9, was placed on top of the mixture within the SGC mold to measure the gyratory loads at three points. The three-point loads were stored in the PDA unit. After the compaction was completed, the data were downloaded onto the computer using the TestQuip software. Figure 4.10 shows the loading data acquired from the PDA. The data file was then saved and used to calculate the eccentricity using a spreadsheet provided by the manufacturer.

The data obtained in the internal angle study included (1) the internal gyration angles measured using the DAV with mix; (2) the internal gyration angles measured using the simulated loading devices, the HMS and RAM; and (3) the eccentricities of the gyratory force induced during compacting the HMA mixtures and the simulated loading devices. The data was reported and analyzed in Chapter 7.

4.3 Summary

The HMA mixtures used in the dynamic modulus study included four aggregate sources, three aggregate sizes and two binder grades. The mixtures were mixed at optimum binder content and compacted at two air void levels based on the binder grade. After a trial compaction program to determine the mix quantities to meet the target air voids, three replicates were compacted for each testing combination, and the test specimens, 100 mm diameter and 150 mm height, were cored and end-cut from the gyratory compacted samples. Finally, the test specimens were inspected for acceptance.

Table 4.11. The Top Eccentricities Measured using PDA with Mix

SGC	Agg.	Size	Binder	Est. Ht. (mm)	Mix Qt. (g)	Replicate
PINE 125X	MCA	12.5	70-22	115	4500	3 Top & 3 Bott
			76-22	115	4500	3 Top & 3 Bott
		25	70-22	115	4500	3 Top & 3 Bott
			76-22	115	4500	3 Top & 3 Bott
	ARK	12.5	70-22	115	4500	3 Top & 3 Bott
			76-22	115	4500	3 Top & 3 Bott
		25	70-22	115	4500	3 Top & 3 Bott
			76-22	115	4500	3 Top & 3 Bott
BABY TROXLER 4141	MCA	12.5	70-22	115	4500	3 Top & 3 Bott
			76-22	115	4500	3 Top & 3 Bott
		25	70-22	115	4500	3 Top & 3 Bott
			76-22	115	4500	3 Top & 3 Bott
	ARK	12.5	70-22	115	4500	3 Top & 3 Bott
			76-22	115	4500	3 Top & 3 Bott
		25	70-22	115	4500	3 Top & 3 Bott
			76-22	115	4500	3 Top & 3 Bott

Figure 4.10. Raw Data Acquired from PDA using TestQuip Software

The dynamic modulus values for each specimen were determined at five temperatures and six frequencies. The test was performed from low to high temperatures and from high to low frequencies. The dynamic modulus data were reported and analyzed in Chapters 5 and 6.

The internal gyration angles were measured using the DAV with eight mixtures from two aggregate sources, two aggregate sizes and two binder grades. In addition, the internal angles were determined using the simulated loading devices, including the HMS with DAV developed by TestQuip, Inc. and the RAM developed by Pine Instrument Company. It was thought that the internal gyration angles measured using the DAV with mix and the simulated loading devices would be similar if the mix and the simulated loading devices induced similar eccentricities for the gyratory force. Therefore, the eccentricities induced by the eight mixtures and the simulated loading devices were also measured in this study. The internal gyration angle and eccentricity data were presented and analyzed in Chapter 7.

CHAPTER 5: LABORATORY TEST RESULTS AND ANALYSES

The raw data acquired from the dynamic modulus test was analyzed in this chapter. The raw data was used to (1) calculate the dynamic modulus and phase angle of the mixture in question; (2) evaluate the dynamic modulus test variability; and (3) construct master curves for the HMA mixtures used in this study. Finally, the dynamic modus values and their associated master curves obtained from this testing program were reported for future usage for level 1 $|E^*|$ inputs in the M-E Design Guide.

5.1 Determination of Dynamic Modulus and Phase Angle

As described in the experimental plan, the dynamic modulus test was performed in a continuous uniaxial sinusoidal (haversine) compressive stress condition with a servo-hydraulic closed-loop testing machine. An environmental chamber was used to control the temperature of the test specimens. In this study, vertical displacements and loading were measured using four LVDTs and a load cell, respectively.

The test was performed on each test specimen at five different temperatures, including -10, 4.4, 21.1, 37.8, and 54.4C (14, 40, 70, 100, and 130F). The test was run from the lowest temperature to the highest temperature. For each temperature level, the test was performed at six different loading frequencies from the highest to the lowest, including 25, 10, 5, 1, 0.5, 0.1 Hz. At each combination of testing temperature and frequency, one dynamic modulus value and one phase angle value were determined for each specimen.

5.1.1 Raw Data Acquisition

The test data obtained include the loading time, axial load, and vertical displacements measured by LVDTs 1 through 4. An example of a partial raw data file obtained from the MTS™ testing data acquisition system is shown in Figure 5.1. The data was recorded for the last six cycles of the test. "Time" was the time at which the data was recorded. The axial load value was recorded in "Load". Displacements of the specimen were recorded in columns "LVDT 1" through "LDVT 4".

For a given test temperature, one data file was acquired for each specimen. The data file started from 25 Hz and ended at 0.1 Hz for each test temperature. The number of recorded data points in each cycle varied upon the test frequency, and the number of data points recorded was set using the test machine controller. In order to use regression process for calculating the dynamic modulus and phase angle, the number of data points recorded should not be less than 200. In this study, the number of data points recorded at each frequency is presented in Table 5.1, which were used to develop a computer program for calculating the dynamic modulus and phase angle as presented in the next section.

MTS793|MPT|ENU|1|2|.|/|:|1|0|0|A

Cyclic Acquisition   Time: 30.025146 Sec

Stored at: 194 cycle   Stored for: 12 segments

Points: 246

Time	Load	LVDT 1	LVDT 2	LVDT 3	LVDT 4
Sec	lbf	in	in	in	in
7.8994141	-185.65471	0.021362329	0.013838176	0.013310348	0.016484257
7.9003906	-206.6362	0.021362329	0.01381907	0.013282047	0.016469955
7.9013672	-225.26775	0.021343233	0.013785632	0.01327733	0.016460422
7.9023438	-241.88507	0.021309817	0.013809515	0.013286764	0.016465189
-----------	-------------	--------------	--------------	--------------	--------------

Figure 5.1. A Part of Raw Data Obtained from MTS™ Data Acquisition

Table 5.1. Number of Data Points Recorded at Each Frequency

Frequency	Number of Data Points Recorded
25 Hz	246
10 Hz	614
5 Hz	1,229
1 Hz	6,144
0.5 Hz	6,144
0.1 Hz	5,994

5.1.2 Dynamic Modulus and Phase Angle Calculation

A complete data set of the dynamic modulus test even at a single combination of test temperature and frequency is quite extensive. In order to efficiently analyze the data, it is necessary to select an analysis method that allows relatively simple manipulation using available computer software. Among different approaches recommended in the proposed test methods, the curve fitting technique is (relatively) easy to accomplish using a spreadsheet, which is utilized and presented in this section.

Fitting Loading Curve. At a given frequency, the sinusoidal equation representing the loading curve is as follows:

$$L = A_L + B_L * \sin(\omega t + \phi_L) = A_L + B_L * \sin(2\pi f t + \phi_L) \tag{5.1}$$

where:

L	= loading curve
A_L	= mean value of loads
B_L	= loading amplitude
ω	= angular velocity
f	= test frequency
t	= recorded loading time
ϕ_L	= loading phase angle

Equation 5.1 can be rewritten as follows:

$$L = A_L + B_L * [\sin(2\pi f t) * \cos(\phi_L) + \cos(2\pi f t) * \sin(\phi_L)] \tag{5.2}$$

In Equation 5.2, only parameters A_L, B_L, and ϕ_L are unknown. Therefore, it can be rewritten:

$$L = A_L + C_L * \cos(2\pi ft) + D_L * \sin(2\pi ft) \tag{5.3}$$

where

$$C_L \quad = B_L * \sin(\phi_L)$$

$$D_L \quad = B_L * \cos(\phi_L)$$

From Equation 5.3, the loading amplitude and phase angle can be expressed in term of C_L and D_L as follows:

Since
$$\frac{C_L}{D_L} = \frac{B_L * \sin(\phi_L)}{B_L * \cos(\phi_L)} = \tan(\phi_L) \tag{5.4}$$

then,
$$\phi_L = \arctan\left(\frac{C_L}{D_L}\right) \tag{5.5}$$

And

Since
$$C_L^2 + D_L^2 = B_L^2\left(\sin^2(\phi_L) + \cos^2(\phi_L)\right) = B_L^2 \tag{5.6}$$

then,
$$B_L = \sqrt{C_L^2 + D_L^2} \tag{5.7}$$

In order to determine the unknown parameters A_L, C_L, and D_L, Equation 5.3 is fitted to the test data using a least-squares fit of a sinusoidal function. The goal is to solve for the unknown parameters that minimize the residual sum of squares:

$$SS_R = \sum_{i=1}^{n}\left\{L_i - \left[A_L + C_L * \cos(2\pi ft_i) + D_L * \sin(2\pi ft_i)\right]\right\}^2 \tag{5.8}$$

The detailed solutions for the regression can be found elsewhere (*101*). The unknown parameters A_L, C_L, and D_L in Equation 5.3 can be determined using Equations 5.9 through 5.11.

$$A_L = \frac{\sum_{i=1}^{n} L_i}{n} \tag{5.9}$$

$$C_L = \frac{2}{n} \sum_{i=1}^{n} L_i \cos(2\pi f t_i) \tag{5.10}$$

$$D_L = \frac{2}{n} \sum_{i=1}^{n} L_i \sin(2\pi f t_i) \tag{5.11}$$

where

L_i = loading data recorded in "Load" column in Figure 5.1

t_i = loading time recorded in "Time" column in Figure 5.1

n = number of data "Points" recorded for the last six cycles in

       Figure 5.1

Fitting Displacement Curves. In this process, four different displacement curves are fitted to the recorded LVDTs 1 through 4 data presented in Figure 5.1. A procedure for fitting a displacement curve is presented in this section. Due to drift in displacement data caused by permanent deformation of the test sample, Equation (5.1) is modified to represent the displacement curves that change with time as shown in Equation 5.12.

$$D = A_D + B_D * \sin(2\pi f t + \phi_D) + R_D * t \tag{5.12}$$

where

D = displacement curve

A_D = mean value of displacements

B_D = displacement amplitude

135

$$R_D \quad = \text{slope of the drift in the displacement}$$

$$f \quad = \text{test frequency}$$

$$t \quad = \text{recorded loading time}$$

$$\phi_D \quad = \text{displacement phase angle}$$

Equation 5.12 can be rewritten so that its right side will share the same form as that of Equation 5.1:

$$D - R_D * t = A_D + B_D * \sin(2\pi f t + \phi_D) \qquad (5.13)$$

Now, if the drift in the displacement can be eliminated before starting the regression process, the solutions in Equations 5.9 through 5.11 can be applied for Equation 5.13. Eliminating the drift can be done as follows:

- Determining the maximum and minimum values of displacements for each cycle

- Determining the slopes for the maximum and minimum values

- Averaging the two slopes, which is the slope of the drift (R_D)

- Calculating the new displacement values using the following equation:

$$D_i^{'} = D_i - R_D * t_i \qquad (5.14)$$

where

$$D'_i \quad = \text{new displacement values}$$

$$D_i \quad = \text{displacement data recorded in columns "LVDT 1" through}$$
$$\quad\quad \text{"LVDT 4" in Figure 5.1}$$

$$R_D \quad = \text{slope of the displacement drift determined in the previous step}$$

$$t_i \quad = \text{loading time recorded in "Time" column in Figure 5.1}$$

Equation 5.13 now has the same form as Equation 5.1:

$$D^{'} = A_D + B_D * \sin(2\pi f t + \phi_D) \qquad (5.15)$$

136

The solution in Equations 5.5, 5.7, and 5.9 to 5.11 can be applied to determine the displacement amplitudes (B_D) and the phase angles (ϕ_D) for LVDT 1 to LVDT 4 displacement data.

Calculating Dynamic Modulus and Phase Angle. Based on the analyses presented in the previous sections, Equations 5.16 and 5.17 can be used to calculate the dynamic modulus and phase angle of the test:

$$\left| E* \right| = \frac{\sigma_0}{\varepsilon_0} = \frac{B_L}{B_D} \frac{L}{A} \tag{5.16}$$

$$\phi = \phi_L - \phi_D \tag{5.17}$$

where

$\left| E* \right|$ = dynamic modulus, psi

B_L = loading amplitude

B_D = displacement amplitude

L = LVDT length, in.

A = cross section area, in^2

ϕ = phase angle, rad.

ϕ_L = loading phase angle, rad.

ϕ_D = displacement phase angle, rad.

Developing DYNMOD. The calculation method presented in the previous sections was used to develop a computer program called DYNMOD to facilitate the determination of the dynamic modulus and phase angle from the dynamic modulus test

data. DYNMOD was programmed using Microsoft™ Visual Basic. The program

performs as an add-in module in Microsoft™ Excel. This program works the best in

Microsoft™ Excel 2000.

The calculation is started by selecting **DYNMOD > Open MTS**, as shown in

Figure 5.2. An **OPEN** window, as shown in Figure 5.3, allows the users to select an

MTS™ data file to open for calculation. The default data life generated by the MTS™

version 793 is **specimen.dat**. All test data in **specimen.data** is then automatically read

in a new spreadsheet named **TextMTS**.

The calculation is performed by selecting **DYNMOD > DYN MOD**, as shown

in Figure 5.4. As described, the data file named **specimen.dat** contained all test data for

a given test temperature across all frequencies from 25 Hz through 0.1 Hz. For each

frequency, **DYNMOD** automatically fit the loading model to the loading data, and then

it calculates the maximum loading magnitude using the fitted loading model. The peak

stress is the ratio of the maximum loading magnitude to the cross section area. The

displacement model is fitted to the displacement data measured by each LVDT, and the

maximum displacement is determined using the fitted displacement model. The peak

stress is the ratio of the maximum displacement to the distance between two aluminum

rings, which is 4 inches. Figure 5.5 shows an example comparison between the

measured and predicted loading curves. Finally, for a given combination of test

frequency and test temperature, the dynamic modulus is the ratio of the peak stress to

the peak strain. The phase angle is determined based on the time lag between the peak

stress and the associated peak strain.
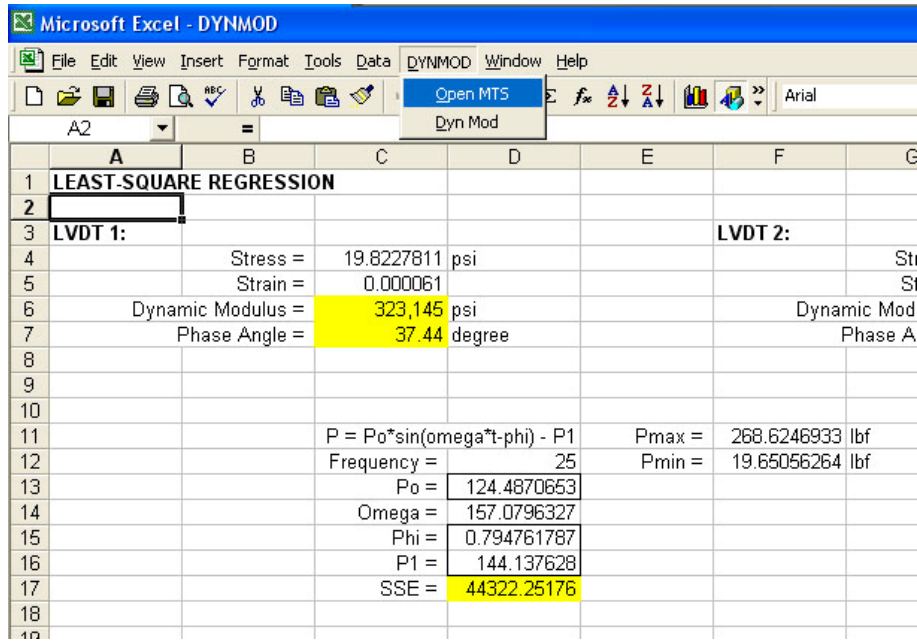
Figure 5.2. Add-in Menu of DYNMOD
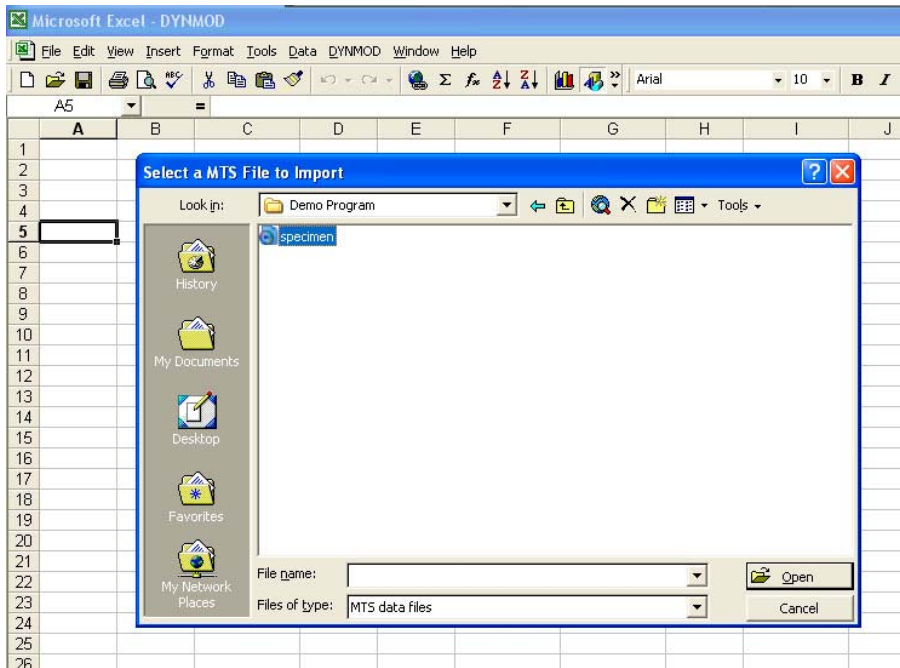
Figure 5.3. Open Window for DYNMOD

Figure 5.4. Performing Calculation
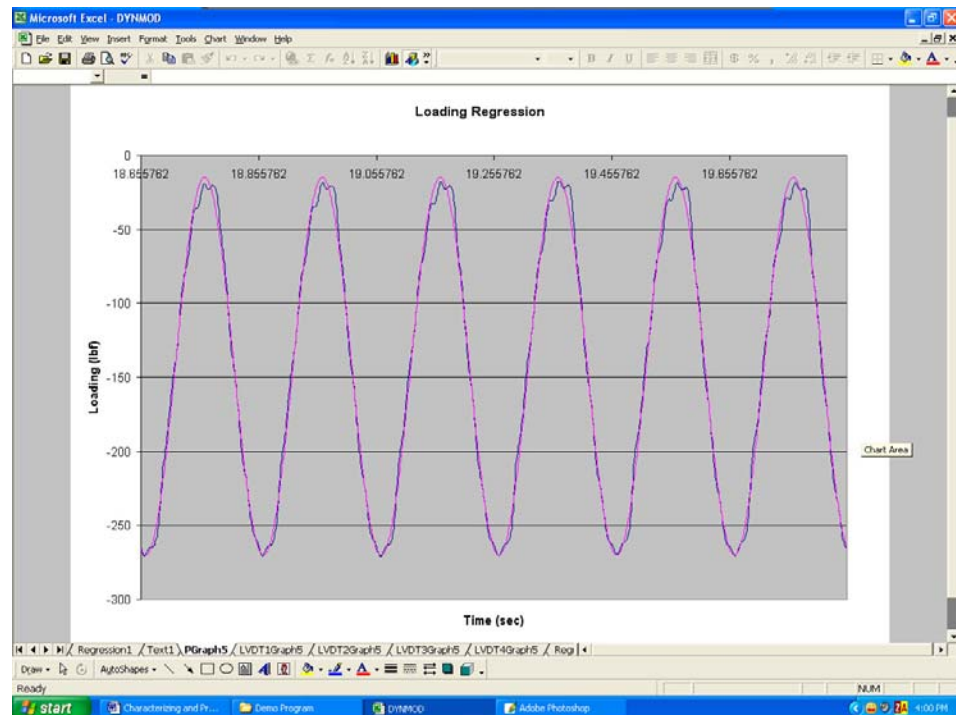
Figure 5.5. Comparison Between Predicted and Measured Loading Data

140

The final results of the program, as shown in Figure 5.6, include: (1) the peak stress level applied on the test sample; (2) the peak strain, the dynamic modulus, and the phase angle measured by each LVDT; and (3) the average strain, dynamic modulus, and phase angle based on four LVDT measurements for each test frequency. Individual responses obtained from each LVDT were used to analyze the variability of the dynamic modulus test results, as presented in the next sections. Average test responses (dynamic modulus and phase angle) were reported for future usage for level 1 dynamic modulus inputs in the M-E Design Guide. The average dynamic modulus and phase angle values for typical mixtures used in Arkansas are summarized in Appendices B and C, respectively.

5.2 Variability Analysis of Dynamic Modulus Test Results

In order to recommend the dynamic modulus test results, including the dynamic modulus and phase angle values obtained in this study, be used for level 1 $|E*|$ inputs in the M-E Design Guide, the objectives of the variability analyses were: (1) to check if the test data contained any potential errors caused by the equipment defects; and (2) to determine the variability of the test data in term of the coefficient of variation and compare the variability of the test data obtained in this study to that of other studies.

Figure 5.6. Final Results of DYNMOD

In this study, the testing conditions, such as temperatures and frequencies, were the same for all replicates, and the testing order of the replicates were randomized. Therefore, it was suggested that the testing order of the replicates would not be a sensitive factor in the test variability. Only LVDT numbering could not be randomized. Therefore, LVDT responses were evaluated to detect any patterned errors due to LVDT measurements. The detailed analysis is presented in the following section.

5.2.1 Evaluation of LVDT Measurements

This analysis was performed to analyze the LVDT measurements. Since the test was performed at –10C (14F) through 54.4C (130F) and from 25 Hz through 0.1 Hz at each temperature level, two extreme combinations, including 14F-25Hz and 130F-0.1Hz, were considered to represent the testing temperature and frequency sweeps. LVDT responses measured at two temperature-frequency combinations (14F-25Hz and 130F-0.1Hz) were analyzed in this study.

The ranges of LVDT responses measured at two extreme combinations were significantly different. The range of LVTD responses (strains) measured at 14F-25F was between 50 and 90 microstrains, and the range of LVTD responses (strains) measured at 130F-0.1F was between 120 and 155 microstrains. To avoid the abovementioned strain differences, two one-way ANOVA tests were separately performed using the testing data measured at the two temperature-frequency combinations.

The ANOVA tests were to check whether the differences between the measurements by four LVDTs were statistically significant. The same fixed effect model for both tests was as follows:

$$y_{ij} = \mu + \tau_i + \varepsilon_{ij} \tag{5.18}$$

where

y_{ij} = LVDT responses, 10^{-6} in/in

μ = overall mean effect

τ_i = effect of ith LVDT

ε_{ij} = random error

The hypotheses for both tests were as follows:

$$H_o : \tau_1 = \tau_2 = \tau_3 = \tau_4 = 0 \tag{5.19}$$

$$H_1: \text{at least one } \tau_i \neq 0 \tag{5.20}$$

The same significance level for both tests was $\alpha = 0.05$. The ANOVA results for the testing data measured at the temperature-frequency combination of -10C (14F) and 25 Hz are presented in Table 5.2, and the ANOVA results for the test data at 54.4C (130F) and 0.1 Hz are presented in Table 5.3.

The adequacy of the fixed effect models was checked using the normal probability plot of residuals and the plot of the residuals versus the fitted values. These plots did not reveal any trouble or tendency. The sample size of 121 observations used in these analyses was checked using the operating characteristic curve. Figure 5.7 shows the sample size check for the ANOVA of the combination of -10C (14F) and 25 Hz. The powers $(1 - \beta)$ of both tests were less than 0.90, so the number of observations used in both ANOVA tests was sufficient.

Table 5.2. ANOVA Test Results for Data Measured at 14F and 25 Hz

Anova: Single Factor

SUMMARY

Groups	Count	Sum	Average	Variance
LVDT 1	121	7482.5	62.54	85.32
LVDT 2	121	7188.1	58.41	71.30
LVDT 3	121	7407.8	61.22	84.07
LVDT 4	121	7203.58	58.53	105.65

ANOVA

Source of Variation	SS	df	MS	F	P-value	F crit
Between Groups (Trt)	537.73	3	179.243	2.070	0.103	2.623
Within Groups (Error)	41561.04	480	86.585			
Total	42098.77	483				

Table 5.3. ANOVA Test Results for Data Measured at 130F and 0.1 Hz

Anova: Single Factor

SUMMARY

Groups	Count	Sum	Average	Variance
LVDT 1	121	16900	139.67	171.92
LVDT 2	121	16822	138.03	171.21
LVDT 3	121	16697	136.99	196.14
LVDT 4	121	17240	143.48	203.61

ANOVA

Source of Variation	SS	df	MS	F	P-value	F crit
Between Groups	1338.1	3	446.041	2.402	0.067	2.623
Within Groups	89145.9	480	185.721			
Total	90484.0	483				

Sample Size Determination

Groups	Count	μ_i	μ	τ_i^2
LVDT 1	121	62.54	60.17	5.59
LVDT 2	121	58.41	60.17	3.13
LVDT 3	121	61.22	60.17	1.10
LVDT 4	121	58.53	60.17	2.69
			$\Sigma =$	12.51

$$\Phi^2 = \frac{n\sum_{i=1}^{4}\tau_i^2}{a\sigma^2} = \frac{121*12.51}{4*86.585} = 4.37$$

$\Phi = 2.09$

$v_1 = a - 1 = 4 - 1 = 3$

$v_2 = a(n-1) = 4*(121-1) = 480$

$\alpha = 0.05$

From OC Chart (*102*):

$\beta = 0.075$

Power (1-β) = 1-0.075=0.925 > 0.90 **OK**

Figure 5.7. Operating Characteristic Curves for Sample Size

The assumption of variance equality in both ANOVA tests was checked using Bartlett's test for equality of variance, as shown in Figure 5.8. The results from Bartlett's test showed that the assumption of variance equality was justified.

In both tests, $F_0 < F_{crit}$, as shown in Tables 5.2 and 5.3, so the null hypothesis was not rejected. Thus, the differences between the measurements by four LVDTs at the two extreme combinations of temperature and frequency were not statistically significant. In addition, if it was true for the data measured at two extreme combinations, the results from the two ANOVA tests could be applicable to the other temperature-frequency combinations. Therefore, the differences between the LVDT responses through all combinations of testing temperature and frequency were not statistically significant. Practically, it inferred that there were no significant errors caused by the LVDT defects in the test data.

5.2.2 Variability of Dynamic Modulus Test

The dynamic modulus test variability was evaluated using the coefficient of variation, which has the ability to represent the test variability across the test temperatures and frequencies. The variability analysis included three steps: (1) determination of the coefficients of variation; (2) investigation of effects of the mixture properties and test parameters on the test variability; and (3) evaluation of the overall test variability.

Test for Equality of Variance

Hypotheses:

$$H_o : \sigma_1^2 = \sigma_2^2 = \sigma_3^2 = \sigma_4^2$$

H_1: above not true for at least one σ_i^2

Analysis:

Groups	n_i	S_i^2	$(n_i-1)S_i^2$	$(n_i-1)\log(S_i^2)$
LVDT 1	121	85.32	10238.4	231.7
LVDT 2	121	71.30	8556.0	222.4
LVDT 3	121	84.07	10088.4	231.0
LVDT 4	121	105.65	12678.0	242.9
Σ	484		41560.8	927.9

a = 4

$$S_p^2 = \frac{\sum\limits_{i=1}^{a}(n_i - 1)S_i^2}{N - a} = 86.585$$

$$q = (N - a)\log_{10} S_p^2 - \sum_{i=1}^{a}(n_i - 1)\log_{10} S_i^2 = 2.054$$

$$c = 1 + \frac{1}{3(a-1)}\left(\sum_{i=1}^{a}(n_i - 1)^{-1} - (N - a)^{-1}\right) = 1.003$$

$$\chi_0^2 = 2.3026\frac{q}{c} = 4.714$$

$\chi_0^2 = 4.714 < \chi_{\alpha,a-1}^2 = 7.81$. **Cannot Reject H_0**

Figure 5.8. Bartlett' Test for Equality of Variance

Determination of Coefficients of Variation. The variability of the dynamic

modulus test was evaluated using the variances related to the measurements within and

between specimens. The "within" specimen variance that measures the variability

between the individual LVDT measurements in a specimen was calculated using

Equation 5.21 (*73*).

$$S_w^2 = \frac{1}{n-1}\sum_{i=1}^{n}\left(x_i - \overline{X}_s\right)^2 \tag{5.21}$$

where:

S_w^2 = "within" specimen variance

x_i = parameter from individual LVDT measurements

$\overline{X}_s$ = specimen average parameter

n = number of LVDTs per specimen

A pooled "within" variance for the replicates was the average of the associated

"within" specimen variances. The "between" specimen variance that measures the

variability between the average parameters of each set of three replicates was computed

using Equation 5.22 (*73*).

$$S_b^2 = \frac{1}{m-1}\sum_{j=1}^{m}\left(\overline{X}_{sj} - \overline{X}\right)^2 \tag{5.22}$$

where:

S_b^2 = "between" specimen variance

$\overline{X}_{sj}$ = specimen average parameter

$\overline{X}$ = grand average

m = number of specimens

The "within" and "between" specimen variances were then used to calculate the "within" and "between" coefficients of variation using Equation 5.23. The coefficient of variation was used to "normalize" the test variability so that the test variability could be compared across the test temperatures and frequencies.

$$CV = \frac{s}{\overline{X}} \times 100 \qquad (5.23)$$

where:

CV   = "within" or "between" coefficient of variation

s   = "within" or "between" standard deviation

$\overline{X}$ = grand average

The standard error of the average response was determined in Equation 5.24 based on the "within" and "between" coefficients of variation. Since the coefficients of variation were normalized, the subsequent standard error of the mean was also normalized across the test temperatures and frequencies.

$$\left(\frac{\sigma}{\sqrt{n}}\right) = \sqrt{\frac{CV_w^2}{ij} + \frac{CV_b^2}{j}} \qquad (5.24)$$

where:

CV_b = "between" specimen standard deviation

CV_w = "within" specimen standard deviation

i   = number of LVDTs per specimen

j   = number of specimens

The "within" and "between" coefficients of variation for the dynamic modulus and phase angle values determined from each set of three replicates were computed and presented in Appendices B and C. Histograms of the "within" and "between"

coefficient of variation, as shown in Figures 5.9 and 5.10, indicated that the CV data was normally distributed.

ANOVA Tests. To investigate the effects of the mixtures properties and test parameters on the variability of the dynamic modulus test results, two ANOVA tests, one for the "within" CVs and the other for the "between" CVs presented in Appendices B and C, were conducted using the SAS™ PROC GLM utility. The responses and possible fixed effects for the ANOVA tests are presented in Table 5.4.

Since only one "within" CV and one "between" CV was determined for three replicates at each combination of temperature and frequency, the number of replicate for the responses ("within" CV and "between" CV) in the ANOVA tests was one. In addition, since the dynamic modulus was not available for the mixtures from JET used PG 76-22, the coefficients of variation for these mixtures were not determined, so the data sets used in the ANOVA were considered unbalanced with one or more empty cells. These two problems must be considered in the analyses.

For "only one replicate" problem, the ANOVA tests were modified. The statistical models were run initially using six main effects and their associated interactions. Since only one replicate was available for each combination of the main effects, there were no degrees of freedom left for the error. Therefore, initially, no F_0 for the main factors was calculated. To estimate the error, it was assumed that all five-way and six-way interactions were insignificant, so these insignificant effects could be pooled for use as an estimate of the error. The sum of squared errors (SSE) was estimated using the sum of squared for all pooled effects. The number of degrees of

freedom of the estimated error equaled to the sum of the degrees of freedom for all pooled effects. Mean square for error (MSE) was calculated using Equation 5.25. Then, F_0 for each factor was estimated using Equation 5.26. Significant effects were justified by comparing their F_0 to the corresponding $F_{critical}$. Finally, all insignificant effects were pooled, and the final ANOVA tables were presented in Tables 5.5 and 5.6.

$$MSE = \frac{SS_{Error}}{df_{Error}}$$
(5.25)

where:

MSE = mean square of error

SS_{Error} = sum of squared errors

df_{Error} = degrees of freedom of error

$$F_{0i} = \frac{MS_i}{MSE}$$
(5.26)

where:

F_{0i} = F factor for *ith* effect

MS_i = Mean square for *ith* effect

MSE = mean square of error
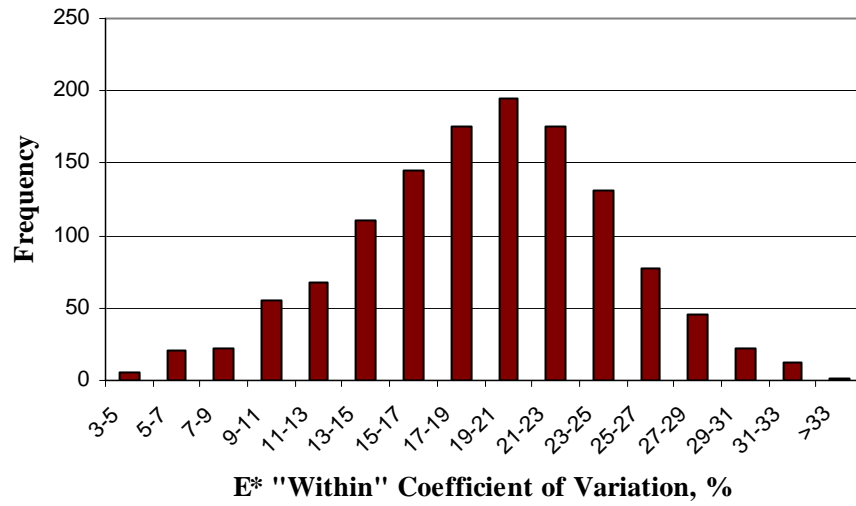
Figure 5.9. Histogram of "Within" Coefficient of Variation
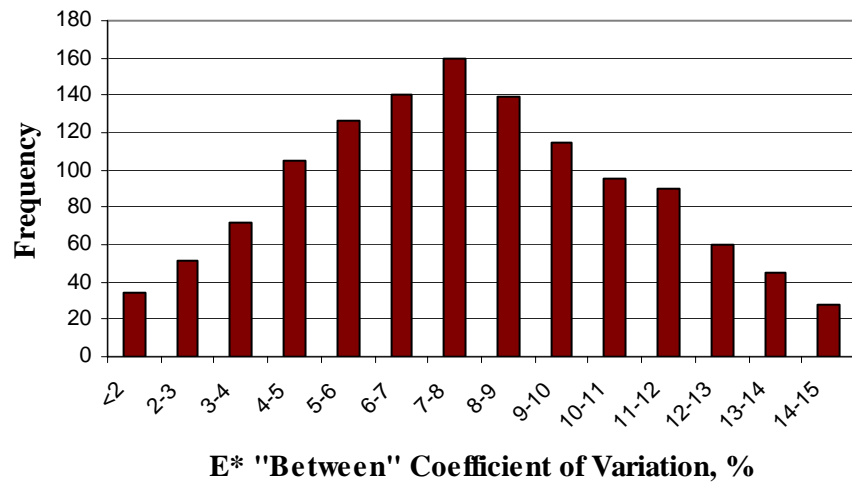
Figure 5.10. Histogram of "Between" Coefficient of Variation

Table 5.4. Responses and Variables for "Within" and "Between" CV Analysis

VARIABLES	Levels	Values
"Within" Coefficient of Variation		Response
"Between" Coefficient of Variation		Response
Aggregate Source (ASRCE)	4	MCA, GMQ, ARK, JET
Aggregate Size (ASIZE)	3	12.5, 25, 37.5 mm
Binder Grade (BGRAD)	2	PG70-22, PG76-22
Air Voids (AVOID)	2	Design (4 or 4.5%), 7%
Temperature (TEMP)	5	14, 40, 70, 100, 130F
Frequency (FREQ)	6	0.1, 0.5, 1, 5, 10, 25 Hz

Table 5.5. ANOVA Tables for "Within" CV Analysis

Source	df	Type III SS	MS	F_0	F_{crit}	$F_0 > F_{crit}$ (Significant)
ASRCE	3	1942.06	647.35	72.678	2.613	Yes
ASIZE	2	2303.60	1151.80	129.311	3.004	Yes
ASRCE*ASIZE	6	796.91	132.82	14.911	2.107	Yes
BGRAD	1	7.45	7.45	0.836	3.850	No
ASRCE*BGRAD	2	57.24	28.62	3.213	3.004	Yes
ASIZE*BGRAD	2	71.89	35.94	4.035	3.004	Yes
ASRCE*ASIZE*BGRAD	4	619.85	154.96	17.397	2.380	Yes
AVOID	1	843.17	843.17	94.661	3.850	Yes
ASRCE*AVOID	3	181.30	60.43	6.785	2.613	Yes
ASIZE*AVOID	2	76.60	38.30	4.300	3.004	Yes
ASRCE*ASIZE*AVOID	6	1116.20	186.03	20.886	2.107	Yes
BGRAD*AVOID	1	70.69	70.69	7.936	3.850	Yes
ASRCE*BGRAD*AVOID	2	167.30	83.65	9.391	3.004	Yes
ASIZE*BGRAD*AVOID	2	361.66	180.83	20.301	3.004	Yes
TEMP	4	908.04	227.01	25.486	2.380	Yes
ASRCE*TEMP	12	1844.97	153.75	17.261	1.761	Yes
ASIZE*TEMP	8	1716.69	214.59	24.091	1.947	Yes
ASRCE*ASIZE*TEMP	24	2238.09	93.25	10.469	1.527	Yes
BGRAD*TEMP	4	297.22	74.31	8.342	2.380	Yes
ASRCE*BGRAD*TEMP	8	313.66	39.21	4.402	1.947	Yes
ASIZE*BGRAD*TEMP	8	506.54	63.32	7.109	1.947	Yes
AVOID*TEMP	4	385.89	96.47	10.831	2.380	Yes
ASRCE*AVOID*TEMP	12	819.56	68.30	7.668	1.761	Yes
ASIZE*AVOID*TEMP	8	771.45	96.43	10.826	1.947	Yes
BGRAD*AVOID*TEMP	4	247.51	61.88	6.947	2.380	Yes
FREQ	5	393.88	78.78	8.844	2.222	Yes
TEMP*FREQ	20	358.71	17.94	2.014	1.580	Yes
ERROR	1101	9806.81	8.91			
TOTAL	1259	29224.9				

Table 5.6. ANOVA Tables for "Between" CV Analysis

Source	df	Type III SS	MS	F_0	F_{crit}	$F_0 > F_{crit}$ (Significant)
ASRCE	3	348.17	116.06	18.863	2.613	Yes
ASIZE	2	250.85	125.42	20.386	3.004	Yes
ASRCE*ASIZE	6	685.37	114.23	18.566	2.107	Yes
BGRAD	1	18.80	18.80	3.056	3.850	No
ASRCE*BGRAD	2	54.64	27.32	4.441	3.004	Yes
ASRCE*ASIZE*BGRAD	4	178.32	44.58	7.246	2.380	Yes
AVOID	1	11.44	11.44	1.859	3.850	No
ASIZE*AVOID	2	173.80	86.90	14.124	3.004	Yes
ASRCE*ASIZE*AVOID	6	231.78	38.63	6.279	2.107	Yes
TEMP	4	1029.69	257.42	41.840	2.380	Yes
ASRCE*TEMP	12	898.99	74.92	12.176	1.761	Yes
ASIZE*TEMP	8	577.13	72.14	11.725	1.947	Yes
ASRCE*ASIZE*TEMP	24	1028.28	42.84	6.964	1.527	Yes
ASRCE*BGRAD*TEMP	8	240.03	30.00	4.877	1.947	Yes
ASIZE*BGRAD*TEMP	8	251.87	31.48	5.117	1.947	Yes
AVOID*TEMP	4	315.80	78.95	12.832	2.380	Yes
ASRCE*AVOID*TEMP	12	364.71	30.39	4.940	1.761	Yes
ASIZE*AVOID*TEMP	8	290.29	36.29	5.898	1.947	Yes
BGRAD*AVOID*TEMP	4	390.01	97.50	15.847	2.380	Yes
FREQ	5	37.92	7.58	1.233	2.222	No
TEMP*FREQ	20	205.62	10.28	1.671	1.580	Yes
ERROR	1115	6860.11	6.15			
TOTAL	1259	14443.6				

Since the above ANOVA tests were performed based on the unbalanced data set, the results may have bias, so they should not be immediately used. In this case, the above ANOVA tests were repeated on two other data sets: (1) balanced data subset that included all the $|E*|$ test data except those for JET mixtures; and (2) balanced data subset that included only the test data for JET mixtures. The results of the ANOVA tests on the balanced data subsets were compared to the results presented in Tables 5.5 and 5.6. The comparisons showed that the significance of the single fixed effects and two-way interactions were similar for the unbalanced and balanced subsets. Therefore, it was decided that the ANOVA results presented in Tables 5.5 and 5.6 be used to draw the conclusions on the effects of the mixture properties and test parameters on the $|E*|$ test variability, as presented in the following sections.

Effects of Mixture Properties. With 95-percent confidence, the effects of aggregate properties, such as aggregate source, aggregate size, and air voids, on both coefficients of variation were significant, as shown in Tables 5.5 and 5.6. The effects of the mixture properties on the test variability are shown in Figures 5.11 through 5.13.

Based on Figures 5.11 and 5.12, the observation was that the aggregate properties significantly affected the coefficient of variation. The larger the maximum nominal aggregate size, the higher the coefficient of variation (the test variability). The differences between the coefficients of variation for 12.5 mm and 37.5 mm mixtures were about two percent for the mean "within" coefficients of variation, and about 0.4 percent for the mean "between" coefficients of variation.

157
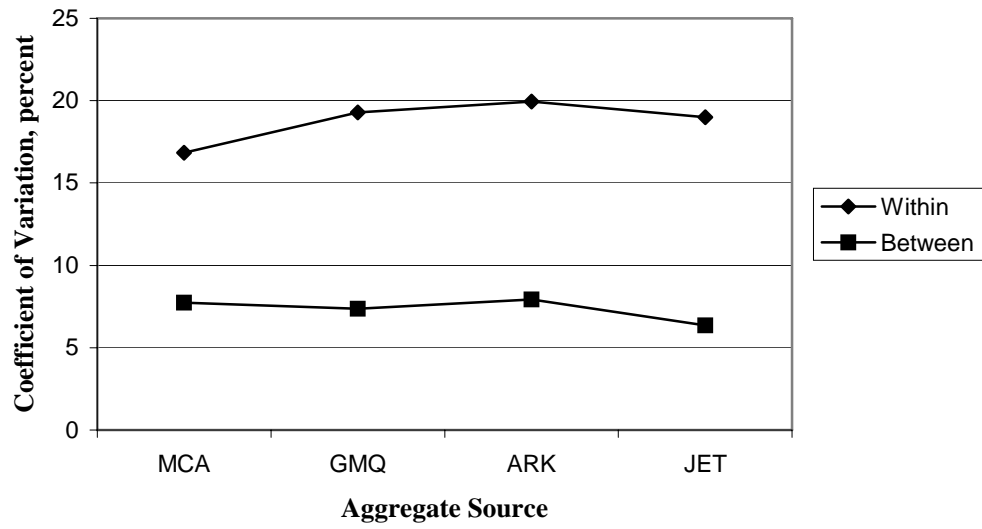
Figure 5.11. Effect of Aggregate Source on Coefficient of Variation
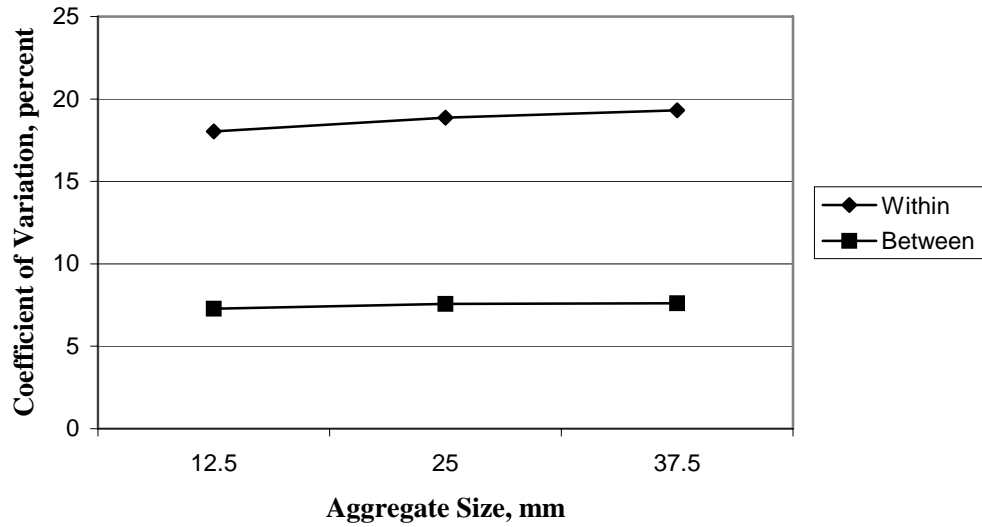
Figure 5.12. Effect of Aggregate Size on Coefficient of Variation
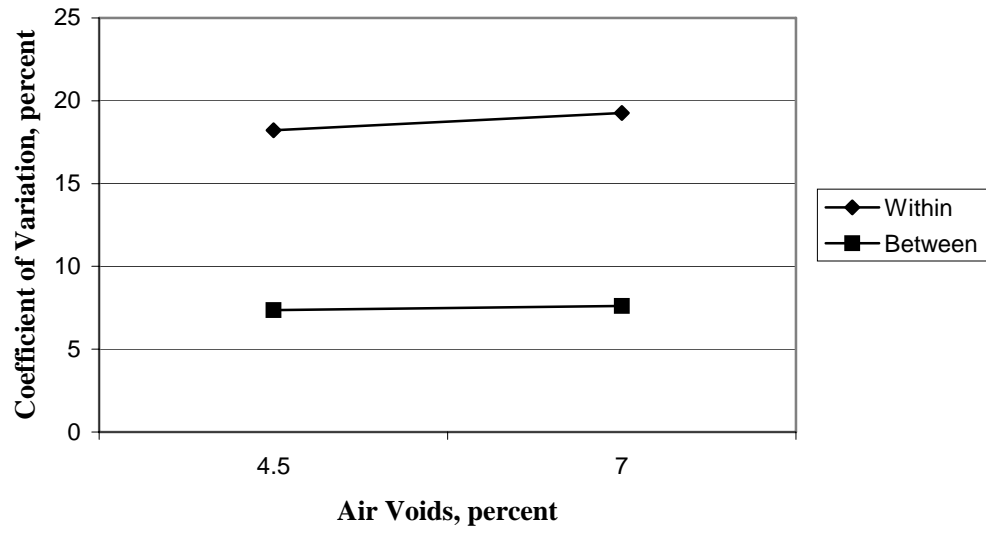
Figure 5.13. Effect of Air Voids on Coefficient of Variation

Figure 5.13 showed that the higher the air voids of the test specimens, the higher the coefficients of variation, especially the "within" values. This was reasonable because with higher air voids in a test specimen, it was more difficult to distribute the voids equally in the sample, which resulted in higher test variability.

Effects of Test Parameters. As illustrated in Tables 5.5 and 5.6, the effects of test temperature and frequency were significant with 95-percent confidence. The effects of test parameters are plotted in Figures 5.14 and 5.15.

It was observed that the test variability was higher at higher temperatures or higher frequencies. At high temperatures, the dynamic modulus of an HMA mixture was dependent on the aggregate structure, and at low temperatures, the dynamic modulus was dependent on the binder stiffness. In term of specimen repeatability, the aggregate structure was not as consistent as the asphalt binder. Therefore, the test variability should be higher at higher test temperatures. The variation ranges of coefficient of variation for both temperature and frequency sweeps were about 1.5 percent for "within" values, and about 0.6 percent for "between" values.
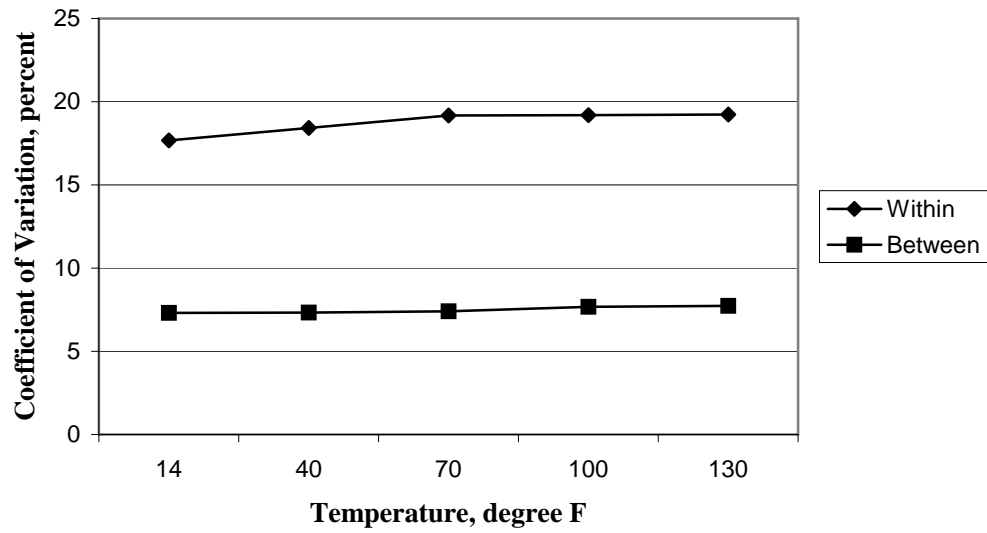
Figure 5.14. Effect of Temperature on Coefficient of Variation
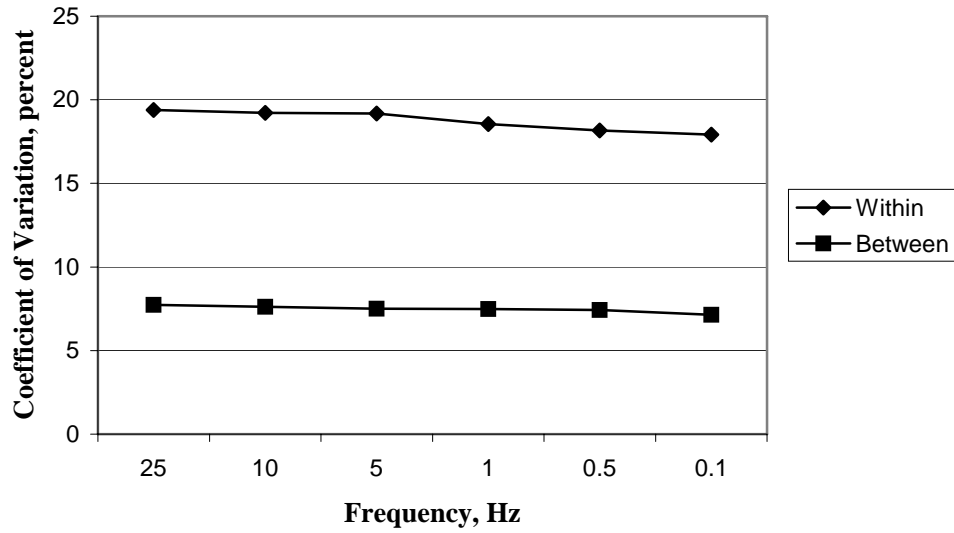
Figure 5.15. Effect of Frequency on Coefficient of Variation

161

Overall Test Variability. The overall coefficients of variation are presented in

Table 5.7. Comparing to other studies, the variability of the test results obtained in this

project was the lowest. However, it was noted that other studies used different testing

program that had two replicate specimens instrumented with two LVDTs per specimen,

comparing to three replicates instrumented with four LVDTs used in this project.

The confidence interval of the average response was then calculated using

Equation 5.27. The 95-percent confidence interval for the dynamic modulus obtained in

this project was ±13.56 percent, which was less than the required value of ±15 percent,

as specified in AASHTO TP 62-03 (*74*).

$$\pm R = z_{\alpha/2}\sqrt{\frac{CV_w^2}{ij} + \frac{CV_b^2}{j}} \tag{5.27}$$

where:

$z_{\alpha/2}$ = standard normal deviate for selected level of significance

CV_w = "within" specimen coefficient of variation

CV_b = "between" specimen coefficient of variation

i = number of LVDTs per specimen

j = number of specimens

In summary, the analysis of variability presented in this project showed that the

variability of the dynamic modulus values obtained in this project was lower than those

in other studies. In addition, the 95-percent confidence interval of the test results was

less than the required value specified in AASHTO TP 62-03 (*74*). It was recommended

that the dynamic modulus values reported in this study be used for level 1 dynamic

modulus inputs of HMA in the M-E Design Guide.

Table 5.7. Analysis of Test Variability

Study	Coefficient of Variation for $|E^*|$ (%)		Coefficient of Variation for ϕ (%)	
	Within	**Between**	**Within**	**Between**
Witczak (*73*)	26.2	15.2	11.0	8.7
Pellinen (*75*)	39.0	13.0	17.0	10.0
Bonaquist (*71*)		13.0		
This Study	18.7	7.5	8.5	7.4

5.3 Development of Master Curve for Dynamic Modulus

As described in the previous section, the dynamic modulus of an asphalt mixture was measured at five different temperatures and at six different frequencies (for each temperature level). The dynamic modulus data collected at different test temperatures can be shifted relative to the frequency to form a single master curve at a reference temperature, usually 21C (70F) for HMA. The master curve describes the loading rate (frequency) and temperature dependent properties of asphalt concrete under linear viscoelastic conditions. By shifting the test data to a reference temperature, the dynamic modulus of the HMA in question could be determined at a broaden range without performing a complex testing program. In addition, the master curves can be used to compare stiffness of the HMA mixtures across the test temperatures and frequencies.

The shift factor for a given temperature, $a(T)$, is a constant to which the test frequency at that temperature must be divided to get a reduced frequency, f_r, for the master curve, as shown in Equation 5.28 (*57*).

$$f_r = \frac{f}{a(T)} \quad \text{or} \quad \log(f_r) = \log f - \log a(T) \tag{5.28}$$

The temperature to which all data are shifted is the reference temperature, T_R. At the reference temperature, the shift factor $a(T) = 1$.

Several mathematical models are used to fit the shifted data, such as a generalized power law for low to intermediate temperatures, and polynomial and sigmoidal functions for higher temperatures (*74*). In this analysis, the method of using a sigmoidal function for developing the master curve was selected. This method was developed at the University of Maryland (*75*). The master curve was developed by fitting a sigmoidal function to the measured dynamic modulus test data using a non-

linear regression analysis procedure. The shift factors were solved simultaneously with

the coefficients of the sigmoidal function presented in Equation 5.29.

$$\log\left(|E*|\right) = \delta + \frac{\alpha}{1 + e^{\beta - \gamma \log f_r}} \tag{5.29}$$

where:

$|E*|$ = predicted dynamic modulus

δ = minimum value of $|E*|$

α = span between maximum and minimum value of $|E*|$

β, γ = parameters describing the shape of the sigmoidal function

f_r = reduced frequency at T_r

Various computer programs are available to fit the model to the test data. In this

analysis, the numerical optimization add-in routine (Solver) contained in a Microsoft

Excel® spreadsheet was used. The Solver is based on the Generalized Reduced

Gradient (GRG2) algorithm developed by Lasdon et al. (*103*) for optimizing nonlinear

problems. In order to determine the best fit of a function, the Solver uses iterative

numerical methods. The results are calculated using the function in the optimum cell

with trial values from the adjustable cells. The outputs and their rates of change are

observed as inputs are varied to guide the selection of new trial values. The

optimization stops when the tolerance meets the criterion. The disadvantage of this

process is that it is highly dependent on the initial starting point. If a process is started in

an infeasible design space, it is likely that no feasible solutions can be found (*103*).

Figure 5.16 presents a spreadsheet used to develop the master curve, and Figure

5.17 presents an example of master curve developed from the data presented in Figure

5.16.

Master Curve Development using Sigmoidal Function

Reference Temperature F: 70

(1)	(2)	(3)	(4)	(5)	(6)	(7)	(8)	(9)	(10)
Temp	f (Hz)	Em (psi)	Em (ksi)	Log(f)	Log(fr)	Epr	log(Epr)	log(Em)	SE
14	25	4181393	4181.4	1.3979	5.8228	4,001.5	3.6022	3.621	3.65E-04
14	10	3890223	3890.2	1.0000	5.4249	3,872.5	3.5880	3.590	3.94E-06
14	5	3767379	3767.4	0.6990	5.1239	3,761.9	3.5754	3.576	4.09E-07
14	1	3431486	3431.5	0.0000	4.4249	3,458.2	3.5389	3.535	1.13E-05
14	0.5	3271928	3271.9	-0.3010	4.1239	3,306.4	3.5194	3.515	2.08E-05
14	0.1	2890897	2890.9	-1.0000	3.4249	2,906.2	3.4633	3.461	5.27E-06
38	25	3421029	3421	1.3979	4.2262	3,359.5	3.5263	3.534	6.21E-05
38	10	3136501	3136.5	1.0000	3.8283	3,145.1	3.4976	3.496	1.42E-06
38	5	2917720	2917.7	0.6990	3.5273	2,968.8	3.4726	3.465	5.68E-05
38	1	2500231	2500.2	0.0000	2.8283	2,518.6	3.4012	3.398	1.01E-05
38	0.5	2281282	2281.3	-0.3010	2.5273	2,311.4	3.3639	3.358	3.25E-05
38	0.1	1852598	1852.6	-1.0000	1.8283	1,818.4	3.2597	3.268	6.54E-05
70	25	1478005	1478	1.3979	1.3979	1,520.6	3.1820	3.170	1.52E-04
70	10	1188869	1188.9	1.0000	1.0000	1,259.7	3.1003	3.075	6.32E-04
70	5	1040951	1041	0.6990	0.6990	1,076.4	3.0320	3.017	2.10E-04
70	1	710365	710.4	0.0000	0.0000	711.2	2.8520	2.852	2.61E-07
70	0.5	592882	592.9	-0.3010	-0.3010	583.3	2.7659	2.773	5.03E-05
70	0.1	378551	378.6	-1.0000	-1.0000	354.3	2.5493	2.578	8.33E-04
100	25	518253	518.3	1.3979	-0.5722	483.5	2.6844	2.715	9.13E-04
100	10	372716	372.7	1.0000	-0.9701	362.2	2.5590	2.571	1.53E-04
100	5	286532	286.5	0.6990	-1.2712	288.8	2.4605	2.457	1.16E-05
100	1	162481	162.5	0.0000	-1.9701	168.1	2.2255	2.211	2.16E-04
100	0.5	127925	127.9	-0.3010	-2.2712	133.0	2.1240	2.107	2.94E-04
100	0.1	77715	77.7	-1.0000	-2.9701	78.5	1.8949	1.890	2.01E-05
130	25	147473	147.5	1.3979	-2.2310	137.2	2.1375	2.169	9.79E-04
130	10	99236	99.2	1.0000	-2.6289	101.2	2.0051	1.997	7.39E-05
130	5	77618	77.6	0.6990	-2.9299	80.8	1.9077	1.890	3.17E-04
130	1	47183	47.2	0.0000	-3.6289	49.6	1.6954	1.674	4.63E-04
130	0.5	39810	39.8	-0.3010	-3.9299	40.9	1.6116	1.600	1.38E-04
130	0.1	29492	29.5	-1.0000	-4.6289	27.4	1.4376	1.470	1.04E-03

SSE = **0.007126**

Shift Factors:

log[a(14)] =	-3.6
log[a(40)] =	-2.0
log[a(100)] =	2.8
log[a(130)] =	4.4

Regression Coefficients:

delta =	0.8298
alpha =	2.8427
beta =	-0.9020
gama =	0.4761

Figure 5.16. An Example of Master Curve Development Spreadsheet
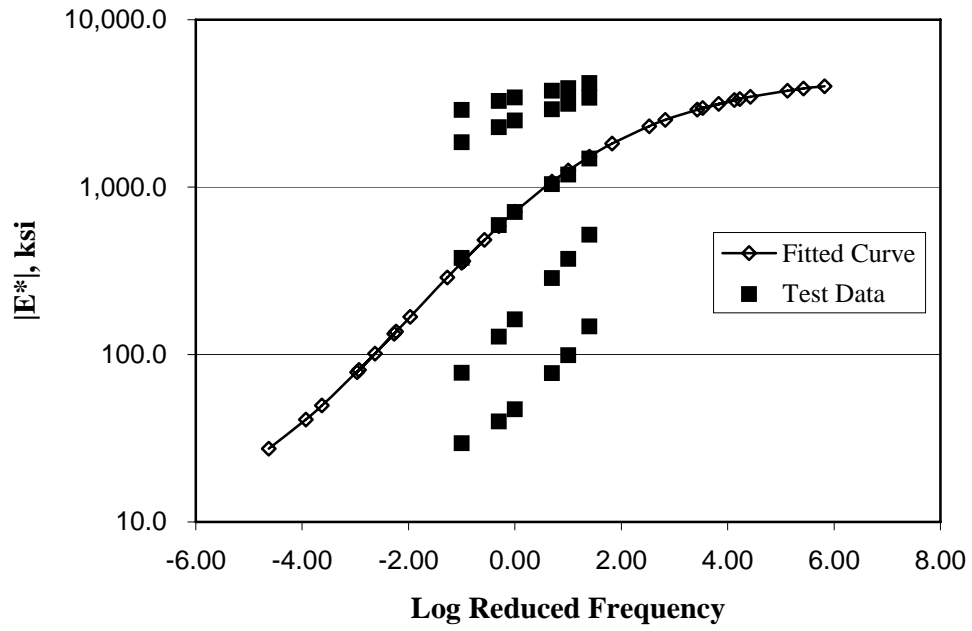
Figure 5.17. Master Curve Developed from Test Data Shown in Figure 3

The spreadsheet in Figure 5.16 was setup using the following steps:

- Columns (1) and (2) are the test temperatures and frequencies

- Column (3) is the dynamic modulus calculated in the previous section

- Column (4) = Column (3) / 1000

- Column (5) = log[Column (2)]

- Use Equation 5.28 to setup Column (6), and log[a(T)] in Equation 5.28 is listed in the "Shift Factors" section shown in Figure 5.16

- Use Equation 5.29 to setup column (8), and the parameters in Equation 5.29 are listed in the "Regression Coefficients" section shown in Figure 5.16

- Column (7) = $10^{\text{Column (8)}}$

- Column (9) = log[Column(4)]

- Column (10) = [Column (8) – Column (9)]^2

- SSE is the sum of Column (10)

To fit the model to the test data, Microsoft Excel™ Solver is used to minimize the sum of square error (SSE) by changing the "Shift Factors" and "Regression Coefficients". Several applications of the Solver algorithm are necessary to fully develop the master curve.

5.4 Presentation of Dynamic Modulus Test Results

This section was designed to present the dynamic modulus test results for all typical mixtures used in Arkansas in the form specified in AASHTO TP 62-03 (*74*). The information reported includes dynamic modulus values determined at each combination of temperature and frequency, their subsequent master curve, shift factors,

168

and regression coefficients, as shown in Figures 5.18 through 5.38. For all master curves in those figures, the lack-of-fit statistic S_e/S_y was less than 0.035, and the correlation coefficient R^2 was 0.999. Each figure presents the test results of one mixture. The dynamic modulus values of the specimens compacted at design air voids are presented in the first table in each figure, and the $|E^*|$ values of those compacted at 7 percent air voids are in the second table. The dynamic modulus values were then used to construct the subsequent master curves. The shift factors and regression coefficients used in the master curve development are presented in the last two tables. The mixture presented in each figure was named as follows:

<div align="center">Aggregate Source-Aggregate Size-Binder Grade</div>

where:

Aggregate source	= MCA, GMQ, ARK, or JET
Aggregate size	= 12.5, 25, or 37.5 mm
Binder grade	= PG70-22 or PG76-22

One of master curve applications is to compare the dynamic modulus of different mixtures across testing temperatures and frequencies. Based on Figures 5.18 through 5.38, it was observed that the dynamic modulus values of lower air void level specimens were higher than those of higher air void level specimens at the same test temperature and frequency.

The dynamic modulus test results showed that the dynamic modulus of HMA was dependent on both loading rate and test temperature. Mixtures were stiffer at low temperature and high frequency, and the $|E^*|$ values were lowest at the combination of highest temperature and lowest frequency (i.e., at 54C (130F) and 0.1 Hz).

Air Voids: 4.5 percent

Temp	Dynamic Modulus (ksi)					
	0.1 Hz	0.5 Hz	1 Hz	5 Hz	10 Hz	25 Hz
14F	2372.73	2807.88	2984.48	3353.73	3553.74	3786.28
40F	1503.64	1949.30	2070.78	2554.90	2786.08	3051.94
70F	378.79	623.58	756.59	1132.81	1336.69	1600.71
100F	75.67	122.80	157.68	293.08	386.10	534.99
130F	26.70	35.80	42.25	71.06	93.24	141.41

Air Voids: 7 percent

Temp	Dynamic Modulus (ksi)					
	0.1 Hz	0.5 Hz	1 Hz	5 Hz	10 Hz	25 Hz
14F	2331.75	2710.14	2861.46	3216.00	3319.34	3495.41
40F	1257.74	1624.13	1746.48	2119.63	2270.65	2471.50
70F	349.82	522.49	597.80	1032.32	1124.07	1289.08
100F	65.21	105.89	133.69	245.93	321.95	451.95
130F	24.58	32.79	38.56	63.80	83.28	125.53
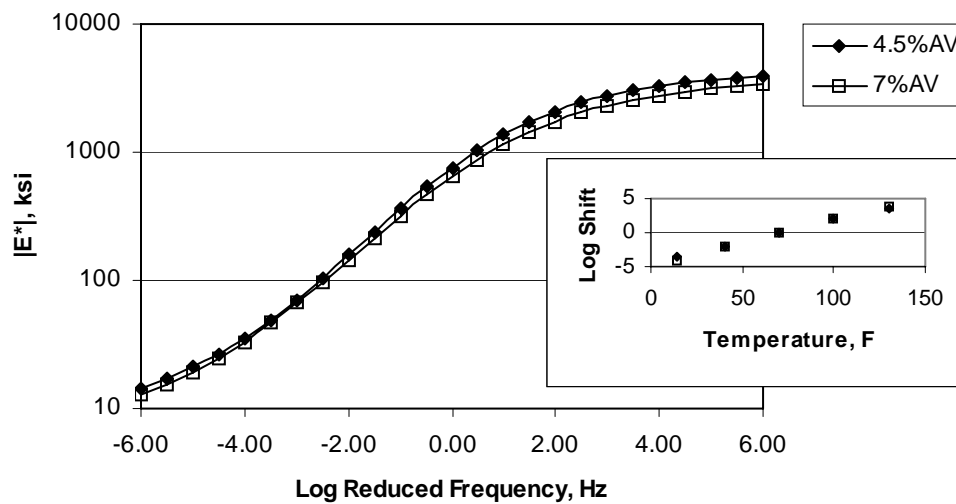
Shift Factors:

Parameter	Air Voids (%)	
	4.5	7
log[a(14)]	-3.47	-4.21
log[a(40)]	-2.12	-2.09
log[a(100)]	1.96	2.03
log[a(130)]	3.64	3.68

Regression Coefficients:

Parameter	Air Voids (%)	
	4.5	7
δ	0.8956	0.7945
α	2.7371	2.7873
β	-0.9716	-0.9627
γ	0.5321	0.5002

Figure 5.18. Dynamic Modulus Test Result for MCA-12.5mm-PG70-22

Air Voids: 4 percent

Temp	Dynamic Modulus (ksi)					
	0.1 Hz	0.5 Hz	1 Hz	5 Hz	10 Hz	25 Hz
14F	2408.42	2856.99	3041.81	3449.33	3633.98	3908.38
40F	1556.13	2029.56	2191.77	2637.59	2836.93	3080.40
70F	336.41	558.68	683.96	1050.27	1229.72	1509.84
100F	74.30	120.38	153.57	287.41	372.46	539.05
130F	30.77	40.72	47.95	79.16	103.83	156.20

Air Voids: 7 percent

Temp	Dynamic Modulus (ksi)					
	0.1 Hz	0.5 Hz	1 Hz	5 Hz	10 Hz	25 Hz
14F	1835.77	2185.92	2336.96	2669.61	2776.7	3038.62
40F	1298.90	1670.79	1771.18	2230.07	2429.92	2691.75
70F	270.58	430.58	520.74	780.28	924.71	1114.98
100F	72.99	113.63	141.69	249.06	318.81	432.42
130F	30.29	40.13	47.03	76.35	98.34	141.85
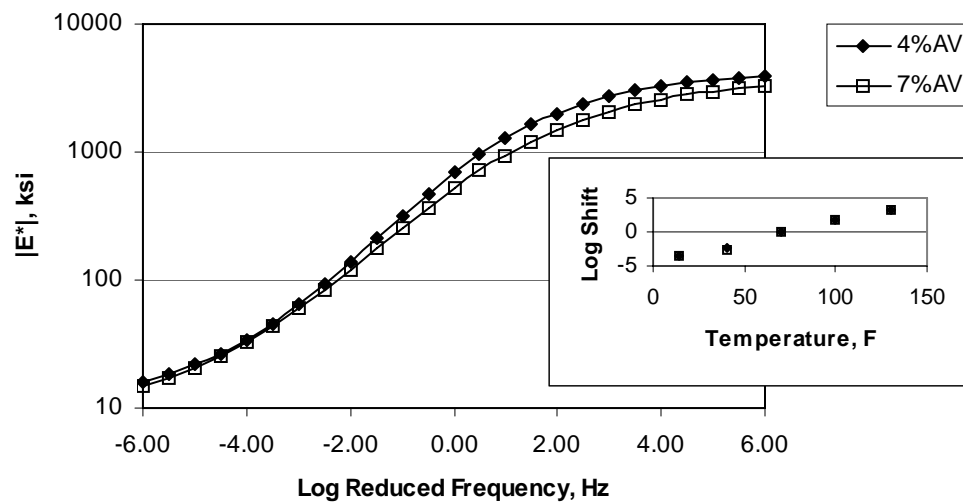
Shift Factors:

Parameter	Air Voids (%)	
	4	7
log[a(14)]	-3.63	-3.55
log[a(40)]	-2.32	-2.62
log[a(100)]	1.83	1.74
log[a(130)]	3.35	3.29

Regression Coefficients:

Parameter	Air Voids (%)	
	4	7
δ	0.9904	0.9041
α	2.6463	2.6755
β	-0.8363	-0.7435
γ	0.5463	0.4890

Figure 5.19. Dynamic Modulus Test Result for MCA-12.5mm-PG76-22

Air Voids: 4.5 percent

Temp	Dynamic Modulus (ksi)					
	0.1 Hz	0.5 Hz	1 Hz	5 Hz	10 Hz	25 Hz
14F	3024.88	3433.97	3658.32	4094.42	4284.89	4547.18
40F	1820.65	2417.03	2634.80	3306.25	3472.09	3824.55
70F	402.51	680.75	834.70	1285.16	1540.99	1878.99
100F	87.59	133.92	167.58	312.54	407.42	568.06
130F	35.81	47.18	55.10	88.68	114.10	170.40

Air Voids: 7 percent

Temp	Dynamic Modulus (ksi)					
	0.1 Hz	0.5 Hz	1 Hz	5 Hz	10 Hz	25 Hz
14F	2612.73	3129.35	3207.25	3545.21	3742.41	3966.54
40F	1742.91	2170.44	2468.47	2890.16	3063.67	3311.37
70F	346.86	590.35	733.78	1141.73	1332.22	1567.53
100F	80.00	120.72	150.25	277.54	368.99	490.69
130F	30.93	39.79	45.88	72.90	93.44	144.72
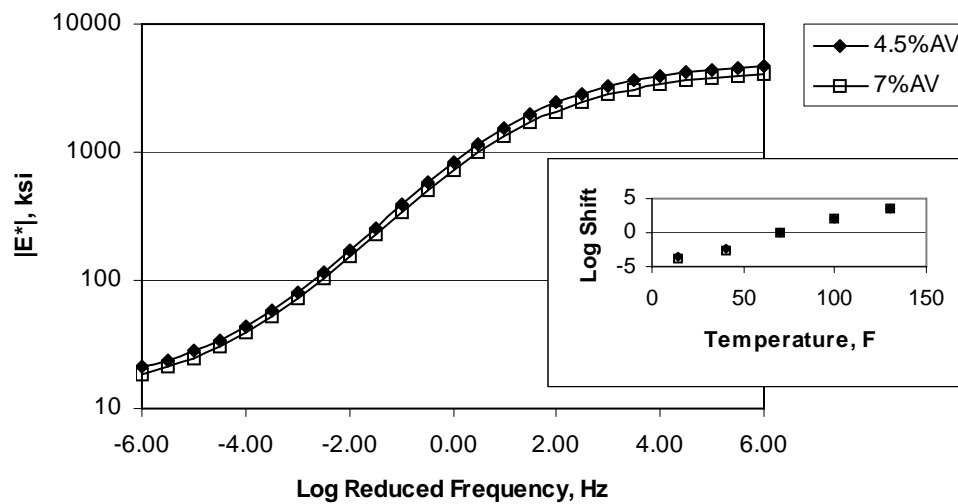
Shift Factors:

Parameter	Air Voids (%)	
	4.5	7
log[a(14)]	-3.61	-3.78
log[a(40)]	-2.29	-2.50
log[a(100)]	1.97	1.95
log[a(130)]	3.51	3.60

Regression Coefficients:

Parameter	Air Voids (%)	
	4.5	7
δ	1.1280	1.0670
α	2.5870	2.5796
β	-0.8201	-0.8281
γ	0.5548	0.5492

Figure 5.20. Dynamic Modulus Test Result for MCA-25mm-PG70-22

Air Voids: 4 percent

Temp	Dynamic Modulus (ksi)					
	0.1 Hz	0.5 Hz	1 Hz	5 Hz	10 Hz	25 Hz
14F	2955.05	3501.90	3557.58	4037.74	4209.63	4482.53
40F	2003.86	2456.56	2711.39	3291.17	3491.26	3986.09
70F	362.75	620.65	769.16	1195.58	1484.80	1724.12
100F	85.53	134.92	172.34	327.80	409.53	577.81
130F	32.90	42.72	49.66	82.08	108.14	167.36

Air Voids: 7 percent

Temp	Dynamic Modulus (ksi)					
	0.1 Hz	0.5 Hz	1 Hz	5 Hz	10 Hz	25 Hz
14F	2486.76	2910.56	3128.67	3490.91	3599.73	3853.98
40F	1453.34	1881.35	2044.48	2494.21	2710.91	2943.04
70F	248.32	420.52	523.13	840.10	1010.98	1242.81
100F	72.19	108.91	136.22	247.66	326.92	476.55
130F	27.95	34.82	39.48	60.67	76.72	115.70
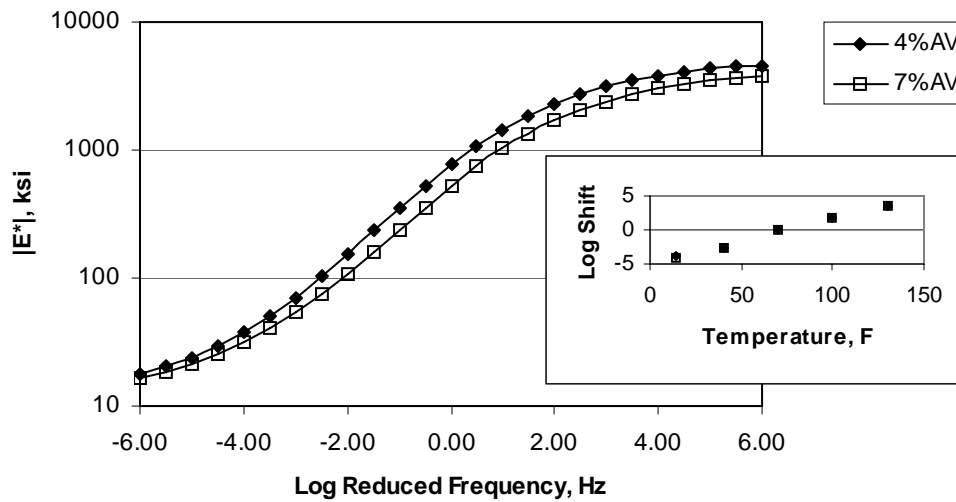
Shift Factors:

Parameter	Air Voids (%)	
	4	7
log[a(14)]	-3.75	-4.19
log[a(40)]	-2.56	-2.55
log[a(100)]	1.81	1.63
log[a(130)]	3.42	3.43

Regression Coefficients:

Parameter	Air Voids (%)	
	4	7
δ	1.0485	1.0611
α	2.6584	2.5670
β	-0.8088	-0.6021
γ	0.5497	0.5476

Figure 5.21. Dynamic Modulus Test Result for MCA-25mm-PG76-22

Air Voids: 4.5 percent

Temp	Dynamic Modulus (ksi)					
	0.1 Hz	0.5 Hz	1 Hz	5 Hz	10 Hz	25 Hz
14F	3314.71	3875.89	4088.09	4514.09	4596.81	4812.61
40F	1696.98	2175.01	2411.65	2954.21	3260.16	3546.82
70F	422.19	712.58	898.09	1412.35	1705.47	2091.09
100F	98.36	149.30	186.88	346.46	470.61	702.62
130F	40.20	49.79	56.28	86.21	111.19	177.91

Air Voids: 7 percent

Temp	Dynamic Modulus (ksi)					
	0.1 Hz	0.5 Hz	1 Hz	5 Hz	10 Hz	25 Hz
14F	2683.37	3072.97	3259.98	3569.46	3628.59	3845.35
40F	1569.42	2046.37	2270.41	2770.00	3001.09	3233.66
70F	304.61	531.62	672.24	1091.80	1323.13	1654.17
100F	68.87	96.79	117.51	209.92	278.66	430.37
130F	32.54	39.07	43.34	63.72	81.43	126.42
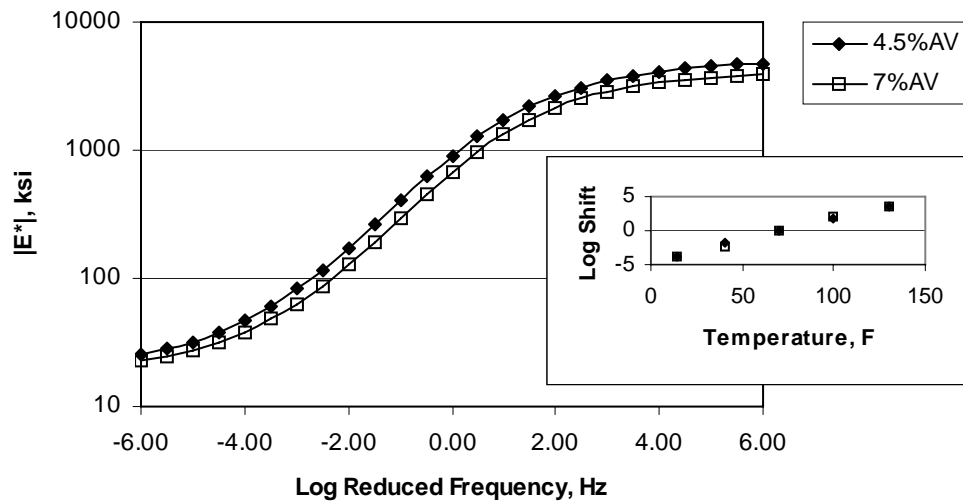
Shift Factors:

Parameter	Air Voids (%)	
	4.5	7
log[a(14)]	-3.93	-3.75
log[a(40)]	-1.84	-2.25
log[a(100)]	1.84	2.04
log[a(130)]	3.52	3.57

Regression Coefficients:

Parameter	Air Voids (%)	
	4.5	7
δ	1.2765	1.2596
α	2.4245	2.3588
β	-0.8157	-0.6921
γ	0.6145	0.6339

Figure 5.22. Dynamic Modulus Test Result for MCA-37.5mm-PG70-22

Air Voids: 4 percent

Temp	Dynamic Modulus (ksi)					
	0.1 Hz	0.5 Hz	1 Hz	5 Hz	10 Hz	25 Hz
14F	3788.75	4407.57	4598.99	5097.63	5319.6	5558.12
40F	2181.84	2788.64	3068.09	3671.47	3908.88	4269.37
70F	427.98	731.26	911.23	1432.32	1699.41	2087.76
100F	105.78	165.58	211.28	405.41	552.19	847.40
130F	44.79	59.38	69.57	117.50	156.30	248.72

Air Voids: 7 percent

Temp	Dynamic Modulus (ksi)					
	0.1 Hz	0.5 Hz	1 Hz	5 Hz	10 Hz	25 Hz
14F	3478.19	3771.23	4339.62	5075.15	5295.5	5520.05
40F	1851.33	2296.39	2565.89	3009.16	3276.63	3542.01
70F	321.17	558.28	699.47	1117.25	1369.02	1710.43
100F	84.89	127.83	159.14	298.50	395.59	596.64
130F	38.83	48.77	55.46	86.06	111.70	182.14
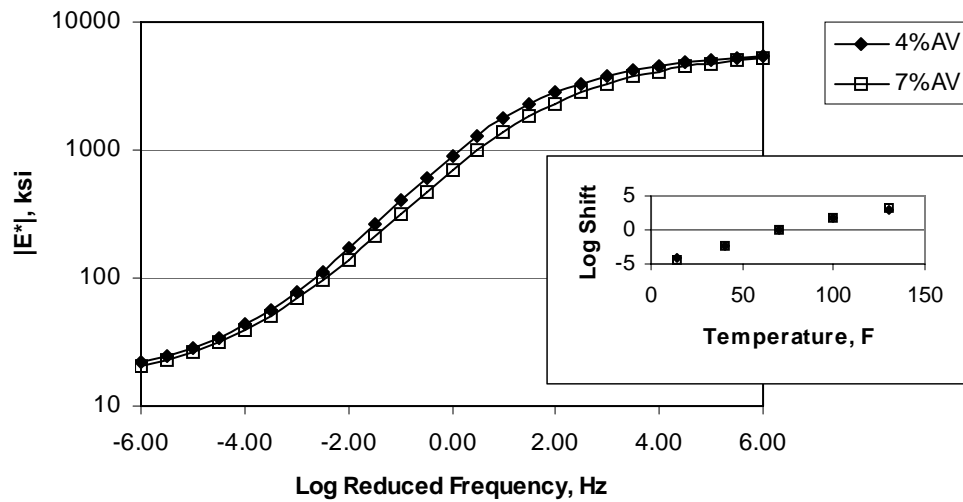
Shift Factors:

Parameter	Air Voids (%)	
	4	7
log[a(14)]	-4.12	-4.31
log[a(40)]	-2.30	-2.30
log[a(100)]	1.65	1.74
log[a(130)]	3.07	3.24

Regression Coefficients:

Parameter	Air Voids (%)	
	4	7
δ	1.1938	1.1329
α	2.5695	2.6365
β	-0.7888	-0.6150
γ	0.5920	0.5421

Figure 5.23. Dynamic Modulus Test Result for MCA-37.5mm-PG76-22

Air Voids: 4.5 percent

Temp	Dynamic Modulus (ksi)					
	0.1 Hz	0.5 Hz	1 Hz	5 Hz	10 Hz	25 Hz
14F	2890.9	3271.93	3431.49	3767.38	3890.22	4181.39
40F	1852.60	2281.28	2500.23	2917.72	3136.50	3421.03
70F	378.55	592.88	710.37	1040.95	1188.87	1478.00
100F	77.71	127.92	162.48	286.53	372.71	518.25
130F	29.49	39.81	47.18	77.62	99.24	147.47

Air Voids: 7 percent

Temp	Dynamic Modulus (ksi)					
	0.1 Hz	0.5 Hz	1 Hz	5 Hz	10 Hz	25 Hz
14F	2427.06	2769.52	2890.38	3125.45	3239.5	3376.53
40F	1605.25	2046.64	2230.27	2626.67	2775.10	3004.52
70F	327.51	519.79	622.58	922.65	1076.93	1310.02
100F	66.71	107.03	134.38	237.02	305.03	418.09
130F	25.10	33.37	39.08	62.92	80.38	118.24
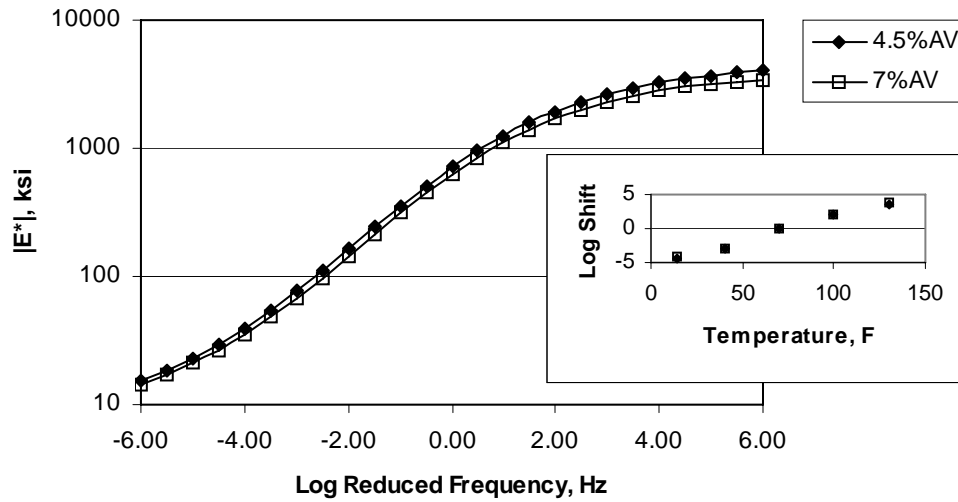
Shift Factors:

Parameter	Air Voids (%)	
	4.5	7
log[a(14)]	-4.43	-4.21
log[a(40)]	-2.83	-2.88
log[a(100)]	1.97	2.05
log[a(130)]	3.63	3.75

Regression Coefficients:

Parameter	Air Voids (%)	
	4.5	7
δ	0.8292	0.8543
α	2.8433	2.7416
β	-0.9022	-0.8891
γ	0.4761	0.4929

Figure 5.24. Dynamic Modulus Test Result for GMQ-12.5mm-PG70-22

Air Voids: 4 percent

Temp	Dynamic Modulus (ksi)					
	0.1 Hz	0.5 Hz	1 Hz	5 Hz	10 Hz	25 Hz
14F	2387.08	2709.14	2847.22	3108.15	3223.28	3498.44
40F	1290.44	1661.21	1808.78	2206.26	2401.97	2623.02
70F	376.84	575.35	684.52	986.10	1140.74	1360.35
100F	91.30	149.33	188.80	330.20	419.08	565.08
130F	40.11	57.41	70.22	119.46	156.26	230.58

Air Voids: 7 percent

Temp	Dynamic Modulus (ksi)					
	0.1 Hz	0.5 Hz	1 Hz	5 Hz	10 Hz	25 Hz
14F	2158.11	2503.92	2634.25	2887.12	3013.19	3262.39
40F	1195.13	1537.53	1695.67	2047.07	2193.83	2428.69
70F	278.29	433.06	518.83	781.70	909.22	1099.20
100F	65.99	104.54	130.88	228.42	289.84	394.56
130F	33.05	46.40	56.21	94.38	123.42	180.66
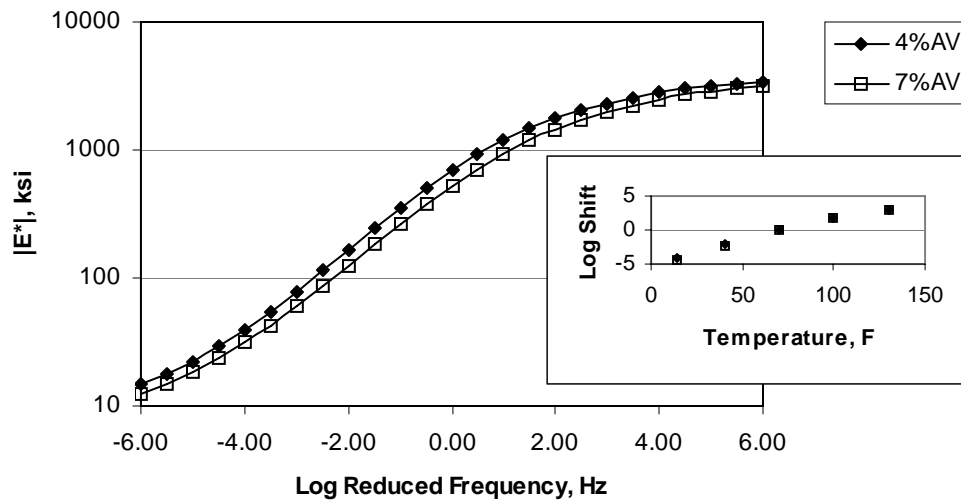
Shift Factors:

Parameter	Air Voids (%)	
	4	7
log[a(14)]	-4.14	-4.38
log[a(40)]	-2.15	-2.48
log[a(100)]	1.80	1.90
log[a(130)]	3.08	3.02

Regression Coefficients:

Parameter	Air Voids (%)	
	4	7
δ	0.7885	0.7191
α	2.8058	2.8587
β	-0.9979	-0.8475
γ	0.4760	0.4582

Figure 5.25. Dynamic Modulus Test Result for GMQ-12.5mm-PG76-22

Air Voids: 4.5 percent

Temp	Dynamic Modulus (ksi)					
	0.1 Hz	**0.5 Hz**	**1 Hz**	**5 Hz**	**10 Hz**	**25 Hz**
14F	3785.02	4236.09	4383.75	4905.14	4958.67	5219.78
40F	2179.32	2566.78	2913.82	3437.50	3640.80	3896.21
70F	498.85	793.06	948.23	1400.12	1640.49	1946.30
100F	96.69	163.20	210.75	399.09	525.54	797.42
130F	37.14	51.65	62.23	107.52	143.77	219.72

Air Voids: 7 percent

Temp	Dynamic Modulus (ksi)					
	0.1 Hz	**0.5 Hz**	**1 Hz**	**5 Hz**	**10 Hz**	**25 Hz**
14F	3291.54	3680.89	3771.76	4186.33	4376.86	4488.92
40F	2032.38	2492.31	2726.48	3097.69	3355.38	3592.05
70F	444.58	694.68	830.78	1210.85	1405.78	1702.34
100F	87.13	142.06	178.82	321.64	411.11	580.91
130F	36.97	51.04	60.91	101.99	133.69	201.54
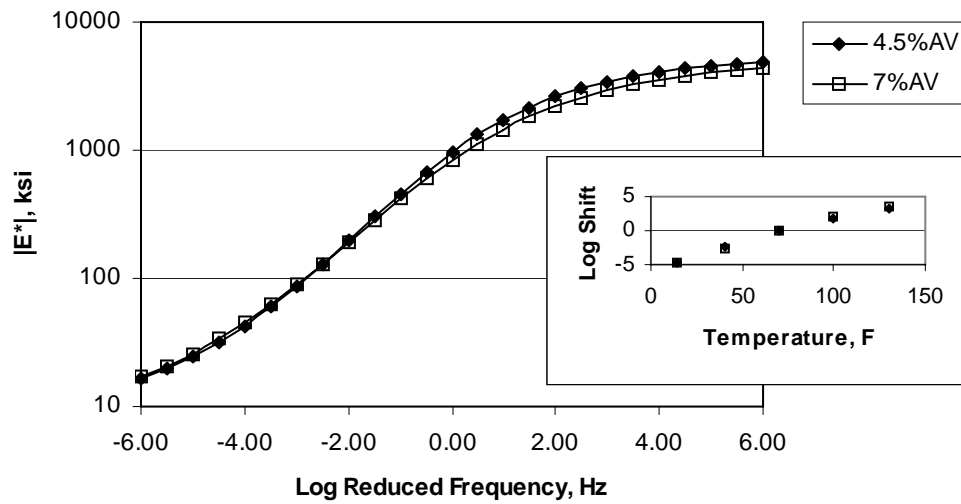
Shift Factors:

Parameter	Air Voids (%)	
	4.5	**7**
log[a(14)]	-4.65	-4.63
log[a(40)]	-2.37	-2.71
log[a(100)]	1.85	2.04
log[a(130)]	3.36	3.45

Regression Coefficients:

Parameter	Air Voids (%)	
	4.5	**7**
δ	0.9353	0.8931
α	2.7968	2.7985
β	-1.0039	-0.9699
γ	0.5292	0.4897

Figure 5.26. Dynamic Modulus Test Result for GMQ-25mm-PG70-22

Air Voids: 4 percent

Temp	Dynamic Modulus (ksi)					
	0.1 Hz	**0.5 Hz**	**1 Hz**	**5 Hz**	**10 Hz**	**25 Hz**
14F	3181.44	3584.14	3721.82	3972.14	4230.60	4486.00
40F	1498.39	1972.41	2154.65	2672.46	2913.40	3215.73
70F	390.43	617.98	749.20	1124.09	1317.36	1572.26
100F	92.64	147.88	186.14	332.36	432.60	590.31
130F	41.29	56.22	67.30	111.87	145.86	216.01

Air Voids: 7 percent

Temp	Dynamic Modulus (ksi)					
	0.1 Hz	**0.5 Hz**	**1 Hz**	**5 Hz**	**10 Hz**	**25 Hz**
14F	2392.80	2788.26	2934.12	3170.20	3409.26	3582.90
40F	1030.91	1348.09	1481.33	1812.13	1937.81	2198.25
70F	281.87	443.72	538.47	819.46	965.10	1191.19
100F	77.87	123.05	154.52	276.09	358.01	501.51
130F	32.21	43.37	51.16	83.57	107.58	156.81
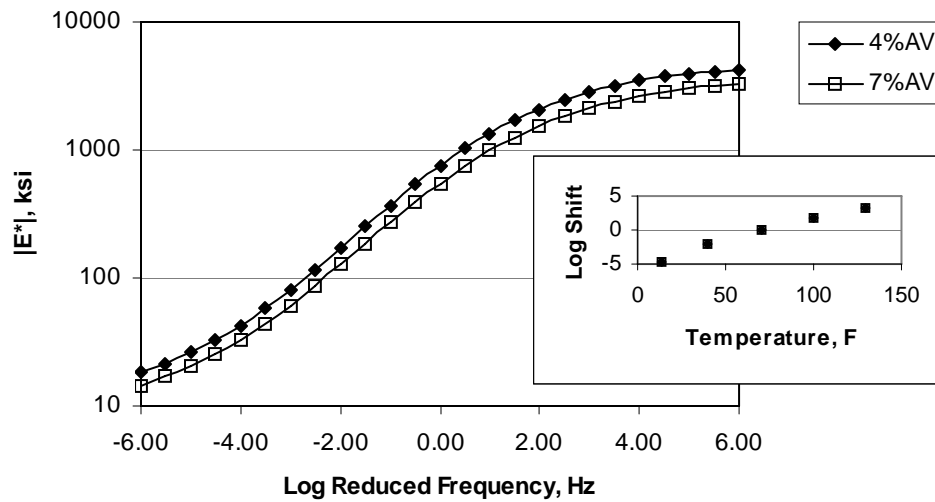
Shift Factors:

Parameter	Air Voids (%)	
	4	**7**
log[a(14)]	-4.56	-4.71
log[a(40)]	-2.16	-1.93
log[a(100)]	1.83	1.66
log[a(130)]	3.20	3.20

Regression Coefficients:

Parameter	Air Voids (%)	
	4	**7**
δ	0.9780	0.8758
α	2.7106	2.7098
β	-0.8494	-0.7850
γ	0.4985	0.4873

Figure 5.27. Dynamic Modulus Test Result for GMQ-25mm-PG76-22

Air Voids: 4.5 percent

Temp	Dynamic Modulus (ksi)					
	0.1 Hz	0.5 Hz	1 Hz	5 Hz	10 Hz	25 Hz
14F	3211.52	3622.01	3743.58	4291.95	4551.61	4976.59
40F	2066.76	2571.76	2766.18	3338.22	3642.27	3323.58
70F	580.53	956.84	1151.62	1693.69	1990.17	2384.65
100F	107.63	179.49	228.69	432.69	572.62	845.10
130F	34.74	47.34	56.83	97.15	129.71	231.37

Air Voids: 7 percent

Temp	Dynamic Modulus (ksi)					
	0.1 Hz	0.5 Hz	1 Hz	5 Hz	10 Hz	25 Hz
14F	2830.17	3373.56	3599.86	3965.74	4030.50	4223.05
40F	1819.10	2350.64	2540.11	2987.00	3180.73	3181.63
70F	509.81	846.59	1069.52	1566.06	1863.94	2174.04
100F	74.05	119.12	151.77	288.38	386.27	571.25
130F	29.68	37.94	43.95	71.48	92.89	149.93
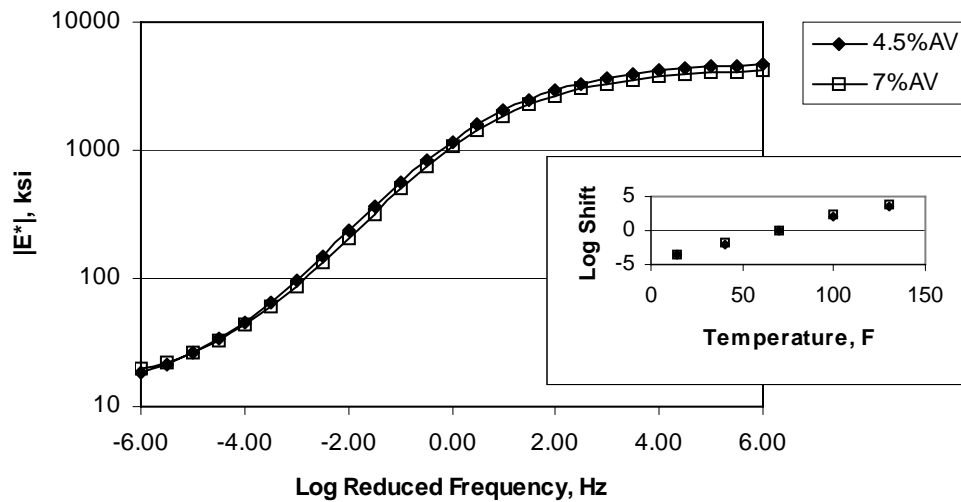
Shift Factors:

Parameter	Air Voids (%)	
	4.5	7
log[a(14)]	-3.46	-3.41
log[a(40)]	-1.92	-1.86
log[a(100)]	1.96	2.29
log[a(130)]	3.60	3.88

Regression Coefficients:

Parameter	Air Voids (%)	
	4.5	7
δ	1.0245	1.1116
α	2.6694	2.5318
β	-1.1841	-1.1325
γ	0.5852	0.6184

Figure 5.28. Dynamic Modulus Test Result for GMQ-37.5mm-PG70-22

Air Voids: 4 percent

Temp	Dynamic Modulus (ksi)					
	0.1 Hz	**0.5 Hz**	**1 Hz**	**5 Hz**	**10 Hz**	**25 Hz**
14F	3927.88	4322.07	4487.96	4843.51	4890.43	5153.19
40F	2391.59	2660.67	2978.29	3544.07	3707.89	3998.99
70F	711.70	1081.41	1297.55	1815.69	2114.40	2463.78
100F	160.91	270.10	341.46	594.89	766.84	987.03
130F	53.28	77.45	95.48	168.44	223.08	334.71

Air Voids: 7 percent

Temp	Dynamic Modulus (ksi)					
	0.1 Hz	**0.5 Hz**	**1 Hz**	**5 Hz**	**10 Hz**	**25 Hz**
14F	2645.01	2950.07	3060.22	3475.69	3592.55	4017.74
40F	2281.64	2638.05	2876.48	3423.13	3255.37	3965.22
70F	544.29	820.99	968.53	1359.22	1581.94	1779.02
100F	135.73	205.52	257.75	428.53	529.42	700.05
130F	51.61	72.71	88.27	152.52	198.79	296.84
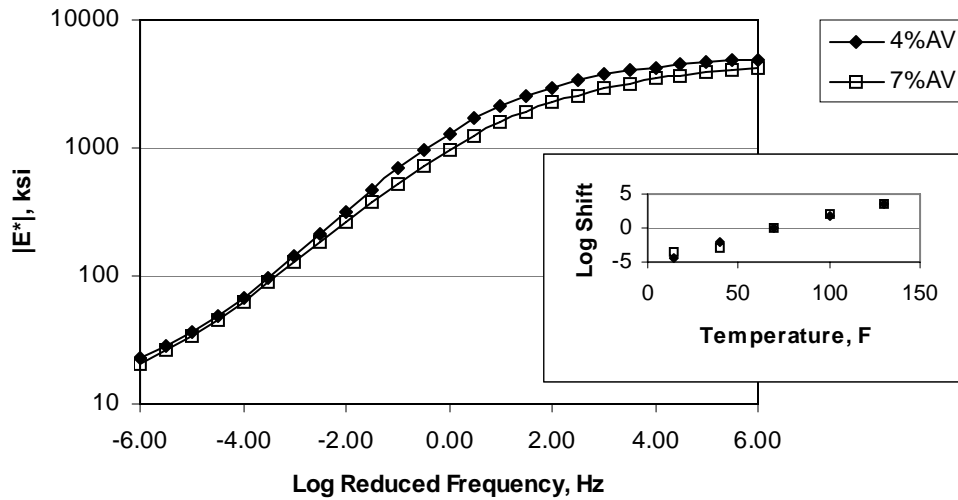
Shift Factors:

	Air Voids (%)	
Parameter	**4**	**7**
log[a(14)]	-4.46	-3.43
log[a(40)]	-2.11	-3.00
log[a(100)]	1.89	2.00
log[a(130)]	3.45	3.39

Regression Coefficients:

	Air Voids (%)	
Parameter	**4**	**7**
δ	0.9732	0.8047
α	2.7586	2.8841
β	-1.2468	-1.1349
γ	0.5108	0.4452

Figure 5.29. Dynamic Modulus Test Result for GMQ-37.5mm-PG76-22

Air Voids: 4.5 percent

Temp	Dynamic Modulus (ksi)					
	0.1 Hz	**0.5 Hz**	**1 Hz**	**5 Hz**	**10 Hz**	**25 Hz**
14F	2672.89	3138.01	3325.35	3671.70	3858.61	4145.23
40F	1573.50	2050.55	2181.59	2700.44	2889.42	3239.76
70F	305.01	513.40	631.68	970.44	1141.88	1395.43
100F	58.35	95.77	123.73	233.57	313.05	448.87
130F	24.44	33.81	40.53	68.59	90.03	139.57

Air Voids: 7 percent

Temp	Dynamic Modulus (ksi)					
	0.1 Hz	**0.5 Hz**	**1 Hz**	**5 Hz**	**10 Hz**	**25 Hz**
14F	2102.57	2449.02	2587.44	2895.42	3065.64	3219.58
40F	1226.71	1579.54	1724.90	2095.87	2262.16	2446.68
70F	242.87	409.70	506.80	785.42	925.25	1139.56
100F	55.52	92.51	119.40	224.86	298.58	419.69
130F	21.69	29.20	34.54	58.85	77.41	117.66
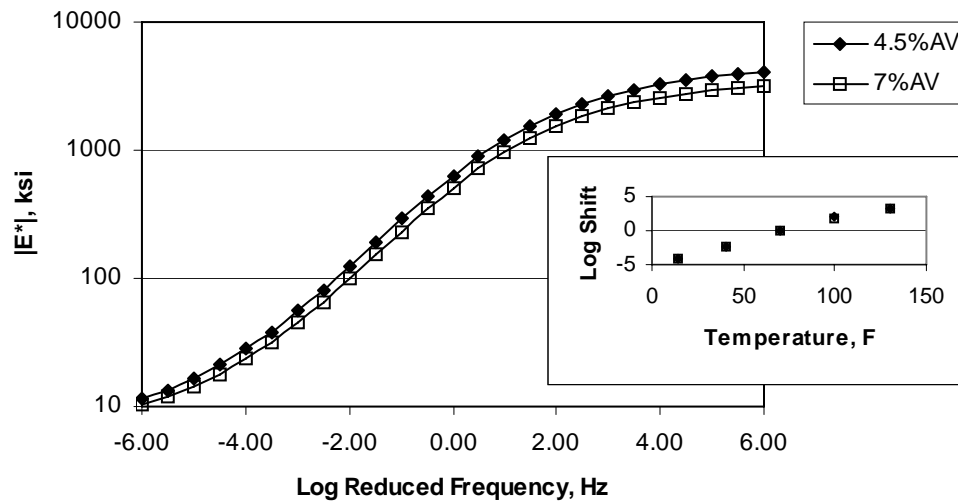
Shift Factors:

Parameter	Air Voids (%)	
	4.5	**7**
log[a(14)]	-4.12	-4.07
log[a(40)]	-2.48	-2.39
log[a(100)]	1.94	1.73
log[a(130)]	3.36	3.29

Regression Coefficients:

Parameter	Air Voids (%)	
	4.5	**7**
δ	0.7750	0.7845
α	2.8908	2.7644
β	-0.8475	-0.8210
γ	0.5113	0.5338

Figure 5.30. Dynamic Modulus Test Result for ARK-12.5mm-PG70-22

Air Voids: 4 percent

Temp	Dynamic Modulus (ksi)					
	0.1 Hz	**0.5 Hz**	**1 Hz**	**5 Hz**	**10 Hz**	**25 Hz**
14F	2757.06	3145.26	3332.71	3707.93	3875.63	4035.88
40F	2125.77	2617.31	2868.29	3312.00	3581.25	3955.13
70F	471.54	728.53	865.19	1246.31	1431.36	1678.70
100F	109.50	184.79	235.76	426.61	529.49	702.52
130F	44.39	66.20	82.12	146.78	193.98	280.37

Air Voids: 7 percent

Temp	Dynamic Modulus (ksi)					
	0.1 Hz	**0.5 Hz**	**1 Hz**	**5 Hz**	**10 Hz**	**25 Hz**
14F	2261.72	2606.61	2778.21	3056.11	3172.76	3329.86
40F	1442.11	1795.07	1975.94	2360.54	2557.11	2770.09
70F	351.51	551.73	660.85	964.97	1117.90	1349.56
100F	82.80	135.58	170.24	296.02	373.15	495.33
130F	35.28	51.70	63.28	109.67	143.84	207.67
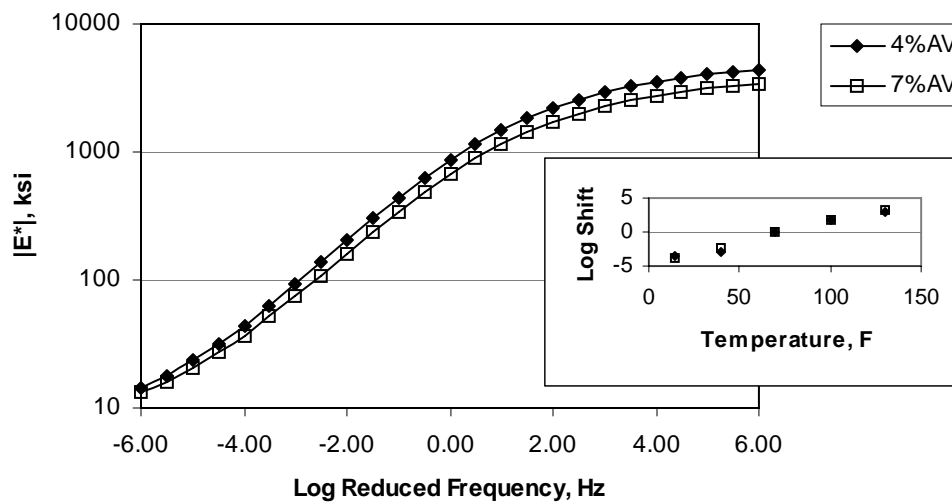
Shift Factors:

Parameter	Air Voids (%)	
	4	**7**
log[a(14)]	-3.67	-3.97
log[a(40)]	-2.92	-2.49
log[a(100)]	1.78	1.88
log[a(130)]	3.08	3.14

Regression Coefficients:

Parameter	Air Voids (%)	
	4	**7**
δ	0.6855	0.7063
α	3.0186	2.8954
β	-1.0791	-0.9985
γ	0.4614	0.4651

Figure 5.31. Dynamic Modulus Test Result for ARK-12.5mm-PG76-22

Air Voids: 4.5 percent

Temp	Dynamic Modulus (ksi)					
	0.1 Hz	0.5 Hz	1 Hz	5 Hz	10 Hz	25 Hz
14F	3070.43	3572.38	3730.56	4139.33	4292.99	4480.82
40F	1712.02	2159.76	2380.42	2820.69	3037.98	3326.18
70F	525.29	831.30	1005.22	1440.48	1634.99	2007.83
100F	102.16	174.31	223.30	420.45	539.98	736.30
130F	36.02	51.19	62.40	110.10	146.19	219.75

Air Voids: 7 percent

Temp	Dynamic Modulus (ksi)					
	0.1 Hz	0.5 Hz	1 Hz	5 Hz	10 Hz	25 Hz
14F	2963.54	3485.65	3694.58	4127.62	4247.35	4556.59
40F	1376.81	1769.36	1950.58	2334.51	2477.41	2737.71
70F	327.48	554.31	680.46	1033.04	1230.78	1465.96
100F	66.41	110.79	142.75	269.55	365.31	529.95
130F	22.45	30.34	35.94	59.71	77.68	119.08
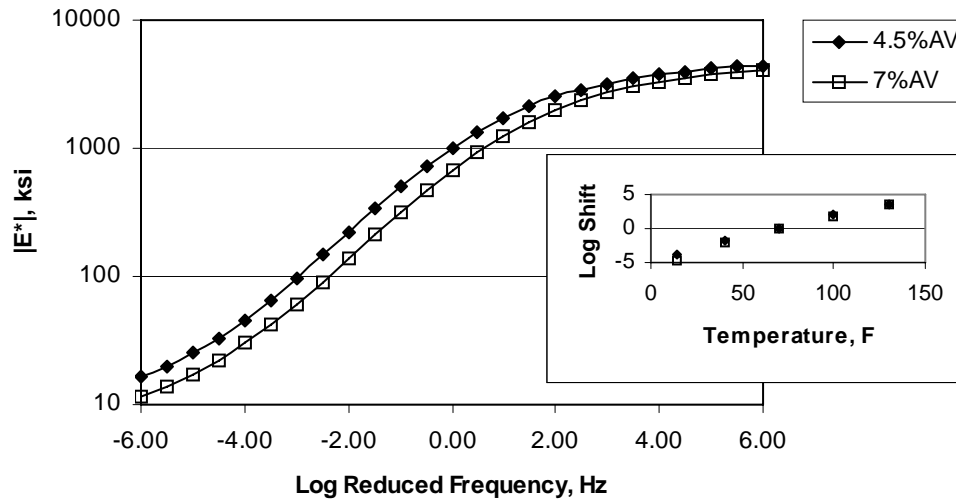
Shift Factors:

Parameter	Air Voids (%)	
	4.5	7
log[a(14)]	-3.95	-4.72
log[a(40)]	-1.88	-2.00
log[a(100)]	1.94	1.88
log[a(130)]	3.49	3.66

Regression Coefficients:

Parameter	Air Voids (%)	
	4.5	7
δ	0.8797	0.7523
α	2.8042	2.9190
β	-1.1350	-0.9046
γ	0.5213	0.5023

Figure 5.32. Dynamic Modulus Test Result for ARK-25mm-PG70-22

Air Voids: 4 percent

Temp	Dynamic Modulus (ksi)					
	0.1 Hz	0.5 Hz	1 Hz	5 Hz	10 Hz	25 Hz
14F	3947.19	4547.38	4739.67	5213.55	5465.02	5768.46
40F	2302.80	2815.34	2980.34	3642.60	3746.13	4198.18
70F	500.53	801.74	959.98	1399.06	1625.62	1908.46
100F	110.59	190.67	245.70	445.56	579.78	766.02
130F	44.11	65.62	81.20	147.00	198.35	301.88

Air Voids: 7 percent

Temp	Dynamic Modulus (ksi)					
	0.1 Hz	0.5 Hz	1 Hz	5 Hz	10 Hz	25 Hz
14F	3076.38	3600.05	3724.15	4197.99	4379.10	4592.93
40F	1662.27	2051.04	2186.24	2630.84	2809.75	3125.75
70F	351.06	563.16	676.69	1012.10	1171.71	1433.88
100F	99.64	163.71	207.08	373.19	475.08	646.39
130F	42.12	60.24	73.19	127.80	169.87	246.36
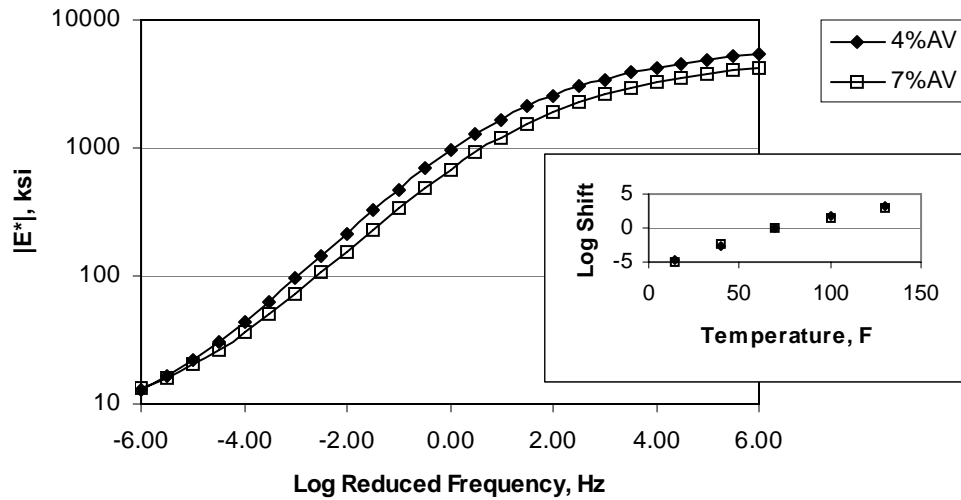
Shift Factors:

Parameter	Air Voids (%)	
	4	7
log[a(14)]	-4.78	-4.88
log[a(40)]	-2.58	-2.49
log[a(100)]	1.80	1.58
log[a(130)]	3.10	2.90

Regression Coefficients:

Parameter	Air Voids (%)	
	4	7
δ	0.5666	0.6903
α	3.2387	3.0185
β	-1.0742	-0.8917
γ	0.4445	0.4491

Figure 5.33. Dynamic Modulus Test Result for ARK-25mm-PG76-22

Air Voids: 4.5 percent

Temp	Dynamic Modulus (ksi)					
	0.1 Hz	0.5 Hz	1 Hz	5 Hz	10 Hz	25 Hz
14F	3425.25	3879.8	4043.86	4463.74	4591.38	4888.31
40F	1722.32	2170.40	2338.76	2812.25	3047.13	3367.01
70F	315.86	527.80	645.64	989.83	1178.43	1419.48
100F	67.82	108.66	138.88	265.40	355.82	537.48
130F	26.00	33.23	38.32	62.43	82.02	131.53

Air Voids: 7 percent

Temp	Dynamic Modulus (ksi)					
	0.1 Hz	0.5 Hz	1 Hz	5 Hz	10 Hz	25 Hz
14F	2742.02	3219.92	3430.62	3856.04	3996.06	4441.54
40F	1145.08	1494.51	1673.60	2036.84	2206.99	2475.72
70F	223.49	385.05	481.65	760.77	915.88	1123.85
100F	53.03	79.44	98.70	180.34	239.13	355.72
130F	25.70	31.35	34.90	51.65	65.06	100.68
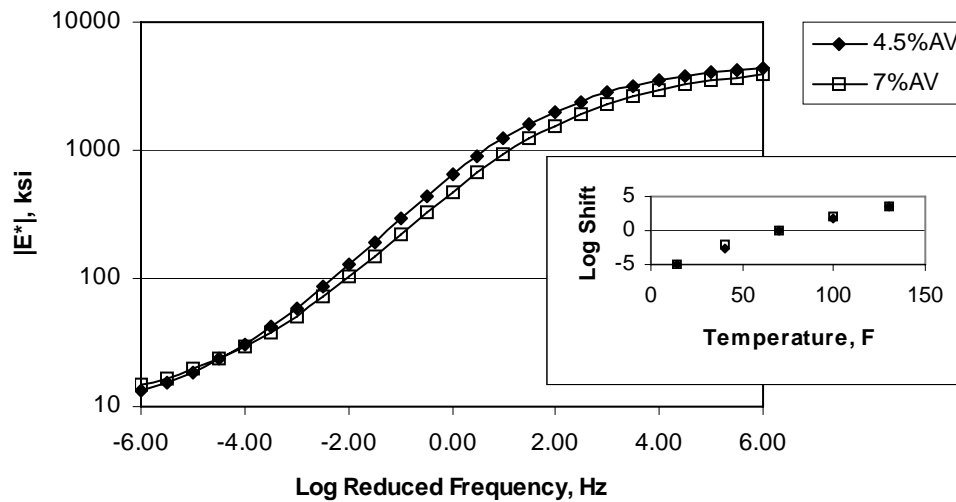
Shift Factors:

Parameter	Air Voids (%)	
	4.5	7
log[a(14)]	-5.12	-4.90
log[a(40)]	-2.51	-2.17
log[a(100)]	1.81	1.94
log[a(130)]	3.51	3.55

Regression Coefficients:

Parameter	Air Voids (%)	
	4.5	7
δ	0.8623	0.9604
α	2.8387	2.7000
β	-0.7789	-0.5561
γ	0.5126	0.5054

Figure 5.34. Dynamic Modulus Test Result for ARK-37.5mm-PG70-22

Air Voids: 4 percent

Temp	Dynamic Modulus (ksi)					
	0.1 Hz	0.5 Hz	1 Hz	5 Hz	10 Hz	25 Hz
14F	3491.46	3856.81	4033.22	4364.61	4456.94	4703.35
40F	1762.41	2223.52	2364.00	2753.04	2963.39	3218.80
70F	401.08	636.32	765.27	1126.97	1295.70	1554.42
100F	100.49	164.70	210.18	381.32	495.66	680.25
130F	40.41	54.50	64.39	107.80	141.49	215.27

Air Voids: 7 percent

Temp	Dynamic Modulus (ksi)					
	0.1 Hz	0.5 Hz	1 Hz	5 Hz	10 Hz	25 Hz
14F	3125.16	3504	3633.19	3988.72	4202.11	4404.07
40F	1583.65	1946.05	2052.19	2488.25	2669.13	2874.88
70F	340.22	545.40	658.99	982.97	1148.95	1407.69
100F	80.94	131.30	164.69	301.82	397.88	557.71
130F	35.20	47.22	55.43	92.43	121.83	194.04
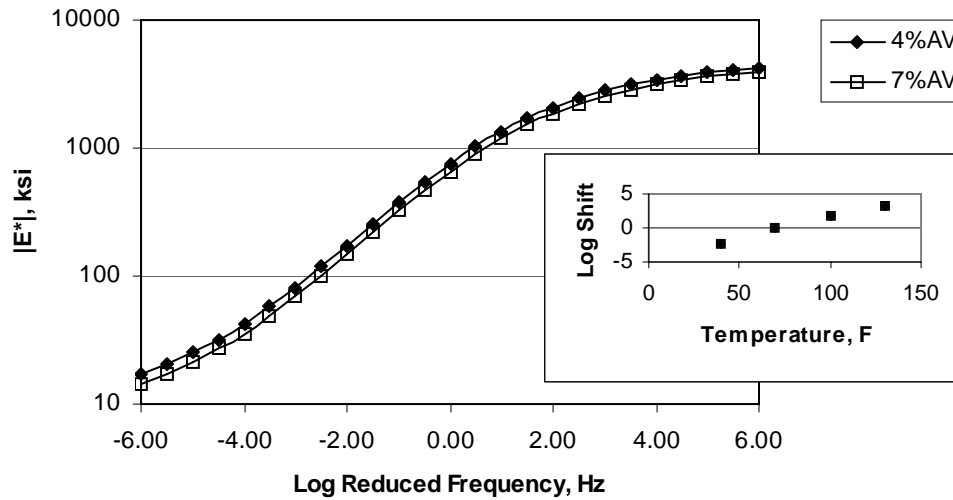
Shift Factors:

Parameter	Air Voids (%)	
	4	7
log[a(14)]	-5.43	-5.23
log[a(40)]	-2.45	-2.40
log[a(100)]	1.70	1.78
log[a(130)]	3.24	3.20

Regression Coefficients:

Parameter	Air Voids (%)	
	4	7
δ	0.9264	0.8514
α	2.7539	2.8031
β	-0.8974	-0.8580
γ	0.4938	0.4893

Figure 5.35. Dynamic Modulus Test Result for ARK-37.5mm-PG76-22

Air Voids: 4.5 percent

Temp	Dynamic Modulus (ksi)					
	0.1 Hz	0.5 Hz	1 Hz	5 Hz	10 Hz	25 Hz
14F	3215.29	3704.89	3912.97	4343.79	4534.73	4798.10
40F	1479.56	1951.98	2185.25	2713.74	2989.88	3381.08
70F	315.39	545.81	676.05	1052.74	1248.78	1549.56
100F	59.61	94.82	120.32	226.82	303.20	443.17
130F	29.47	40.77	49.00	84.62	113.70	179.37

Air Voids: 7 percent

Temp	Dynamic Modulus (ksi)					
	0.1 Hz	0.5 Hz	1 Hz	5 Hz	10 Hz	25 Hz
14F	2517.74	2937.65	3104.72	3511.12	3740.15	4024.39
40F	1177.35	1574.93	1752.28	2171.24	2419.17	2709.17
70F	262.96	432.29	531.33	828.14	982.42	1226.12
100F	57.48	90.38	113.02	202.86	263.59	373.83
130F	25.87	35.63	42.42	71.06	92.75	140.44
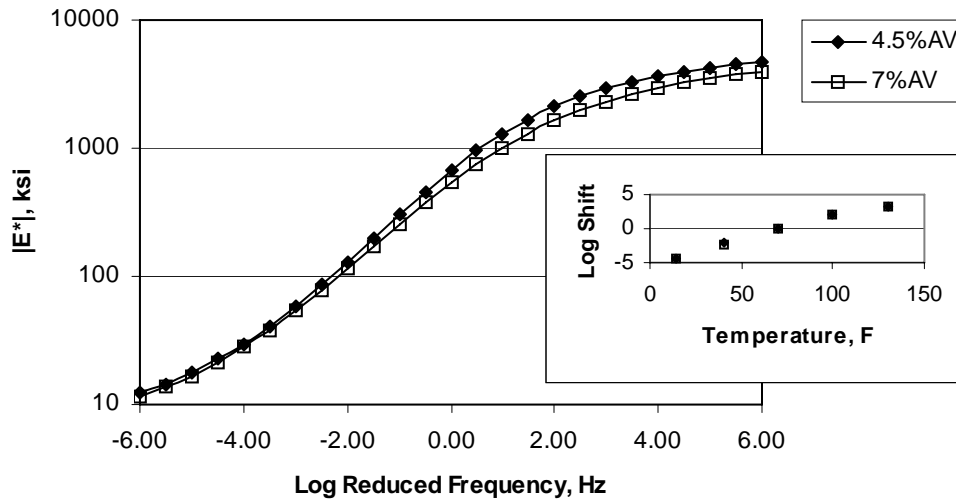
Shift Factors:

Parameter	Air Voids (%)	
	4.5	7
log[a(14)]	-4.42	-4.31
log[a(40)]	-2.16	-2.21
log[a(100)]	2.03	1.97
log[a(130)]	3.15	3.27

Regression Coefficients:

Parameter	Air Voids (%)	
	4.5	7
δ	0.8130	0.7187
α	2.9133	2.9568
β	-0.8065	-0.7510
γ	0.5085	0.4659

Figure 5.36. Dynamic Modulus Test Result for JET-12.5mm-PG70-22

Air Voids: 4.5 percent

Temp	Dynamic Modulus (ksi)					
	0.1 Hz	0.5 Hz	1 Hz	5 Hz	10 Hz	25 Hz
14F	2611.91	3125.86	3331.09	3738.10	3888.97	4222.86
40F	1232.60	1617.50	1824.53	2283.74	2605.59	3055.12
70F	331.94	587.89	726.80	1162.46	1370.63	1694.48
100F	65.05	107.50	138.95	269.21	361.55	545.76
130F	27.97	38.37	45.92	79.23	106.57	169.14

Air Voids: 7 percent

Temp	Dynamic Modulus (ksi)					
	0.1 Hz	0.5 Hz	1 Hz	5 Hz	10 Hz	25 Hz
14F	1770.45	2139.2	2313.39	2740.55	2809.18	3268.83
40F	1076.57	1435.80	1601.66	2063.34	2268.39	2534.13
70F	301.17	476.45	580.53	900.02	1067.42	1315.25
100F	82.79	134.11	168.39	296.62	378.31	527.11
130F	30.23	41.99	50.44	86.71	114.84	179.40
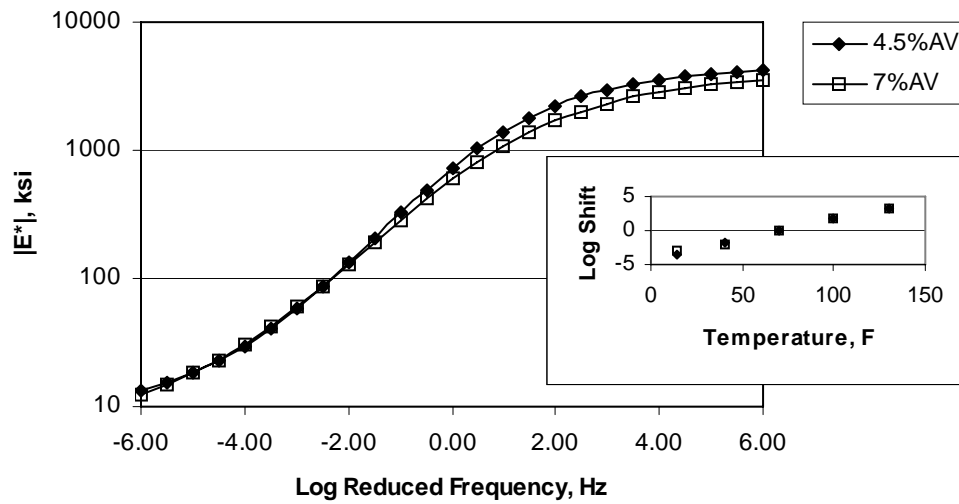
Shift Factors:

Parameter	Air Voids (%)	
	4.5	7
log[a(14)]	-3.58	-3.08
log[a(40)]	-1.62	-1.93
log[a(100)]	1.88	1.63
log[a(130)]	3.22	3.14

Regression Coefficients:

Parameter	Air Voids (%)	
	4.5	7
δ	0.9329	0.7890
α	2.7265	2.8224
β	-0.8889	-0.8622
γ	0.5744	0.4937

Figure 5.37. Dynamic Modulus Test Result for JET-25mm-PG70-22

Air Voids: 4.5 percent

Temp	Dynamic Modulus (ksi)					
	0.1 Hz	0.5 Hz	1 Hz	5 Hz	10 Hz	25 Hz
14F	3791.24	4397.62	4611.4	5133.60	5305.21	5637.99
40F	1668.87	2207.03	2407.73	3022.12	3296.95	3681.02
70F	300.19	537.81	679.10	1133.44	1398.24	1778.35
100F	66.15	97.12	120.28	223.67	303.70	483.34
130F	27.44	32.95	36.43	52.89	66.32	100.45

Air Voids: 7 percent

Temp	Dynamic Modulus (ksi)					
	0.1 Hz	0.5 Hz	1 Hz	5 Hz	10 Hz	25 Hz
14F	2921.22	3414.6	3646.94	3949.19	4130.71	4395.46
40F	1224.58	1658.33	1791.92	2237.73	2368.88	2693.72
70F	217.86	390.77	494.61	833.54	1023.91	1347.66
100F	47.31	67.12	81.99	147.20	200.04	312.35
130F	23.01	27.53	30.34	43.71	54.78	83.85
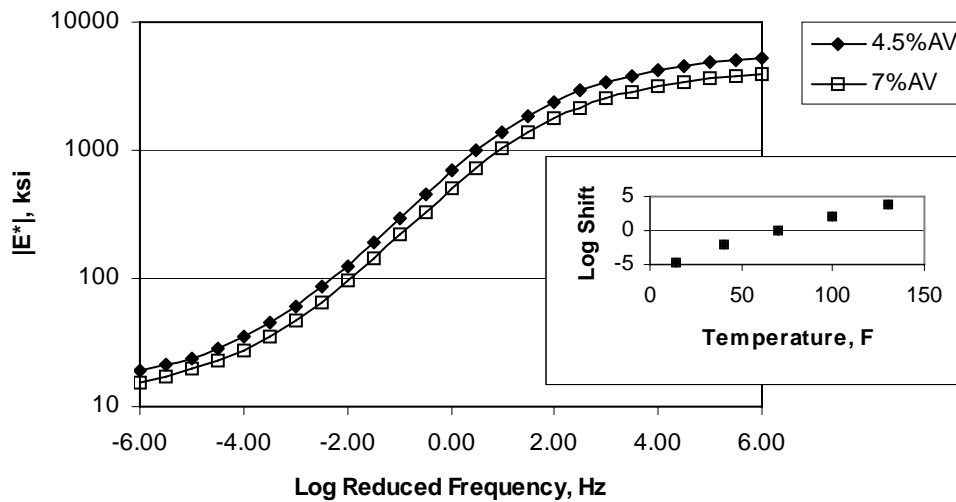
Shift Factors:

Parameter	Air Voids (%)	
	4.5	7
log[a(14)]	-4.62	-4.81
log[a(40)]	-2.12	-2.11
log[a(100)]	1.96	2.10
log[a(130)]	3.81	3.70

Regression Coefficients:

Parameter	Air Voids (%)	
	4.5	7
δ	1.1378	1.0577
α	2.6236	2.5886
β	-0.6074	-0.5506
γ	0.5765	0.5733

Figure 5.38. Dynamic Modulus Test Result for JET-37.5mm-PG70-22

The mixtures used in this project were evaluated further by comparing the corresponding dynamic modulus values determined at high temperature (54C (130F)), intermediate temperature (21C (70F)), low temperature (-10C (14F)), and at intermediate frequency (10Hz) for all of the above test temperatures.

Figures 5.39 through 5.41 present the dynamic modulus values of all mixtures used in this study measured at 54C (130F), 21C (70F), and –10C (14F), respectively. In all figures, the variability of the dynamic modulus values of the specimens prepared at design air void levels are similar to those prepared at seven percent air voids.

Based on Figure 5.39, the effects of binder grade on HMA stiffness are more significant than those of aggregate source and size at high temperature. At high temperature, the mixtures used binder grade PG 76-22 seemed to be stiffer than the others. Those mixtures used binder grade PG 76-22 could prevent the pavement from rutting better than the others. At intermediate and low temperatures, the mixtures with greater nominal aggregate size and stiffer binder are generally stiffer, as shown in Figure 5.40 and 5.41. The effects of mixture volumetric properties are further studied in the next chapter.

Figures 5.42 though 5.45 compare the shift factors, log $a(T)$, obtained during the master curve development. These figures show that the shift factors vary with the HMA mixtures and test temperatures. The shift factors were the most varied at low and high temperatures (i.e, -10C (14F), 4C (40F), and 54C (130F). Figure 5.46 present the average shift factors. The average values can be used as initial shift factors to develop the master curve as presented in Figure 5.16.
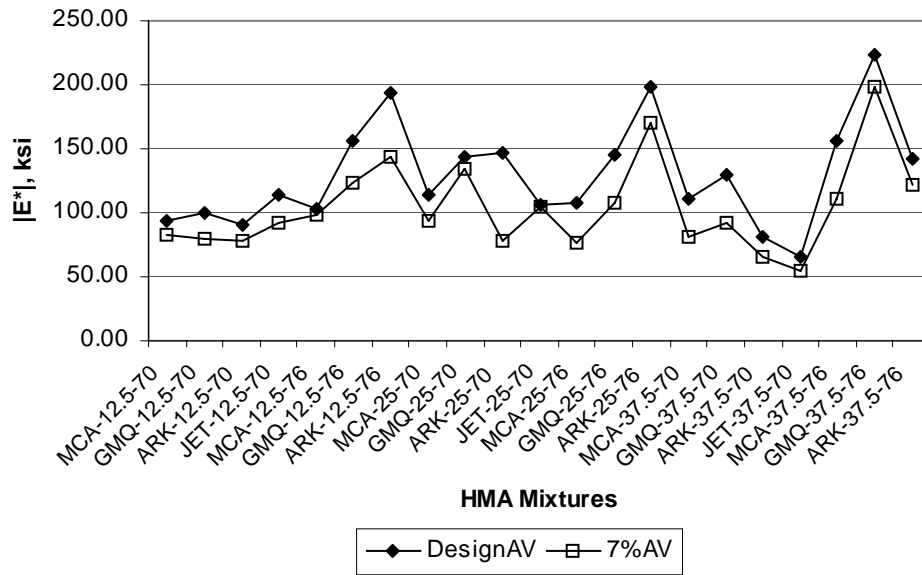
Figure 5.39. Dynamic Modulus Determined at 130F and 10 Hz
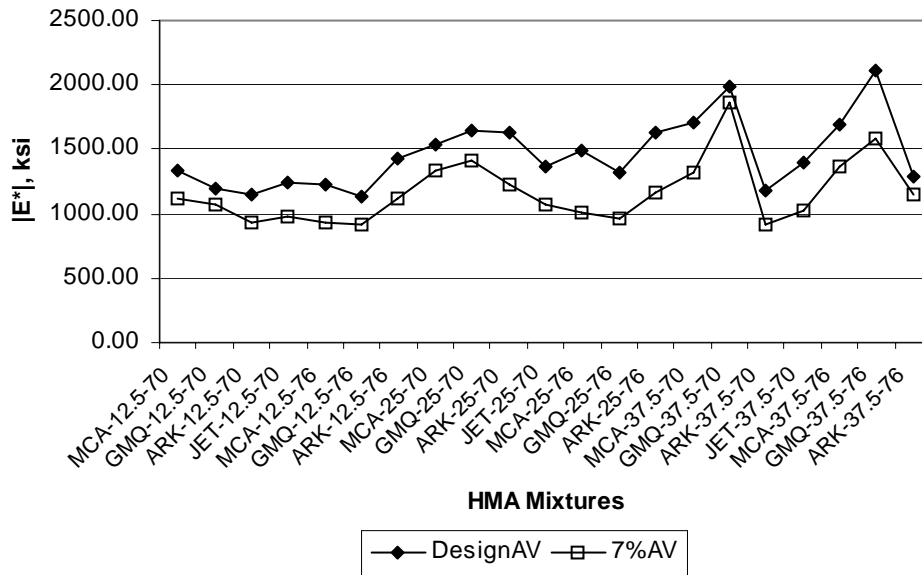
Figure 5.40. Dynamic Modulus Determined at 70F and 10 Hz
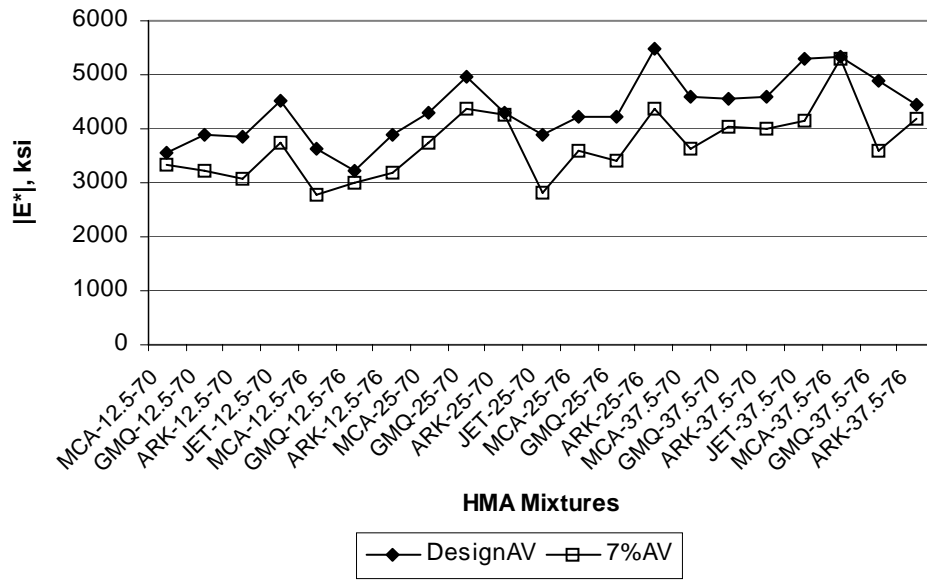
Figure 5.41. Dynamic Modulus Determined at 14F and 10 Hz
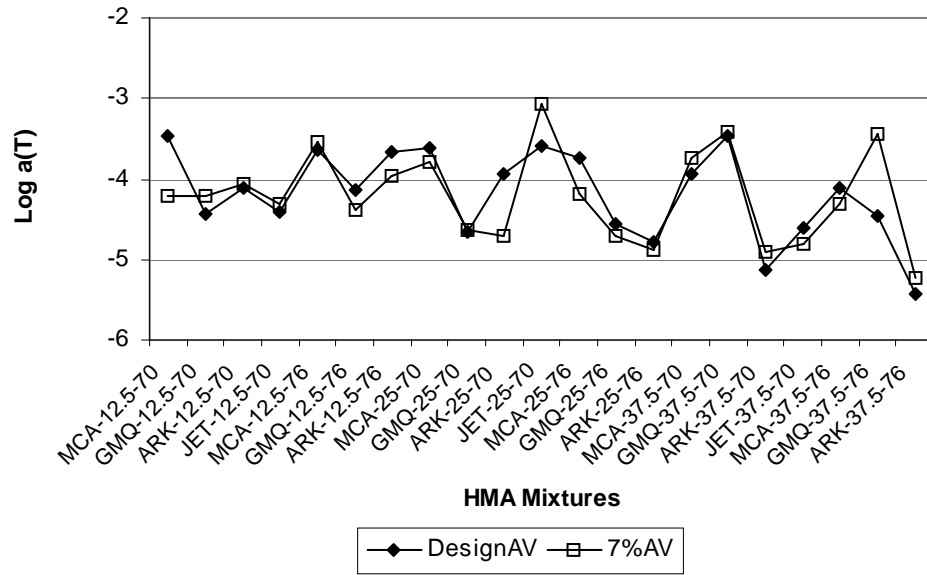
Figure 5.42. Shift Factors for Dynamic Modulus at 14F
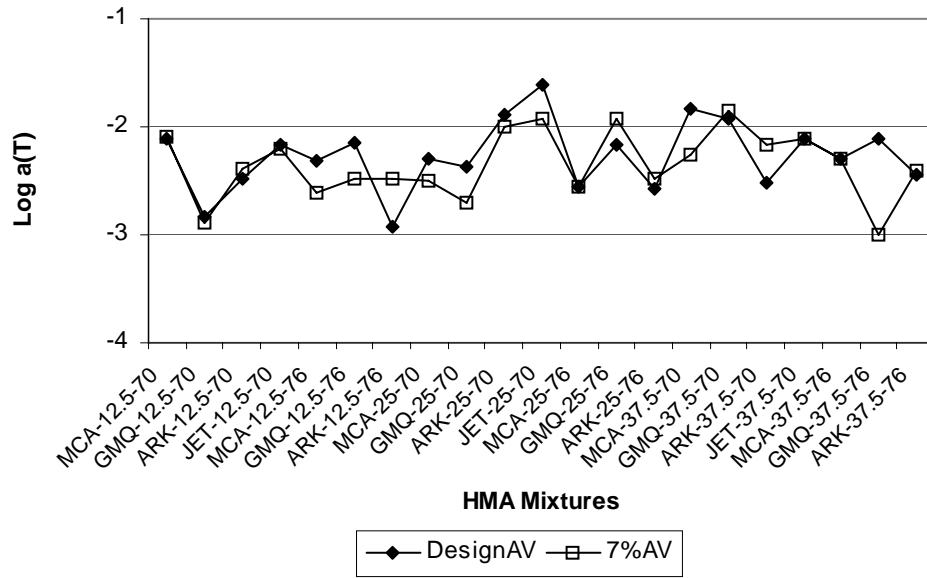
Figure 5.43. Shift Factors for Dynamic Modulus at 40F
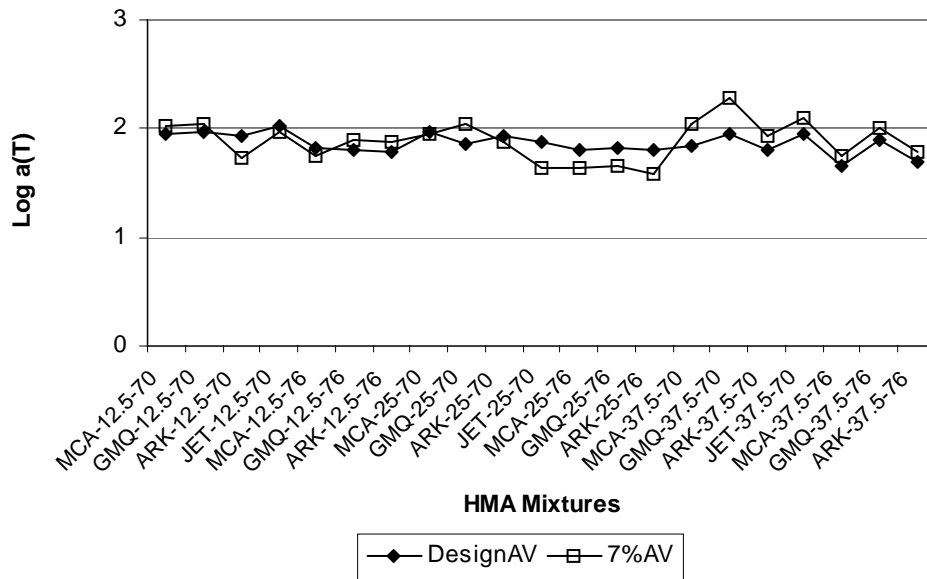
Figure 5.44. Shift Factors for Dynamic Modulus at 100F
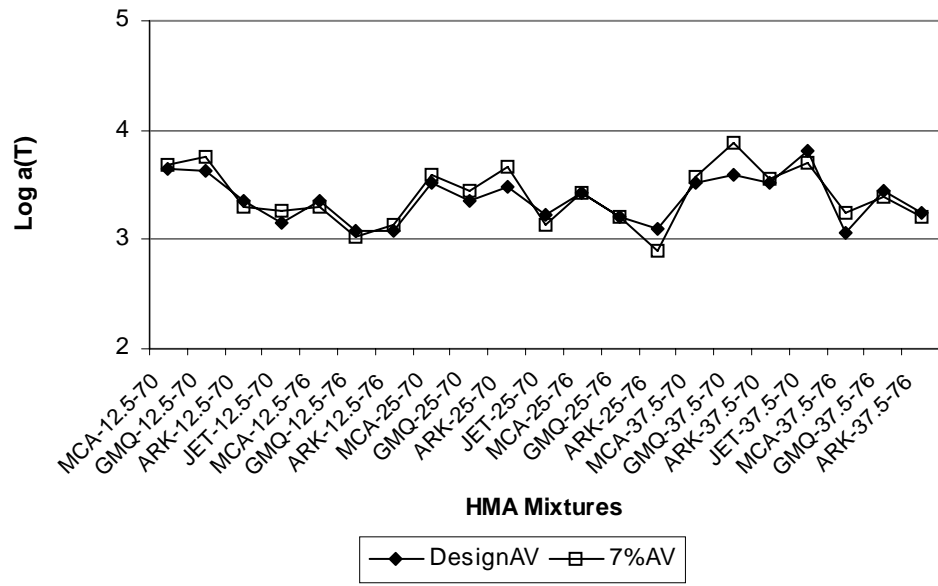
Figure 5.45. Shift Factors for Dynamic Modulus at 130F
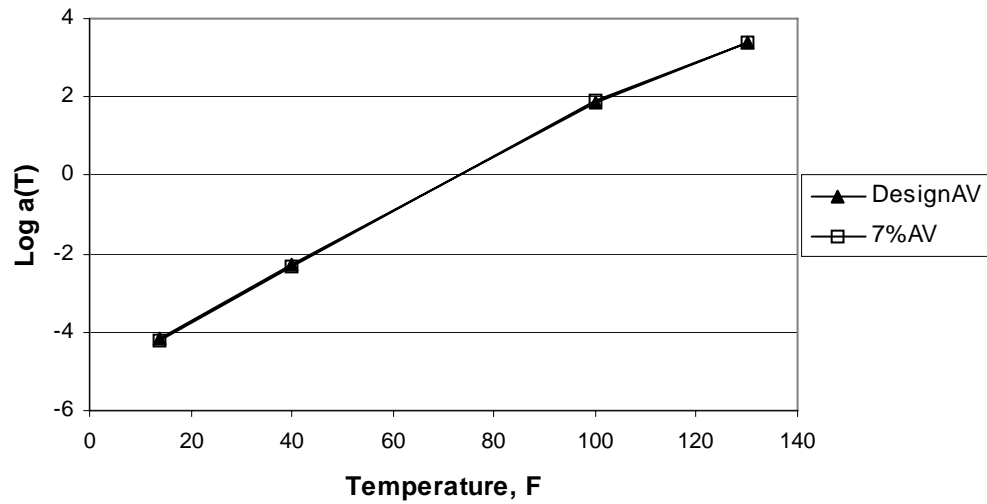
Figure 5.46. Average Shift Factors

195

5.5 Summary

This chapter first presented the methodology to determine the dynamic modulus and phase angle based on the raw data acquired from the testing process. There are several methods available to calculate the dynamic modulus and phase angle. The curve fitting technique was chosen in this study because it is easy to accomplish using a spreadsheet.

After the test results were obtained, the variability of the results was analyzed. It was concluded that there were no patterned errors due to the LVDT measurements through all combinations of testing temperature and frequency. The variability of the dynamic modulus test was evaluated by performing the ANOVA tests on the "within" and "between" coefficients of variation.

With 95-percent confidence, all of the single fixed effects except the binder grade were significant. However, the interactions between the binder grade and temperature were significant. The observations based on the ANOVA tests were: (1) the greater the maximum nominal aggregate size, the higher the coefficient of variation (the test variability); (2) the higher the air voids of the test specimens, the higher the coefficient of variation; and (3) the test variability was higher at higher temperatures or higher frequencies.

The analysis of variability showed that the variability of the test results obtained in this study was lower than those in other studies, and it was in compliance with the requirements specified in AASHTO TP 62-03 (*74*).

Since the stiffness of HMA mixtures is dependent on temperature and loading rate, the use of the master curve to determine the dynamic modulus in a broaden range

of temperature and frequency without having a complex testing program is very useful. The master curve development method introduced in this chapter solved the shift factors simultaneously with the coefficient of the sigmoidal function. The use of the numerical optimization (Solver) to construct the master curve was also presented in detail.

Finally, the dynamic modulus values were then presented in the same form required in the M-E Design Guide. The subsequent master curves were also developed, and the associate shift factors and regression coefficients were reported. It was observed that the shift factors varied with the HMA mixtures and test temperatures. The shift factors were the most varied at low and high temperatures.

It was concluded that the dynamic modulus values obtained in this study be used with confidence for level 1 dynamic modulus inputs of HMA in the M-E Design Guide.

CHAPTER 6: PREDICTION OF DYNAMIC MODULUS

6.1 Dynamic Modulus Prediction

The dynamic (complex) modulus $|E^*|$ is one of the fundamental inputs in the M-E Design Guide (*1*) and is a promising candidate for the Simple Performance Test recommended by NCHRP Project 9-19 (*60*).

The M-E Design Guide incorporates the hierarchical method that includes three levels for specifying pavement design inputs. Level 1 inputs provide the highest level of accuracy and would typically be used for designing heavily trafficked pavements. Level 2 inputs provide an intermediate level of accuracy and could be used when inputs are not available for level 1 characterization. Level 3 inputs provide the lowest level of accuracy and are intended for designing low volume roads.

Level 1 inputs for HMA material characterization in the M-E Design Guide require the dynamic modulus $|E^*|$ tested in the laboratory. Level 1 inputs were presented in the previous chapter. Level 2 inputs are based on a prediction model combined with the laboratory measured binder properties. Level 3 inputs predict the dynamic modulus using the same predictive model with the default binder properties determined by the binder grade. Level 2 and 3 dynamic modulus inputs are documented in this chapter.

The dynamic modulus test is relatively complex and expensive to perform. Therefore, many efforts have been spent to develop prediction models to calculate the dynamic modulus from mixture properties. Two predictive equations that are claimed the most comprehensive today are Witczak's predictive equation developed by Witczak et al. (*2*) and Hirsch model developed by Christensen et al. (*81*). The Witczak's

predictive model was incorporated in the M-E Design Guide to estimate the dynamic modulus for Level 2 and 3 inputs.

This chapter presents the evaluation of the aforesaid predictive models by comparing the predicted dynamic modulus values to those measured in the laboratory.

6.2 Evaluation Methodologies

To recommend the abovementioned models for the future applications, bias and precision of the models were evaluated in this study. Bias is defined as the difference between the mean predicted and the mean observed. Bias is a systematic difference that occurs between the observed and predicted values. Precision is a measure of how close the observed and predicted values are to each other. Precision is influenced by errors and other factors unexplained by the model. The concepts of bias and precision are illustrated in four scenarios in Figure 6.1. In a calibration process, the bias is eliminated by minimizing the sum of errors, and the precision is improved by minimizing the sum of square of errors.

In this study, in order to evaluate the performance of the predictive equation in determining the dynamic moduli of typical mixtures used in Arkansas, the accuracy of the predicted dynamic modulus values was assessed using goodness-of-fit statistics. The statistical parameters include lack of fit statistic, S_e/S_y (the standard error of estimate/standard deviation), and correlation coefficient, R^2.
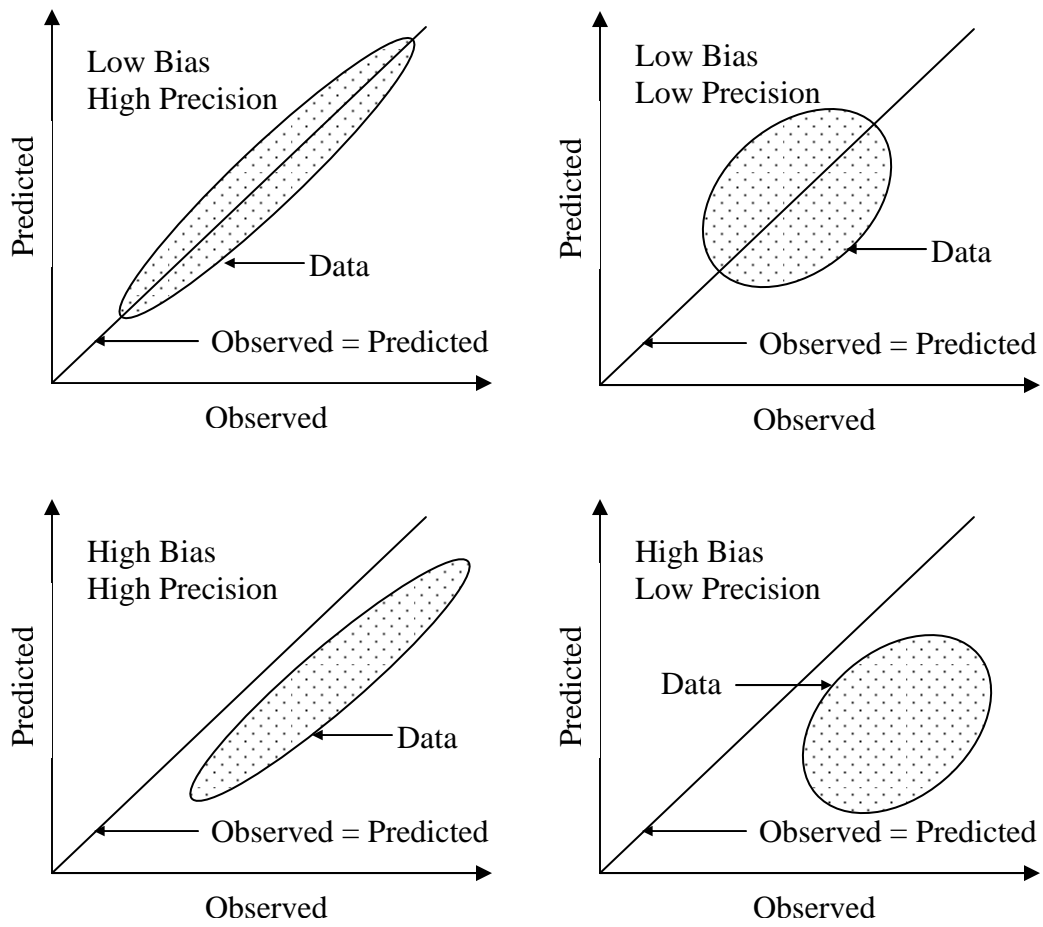
Figure 6.1. Illustrations of Bias and Precision (*104*)

The lack of fit statistic, S_e/S_y, is a measure of the improvement in the accuracy of prediction due to the prediction equation. When the ratio is small, e.g. near zero, more variation in the dynamic modulus values about their mean can be explained by the predictive equation. Thus, the smaller the value, the better the prediction (*105*).

The correlation coefficient, R^2, is a measure of model accuracy. The higher the value, e.g. near 100 percent, the better the prediction. The correlation coefficient is a better measure for linear models with a large sample size. However, for non-linear equations, such as the predictive models for the dynamic modulus, the lack of fit statistic, S_e/S_y, is a more rational measure of prediction reliability (*105*).

For the lack-of-fit statistic, the standard error of estimate, S_e, is calculated using Equation 6.1, and the standard deviation, S_y, is computed using Equation 6.2. The correlation coefficient, R^2, is determined using Equation 6.3.

$$S_e = \sqrt{\frac{\sum(y-\hat{y})^2}{(n-k)}} \tag{6.1}$$

$$S_y = \sqrt{\frac{\sum(y-\bar{y})^2}{(n-1)}} \tag{6.2}$$

$$R^2 = 1 - \frac{(n-k)}{(n-1)}\left(\frac{S_e}{S_y}\right)^2 \tag{6.3}$$

where

S_e = standard error of estimate

S_y = standard deviation

R^2 = correlation coefficient

y = measured dynamic modulus

$\hat{y}$ = predicted dynamic modulus

$\bar{y}$ = mean value of tested dynamic modulus

n = sample size

k = number of independent variables in the model

Based on the lack-of-fit statistic and correlation coefficient, the performance of the prediction model in question can be ranked using the subjective criteria established in NCHRP Project 9-19 Task C (*60*). The subjective criteria are presented in Table 6.1.

The measured and predicted dynamic modulus values were also compared by matching the two values in a normal scale graph. If the matching points are fairly distributed around the equality line, the predicted model should have a good correlation to the measured data.

Another evaluation method is to compare the master curves of the measured and predicted dynamic modulus values at a reference temperature. Depending on how close the master curves are to each other, the dynamic modulus predictions can be assessed.

In addition to the accuracy evaluation, the prediction errors are evaluated by analyzing the graphs of errors versus mixture properties, test parameters, and predicted $|E^*|$ values.

In order to recommend the prediction models for the future applications, in addition to the accuracy and error requirements, the uses of the dynamic modulus predictions in the M-E Design Guide should predict reasonable pavement performance that is favorably compared to the pavement performance predictions using the corresponding level 1 $|E^*|$ inputs. Therefore, the $|E^*|$ predictions are also evaluated using the pavement performance analyses.

Table 6.1. Criteria for Goodness-of-Fit Statistical Parameters

Criteria	R^2	S_e/S_y
Excellent	≥ 0.90	≤ 0.35
Good	$0.70 - 0.89$	$0.36 - 0.55$
Fair	$0.40 - 0.69$	$0.56 - 0.75$
Poor	$0.20 - 0.39$	$0.76 - 0.89$
Very Poor	≤ 0.19	≥ 0.90

6.3 The Witczak Prediction Model

The Witczak's prediction model is an empirical regression model developed based on 2750 laboratory measurements of the dynamic modulus tested over the last 30 years. The model was discussed in detail in section 3.10.1. The Witczak model for predicting the dynamic modulus of HMA, which is incorporated in the M-E Design Guide, is presented in Equation 6.4 (*1*).

$$\log E = -1.249937 + 0.02932\rho_{200} - 0.001767\rho_{200}^2$$

$$- 0.002841\rho_4 - 0.058097V_a - 0.802208\left(\frac{V_{b0eff}}{V_{beff} + V_a}\right)$$

$$+ \frac{3.871977 - 0.0021\rho_4 + 0.003958\rho_{38} - 0.000017\rho_{38}^2 + 0.005470\rho_{34}}{1 + e^{(-0.603313 - 0.313351\log(f) - 0.393532\log(\eta))}} \qquad (6.4)$$

where:

E = dynamic modulus, 10^5 psi

η = bitumen viscosity, 10^6 Poise

f = loading frequency, Hz

V_a = air void content, %

V_{beff} = effective bitumen content, % by volume

ρ_{34} = cumulative % retained on the 19-mm sieve

ρ_{38} = cumulative % retained on the 9.5-mm sieve

ρ_4 = cumulative % retained on the 4.76-mm sieve

ρ_{200} = % passing the 0.075-mm sieve

Equation 6.4 was calibrated in log space, and its statistical summary is as follows (*2*):

- R^2 = 0.941 in log space (0.886 in arithmetic space)

- S_e/S_y = 0.244 in log space (0.338 in arithmetic space)

6.3.1 Input Data for Witczak's Predictive Model

The Witczak predictive model requires binder and mixture inputs to estimate the dynamic modulus. In the model, the frequency is an independent input, but the temperature is included in the viscosity term (η). The viscosity of the asphalt binder at a given temperature can be estimated using Equation 6.5 (*53*). This equation was reviewed in detail in section 3.2.2.

$$\log\log\eta = A + VTS\log T_R \qquad (6.5)$$

where:

η = viscosity, cP

T_R = temperature, Rankine

$(T_R = T_F + 460, T_F$ = temperature, Fahrenheit)

A = regression intercept

VTS = regression slope of Viscosity-Temperature Susceptibility

The *A* and *VTS* parameters in Equation 6.5 are a function of binder type. The *A* and *VTS* parameters can be determined for level 2 |*E**| inputs using the data from different test methods, such as penetration, Brookfield viscosity, and dynamic shear rheometer (DSR). In this study, the *A* and *VTS* parameters for level 2 |*E**| inputs were determined using the DSR results. A detailed procedure for determining the *A* and *VTS*

parameters were presented later in this section. For level 3 |E^*| inputs, the A and VTS

parameters are the default rolling thin film oven (RTFO) aged values based on the

binder grades recommended in the M-E Design Guide (*1*).

The DSR test properties for determining the A and VTS parameters for level 2

|E^*| inputs, including the complex shear modulus and phase angle of the original

binders, are presented in Tables 6.2 and 6.3. The DSR test results were converted to the

viscosity using Equation 6.6. The corresponding estimated viscosity values are

presented in Tables 6.2 and 6.3.

$$\eta = \frac{G^*}{10}\left(\frac{1}{\sin\delta}\right)^{4.8628}$$

(6.6)

where:

η = viscosity, Pa·s

G^* = complex shear modulus of binder, Pa

δ = phase angle, degree

Equation 6.4 requires the viscosity of the binder after being short-term aged in

RTFO, which accounts for mixing and compaction effects in the field. The effect of

short-term aging on the viscosity presented in Tables 6.2 and 6.3 was accounted using

the Global Aging System model for RTFO aging, as presented in Equation 6.7 (*106*).

Table 6.2. Dynamic Shear Rheometer Test Results for Original PG 70-22

Temperature	Complex Modulus	PHASE ANGLE	Viscosity
(Deg C)	(Pa)	(Deg)	(Pa·s)
20	2.03E+06	57.0	4.77E+05
35	1.96E+05	73.8	2.38E+04
50	1.58E+04	77.3	1.78E+03
65	1.45E+03	80.3	1.55E+02

Table 6.3. Dynamic Shear Rheometer Test Results for Original PG 76-22

Temperature	Complex Modulus	Phase Angle	Viscosity
(Deg C)	(Pa)	(Deg)	(Pa·s)
20	1.60E+06	55.3	4.14E+05
35	1.60E+05	67.3	2.37E+04
50	2.02E+04	67.1	3.02E+03
65	3.77E+03	68.3	5.38E+02

$$\log \log \left(\eta_{t=0} \right) = a_0 + a_1 \log \log \left(\eta_{orig} \right) \tag{6.7}$$

$$a_0 = 0.054405 + 0.004082 \times code$$

$$a_1 = 0.972035 + 0.010886 \times code$$

where:

$\eta_{t=0}$ = mixing/compaction viscosity, cP (1000 cP = 1 Pa·s)

η_{orig} = original viscosity, cP

code   = dependent on hardening ratio, as presented in Table 6.4

However, the aging condition (hardening ratio) for the binder used to fabricate the |E*| test specimens was unknown. Therefore, for level 2 inputs, it was decided that three asphalt binder aging conditions were evaluated: (1) original binder; (2) RTFO aged using Equation 6.7 with the *code* value of 0; and RTFO aged using Equation 6.7 with the *code* value of –1.

After the viscosity of the RTFO aged binders was calculated using Equation 6.7 based on the original binder data presented in Tables 6.2 and 6.3, the RTFO aged binder viscosity was used to determine the parameters *A* and *VTS* using Equation 6.5. The A and VTS parameters for predicting level 2 |E*| inputs are presented in Table 6.5. For level 3 inputs, the default RTFO aged parameters recommended in the M-E Design Guide were used, as presented in Table 6.5. The viscosity of the binders at the temperatures of interest was estimated using Equation 6.5 and the *A* and *VTS* parameters in Table 6.5.

Table 6.4. Recommended Code Values

Mix/Lay-Down Hardening Resistence	Expected Hardening Ratio Values	Code Value
Excellent to Good	HR ≤ 1.030	-1
Average	1.030 < HR ≤ 1.075	0
Fair	1.075 < HR ≤ 1.100	1
Poor	HR > 1.100	2

Table 6.5. *A* and *VTS* Parameters Used in this Study

Parameter	Input Level	Aging	PG 70-22	PG 76-22
A	2	Original	10.706	8.682
	2	RTFO (code = 0)	10.461	8.493
	2	RTFO (code = -1)	10.340	8.395
	3	RTFO default (1-37A)	10.299	9.715
VTS	2	Original	-3.586	-2.846
	2	RTFO (code = 0)	-3.486	-2.767
	2	RTFO (code = -1)	-3.447	-2.736
	3	RTFO default (1-37A)	-3.426	-3.208

Figures 6.2 and 6.3 presents the viscosity of binder grades PG70-22 and PG76-22 estimated at the dynamic modulus test temperatures of -10, 4, 21, 38, and 54C (14, 40, 70, 100, and 130F). For both binder grades, the viscosity estimated using the default *A* and *VTS* parameters was the highest and close to that estimated using the RTFO (*code* = 0) aged parameters. The original viscosity was the lowest, and the RTFO (*code* = -1) aged viscosity was intermediate.

Other input data for Equation 6.4 were mixture properties obtained from the HMA mix designs used in this study. The effective binder content (V_{beff}) was determined using Equation 2.3. The mixture properties for the Witczak predictive model are summarized in Table 6.6.

6.3.2 Evaluation of the Witczak Prediction Model

The dynamic modulus values were estimated at five temperature levels, including -10, 4, 21, 38, and 54C (14, 40, 70, 100, and 130F), and at six frequency levels for each temperature level, including 25, 10, 5, 1, 0.5, and 0.1 Hz. The temperature and frequency levels at which the dynamic modulus values were estimated using the Witczak predictive model were corresponding to those the dynamic modulus values were measured in the laboratory.

One set of mixture properties, as presented in Table 6.6 and four sets of *A* and *VTS* parameters, as presented in Table 6.5, were used to estimate the dynamic modulus values. For each combination of mixture and binder properties, 1,260 dynamic modulus values were estimated. The estimated dynamic modulus values for level 2 and 3 inputs were then evaluated following the evaluation methodologies presented in section 6.2.
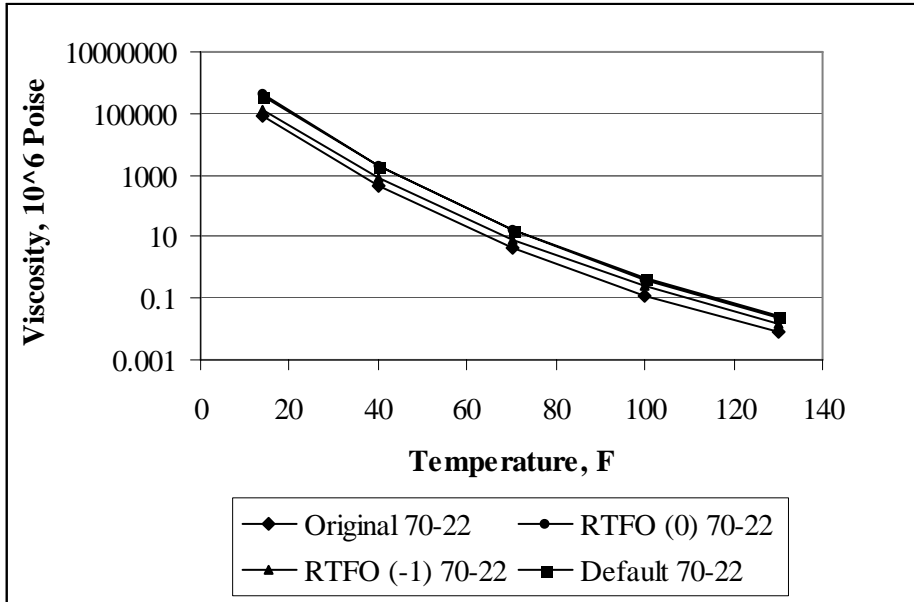
Figure 6.2. Viscosity of Binder Grade PG70-22 at Test Temperatures
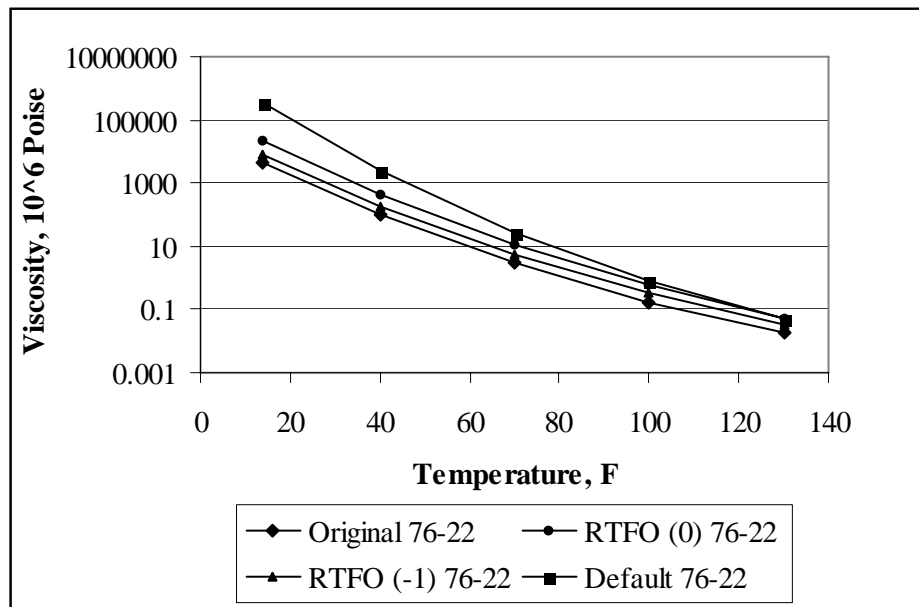
Figure 6.3. Viscosity of Binder Grade PG76-22 at Test Temperatures

Table 6.6. Mixture Properties for Witczak's Predictive Model

Mix ID	Agg.	Binder	Va (%)	Vbeff (%)	R34 (%)	R38 (%)	R4 (%)	P200 (%)
MCA_12.5_70_4.5	Limestone	PG70-22	4.8	10.1	0	20	49	4.2
MCA_12.5_70_7.0	Limestone	PG70-22	7.3	9.8	0	20	49	4.2
MCA_12.5_76_4.0	Limestone	PG76-22	3.7	11.1	0	25	57	4.0
MCA_12.5_76_7.0	Limestone	PG76-22	6.6	10.7	0	25	57	4.0
MCA_25_70_4.5	Limestone	PG70-22	4.2	8.7	15	36	66	3.6
MCA_25_70_7.0	Limestone	PG70-22	7.0	8.5	15	36	66	3.6
MCA_25_76_4.0	Limestone	PG76-22	4.0	9.9	15	37	68	3.3
MCA_25_76_7.0	Limestone	PG76-22	7.2	9.6	15	37	68	3.3
MCA_37.5_70_4.5	Limestone	PG70-22	4.7	7.3	26	52	69	3.1
MCA_37.5_70_7.0	Limestone	PG70-22	7.1	7.1	26	52	69	3.1
MCA_37.5_76_4.0	Limestone	PG76-22	3.6	7.9	27	53	69	3.1
MCA_37.5_76_7.0	Limestone	PG76-22	7.1	7.6	27	53	69	3.1
GMQ_12.5_70_4.5	Granite	PG70-22	4.9	9.9	0	20	44	4.2
GMQ_12.5_70_7.0	Granite	PG70-22	7.3	9.6	0	20	44	4.2
GMQ_12.5_76_4.0	Granite	PG76-22	4.2	11.7	0	14	38	3.9
GMQ_12.5_76_7.0	Granite	PG76-22	7.1	11.3	0	14	38	3.9
GMQ_25_70_4.5	Granite	PG70-22	4.2	8.9	14	49	71	3.1
GMQ_25_70_7.0	Granite	PG70-22	7.0	8.6	14	49	71	3.1
GMQ_25_76_4.0	Granite	PG76-22	3.8	9.8	13	54	72	3.2
GMQ_25_76_7.0	Granite	PG76-22	6.8	9.5	13	54	72	3.2

Table 6.6. Mixture Properties for Witczak's Predictive Model (Cont.)

Mix ID	Agg.	Binder	Va (%)	Vbeff (%)	R34 (%)	R38 (%)	R4 (%)	P200 (%)
GMQ_37.5_70_4.5	Granite	PG70-22	4.3	7.7	29	41	54	3.8
GMQ_37.5_70_7.0	Granite	PG70-22	6.6	7.5	29	41	54	3.8
GMQ_37.5_76_4.0	Granite	PG76-22	3.8	7.7	29	41	54	3.8
GMQ_37.5_76_7.0	Granite	PG76-22	6.9	7.4	29	41	54	3.8
ARK_12.5_70_4.5	Sandstone	PG70-22	4.3	10.8	0	15	45	5.7
ARK_12.5_70_7.0	Sandstone	PG70-22	6.8	10.5	0	15	45	5.7
ARK_12.5_76_4.0	Sandstone	PG76-22	3.8	10.4	0	14	45	5.7
ARK_12.5_76_7.0	Sandstone	PG76-22	7.3	10.0	0	14	45	5.7
ARK_25_70_4.5	Sandstone	PG70-22	4.3	8.5	18	40	60	4.7
ARK_25_70_7.0	Sandstone	PG70-22	7.0	8.3	18	40	60	4.7
ARK_25_76_4.0	Sandstone	PG76-22	4.0	8.5	21	42	64	4.3
ARK_25_76_7.0	Sandstone	PG76-22	6.9	8.2	21	42	64	4.3
ARK_37.5_70_4.5	Sandstone	PG70-22	4.8	8.0	30	54	74	5.0
ARK_37.5_70_7.0	Sandstone	PG70-22	7.0	7.8	30	54	74	5.0
ARK_37.5_76_4.0	Sandstone	PG76-22	4.3	7.6	28	54	74	4.3
ARK_37.5_76_7.0	Sandstone	PG76-22	6.9	7.3	28	54	74	4.3
JET_12.5_70_4.5	Gravel	PG70-22	4.4	10.6	0	14	44	3.5
JET_12.5_70_7.0	Gravel	PG70-22	6.8	10.3	0	14	44	3.5
JET_25_70_4.5	Gravel	PG70-22	4.5	9.0	10	46	63	3.2
JET_25_70_7.0	Gravel	PG70-22	7.4	8.7	10	46	63	3.2
JET_37.5_70_4.5	Gravel	PG70-22	4.6	8.4	31	52	69	3.0
JET_37.5_70_7.0	Gravel	PG70-22	7.0	8.2	31	52	69	3.0

Accuracy Analyses. The goodness-of-fit statistics in arithmetic space for four combinations of binder parameters and mixture properties were determined to evaluate the dynamic modulus predictions, as presented in Table 6.7. The rankings in Table 6.7 were made based upon the evaluation criteria presented in Table 6.1. In general, the predicted dynamic modulus values agreed quite well with the measured dynamic modulus values. Measured vs. predicted dynamic modulus values are summarized in Figures 6.4 through 6.7. Figure 6.8 illustrates the effects of the binder viscosity inputs on the $|E^*|$ predictions using the Witczak predictive equation. Level 2 inputs using the RTFO binder viscosity with the *code* value of 0 had the best agreement with level 1 measured $|E^*|$ values. It was decided that for level 2 inputs, only RTFO binder viscosity with the *code* of zero was used later in this analysis.

In addition, the evaluation was performed by comparing level 2 and 3 $|E^*|$ predictions to level 1 measured $|E^*|$ values for individual HMA mixture. The goodness-of-fit statistics were determined for each mixture used in this study. The results were compiled and illustrated in Figures 6.9 and 6.10.

As presented in Figure 6.9, the $|E^*|$ predictions using level 2 inputs were rated excellent for 64 percent of the mixtures used in this study, good for 31 percent, and fair for 5 percent. As presented in Figure 6.10 for level 3 inputs, the excellent $|E^*|$ predictions were 62 percent, good 19 percent, and fair 19 percent of the mixtures used in this study. It showed that level 2 dynamic modulus inputs were slightly better than level 3.

Table 6.7. Comparisons of Level 2 and 3 Inputs to Level 1 Input

Statistic	Level 2 vs Level 1			Level 3 vs Level 1
	Original	RTFO-Aged (*Code* = 0)	RTFO-Aged (*Code* = -1)	RTFO-Aged Default
S_e/S_y	0.379	0.318	0.332	0.334
R^2	0.857	0.900	0.891	0.889
Ranking	Good	Excellent	Excellent	Excellent

Measured vs Predicted (Original)
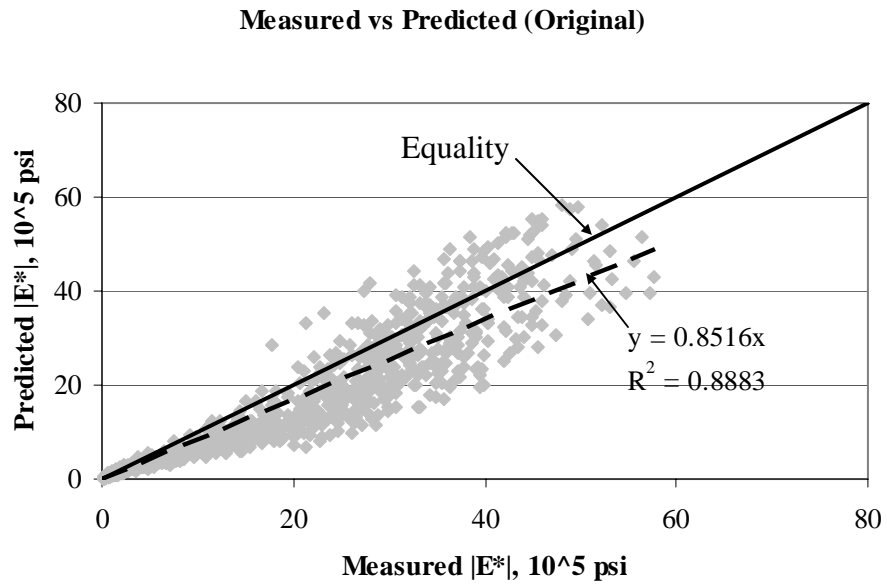
Figure 6.4. Measured vs Level 2 Predicted |*E**| Based on Original Binder

Measured vs Predicted (RTFO (code = 0))

$y = 1.0218x$
$R^2 = 0.9136$

Equality

Predicted |E*|, 10^5 psi

Measured |E*|, 10^5 psi
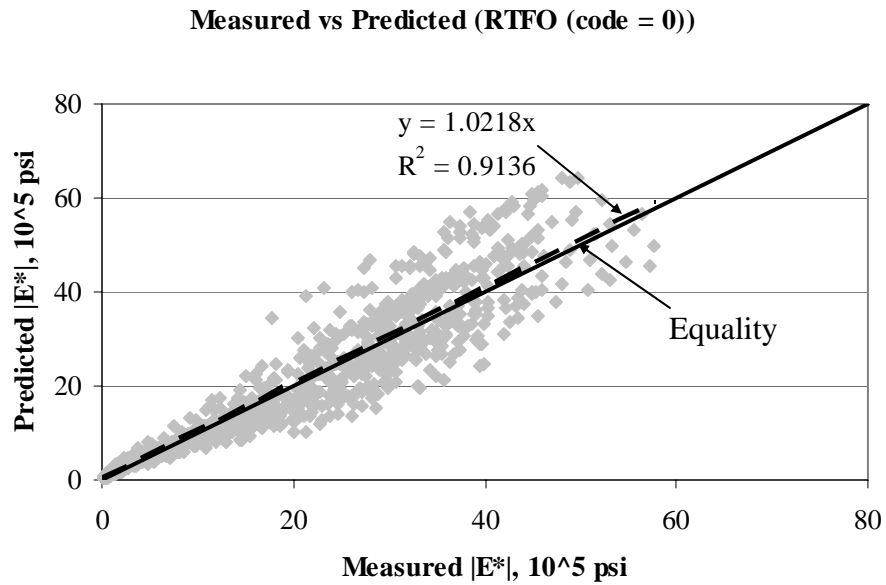
Figure 6.5. Measured vs Level 2 Predicted |*E**| Based on RTFO (*code* = 0) Binder

Measured vs Predicted (RTFO (code = -1))

Equality

$y = 0.9078x$
$R^2 = 0.9028$

Predicted |E*|, 10^5 psi

Measured |E*|, 10^5 psi
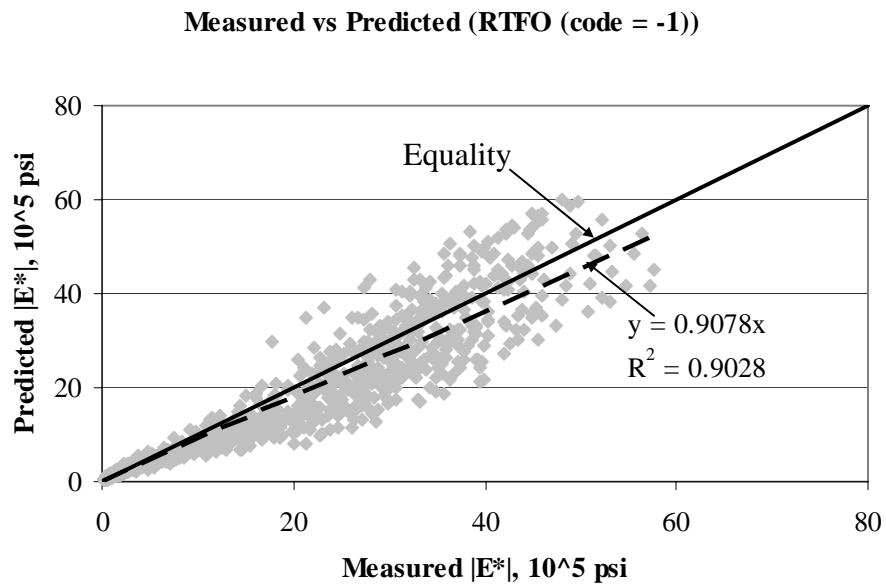
Figure 6.6. Measured vs Level 2 Predicted |*E**| Based on RTFO (*code* = -1) Binder

216

Measured vs Predicted (Default)

$y = 1.1411x$
$R^2 = 0.9489$

Equality

Predicted |E*|, 10^5 psi

Measured |E*|, 10^5 psi
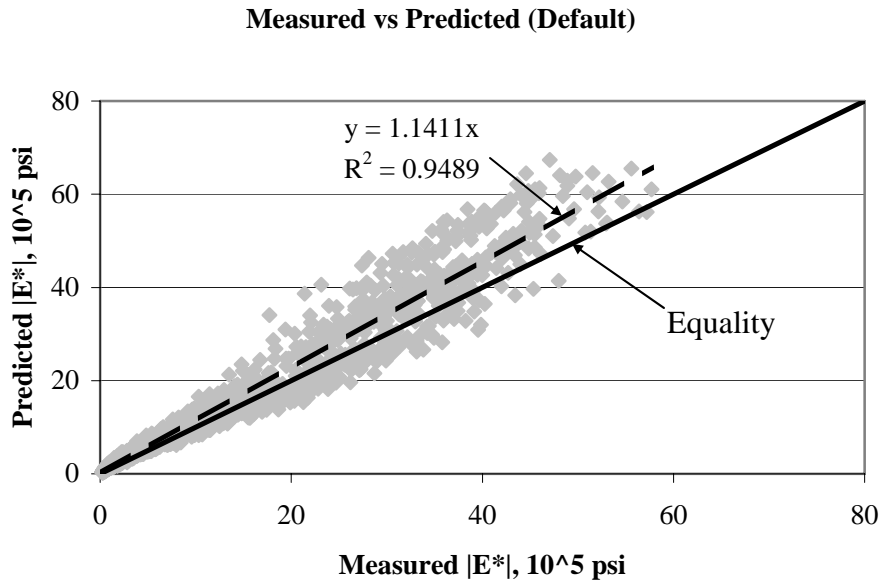
Figure 6.7. Measured vs Level 3 Predicted |*E**| Based on Default Binder Parameters

Measured |E*| vs Predicted |E*|

Equality Line

Predicted |E*|, 10^5 psi

Measured |E*|, 10^5 psi

Equality Line —— Default — — RTFO (0)

· · · RTFO (-1) — · — Original
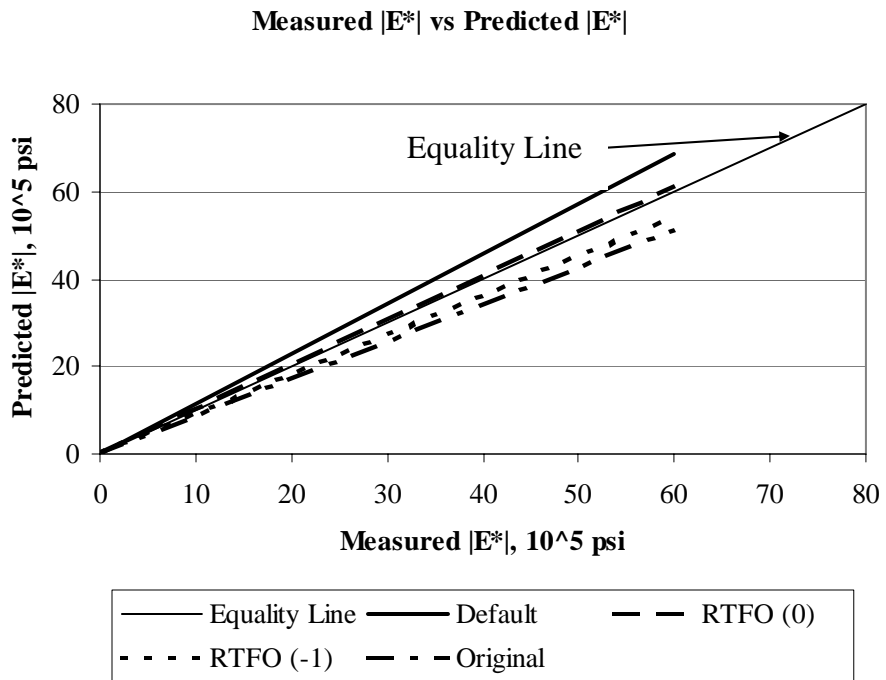
Figure 6.8. Effects of Binder Viscosity Inputs on Level 2 and 3 |*E**| Predictions
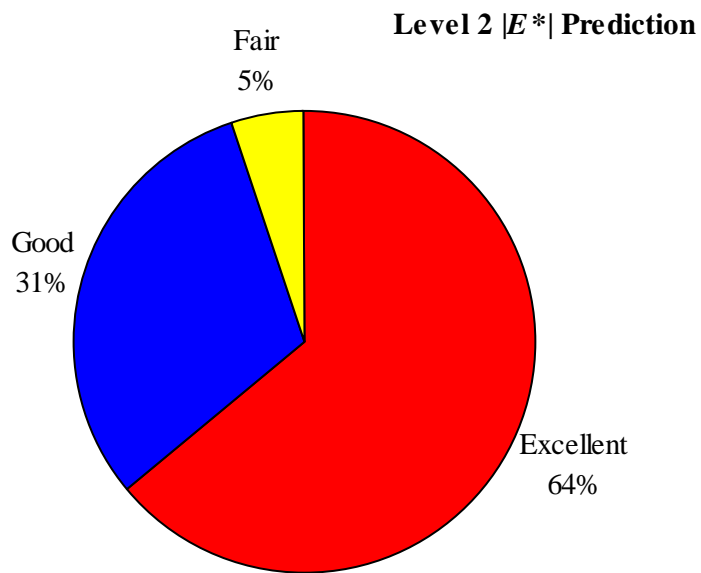
Figure 6.9. Distribution of Level 2 |*E**| Prediction Accuracy for All Mixtures
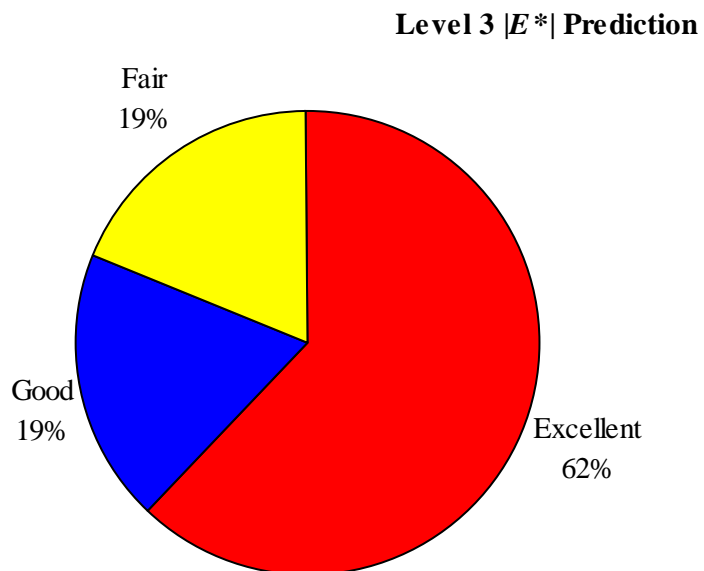
Figure 6.10. Distribution of Level 3 |*E**| Prediction Accuracy for All Mixtures

To illustrate the differences between the dynamic modulus predictions ranked at different levels in Table 6.7, level 2 dynamic modulus predictions for two mixtures ranked excellent (high) and fair (low) are presented in Figures 6.11 and 6.12. Figures 6.13 and 6.14 illustrate the excellent (high) and fair (low) dynamic modulus predictions for Level 3 inputs. It was very clear that the excellent-ranked predictions were much accurate than those ranked fair.

Error Analyses. The next step was the evaluation of the errors of the dynamic modulus predictions to detect any bias (systematic errors) in the predictions. Since the dynamic modulus values varied greatly across the temperatures and frequencies, the errors were calculated in percent using Equation 6.8.

$$error = \frac{|E^*|_{measured} - |E^*|_{predicted}}{|E^*|_{measured}} \times 100 \tag{6.8}$$

where:

$error$ = errors, percent

$|E^*|_{measured}$ = measured dynamic modulus, psi

$|E^*|_{predicted}$ = predicted dynamic modulus, psi

Figures 6.15 and 6.16 present the distribution of $|E^*|$ prediction errors and plot of prediction errors vs. predicted $|E^*|$ for level 2 inputs. The prediction error range was between –160 percent and +50 percent, and the mean prediction error was –15.55 percent. Figure 6.16 shows that the bias in prediction existed, and the prediction errors were larger at higher temperatures.

Jet-12.5mm-PG70-22-7.0

Se/Sy = 0.13

$R^2 = 0.99$

Equality

y = 0.9451x

Predicted |E*|, 10^5 psi

Measured |E*|, 10^5 psi
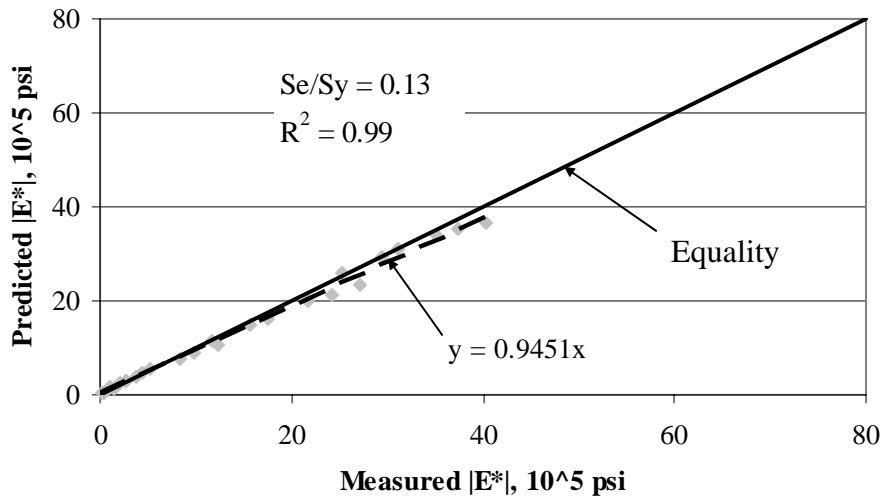
Figure 6.11. Excellent |*E*| Predictions for Level 2 Input

GMQ-37.5mm-PG70-22-4.5

y = 1.2117x

Equality

Se/Sy = 0.55

$R^2 = 0.80$

Predicted |E*|, 10^5 psi

Measured |E*|, 10^5 psi
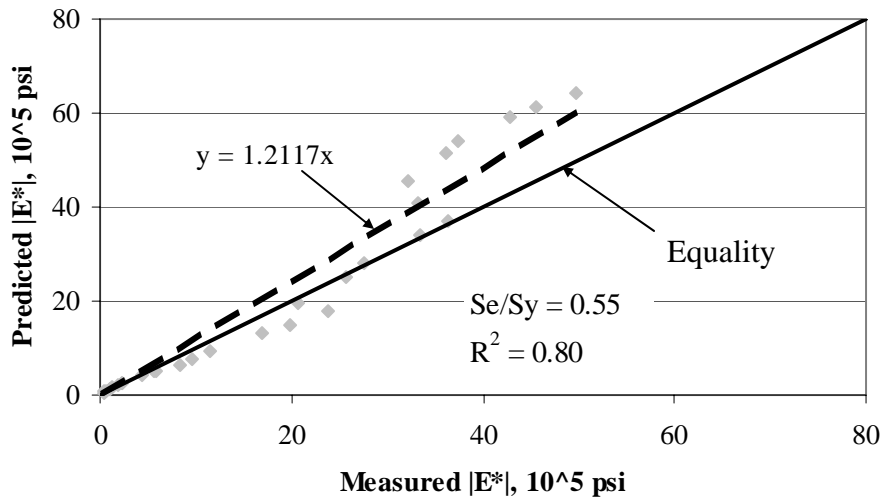
Figure 6.12. Fair |*E*| Predictions for Level 2 Input

MCA-12.5mm-PG76-22-4.0

y = 1.0928x

Equality

Se/Sy = 0.20

R^2 = 0.97
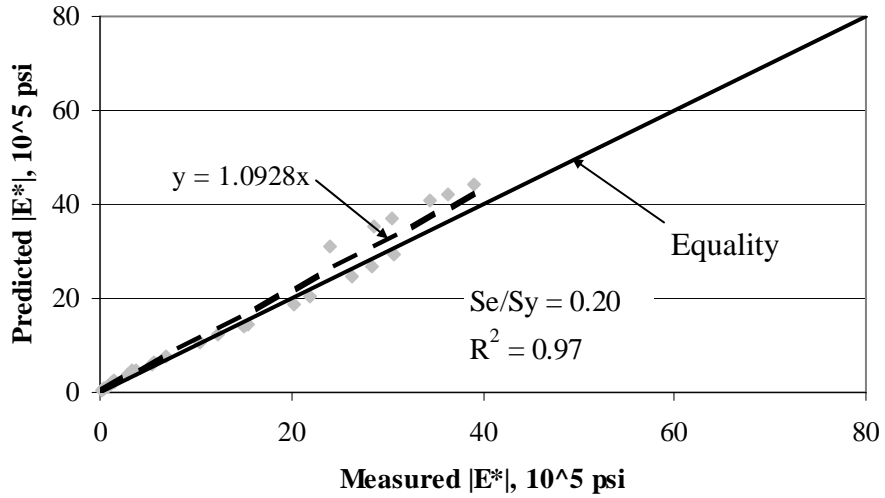
Figure 6.13. Excellent |*E*| Predictions for Level 3 Input

GMQ-37.5mm-PG70-22-4.5

y = 1.2067x

Equality

Se/Sy = 0.53

R^2 = 0.81
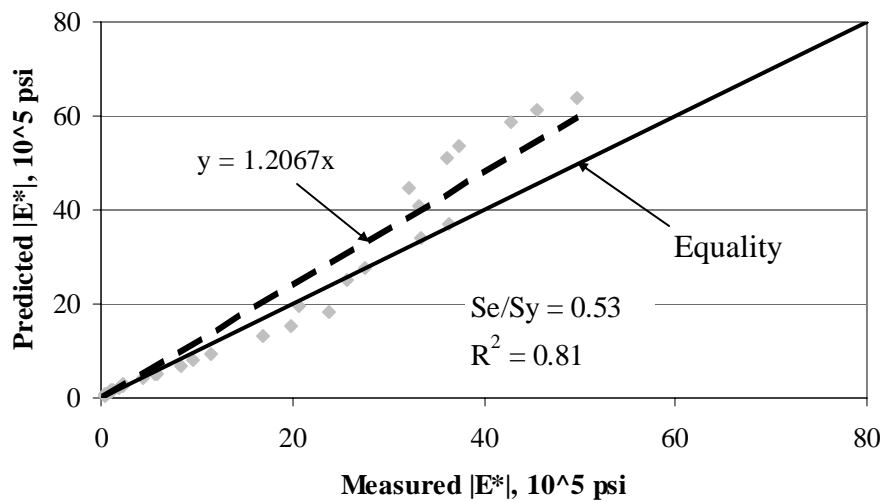
Figure 6.14. Fair |*E*| Predictions for Level 3 Input
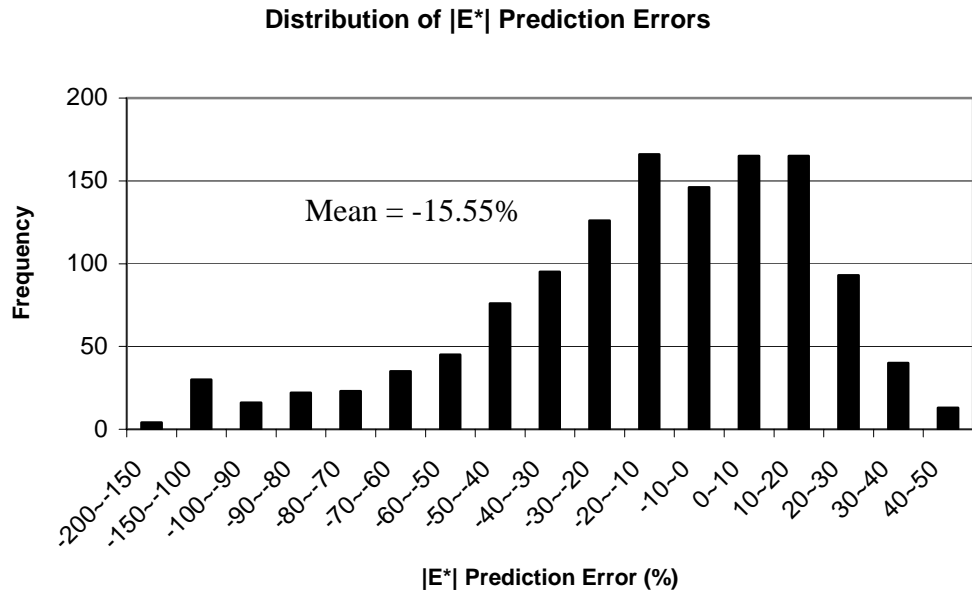
Figure 6.15. Distribution of |*E**| Prediction Errors for Level 2 Input
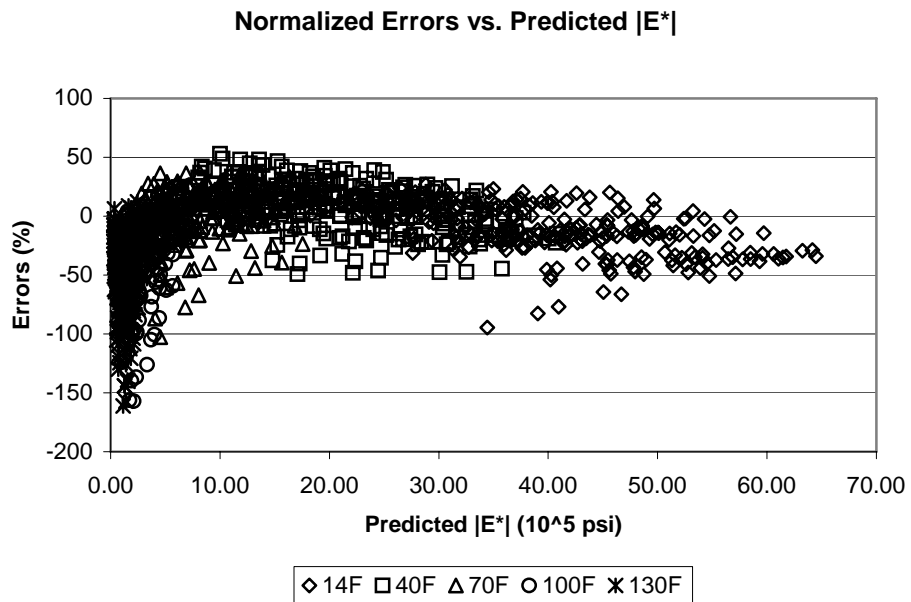
Figure 6.16. Plot of Errors vs Predicted |*E**| for Level 2 Inputs

The prediction errors were investigated further by plotting level 2 $|E^*|$ prediction errors against the mixture properties and test parameters, as shown in Figures 6.17 through 6.21. It was observed that level 2 $|E^*|$ predictions lost the accuracy for larger aggregate sizes, lower binder grade and higher test temperatures.

The prediction errors of level 3 inputs were similar to those of level 2, as illustrated in Figures 6.22 through 6.28. The prediction error range was between –180 percent and +30 percent, and the mean prediction error was –26.57 percent.

The above error analyses showed that the Witczak prediction model had potential systematic errors in predicting dynamic modulus across the aggregate size and test temperatures. In addition, level 2 dynamic modulus inputs were slightly more accurate than level 3.

Overall, the Witczak prediction equation can reasonably estimate the dynamic modulus. The statistics (R^2 and S_e/S_y) obtained in this study, as presented in Table 6.7, compared favorably with those reported by Witczak et al. (*1*) ($R^2 = 0.886$ and $S_e/S_y = 0.338$ in arithmetic space). The evaluation results confirmed the good agreement between predictions and measurements, and they agreed with the results reported by other authors, including Pellinen (*75*, *107*), Dongre et al. (*84*), and Birgisson (*108*). However, prediction bias was existed. The prediction errors were higher for larger aggregate sizes and at higher temperatures. The prediction errors at higher temperatures were expected to influence rutting prediction in the M-E Design Guide. The same conclusions on bias of the Witczak prediction model were reported by Schwartz (*107*).
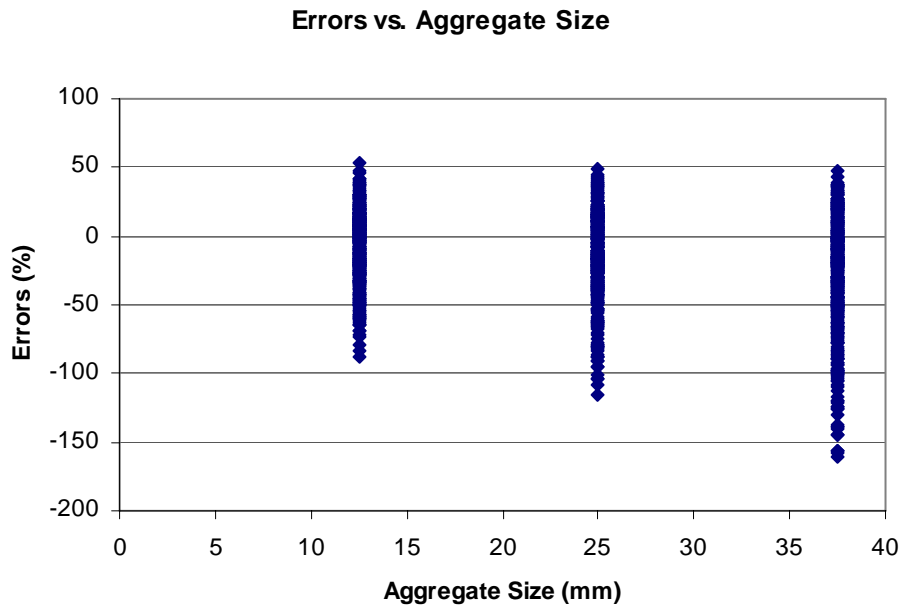
Figure 6.17. Level 2 |*E**| Prediction Errors vs. Aggregate Size
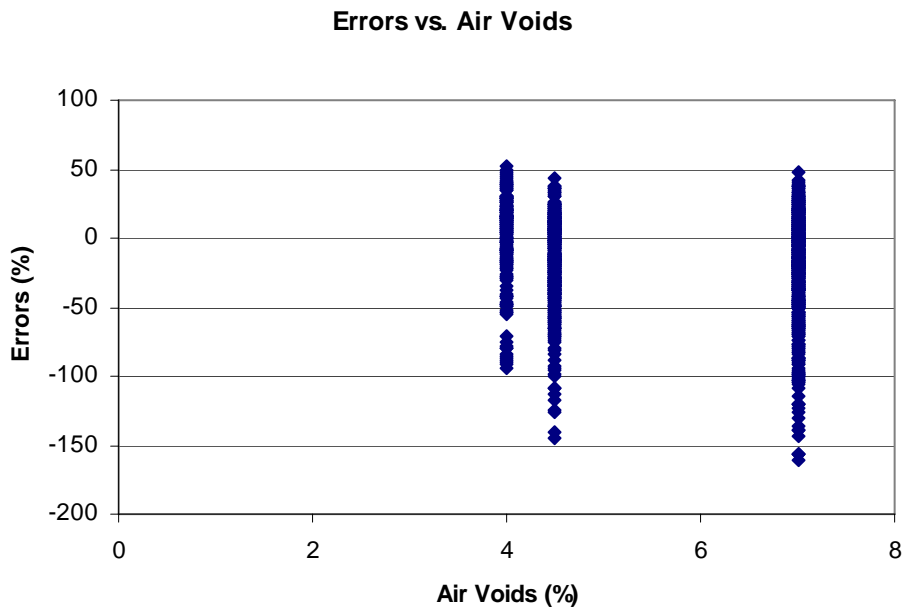
Figure 6.18. Level 2 |*E**| Prediction Errors vs. Air Voids
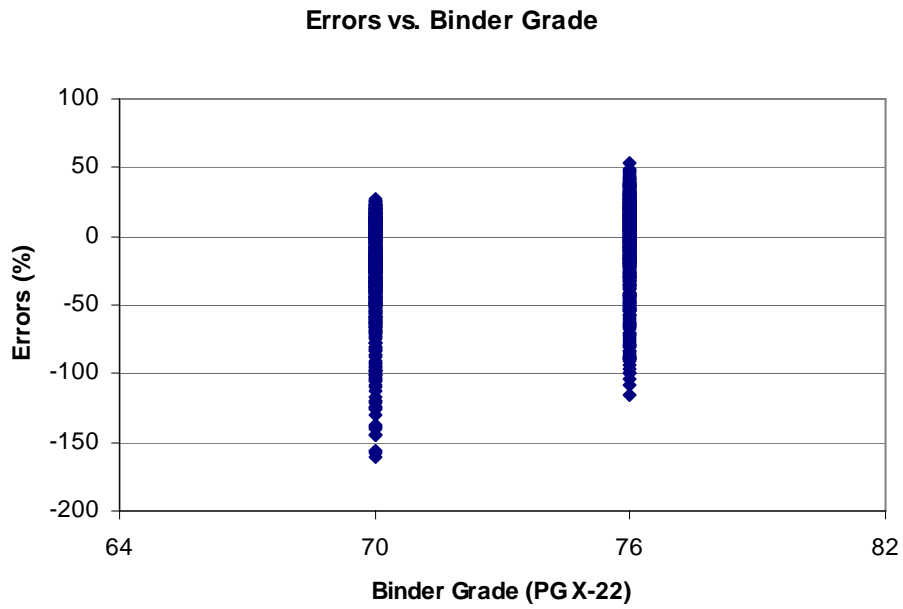
Figure 6.19. Level 2 |*E**| Prediction Errors vs. Binder Grade
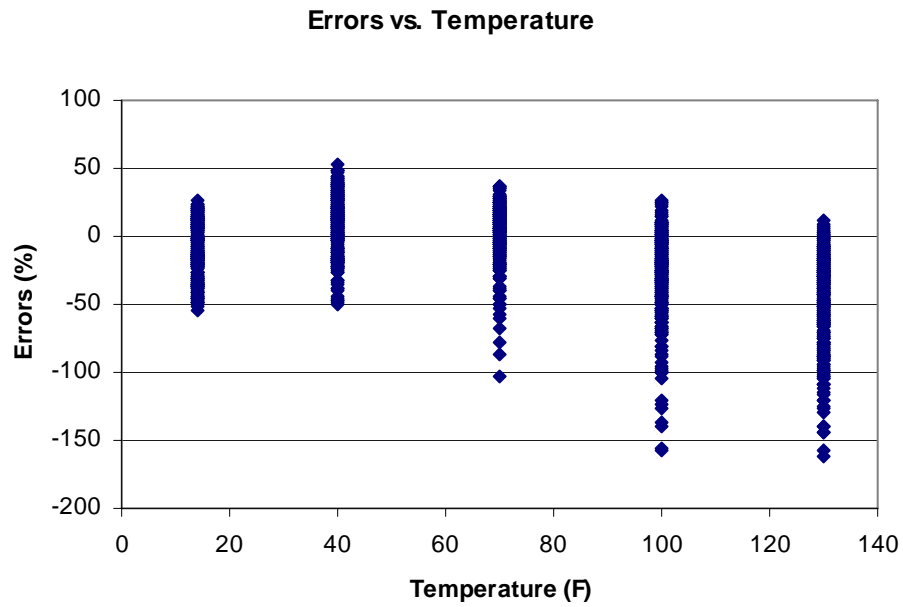
Figure 6.20. Level 2 |*E**| Prediction Errors vs. Test Temperature

Errors vs. Frequency
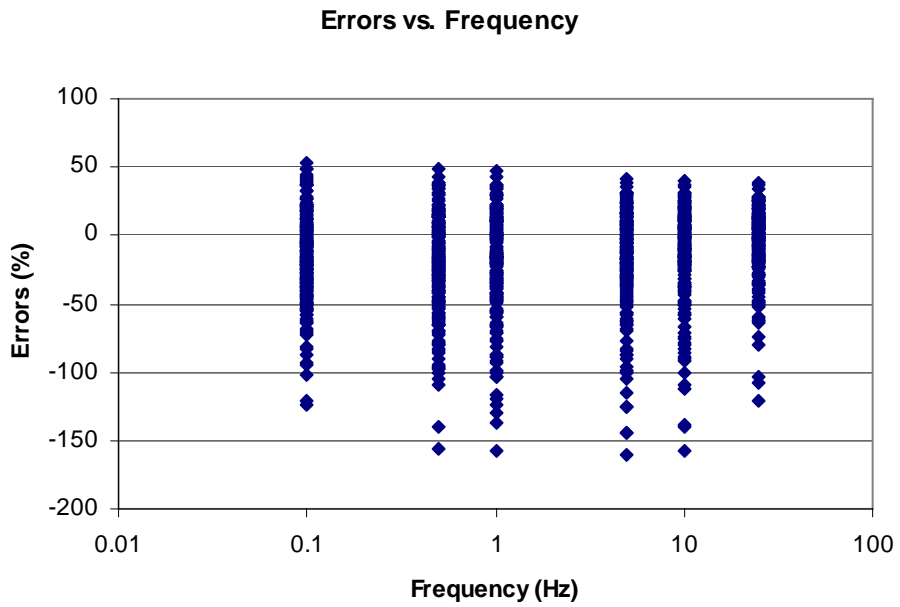
Figure 6.21. Level 2 |*E**| Prediction Errors vs. Test Frequency

Distribution of |E*| Prediction Errors

Mean = -26.57%
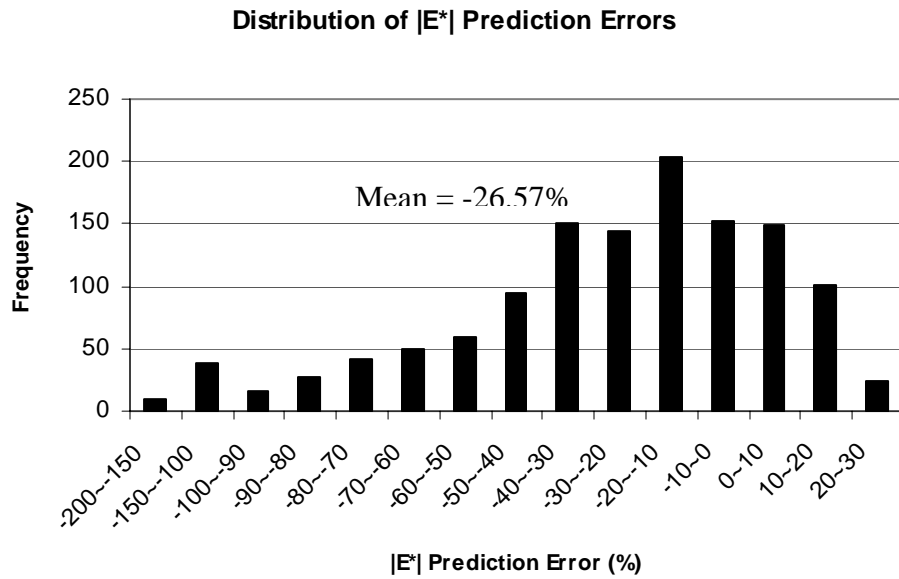
Figure 6.22. Distribution of |*E**| Prediction Errors for Level 3 Inputs

Errors vs. Predicted |E*|
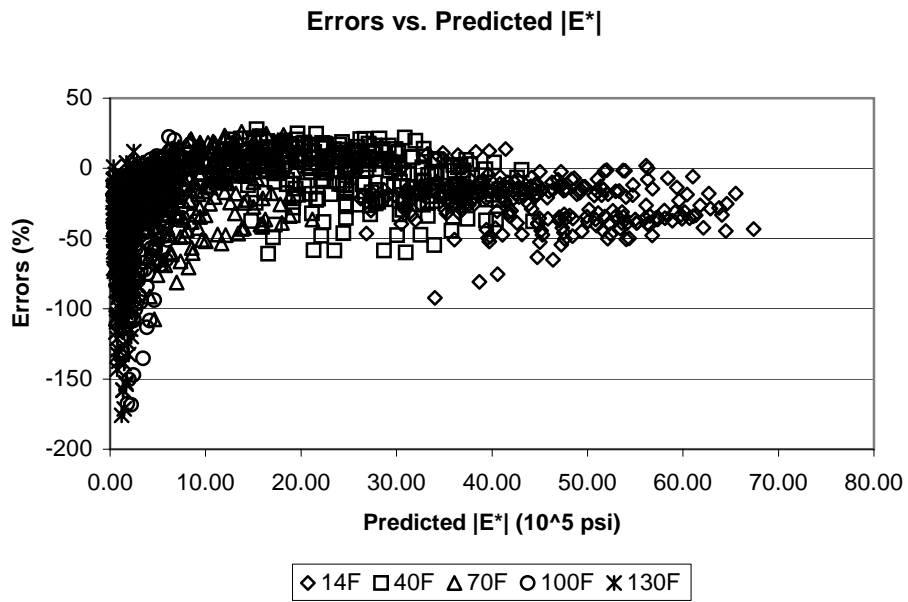
Figure 6.23. Plot of Errors vs Predicted |*E**| for Level 3 Inputs

Errors vs. Aggregate Size
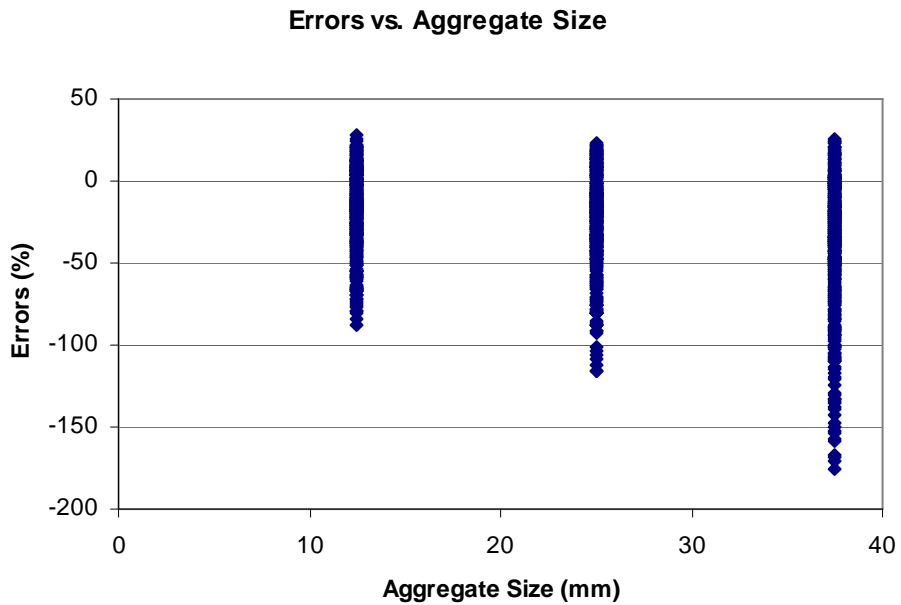
Figure 6.24. Level 3 |*E**| Prediction Errors vs. Aggregate Size
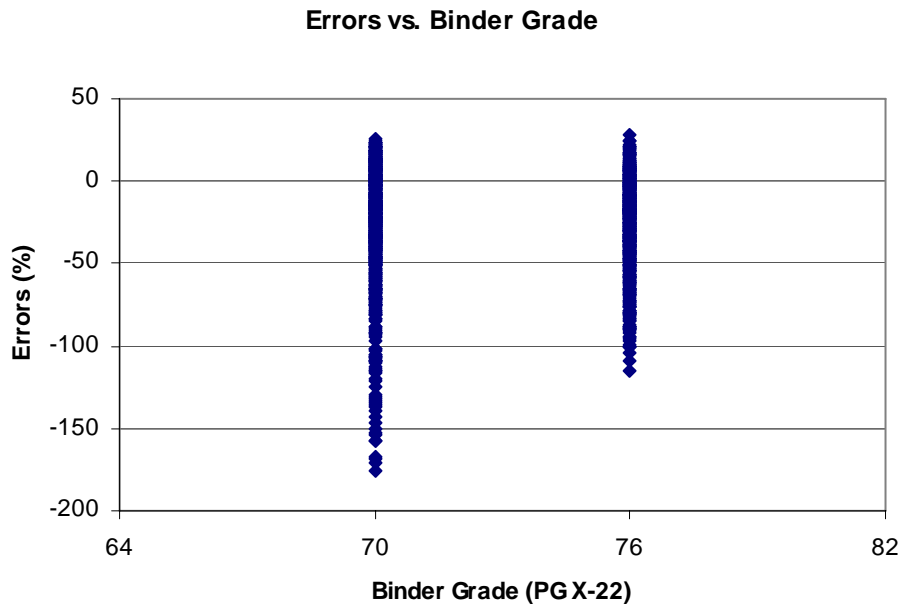
Figure 6.25. Level 3 |*E|* Prediction Errors vs. Binder Grade**
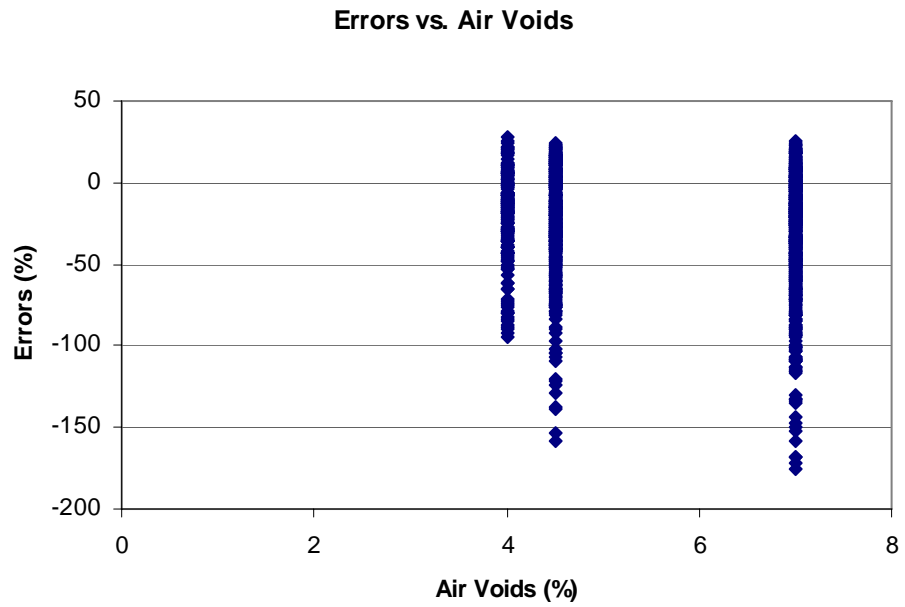
Figure 6.26. Level 3 |*E|* Prediction Errors vs. Air Voids**

Errors vs. Temperature
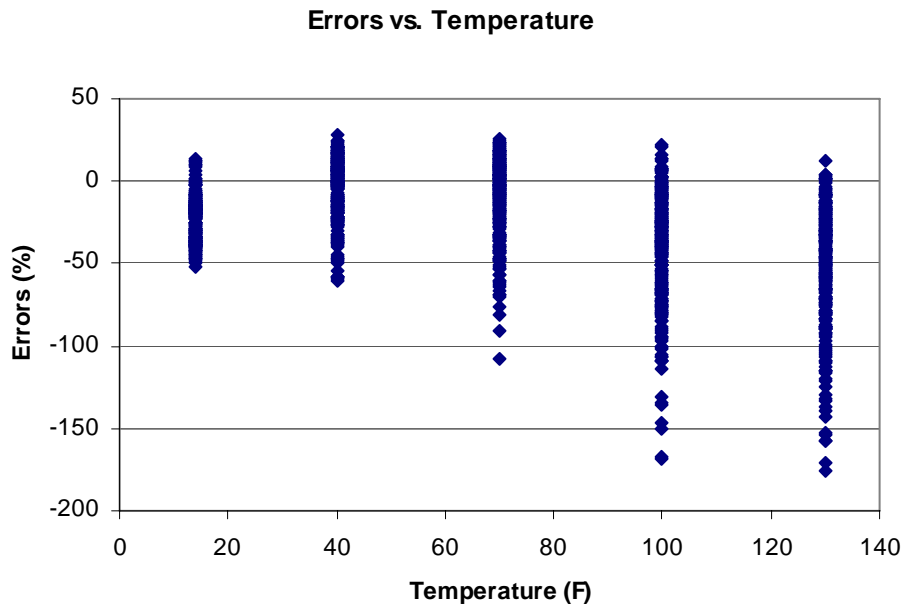
Figure 6.27. Level 3 |*E**| Prediction Errors vs. Temperature

Errors vs. Frequency
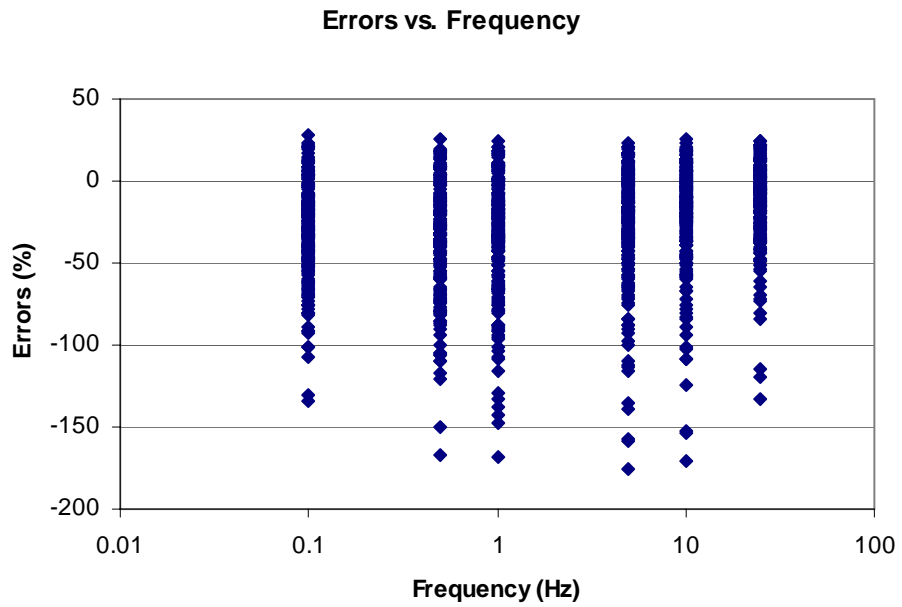
Figure 6.28. Level 3 |*E**| Prediction Errors vs. Frequency

It was questioned whether the above accuracy and bias could be accepted for design applications, and this question could be only answered by analyzing their effects on predicted pavement performance, as presented in the following section.

6.3.3 Effects of |E*| Predictions on Predicted Pavement Performance

The 2002 design software version 0.700 as part of the M-E Design Guide was used to investigate the effects of level 2 and 3 |E*| predictions on predicted pavement performance. The software was employed to design a new pavement consisting of 6 inches of asphalt concrete (AC) over 18 inches of crushed stone built on AASHTO A-7-5 subgrade. The pavement was expected to have average daily traffic of 2500 and last 20 years of service. In order to investigate the differences between the pavement performance predictions using level 1, 2 and 3 |E*| inputs for all mixtures used in this study, all of the performance predictions were determined based on the same design conditions except the |E*| inputs.

The maximum errors for predicted longitudinal cracking and alligator cracking using the measured and predicted |E*| inputs was 55 percent and 25 percent, respectively, and those for predicted AC layer rutting and total rutting at the pavement surface was 26 percent and 14 percent, accordingly. The errors in predicting pavement rutting were considered reasonable. The effects of the dynamic modulus prediction errors (up to 180 percent) at high temperatures on predicted rutting was not very significant in this case.

Due to tremendous amount of predicted pavement performance data, only performance data of five mixtures listed in Table 6.8 was presented later in this study. These HMA mixtures were chosen so that they represented all levels of the $|E^*|$ prediction accuracy and their performance results represented the impact of the $|E^*|$ predictions on predicted pavement performance. Three mixtures were chosen to represent excellent, good and fair predictions. The other two mixtures represented the accuracy boundaries between excellent, good and fair levels.

The data required for level 1, 2 and 3 dynamic modulus inputs in the M-E design software are summarized for the five mixtures in Tables 6.9 through 6.13. For each mixture presented in the aforesaid tables, level 1 dynamic modulus inputs required the measured $|E^*|$ for the HMA mixture and the measured G^* for the binder, and level 2 $|E^*|$ inputs required the mixture volumetric properties and the measured G^* for the binder. Level 3 $|E^*|$ inputs required only the mixture volumetric properties.

Predicted pavement performance based on the input data for the five mixtures, including longitudinal cracking, alligator cracking, AC layer rutting, and total rutting at the pavement surface, was presented in Tables 6.14 though 6.17. The results included the pavement performance predictions after 5, 10, 15 and 20 years in service.

Using the data presented in Tables 6.14 through 6.17, the pavement performance predictions based on level 2 and 3 $|E^*|$ inputs were plotted against those based on level 1 $|E^*|$ inputs, as shown in Figures 6.29 through 6.32. It was observed that the predicted distresses based on level 2 and 3 $|E^*|$ inputs were not distinguishable in this study. All of the data points except for those of longitudinal cracking plotted in the aforesaid figures were relatively close to the equality line.

Table 6.8. Selected Mixtures Used in Predicted Performance Analysis

ID	Aggregate Source	Size (mm)	Binder Grade	$|E^*|$ Prediction	Notes
1	ARK	12.5	70-22	Excellent	$S_e/S_y = 0.18$ $R^2 = 0.98$
2	MCA	25	70-22	Excellent - Good Boundary	$S_e/S_y = 0.34$ $R^2 = 0.93$
3	JET	25	70-22	Good	$S_e/S_y = 0.41$ $R^2 = 0.89$
4	GMQ	37.5	70-22	Good – Fair Boundary	$S_e/S_y = 0.56$ $R^2 = 0.80$
5	GMQ	37.5	76-22	Fair	$S_e/S_y = 0.70$ $R^2 = 0.68$

Table 6.9. Data for Level 1, 2 and 3 |*E**| Inputs for ARK-12.5mm-PG70-22

Measured |E*|:

Temp.	Mixture |E*| (psi)			
(F)	0.1 Hz	1 Hz	10 Hz	25 Hz
10	2,102,570	2,587,440	3,065,640	3,219,580
40	1,226,710	1,724,900	2,262,160	2,446,680
70	242,870	506,800	925,250	1,139,560
100	55,520	119,400	298,580	419,690
130	21,690	34,540	77,410	117,660

Measured G* for RTFO-Aged PG 70-22

Temp.	G*	Delta
(F)	(Pa)	(deg)
50 (10C)	61,300,000	43.74
68 (20C)	2,880,000	53.61
158 (70C)	2,536	82.85

Mix Design Properties

Binder Grade	PG 70-22
Air Voids (%)	6.8
Effective Binder Content (%)	10.5
Cumulative % Retained on 3/4" Sieve	0
Cumulative % Retained on 3/8" Sieve	15
Cumulative % Retained on #4 Sieve	45
% Passing #200 Sieve	5.7

Table 6.10. Data for Level 1, 2 and 3 |*E**| Inputs for MCA-25mm-PG70-22

Measured |E*|:

Temp.	Mixture |E*| (psi)			
(F)	0.1 Hz	1 Hz	10 Hz	25 Hz
10	2,612,730	3,207,250	3,742,410	3,966,540
40	1,742,910	2,468,470	3,063,670	3,311,370
70	346,860	733,780	1,332,220	1,567,530
100	80,000	150,250	368,990	490,690
130	30,930	45,880	93,440	144,720

Measured G* for RTFO-Aged PG 70-22

Temp.	G*	Delta
(F)	(Pa)	(deg)
50 (10C)	61,300,000	43.74
68 (20C)	2,880,000	53.61
158 (70C)	2,536	82.85

Mix Design Properties

Binder Grade	PG 70-22
Air Voids (%)	7.0
Effective Binder Content (%)	8.5
Cumulative % Retained on 3/4" Sieve	15
Cumulative % Retained on 3/8" Sieve	36
Cumulative % Retained on #4 Sieve	66
% Passing #200 Sieve	3.6

Table 6.11. Data for Level 1, 2 and 3 |*E**| Inputs for JET-25mm-PG70-22

Measured |E*|:

Temp.	Mixture |E*| (psi)			
(F)	0.1 Hz	1 Hz	10 Hz	25 Hz
10	1,770,450	2,313,390	2,809,180	3,268,830
40	1,076,570	1,601,660	2,268,390	2,534,130
70	301,170	580,530	1,067,420	1,315,250
100	82,790	168,390	378,310	527,110
130	30,230	50,440	114,840	179,400

Measured G* for RTFO-Aged PG 70-22

Temp.	G*	Delta
(F)	(Pa)	(deg)
50 (10C)	61,300,000	43.74
68 (20C)	2,880,000	53.61
158 (70C)	2,536	82.85

Mix Design Properties

Binder Grade	PG 70-22
Air Voids (%)	7.4
Effective Binder Content (%)	8.7
Cumulative % Retained on 3/4" Sieve	10
Cumulative % Retained on 3/8" Sieve	46
Cumulative % Retained on #4 Sieve	63
% Passing #200 Sieve	3.2

Table 6.12. Data for Level 1, 2 and 3 |*E**| Inputs for GMQ-37.5mm-PG70-22

Measured |E*|:

Temp.	Mixture |E*| (psi)			
(F)	0.1 Hz	1 Hz	10 Hz	25 Hz
10	2,830,170	3,599,860	4,030,500	4,223,050
40	1,819,100	2,540,110	3,180,730	3,181,630
70	509,810	1,069,520	1,863,940	2,174,040
100	74,050	151,770	386,270	571,250
130	29,680	43,950	92,890	149,930

Measured G* for RTFO-Aged PG 70-22

Temp.	G*	Delta
(F)	(Pa)	(deg)
50 (10C)	61,300,000	43.74
68 (20C)	2,880,000	53.61
158 (70C)	2,536	82.85

Mix Design Properties

Binder Grade	PG 70-22
Air Voids (%)	6.6
Effective Binder Content (%)	7.5
Cumulative % Retained on 3/4" Sieve	29
Cumulative % Retained on 3/8" Sieve	41
Cumulative % Retained on #4 Sieve	54
% Passing #200 Sieve	3.8

Table 6.13. Data for Level 1, 2 and 3 |*E**| Inputs for GMQ-37.5mm-PG76-22

Measured |E**|:

Temp.	Mixture |E**| (psi)			
(F)	0.1 Hz	1 Hz	10 Hz	25 Hz
10	2,645,010	3,060,220	3,592,550	4,017,740
40	2,281,640	2,876,480	3,255,370	3,965,220
70	544,290	968,530	1,581,940	1,779,020
100	135,730	257,750	529,420	700,050
130	51,610	88,270	198,790	296,840

Measured G* for RTFO-Aged PG 76-22

Temp.	G*	Delta
(F)	(Pa)	(deg)
50 (10C)	13,200,000	43.57
68 (20C)	2,680,000	52.77
169 (76C)	2,698	64.59

Mix Design Properties

Binder Grade	PG 76-22
Air Voids (%)	6.9
Effective Binder Content (%)	7.4
Cumulative % Retained on 3/4" Sieve	29
Cumulative % Retained on 3/8" Sieve	41
Cumulative % Retained on #4 Sieve	54
% Passing #200 Sieve	3.8

Table 6.14. Predicted Longitudinal Cracking

Mixture	Service Year	Longitudinal Cracking (m/km)		
		Level 1	Level 2	Level 3
ARK_12.5_70-22	5	11	14	14
	10	34	44	44
	15	72	90	91
	20	125	157	157
MCA_25_70-22	5	22	35	34
	10	69	106	106
	15	141	212	212
	20	241	350	352
JET_25_70-22	5	34	40	40
	10	106	123	123
	15	212	242	242
	20	350	398	400
GMQ_37.5_70-22	5	22	30	30
	10	68	94	92
	15	139	189	186
	20	237	316	311
GMQ_37.5_76-22	5	24	40	32
	10	76	121	100
	15	155	241	203
	20	261	394	339

Table 6.15. Predicted Alligator Cracking

Mixture	Service Year	Alligator Cracking (%)		
		Level 1	Level 2	Level 3
ARK_12.5_70-22	5	1.46	1.55	1.51
	10	3.37	3.59	3.50
	15	5.74	6.11	5.96
	20	8.57	9.15	8.93
MCA_25_70-22	5	2.32	2.98	2.89
	10	5.30	6.75	6.57
	15	8.88	11.20	10.90
	20	13.10	16.30	16.00
JET_25_70-22	5	2.73	3.37	3.27
	10	6.26	7.60	7.40
	15	10.40	12.60	12.20
	20	15.30	18.10	17.80
GMQ_37.5_70-22	5	2.33	2.46	2.36
	10	5.33	5.61	5.41
	15	8.93	9.41	9.09
	20	13.10	13.80	13.40
GMQ_37.5_76-22	5	2.16	2.72	2.38
	10	5.01	6.18	5.44
	15	8.44	10.30	9.11
	20	12.40	15.10	13.40

Table 6.16. Predicted AC Layer Rutting

Mixture	Service Year	AC Layer Rutting (mm)		
		Level 1	Level 2	Level 3
ARK_12.5_70-22	5	5.79	5.46	5.21
	10	8.36	7.80	7.44
	15	10.54	9.91	9.42
	20	12.65	11.99	11.38
MCA_25_70-22	5	4.62	5.21	4.95
	10	6.63	7.47	7.09
	15	8.38	9.53	9.02
	20	10.03	11.51	10.95
JET_25_70-22	5	4.06	5.38	5.13
	10	5.92	7.72	7.32
	15	7.49	9.83	9.32
	20	9.02	11.86	11.28
GMQ_37.5_70-22	5	4.04	3.51	3.33
	10	5.77	5.13	4.85
	15	7.26	6.53	6.20
	20	8.69	7.85	7.47
GMQ_37.5_76-22	5	2.57	2.90	2.69
	10	3.76	4.22	3.86
	15	4.78	5.44	4.88
	20	5.74	6.55	5.87

Table 6.17. Predicted Total Rutting

Mixture	Service Year	Total Rutting (mm)		
		Level 1	Level 2	Level 3
ARK_12.5_70-22	5	12.65	12.37	12.09
	10	16.15	15.65	15.27
	15	19.00	18.42	17.88
	20	21.62	21.01	20.35
MCA_25_70-22	5	11.25	12.07	11.79
	10	14.17	15.27	14.86
	15	16.54	17.96	17.42
	20	18.69	20.45	19.86
JET_25_70-22	5	10.74	12.27	11.96
	10	13.49	15.52	15.11
	15	15.72	18.29	17.73
	20	17.75	20.85	20.22
GMQ_37.5_70-22	5	10.52	10.01	9.78
	10	13.13	12.50	12.19
	15	15.24	14.50	14.15
	20	17.17	16.33	15.93
GMQ_37.5_76-22	5	8.84	9.32	9.04
	10	10.90	11.53	11.07
	15	12.50	13.31	12.67
	20	13.94	14.96	14.15
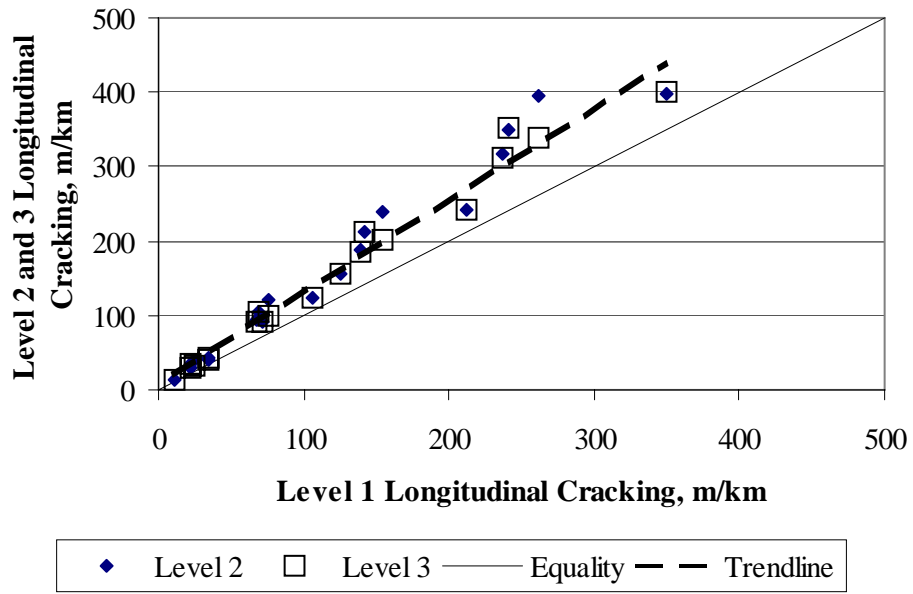
Figure 6.29. Predicted Longitudinal Cracking using Predicted and Measured |*E**|
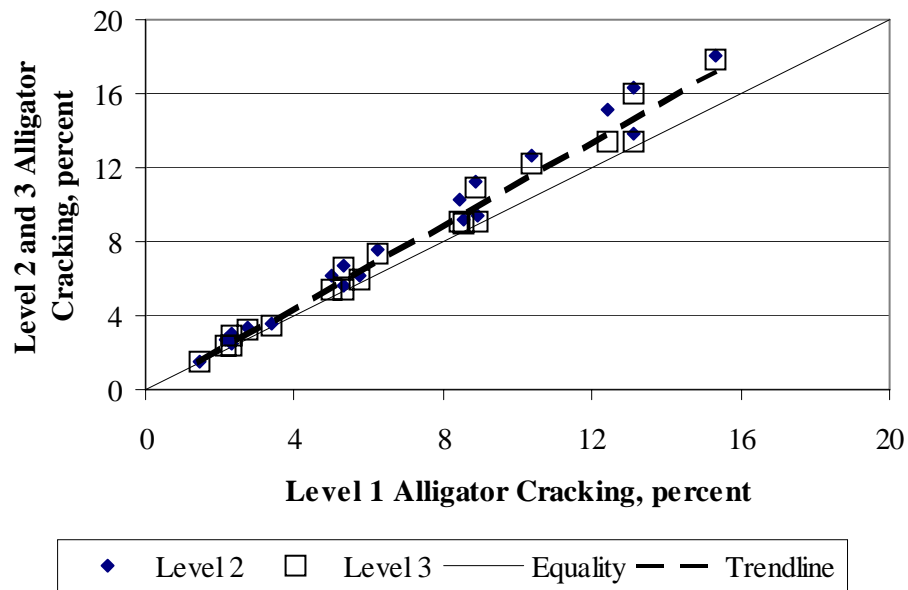
Figure 6.30. Predicted Alligator Cracking using Predicted and Measured |*E**|
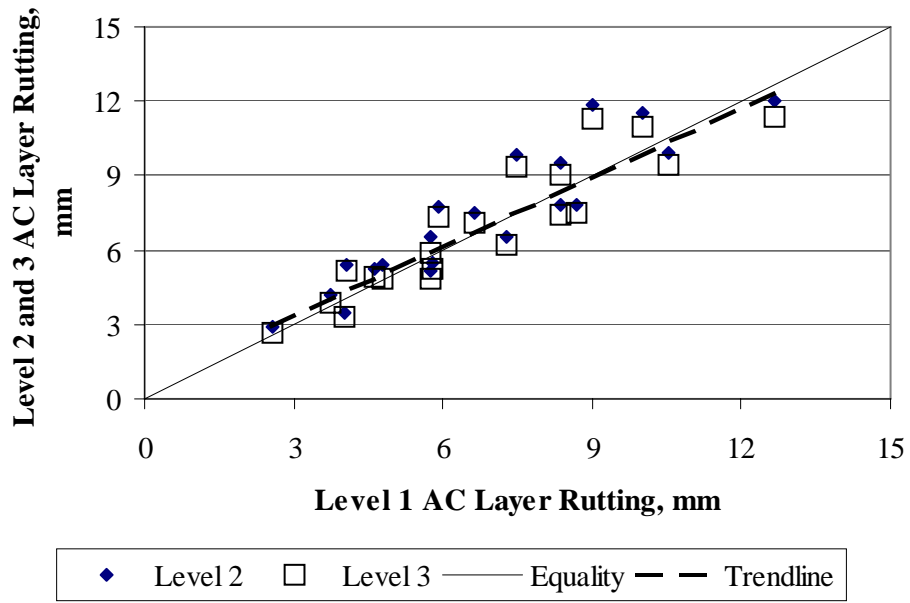
Figure 6.31. Predicted AC Layer Rutting using Predicted and Measured |*E**|
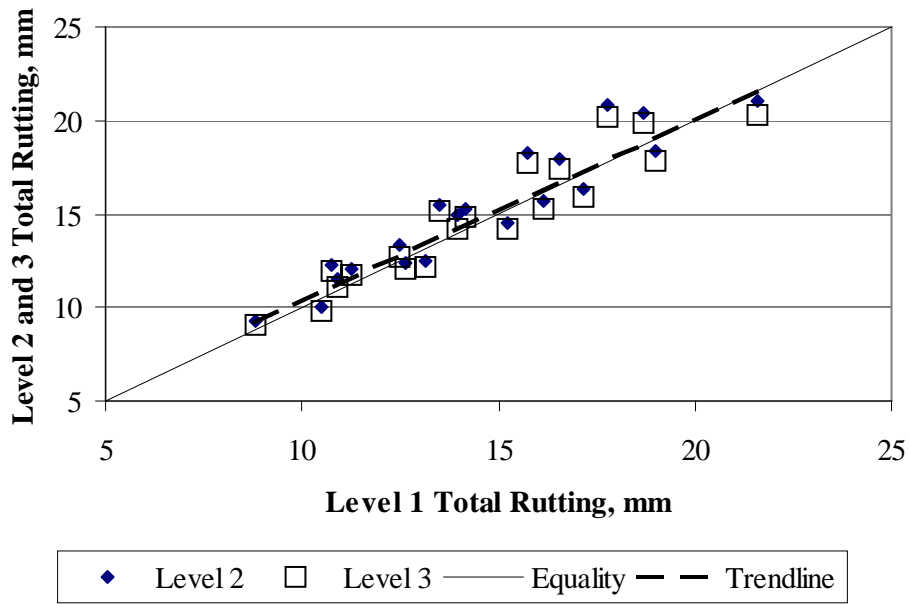
Figure 6.32. Predicted Total Rutting using Predicted and Measured |*E**|

In summary, based on the analyses of pavement performance predicted using the measured and predicted dynamic modulus values, the differences between level 2 and 3 predicted distresses were not significant, so it was recommended that level 3 $|E^*|$ inputs be used instead of level 2 for simplicity. The pavement distresses predicted using the predicted $|E^*|$ inputs were relatively close to those using the measured $|E^*|$ inputs. At this moment, it was not sure which design level could better predict performance of the pavement in service because the distress prediction models incorporated in the M-E software were calibrated using the default values. Therefore, it was recommended that level 3 $|E^*|$ inputs be used for initial implementation of the M-E Design Guide. However, it was recommended that the effects of the dynamic modulus predictions on predicted pavement performance be re-evaluated when the performance data of pavements in service is available.

6.3.4 Sensitivity Analysis

As recommended in the previous section, level 3 $|E^*|$ inputs would be used in the early stages of the M-E Design Guide implementation. However, the mixtures used in this study would not cover all HMA mixtures available in Arkansas. Many HMA mixtures used in the future would not be the same as those studied in this project. To help designers decide whether those mixtures can be used in the design with reasonable effects on predicted pavement performance, a sensitivity analysis was performed in this research. In this study, the changes of the predicted dynamic modulus values caused by the changes of each variable in the Witczak prediction model were evaluated.

The ranges of input parameters for the Witczak predictive model evaluated in this sensitivity analysis were determined based on the data presented in Table 6.6. Three levels of each independent variable, maximum, minimum, and mean, as presented in Table 6.18, were used for the sensitivity analysis. The mean frequency of 10 Hz was selected because it is a reasonable value for traffic speeds, and the mean temperature of 21C (70F) was chosen since it is the reference temperature for the master curve development in the M-E Design Guide.

The dynamic modulus values were first determined at –10, 21, and 54C (14, 70, and 130) using the Witczak prediction model based on the mean values of the input parameters presented in Table 6.18. Each parameter, which was assumed to be independent to other parameters, was then varied, and the corresponding dynamic modulus values were determined at the three temperatures while other parameters were kept constant.

Since the range of the dynamic modulus values determined in this analysis was largely varied, the percent change in |E*| for a given change in a variable was determined using Equation 6.9 to evaluate the sensitivity of the estimated |E*| values to the change of the variable.

$$PC = \frac{\Delta |E^*|}{|\bar{E}^*|} \times 100 \tag{6.9}$$

where:

PC = percent change in |E*|, percent

$\Delta|E^*|$ = change in |E*| for a change in a variable

$\left|\bar{E}^*\right|$ = estimated |E*| using mean values in Table 6.18

245

Table 6.18. Input Parameters for Sensitivity Analysis

Parameter	Unit	Minimum	Mean	Maximum
Va	percent	3.6	5.5	7.4
Vbeff	percent	7.1	9.4	11.7
R34	percent	0	16	31
R38	percent	14	34	54
R4	percent	38	56	74
P200	percent	3.0	4.4	5.7
Frequency	Hz	25	10	0.1
Binder		70-22		76-22
A		10.299	10.007	9.715
VTS		-3.426	-3.317	-3.208
Temperature	F	14	70	130

Sensitivity to Test Parameters. Frequency and temperature are test parameters that significantly affect the dynamic modulus magnitude. While frequency is a direct input for the Witczak prediction model, temperature influences the dynamic modulus through the viscosity term η, which is a function of temperature and binder properties.

The effects of test temperature and frequency on the dynamic modulus are presented in Figures 6.33 and 6.34, respectively. The dynamic modulus decreased sharply with increasing test temperature. The effect was more significant at lower temperatures, and it was lesser when the temperature reached about 21C (70F). Unlike test temperature, increasing test frequency increased the dynamic modulus. The dynamic modulus increased sharply at low frequencies, and it slightly increased with increasing test frequency higher than 5 Hz.

Figure 6.35 compares the influence of temperature on the dynamic modulus values estimated at 10 Hz and the effect of frequency on $|E^*|$ predicted at 21C (70F). It was obvious that test temperature dominantly influenced the dynamic modulus magnitude through its range. Increasing test temperature from the lowest [-10C (14F)] to the highest [54C (130F)] caused 367 percent change in $|E^*|$, while increasing frequency from the minimum (0.1 Hz) to the maximum (25 Hz) caused only 83 percent change in $|E^*|$.

To evaluate the rationality of the Witczak model in predicting $|E^*|$, the dynamic modulus values measured in the laboratory were used to develop dynamic modulus versus temperature and frequency graphs. Typical measured $|E^*|$ versus temperature and frequency graphs are presented in Figures 6.36 and 6.37.
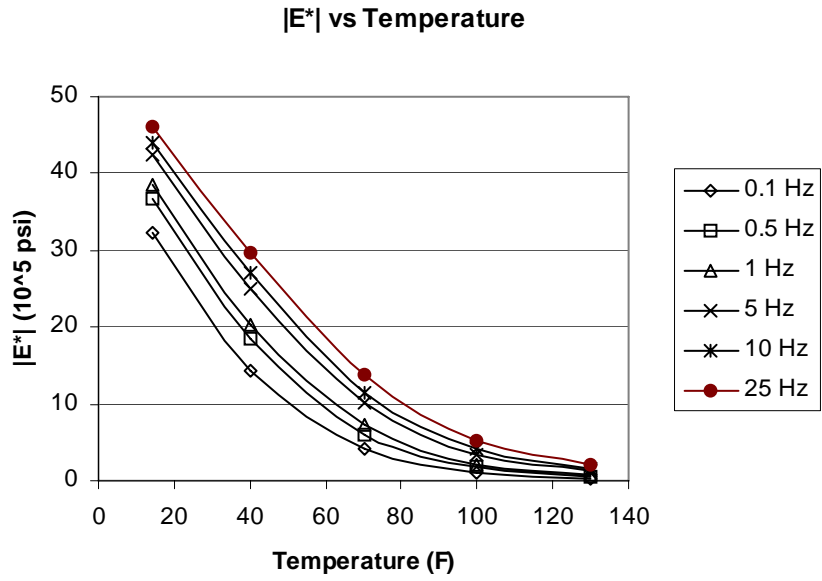
Figure 6.33. Effect of Test Temperature on Estimated |*E**|
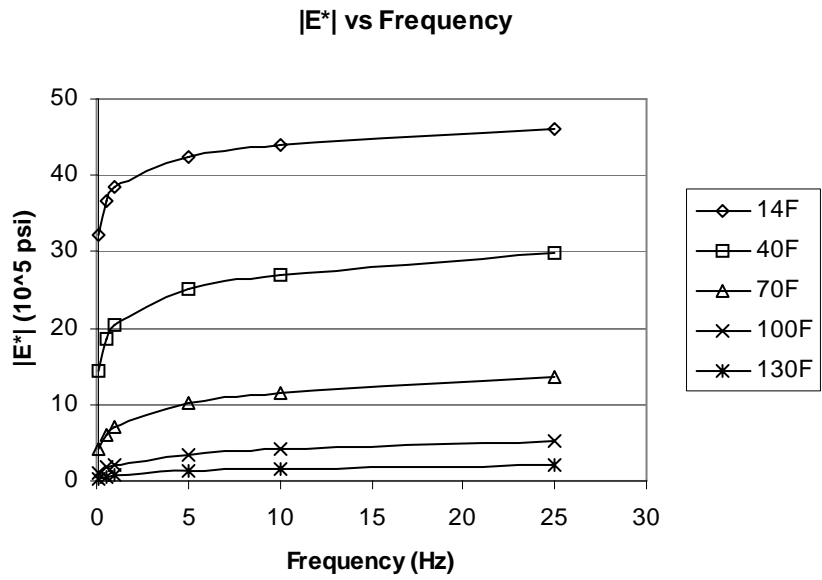
Figure 6.34. Effect of Test Frequency on Estimated |*E**|
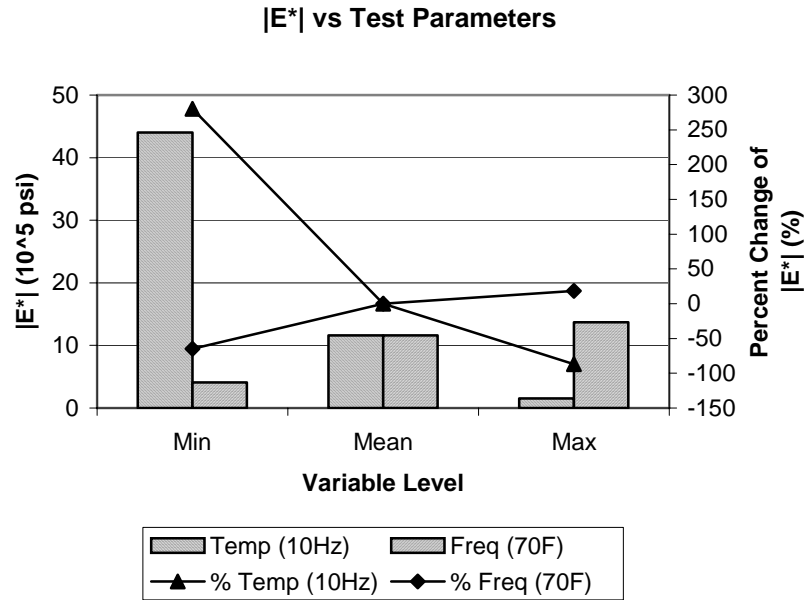
Figure 6.35. Effect of Temperature and Frequency on Estimated |*E**|

Measured |E*| vs Temperature
(GMQ-12.5mm-PG 70-22)
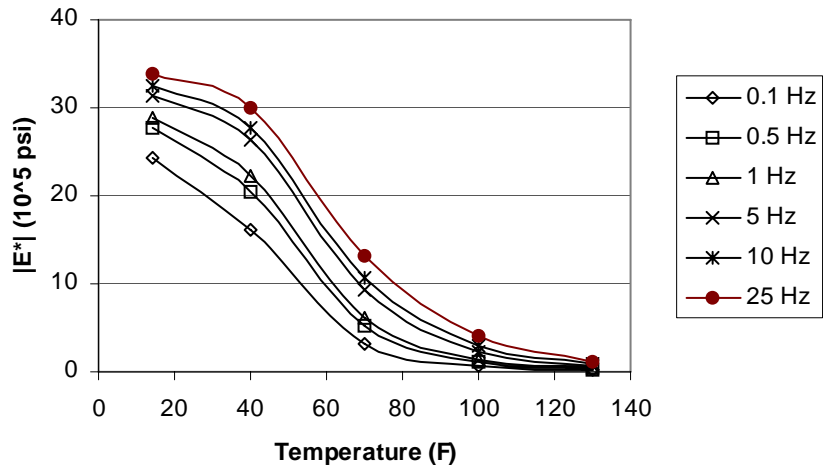
Figure 6.36. Effect of Temperature on Measured |*E**|

Measured |E*| vs Frequency
(GMQ-12.5mm-PG 70-22)
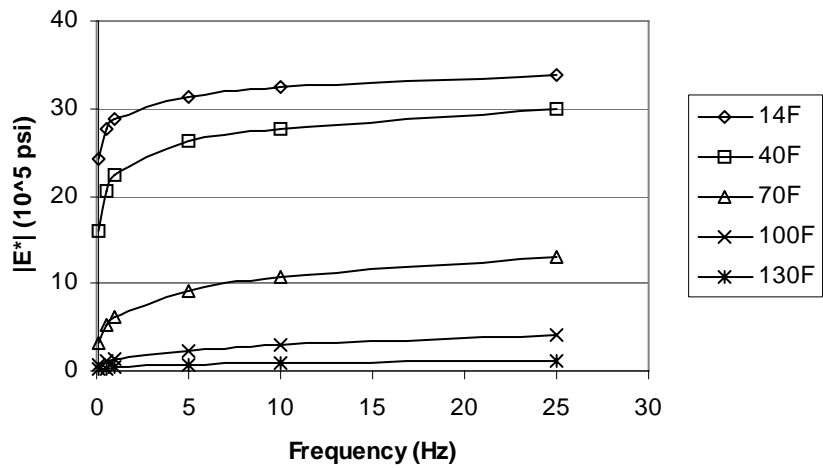
Figure 6.37. Effect of Frequency on Measured |*E**|

The effect of frequency on predicted and measured dynamic modulus, as presented in Figures 6.34 and 6.37, was similar to each other. However, comparing Figure 6.36 to Figure 6.33, it was observed that the Witczak prediction model predicted the effect of temperature on $|E^*|$ differently compared to that found on the measured $|E^*|$. In Figure 6.36, the influence of temperature was more pronounced at intermediate temperatures and lesser at lower and higher temperatures. However, in Figure 6.33, the effect was more significant at lower and intermediate temperatures and lesser at higher temperatures.

Sensitivity to Mixture Properties. As described above, the effect of the mixture properties, such as air voids, effective binder content, gradation, and binder properties, was evaluated at three temperatures, including –10, 21, and 54C (14, 70, and 130). The influence of mixture properties on $|E^*|$ at the three temperatures was presented in Figures 6.38 through 6.40. Based on these figures, the observations are as follows:

- Estimated $|E^*|$ decreased with increasing air voids or effective binder volume. The effect of air voids on predicted $|E^*|$ is reasonable because the lower compacted density, the less stiff HMA mixture. However, the effect of effective binder volume is not clear.

- For gradation properties, predicted $|E^*|$ increased with increasing cumulative percent retained on ¾ in. and 3/8 in. sieves. These effects are expected because the coarser mixtures, the stiffer HMA mixtures.

14F
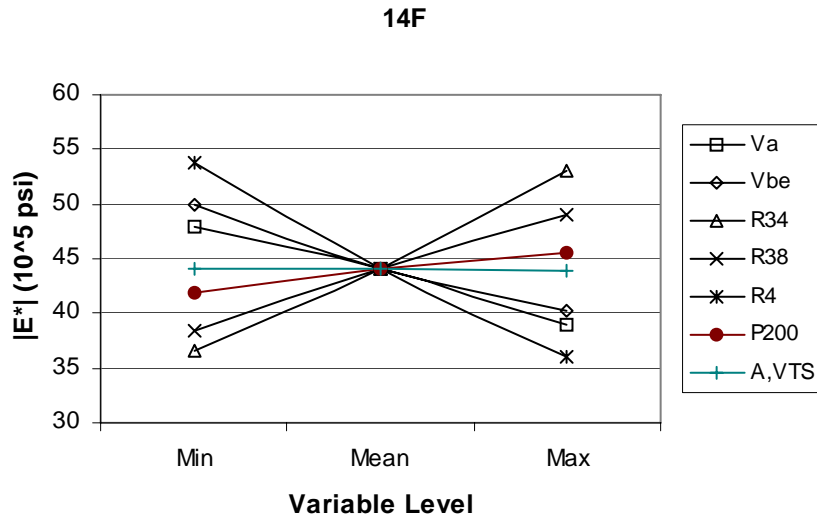
Figure 6.38. Effect of Mixture Properties on Estimated |*E**| at –10C (14F)

70F
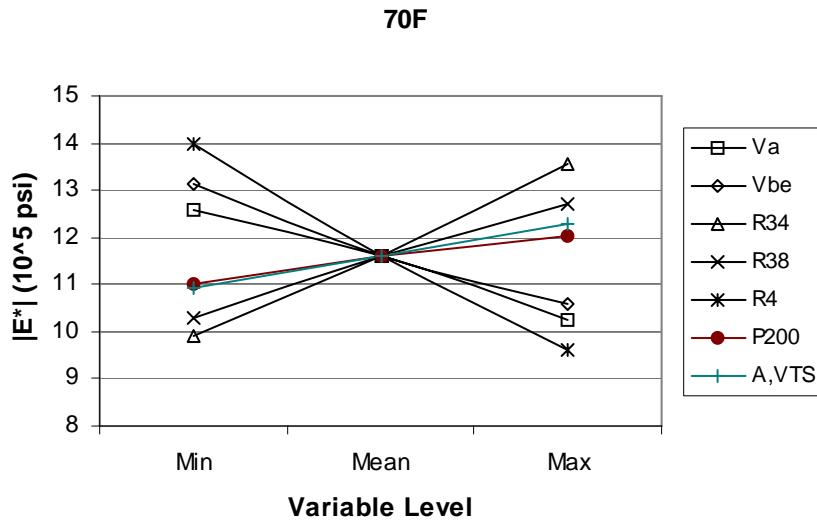
Figure 6.39. Effect of Mixture Properties on Estimated |*E**| at 21C (70F)
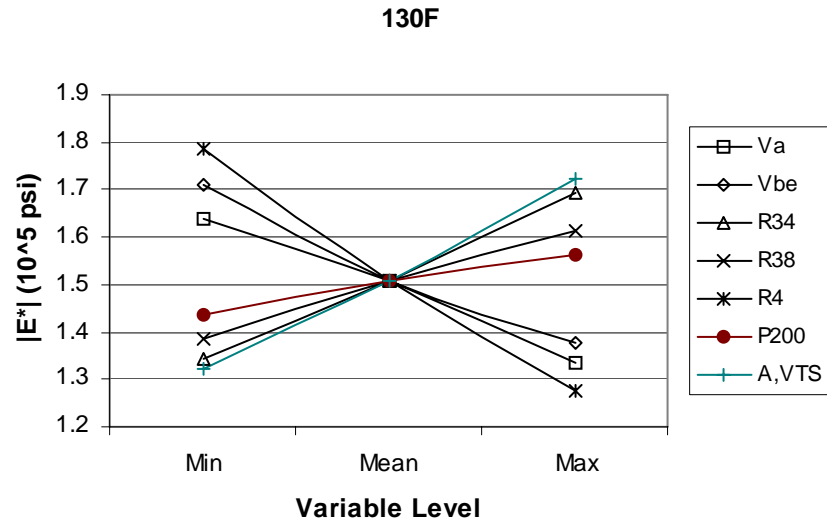
130F

Figure 6.40. Effect of Mixture Properties on Estimated |*E**| at 54C (130F)

- Increasing cumulative percent retained on No. 4 sieve caused a decrease in estimated $|E^*|$. In addition, predicted $|E^*|$ slightly increased with increasing percent passing No. 200 sieve.

- The effect of A and VTS parameters on predicted $|E^*|$ was not significant at –10C (14F), but it was more pronounced as temperature increased. In general, the higher binder viscosity (or higher binder PG), the stiffer HMA mixtures.

Figure 6.41 presents the change in predicted $|E^*|$ caused by the expected variation of each mixture parameter. For this analysis, increasing cumulative percent retained on No. 4 sieve from the minimum value to the maximum value caused the greatest change in predicted $|E^*|$. It was observed that all mixture parameters significantly affect predicted $|E^*|$, but the effect varies at different temperature levels.

Figure 6.42 presents the change in predicted $|E^*|$ caused by a unit change in each parameter. Air voids and effective binder volume had the most significant effects on predicted $|E^*|$. Increasing air voids or effective binder volume by one percent caused 5.3 or 4.7 percent change in predicted $|E^*|$, respectively. Among gradation properties, percent passing No. 200 sieve was the most sensitive.

In this study, among mixture properties, air voids were the most sensitive parameter to predicted $|E^*|$. However, if it varied through its range (variation), it caused only 20.2 percent change in predicted $|E^*|$. Percent retained on No. 4 sieve was the second less sensitive parameter, as presented in Figure 6.42, but its variation caused up to 40.5 percent change in estimated $|E^*|$. Therefore, the influence of a mix parameter on predicted $|E^*|$ should be determined based on the combination of the parameter variation range and sensitivity. This issue was also addressed by Schwartz (*107*).
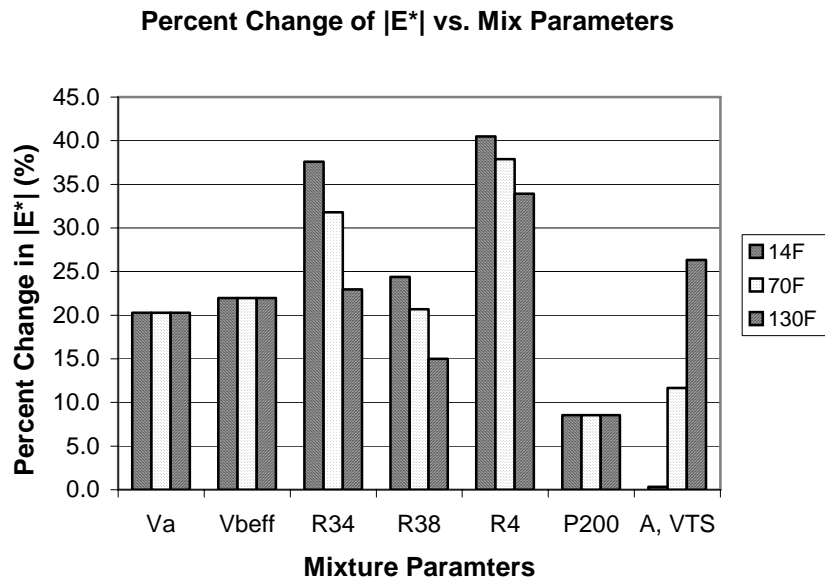
Figure 6.41. Change in Estimated |*E**| Caused by Variation of Mix Parameters
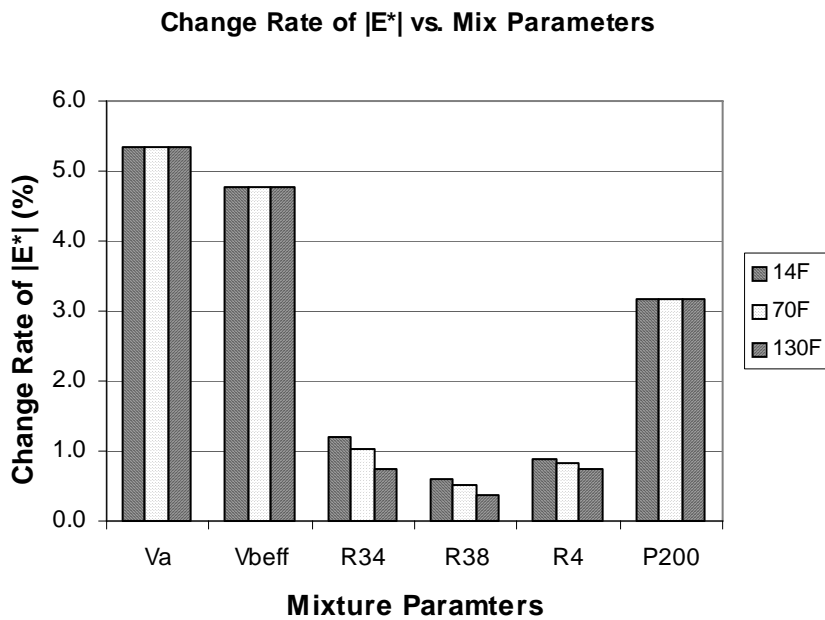
Figure 6.42. Change in Estimated |*E**| Caused by A Unit Change of Parameters

An interesting observation in Figure 6.41 was that the change in predicted $|E^*|$ of a given mixture, determined using Equation 6.9, caused by the change in air voids was the same for all temperatures at a given frequency (10Hz). This observation was investigated using measured dynamic modulus values. Figure 6.43 plots the change in measured $|E^*|$ for five different mixtures determined using Equation 6.9 caused by the change in air voids. It was observed that the change in measured $|E^*|$ caused by the change in air voids was not the same for all temperatures, and it was actually vastly varied. It is obvious that the Witczak prediction model is not able to predict the effect of the interaction between air voids and temperature. With this potential problem, the Witczak prediction model may not accurately estimate the change in the dynamic modulus values due to the variability of air voids in the field for a given mixture.

The above sensitivity analysis showed that the maximum change in predicted $|E^*|$ due to the change in the mixture volumetric properties except for binder parameters (*A* and *VTS*) in this study was about 50 percent. To estimate how this change influences predicted pavement performance, the M-E Design Guide software was used. A new pavement was design using the same input data described in section 6.3.3 except for the dynamic modulus. The dynamic modulus values estimated based on the mean volumetric properties in Table 6.18 were first used. Then, the master curve of the estimated dynamic modulus was shifted up and down by increasing all of the estimated dynamic modulus values 50 percent and decreased them 50 percent and 100 percent. Consequently, four sets of pavement performance predictions were obtained, and the sensitivity of predicted performance to the dynamic modulus was presented in Figure 6.44.

Percent Change in |E*| vs. Change in Air Voids
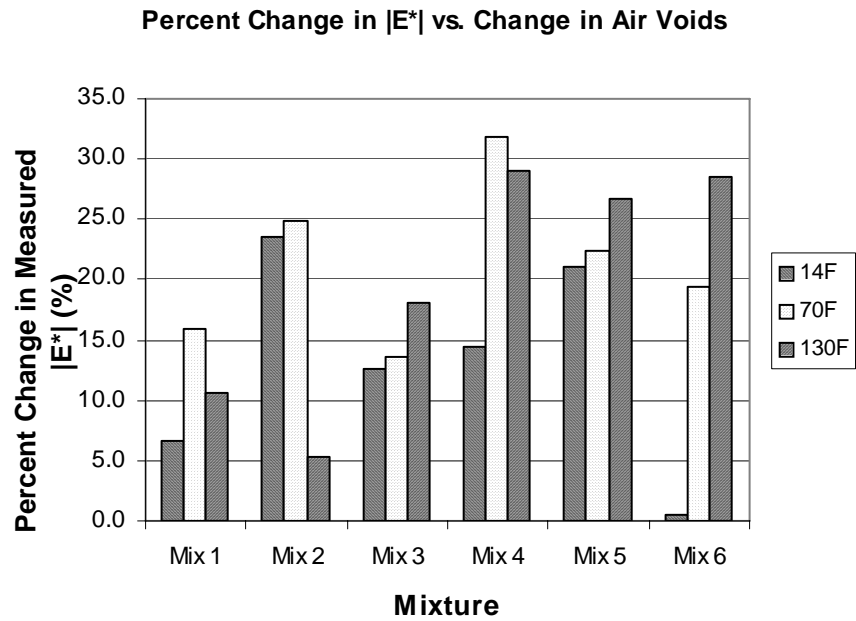
Figure 6.43. Change in Measured |*E**| Caused by Change in Air Voids

|E*| vs Predicted Performance
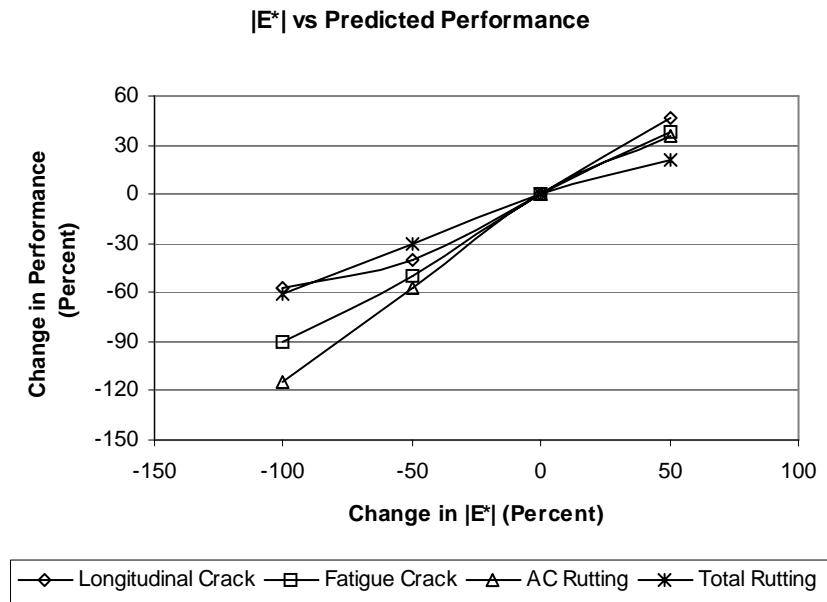
Figure 6.44. Change in Predicted Performance Caused by Change in |*E**|

It was noted that the M-E Design Guide software produced errors when the dynamic modulus master curve was shifted up 100 percent, so the corresponding data were not included in Figure 6.44. It was observed in Figure 6.44 that one percent change in $|E*|$ caused about one percent change in predicted fatigue cracking and AC rutting. As presented in Figure 6.41, the volumetric properties can cause up to 50 percent change in the dynamic modulus values, and as a result, it can cause up to 50 percent change in predicted performance. This equals to a safety factor of 1.5.

In summary, the sensitivity analysis showed that the test temperature is the most sensitive factor to the predicted dynamic modulus. Increasing test temperature from the lowest [-10C (14F)] to the highest [54C (130F)] caused 367 percent change in $|E*|$. Among volumetric properties, air void content is the most sensitive factor, but its variation through its range just causes up to 20 percent change in the predicted $|E*|$. In contrast, percent retained on No. 4 sieve seems to be a moderately sensitive factor, but its variation through its range can cause up to 50 percent change in the predicted $|E*|$. As a result, it can cause up to 50 percent change in predicted fatigue cracking and AC rutting, which equals to the safety factor of 1.5.

The sensitivity analysis shows that the Witczak model exhibits some errors in predicting the dynamic modulus across test temperatures and does not account for the interaction effects between air voids and test temperature.

6.4 Summary

The Witczak prediction model was evaluated in this chapter. The accuracy and error of the model was assessed by comparing the measured $|E*|$ and the corresponding

predicted values. The Witczak model can reasonably predict the dynamic modulus of HMA mixtures even though it still has some errors. Level 2 |E*| inputs can estimate the dynamic modulus more accurate than level 3 |E*| inputs. However, the associated performance predictions due to level 2 and 3 |E*| inputs were not distinguished in this study. In addition, the variation of volumetric properties of the mixtures used in this study can cause up to 50 percent change in predicted performance, and this change equals to the safety factor of 1.5, which is less than the normally used safety factor of 2. Therefore, it is recommended that level 3 |E*| inputs be used for initial implementation of the M-E Design Guide.

CHAPTER 7: INTERNAL GYRATION ANGLE STUDY

The Superpave gyratory compactor (SGC) is a key component of the Superpave system. It is used to simulate the field compaction of HMA mixtures. The HMA specimens are compacted in the SGCs using a combination of pressure and a gyratory angle. The angle of gyration significantly influences the compaction effort. A current standard (AASHTO T312) requires the gyration angles of all compactors to be calibrated externally and/or internally. In many cases, the externally calibrated gyratory compactors do not produce HMA specimens having similar densities. Unlike the external angle calibration, the internal angle calibration can adjust different SGCs to produce similar HMA mixture densities (*3,4,98*).

The internal angle calibration can be performed using the Dynamic Angle Validation (DAV) kit with mix. However, many researchers suspected that the magnitude of the internal angle was dependent upon stiffness (dynamic modulus) or shear resistance of the mixture used in the calibration. If that is the case, the internal angle calibration procedure for SGCs becomes mix-dependent calibration method, and it is complicated. Therefore, the effect of HMA mixture stiffness on the internal gyration angle measurements was studied in this chapter.

Even though the internal gyration angle calibration is an effective method, it is still considered labor intensive and time consuming, and a simple calibration method using a simulated loading device instead of a HMA mixture is desired. The other study presented in this chapter is to investigate the potential of using the simulated loading devices to calibrate the internal gyration angle of gyratory compactors.

7.1 Effect of Hot-Mix Asphalt Stiffness on Internal Gyration Angle Measurements

7.1.1 Internal Gyration Angles Measured by DAV with Mix

The internal gyration angles of the Pine and Troxler SGCs were measured using the DAV with eight different HMA mixtures. The testing program was presented in Section 4.2.1. In order to avoid data deviations caused by measurement errors, the test data were screened for outlying observations. Since only three replicates were measured for each test combination, the Dixon outlier test method was used (*109*).

Three replicate observations are denoted in order of increasing magnitude $x_1 \leq x_2 \leq x_3$. The statistics recommended for testing low side and high side outliers are presented in Equations 7.1 and 7.2, respectively.

$$r_{low} = \frac{x_2 - x_1}{x_3 - x_1} \tag{7.1}$$

$$r_{high} = \frac{x_3 - x_2}{x_3 - x_1} \tag{7.2}$$

If the aforesaid statistics are higher than the 5 percent critical value, which is 0.941 for *n* = 3, the corresponding measurements are considered outliers at the 5 percent level of significance. The outlying observations were reviewed, and the outlying data were replaced with new measurements as required.

Since the Pine gyratory compactor molds can handle the DAV with the mixture for 115 mm specimen, the mean and standard deviation of the test data for the Pine SGC were determined using Equations 7.3 and 7.4b.

$$DIA = \frac{DIA_{top} + DIA_{bottom}}{2} \tag{7.3}$$

$$Var(DIA) = Var\left(\frac{DIA_{top} + DIA_{bottom}}{2}\right) \tag{7.4a}$$

$$\sigma_{DIA} = \sqrt{Var(DIA)} = \frac{1}{2}\sqrt{Var\left(DIA_{top}\right) + Var\left(DIA_{bottom}\right)} \tag{7.4b}$$

where:

DIA_{top} = average top internal gyration angle

DIA_{bottom} = average bottom internal gyration angle

$Var(DIA_{top})$ = variance of top internal gyration angles

$Var(DIA_{bottom})$ = variance of bottom internal gyration angles

Unlike the Pine SGC molds, the Troxler SGC molds cannot handle the DAV and the mix for full height sample, so the top and bottom internal gyration angles in Equation 7.3 were not direct measurements but calculated values based on the extrapolation method. The internal gyration angles for the 115 mm specimens were estimated based on a linear model determined by the internal angles for short specimens (1250 g of HMA mix) and tall samples (2450 g of mixture). The extrapolation can be done using Equation 7.5.

$$DIA_{115} = DIA_s + \left(DIA_t - DIA_s\right)\frac{\left(115 - h_s\right)}{\left(h_t - h_s\right)} \tag{7.5}$$

where:

DIA_{115} = internal gyration angle of 115 mm specimen

DIA_s = internal gyration angle of short specimen

DIA_t = internal gyration angle of tall specimen

h_s = height of short specimen

h_t = height of tall specimen

The standard deviation for the calculated internal gyration angles of 115 mm specimens can be determined using Equation 7.6a.

$$Var(DIA_{115}) = Var\left[DIA_s + (DIA_t - DIA_s)\frac{(115 - h_s)}{(h_t - h_s)}\right]$$ (7.6a)

The AASHTO standard PP 48-03 allows the height of the test samples varies within $\pm$ 5mm. Therefore, the height of the test samples does not significantly affect the internal gyration angle measurements if it varies within $\pm$ 5mm around its mean, and thus Equation 7.6a can be rewritten as follows:

$$Var(DIA_{115}) = \left[1 - \frac{(115 - h_s)}{(h_t - h_s)}\right]^2 Var(DIA_s) + \left[\frac{(115 - h_s)}{(h_t - h_s)}\right]^2 Var(DIA_t)$$ (7.6b)

If the height of the test specimens varies more than $\pm$ 5mm, the deviation of the height of the short and tall specimens should be accounted in Equation 7.6a, and Equation 7.6b would be in a more complicated form.

The results of the internal gyration angle Study 1, including the mean and standard deviation, are presented in Appendix D. Figures 7.1 and 7.2 summarize the average internal angle and standard deviation for each compactor and mixture. The figures show that the Pine SGC was less influenced by the HMA mixture used in the internal angle measurements. The ranges of the mean internal angles for the Pine and Troxler SGCs were 1.16 through 1.18 and 1.03 through 1.09, respectively. The standard deviation values for the internal angles of the Troxler SGC were much higher than those of the Pine SGC, and this observation was expected because the variation of the Troxler SGC test results included the errors due to the internal gyration angle test method and the errors due to the linear extrapolation procedure.

Internal Gyration Angle (DAV with Mix)
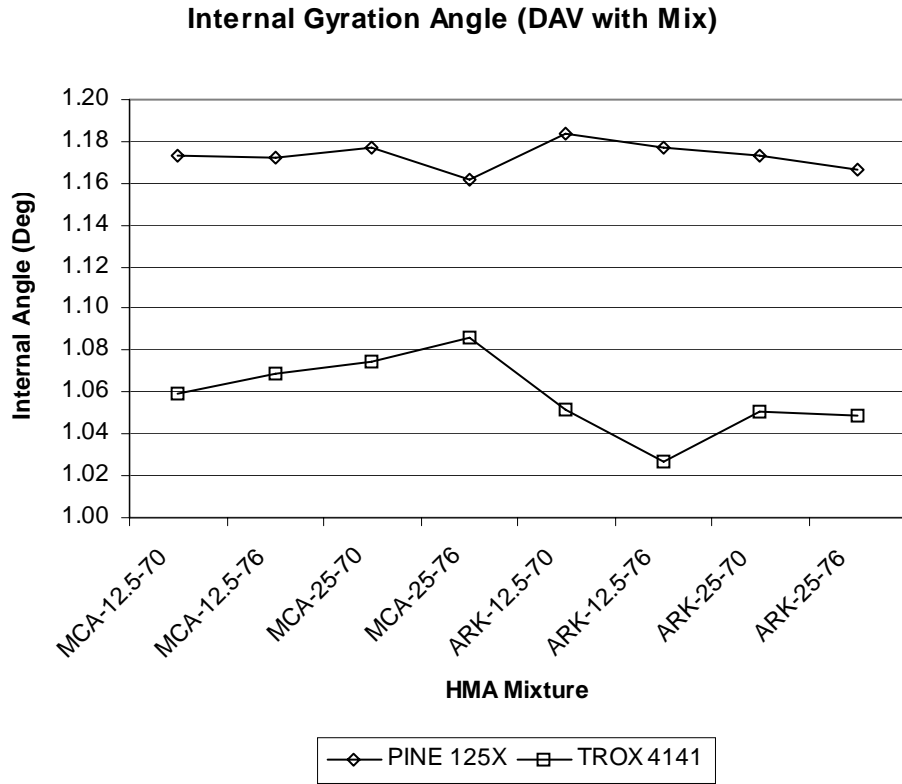
Figure 7.1. Internal Gyration Angles for Different HMA Mixtures

Standard Deviation of Internal Angle (DAV with Mix)
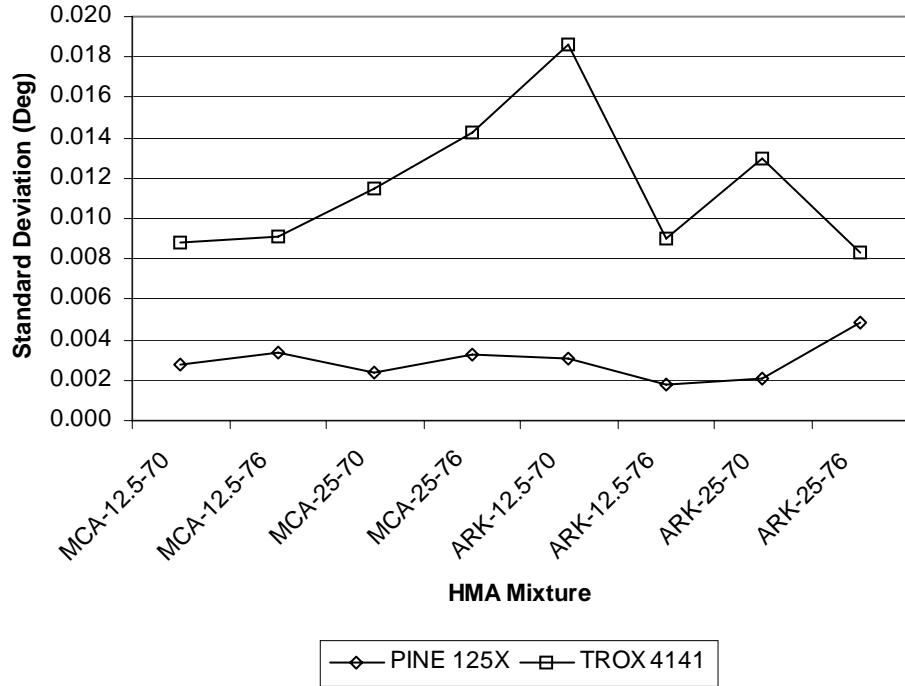
Figure 7.2. Standard Deviation of Internal Angles for Different Mixes

7.1.2 Effect of Mix Stiffness on Internal Gyration Angle Measurements

In this study, two measurements were determined to investigate the affect of HMA mixture stiffness on the internal gyration angle measurements: (1) the dynamic (complex) modulus measured by the dynamic modulus test; and (2) the mixture resistance to the compaction effort measured by the eccentricity of the gyratory force.

Dynamic (Complex) Modulus. The dynamic modulus values used in this study include: (1) the dynamic modulus measured at 54C (130F) and 10 Hz; and (2) the dynamic modulus estimated at the compaction temperature of 148C (302F) and 10 Hz using the Witczak prediction equation. The frequency of 10Hz was chosen because it is normally used to simulate traffic speed in the field. The dynamic modulus values of the HMA mixtures used in the internal gyration angle study are presented in Table 7.1. The internal gyration angles are plotted against the corresponding dynamic modulus values in Figures 7.3 and 7.4. The figures show that the internal gyration angles were lower when the stiffer mixtures were used. The effect of mixture stiffness on the internal gyration angle measurement was different for the two SGCs used in this study. The effect was more pronounced for the Troxler SGC and less for the Pine SGC. The influence was observed for both the measured dynamic modulus at 54C and the predicted dynamic modulus at 148C. However, since the number of HMA mixtures tested in this study was not enough to gain good correlations, this observation must be further investigated.

Table 7.1. Dynamic Modulus of Mixtures for Internal Angle Study

Mixture	Dynamic Modulus at 10 Hz (ksi)	
	54C (130F)	148C (300F)
MCA-12.5-70	83.3	5.3
MCA-12.5-76	98.3	6.1
MCA-25-70	93.4	5.3
MCA-25-76	76.7	5.9
ARK-12.5-70	77.4	5.7
ARK-12.5-76	143.8	6.7
ARK-25-70	77.7	6.0
ARK-25-76	169.9	7.1

Internal Angle vs. E* at 54C
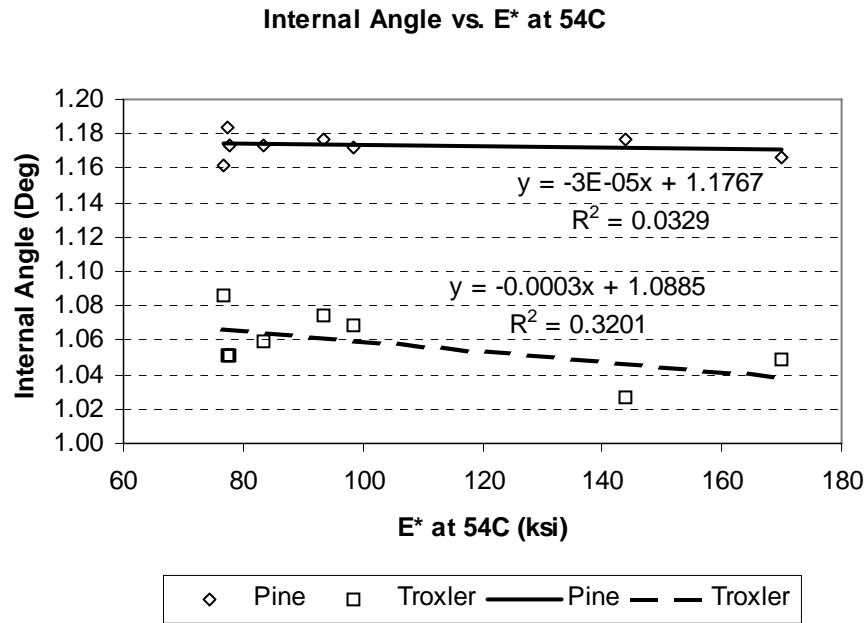
Figure 7.3. Relationship between the Internal Angle and Mix Stiffness at 54C

Internal Angle vs. E* at 148C
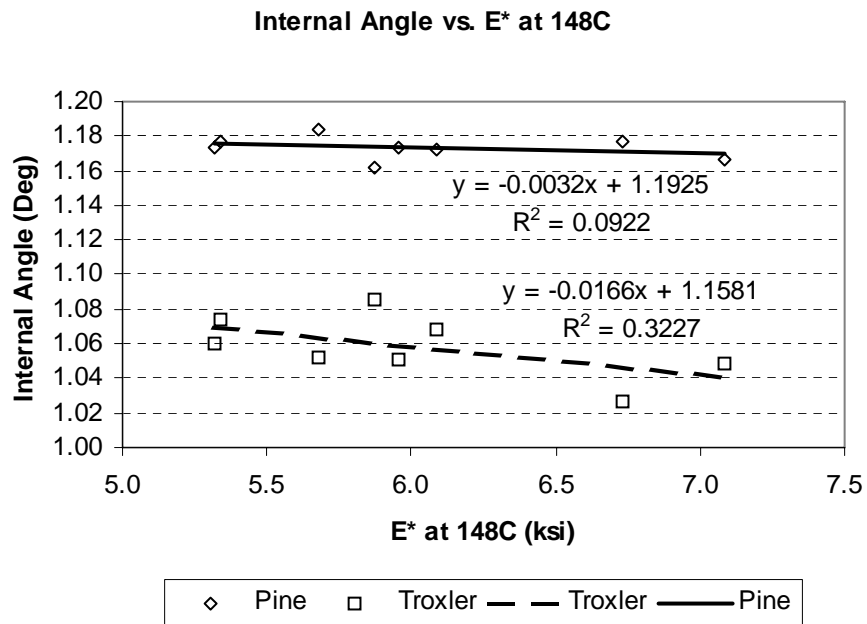
Figure 7.4. Relationship between the Internal Angle and Mix Stiffness at 148C

Eccentricity of Gyratory Force. The eccentricity of the gyratory force is generated by tilting the SGC mold to a gyration angle, which can be calibrated by the internal/external angle calibration method. The gyration angle varied depending upon the relative stiffness between the mixture and the SGC frame. As a result, a change in the gyration angle can cause a change in the eccentricity of the gyratory force. In other words, stiffness of the mixture can cause a change in the eccentricity, resulting a change in the gyration angle.

The eccentricities of the gyratory force were measured using the Pressure Distribution Analyzer (PDA) with the eight different mixtures used in the aforesaid DAV study. The detailed test results are presented in Appendix E. Figures 7.5 and 7.6 summarize the eccentricity and standard deviation values for each compactor and mixture. Like the internal gyration angle values, the eccentricity values for the Pine SGC are less variable than those for the Troxler SGC.

The internal gyration angles are plotted against the corresponding eccentricities in Figure 7.7. The correlations between the internal gyration angles and the eccentricities were very poor.

Based on the detailed test results presented in Appendix E, it was observed that the gyratory force was varied when different samples were compacted. In order to account for the compaction load variation, the tilting moment (a product of the eccentricity and the gyratory force) of different HMA mixtures was determined and presented in Figure 7.8. The tilting moments are plotted against the internal gyration angles in Figure 7.9. Like the eccentricity, the tilting moment had a poor correlation with the internal gyration angle.
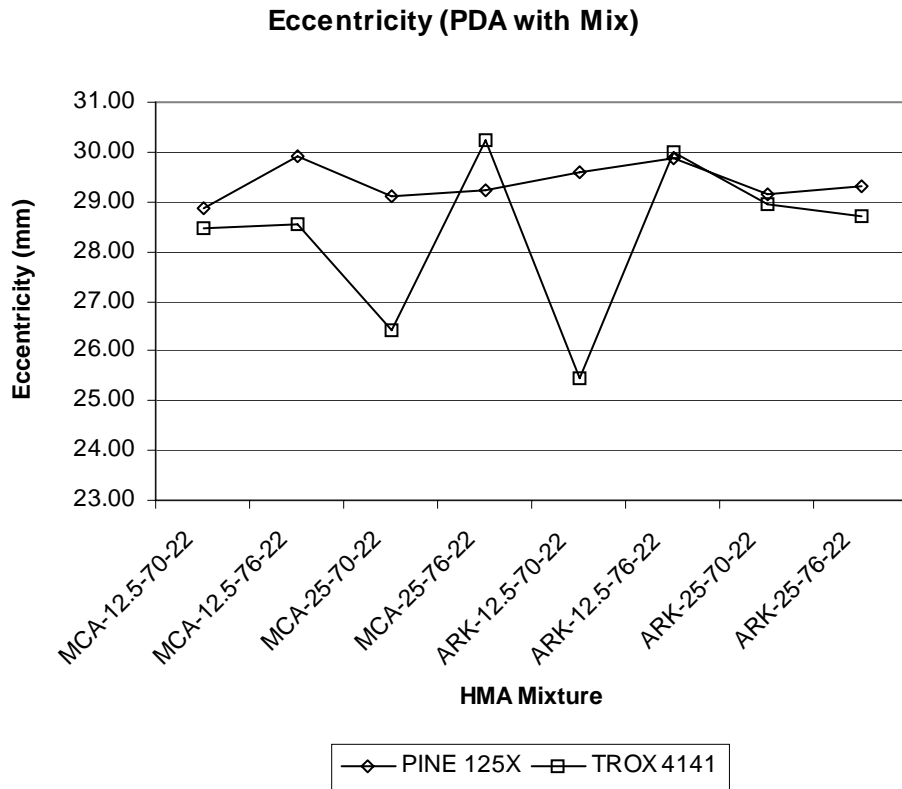
Figure 7.5. Eccentricities for Different HMA Mixtures

Figure 7.6. Standard Deviation of Eccentricities for Different Mixes
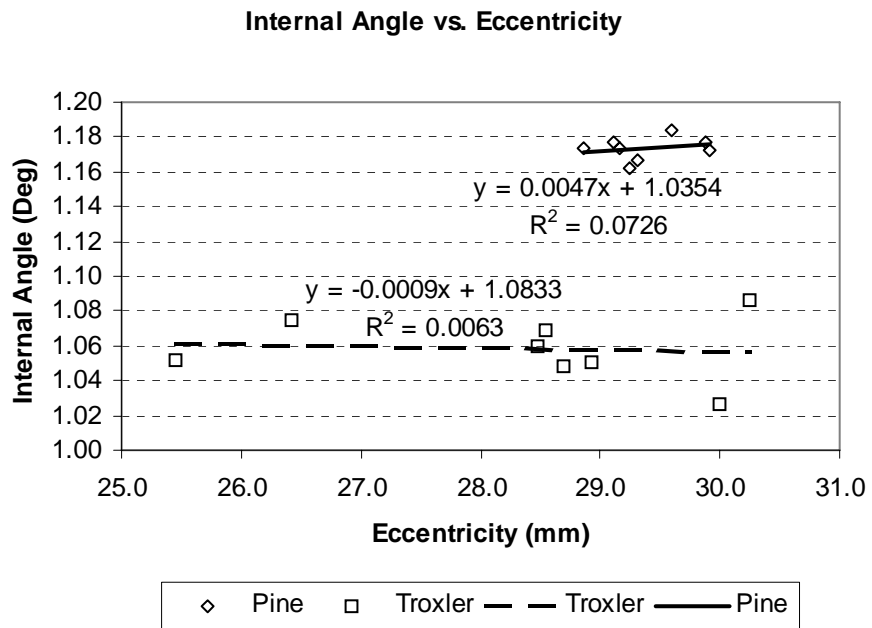
Figure 7.7. Relationship between Internal Angles and Eccentricities

Tilting Moment (PDA with Mix)
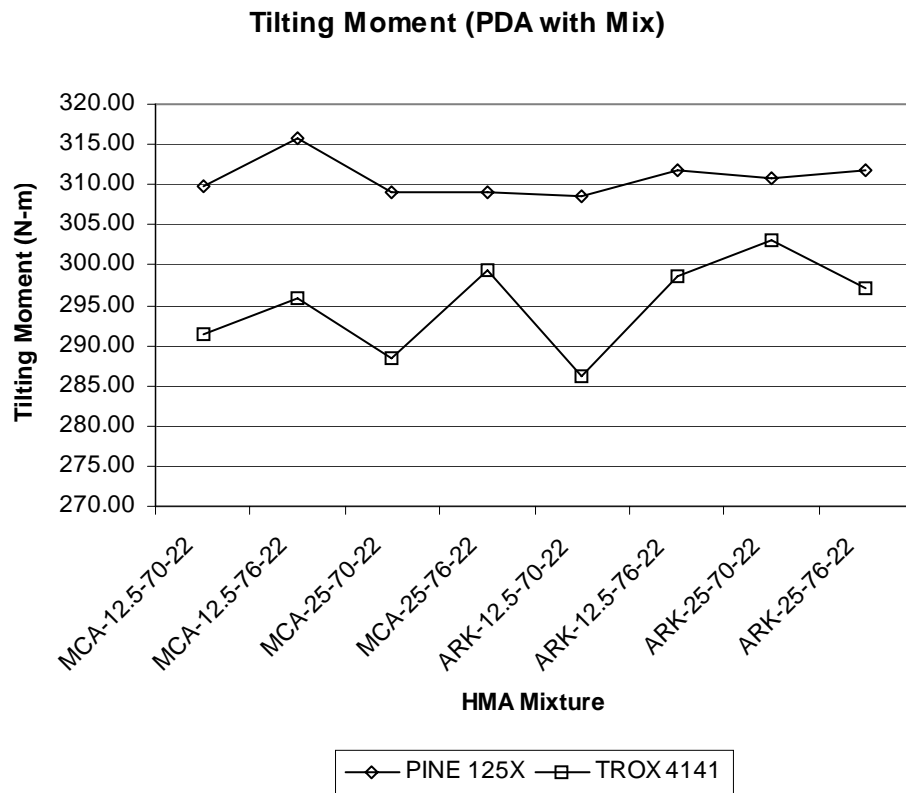
Figure 7.8. Tilting Moments for Different HMA Mixtures

Internal Angle vs. Tilting Moment
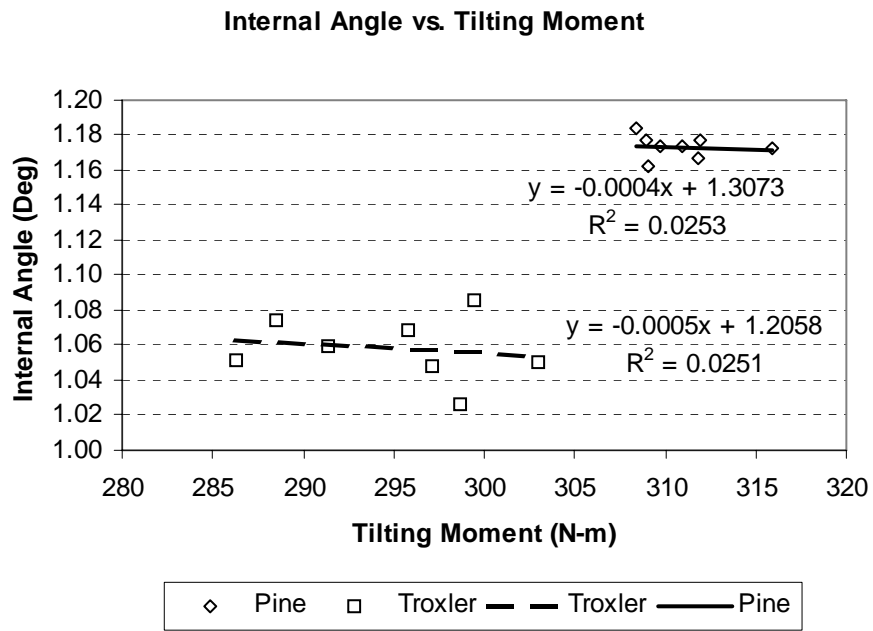
Figure 7.9. Relationship between Internal Angles and Tilting Moments

In summary, the effect of HMA mixture stiffness in term of the dynamic modulus and eccentricity/tilting moment was investigated. It was observed that the internal gyration angles had the tendency to be lower when stiffer (higher dynamic modulus) mixtures were used. In addition, the correlations between the internal angle and the eccentricity/tilting moment were very poor. Since the number of mixtures used in this study was limited, it was recommended that the aforesaid observations be further investigated.

7.2 Use of Simulated Loading Devices for Internal Angle Measurement

The internal gyration angle calibration using the DAV with mix is an effective method. However, it is considered time consuming, labor intensive and mix dependent, as presented in the aforesaid study. Therefore, a new calibration method using the simulated loading devices is desired. Two simulated loading devices available in the market are: (1) the Hot Mix Simulator (HMS) that needs to use with the DAV; and (2) the Rapid Angle Measurement (RAM) that can be used without the DAV.

The following study was designed to investigate the use of the DAV with HMS and the RAM to calibrate the internal gyration angle of SGCs. The internal gyration angles of the Pine and Troxler SGCs were measured using the DAV with HMS and the RAM.

In order to avoid data deviations caused by measurement errors, the test data were screened for outlying observations. Since only three replicates were measured for each test combination, the Dixon outlier test method, as presented in Section 7.1.1, was used.

The internal gyration angle results measured using the DAV with HMS and the RAM are presented in Appendix F. The test results are summarized in Figures 7.10 and 7.11. The figures show that the lines for the Troxler SGC were steeper than those for the Pine SGC. This means the Pine SGC frame is stiffer than that of the Troxler.

The eccentricities, which were occurred when the simulated loading devices were gyrated in the SGCs, were measured using the PDA. The detailed test results are presented in Appendix G, and the results are summarized in Figures 7.12 and 7.13. The eccentricity test results were very similar for the Pine and Troxler SGCs.

The eccentricities of the RAM can be estimated using the radius of the raised contact rings. For the 44 mm ring, the eccentricity is 22 mm, and it is 32 mm for the 64 mm ring. For the RAM, the measured and estimated eccentricities were similar.

The eccentricities of the DAV can be estimated using the moment balance equations. Figure 7.14 shows how the DAV with HMS is loaded in SGCs. It is assumed that (1) the top and bottom eccentricities are equal; (2) the top and bottom plates are parallel during the compaction. Equation 7.7 is established by balancing the moments for the top portion at point A, and Equation 7.8 is established by balancing the moments for the bottom portion at point A.

$$(e - r) \times F = L \times P \tag{7.7}$$

$$(e + r) \times F = H \times P \tag{7.8}$$

Solve Equations 7.7 and 7.8 for the eccentricity (e).

$$e = \frac{r\left(1 + \dfrac{L}{H}\right)}{1 - \dfrac{L}{H}} \tag{7.9}$$

Internal Gyration Angle vs. Cone Angle
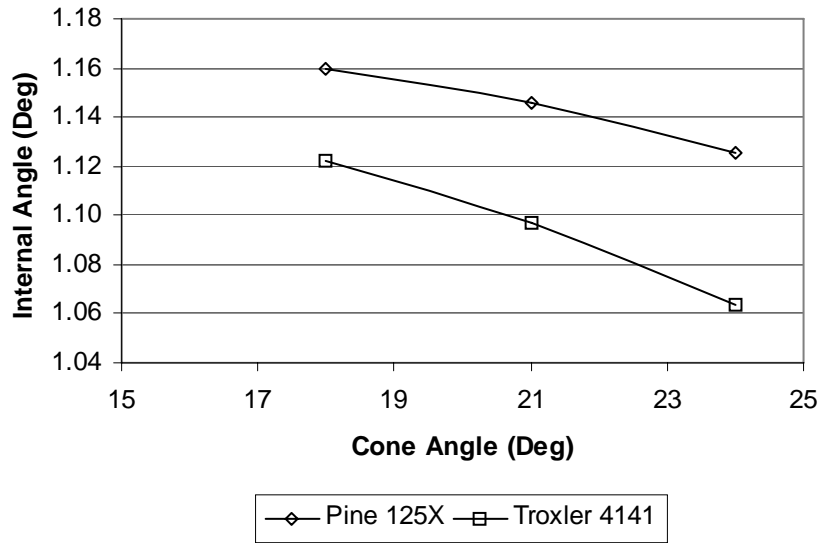
Figure 7.10. Internal Gyration Angle Measured by DAV with HMS

Internal Gyration Angle vs. Ring Diameter
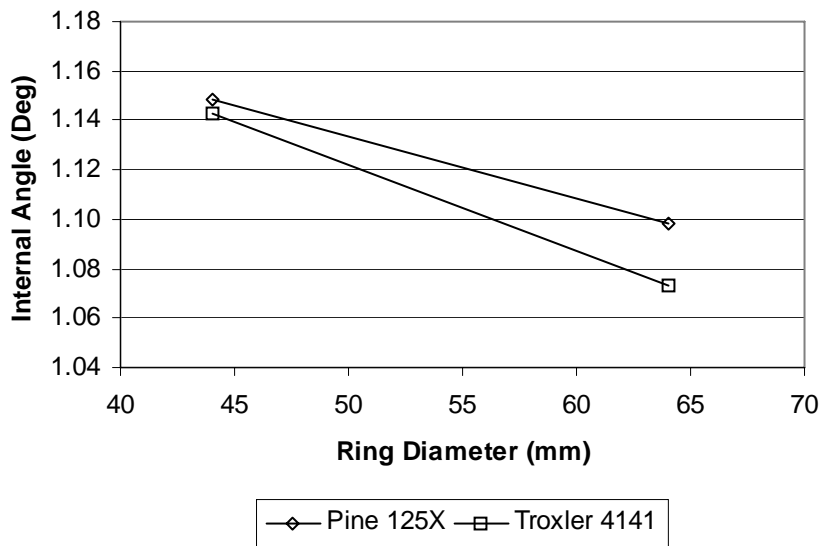
Figure 7.11. Internal Gyration Angle Measured by RAM

277

Eccentricity vs. Cone Angle
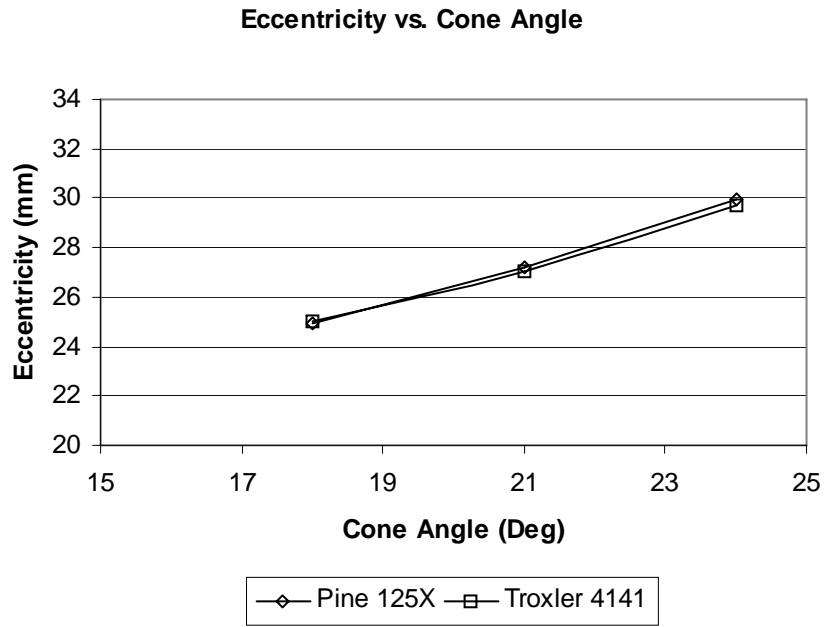
Figure 7.12. Eccentricities Measured by PDA with HMS

Eccentricity vs. Ring Diameter
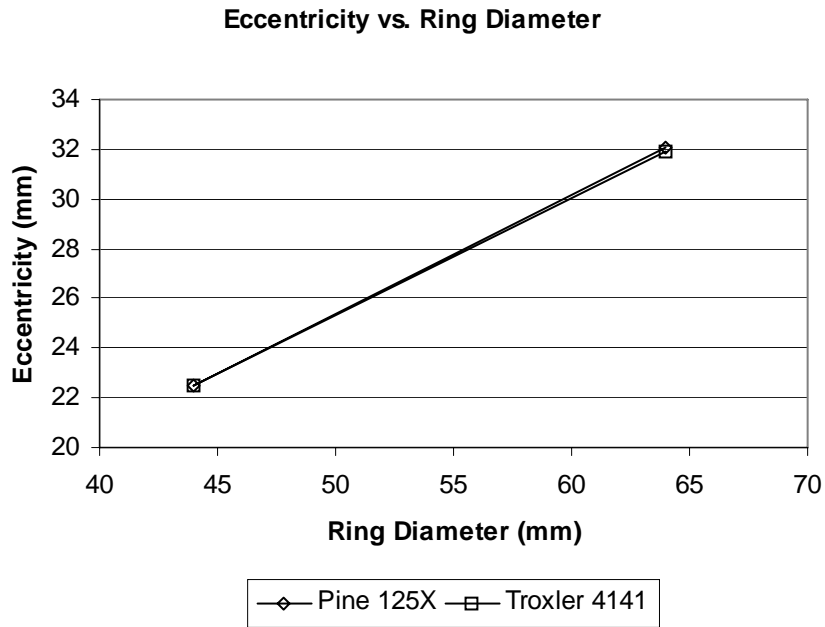
Figure 7.13. Eccentricities Measured by PDA with RAM
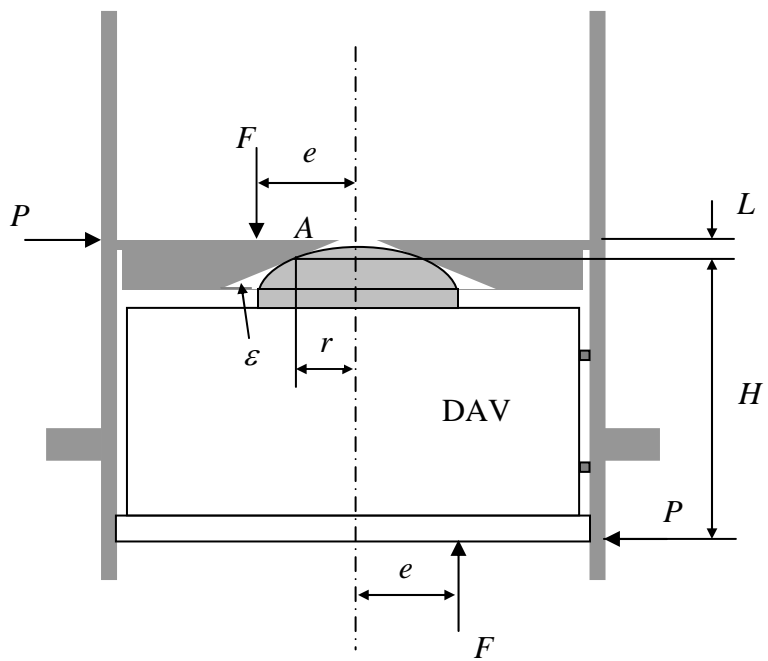
Figure 7.14. Loading Schematic for DAV with HMS

The eccentricities of the DAV with HMS estimated using Equation 7.9 are compared to the eccentricities measured using the PDA, as presented in Figure 7.15. The difference between the estimated and measured eccentricities was about 2 mm. The difference was expected because (1) the top and bottom eccentricities were not equal; and (2) the top and bottom plates were not properly parallel during compaction.

Since the use of the DAV with mix to calibrate the internal angle of gyration is time consuming, labor intensive, and mix dependent, new calibration methods of using the simulated loading devices are desired. The potential of using the simulated loading devices instead of HMA mixtures in the calibration was investigated using the following criteria:

- The internal angles of the simulated loading devices and the HMA mixture should be within the tolerance of $\pm\ 0.03^{\circ}$

- The eccentricities of the simulated loading devices and the HMA mixtures should be similar.

The internal angles of gyration of the Pine and Troxler SGCs measured using the DAV with HMS and the DAV with mix are plotted against the corresponding eccentricities in Figure 7.16. Based on Figure 7.16, the observations are as follows:

- For the Pine SGC, the average internal gyration angle and eccentricity for the DAV with mix were 1.17° and 29.4 mm, respectively. The internal angle and eccentricity for the DAV with 21° HMS were 1.15° and 27.2 mm, and those for the 24° HMS were 1.13° and 30 mm.

Estimated vs Measured Eccentricities
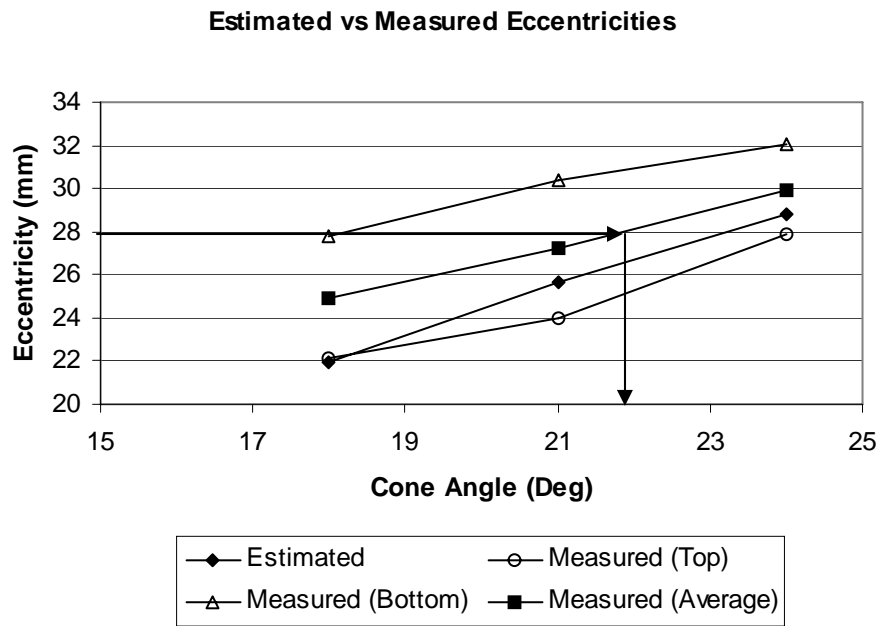
Figure 7.15. Estimated versus Measured Eccentricities
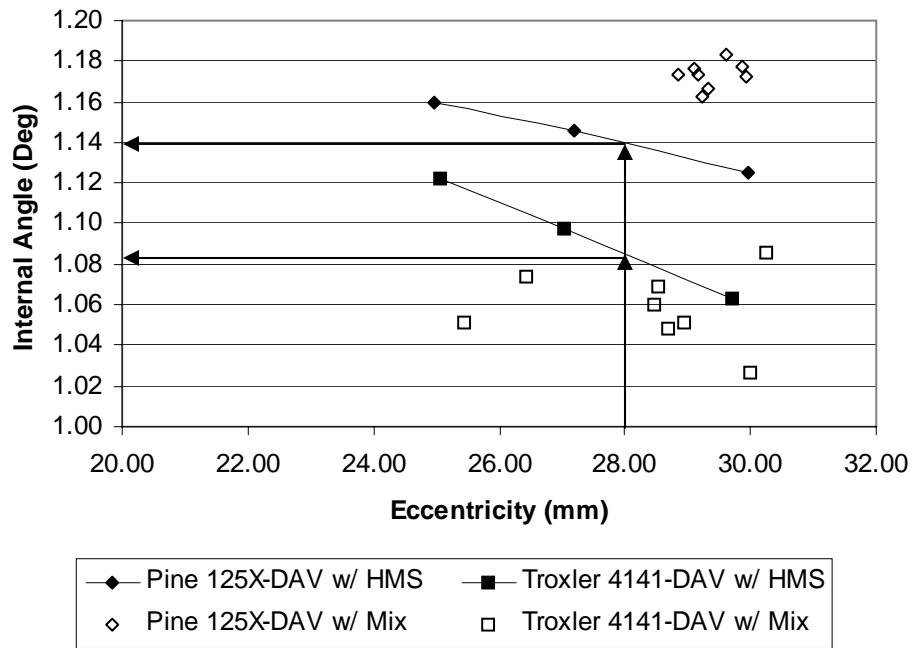
Figure 7.16. Internal Angle versus Eccentricity for DAV with HMS/Mix

- For the Troxler SGC, the average internal gyration angle and eccentricity for the DAV with mix were 1.06^o and 28.3 mm, respectively. The internal angle and eccentricity for the DAV with the 21° HMS were 1.10^o and 27 mm, and those for the 24° HMS were 1.06^o and 30 mm.

- An HMS device, whose eccentricity is 28 mm, can be used to calibrate both SGCs. As shown in Figure 7.15, this device can have 22° cone angle. Figure 7.16 shows that the internal angle for the 22° HMS device, which has 28 mm eccentricity, are 1.14^o for the Pine SGC and 1.08^o for the Troxler, which are 0.03^o and 0.02^o different from the average internal gyration angle values measured using the DAV with mix. In addition, the differences in the eccentricity are about 1 mm for the Pine and similar for the Troxler SGC. This result is similar to what reported by Harman et al. (*93*).

Figure 7.17 present the internal gyration angle values measured using the DAV with mix and the RAM. It was difficult to find a single size of the raised contact ring for the RAM to meet the aforesaid criteria. However, a study by Easley (*110*) at the University of Arkansas showed that the RAM with the 44 mm diameter raised contact ring could be used to calibrate the internal gyration angles of five different SGCs, including Pine 125X, Pine AFG1, Brovold B1, Troxler 4140A, and Troxler 4141, to produce similar mixture densities.
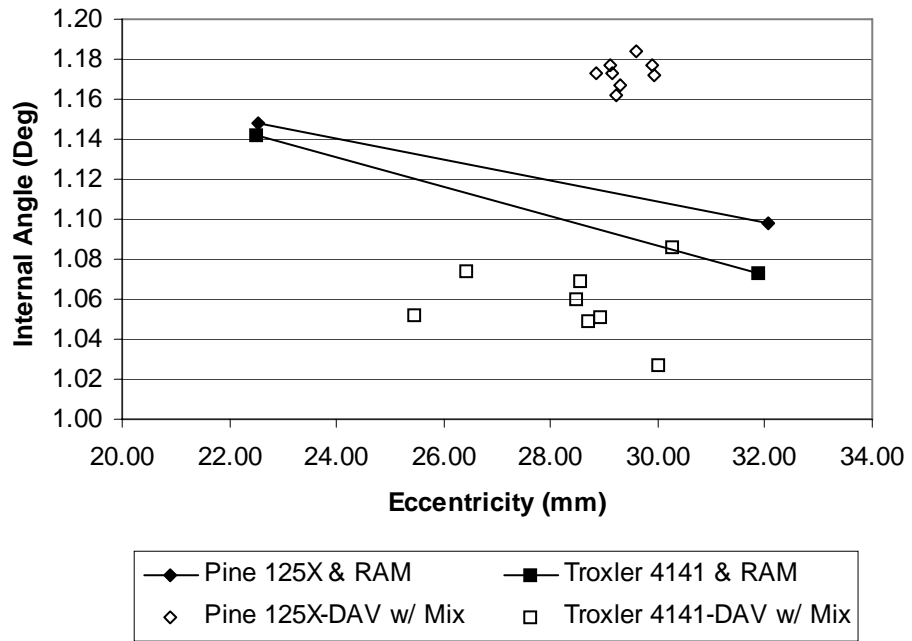
Figure 7.17. Internal Angle versus Eccentricity for DAV with Mix and RAM

7.3 Summary

This chapter presented the test results of the following studies:

- The internal angles of gyration of the Pine and Troxler SGCs measured using the DAV with eight different mixtures

- The eccentricities of the gyratory force of the Pine and Troxler measured using the PDA with the aforesaid eight mixtures

- The internal angles of the two SGCs measured using the simulated loading devices, including the DAV with HMS and the RAM

- The eccentricities of the gyratory force of the two SGCs measured using the PDA and the simulated loading devices

The analyses of the test results showed that the internal angles of gyration had the tendency to be lower in case of stiffer HMA mixtures. The correlations between the internal angle and the eccentricity/tilting moment, which represents the mix resistance to the compaction effort, were very poor. These observations need further verification since the number of mixtures used in this study was limited.

The simulated loading devices can be used to calibrate the internal gyration angles of gyratory compactors. In this study, the DAV with the 22° HMS can be used to calibrate the internal gyration angles for the Pine and Troxler SGCs within 0.03^{o} and 0.02^{o} different from the values measured using the DAV with mix.

This study was not able to determine a single size of the raised contact ring for the RAM to calibrate the two SGCs. However, a study by Easley (*110*) showed that the 44 mm diameter raised contact ring can be used for the RAM to calibrate five different SGCs.

285

CHAPTER 8: SUMMARY, CONCLUSIONS AND RECOMMENDATIONS

8.1 Summary

8.1.1 Research Objectives

The objectives of this project were:

- To develop a dynamic modulus database and determine the data variability for level 1 $|E^*|$ inputs in the M-E Design Guide;

- To evaluate the Witczak predictive equation for level 2 and 3 inputs in the Guide;

- To identify the appropriate $|E^*|$ input level for initial implementation of the Guide;

- To investigate the effects of HMA mixture stiffness on the associated internal angles of gyration; and

- To evaluate the potential of using the simulated loading devices for the calibration of SGCs.

8.1.2 Testing Programs

Two major testing programs were performed in this project. One testing program involved in the dynamic modulus testing, and the other program dealt with the internal gyration angle of SGCs. The testing program for the dynamic modulus used 21 HMA mixtures based on four aggregate sources, three aggregate sizes, and two binder grades. Three replicates for each HMA mixture were prepared at optimum binder content. After the mixtures were compacted to 150 mm diameter and 170 mm height at two air void levels, the test specimens, 100 mm diameter and 150 mm height, were

cored and end-cut from the compacted samples. The test specimens were inspected in terms of geometric dimensions and air voids before the dynamic modulus testing.

The dynamic modulus test was performed at five temperatures, including -10, 4.4, 21.1, 37.8, and 54.4C (14, 40, 70, 100, and 130F), and six frequencies, including 25, 10, 5, 1, 0.5, 0.1 Hz, on each test specimen. The test was performed from low to high temperatures and from high to low frequencies. The raw dynamic modulus test data were acquired and stored for analyses.

The second testing program included:

- Determining the internal angles of gyration using the DAV with mix;

- Obtaining the internal angles of gyration using the simulated loading devices, including the DAV with HMS and the RAM; and

- Determining the eccentricities of the gyratory force using the PDA with mix or the PDA with the simulated loading devices.

The testing program for the internal angle of gyration used eight HMA mixtures from two aggregate sources, two aggregate sizes, and two binder grades. Two SGCs, including Pine 125X and Troxler 4141, were employed for this study. The Pine SGC was calibrated to the internal gyration angle of 1.17^o, which is within the internal angle specification range of $1.16^o \pm 0.03^o$, whereas the Troxler SGC had the internal gyration angle of 1.06^o.

Since the molds of the Pine SGC can handle the DAV and the mixture for a full height (115 mm) specimen, three top and three bottom internal angles of gyration were determined using the DAV placed on top or bottom of the full height specimens. However, the molds for the Troxler SGC are not tall enough for the DAV and the

mixture for a full height specimen, the top or bottom internal gyration angles for the full height specimens were determined from the angles for two shorter specimens using the linear extrapolation method. Three internal angles of gyration for each mixture and SGC were the averages of the top and bottom internal gyration angles.

The internal angles of gyration for each SGC were also determined using the simulated loading devices, including the DAV with HMS and the RAM. The top and bottom internal angles of gyration were measured using the DAV with three HMS cone angles, including 18, 21 and 24°, or using the RAM with two raised contact ring sizes, including 44 and 64 mm diameter. The internal gyration angles were then the mean of the top and bottom angles.

The eccentricities of the gyratory force were determined using the PDA with the eight HMA mixtures used in the internal angle study. The top and bottom eccentricities were measured with the PDA placed on top and bottom of the mixture. The top and bottom eccentricities were also measured using the PDA with the simulated loading devices. The average of the top and bottom eccentricities was used for further analyses.

8.1.3 Laboratory Dynamic Modulus Test Results and Analyses

The raw data acquired from the dynamic modulus testing, including recording time, loading magnitude, and displacements of the LVDTs, were used to determine the dynamic moduli and phase angles of the mixture in question using the DYNMOD program. The DYNMOD was developed in this project to fit the loading and displacement curves to the test data based on the numerical optimization method. The

dynamic modulus and phase angle were then determined based on the loading and displacement data obtained from the curves.

After the dynamic modulus and phase angle values were determined, the variability of the test results was analyzed. The variability analysis included:

- ANOVA tests to determine if the test results contained any errors caused by the measurement device defects; and

- The variability of the test results in term of the coefficient of variation.

The dynamic modulus test results were also used for developing the subsequent master curves for each HMA mixture. The master curves were constructed using a spreadsheet developed in this project. The spreadsheet used the Solver function in Microsoft Excel® to fit the master curve sigmoidal function to the associated test data.

Finally, the dynamic modulus database included:

- The dynamic modulus test results presented in the form specified for level 1 inputs in the Design Guide; and

- The master curves for each HMA mixture tested in this project.

8.1.4 Dynamic Modulus Prediction

The dynamic modulus test is relatively complex and expensive to perform, so it is desirable to predict the dynamic modulus from the mixture volumetric properties. The dynamic modulus can be estimated using the Witczak or Hirsch predictive equation. The Witczak predictive equation is incorporated in the Design Guide as part of level 2 and 3 $|E^*|$ inputs.

The Witczak equation was evaluated using the dynamic modulus test results obtained in this study. The accuracy of the equation was evaluated using the goodness-of-fit statistics, including lack of fit statistic, S_e/S_y, and correlation coefficient, R^2. The bias of the equation was assessed using the graphs of prediction errors versus mixture properties, test parameters, and predicted $|E^*|$ values. Finally, the effects of the $|E^*|$ prediction errors on the pavement performance, such as rutting and fatigue cracking were evaluated.

The mixtures used in this study would not cover all HMA mixtures available in Arkansas, so many HMA mixtures used in the future would not be the same as those studied in this project. To help designers decide whether those mixtures can be used in the design with reasonable effects on predicted pavement performance, a sensitivity analysis was performed in this research. In this study, the changes of the predicted dynamic modulus values caused by the changes of each variable in the Witczak prediction model were evaluated.

8.1.5 Internal Gyration Angle Study

The results obtained from the internal angle study program included:

- The internal gyration angles of the Pine and Troxler SGCs measured using the DAV with mix;

- The eccentricities of the gyratory force of the Pine and Troxler measured using the PDA with mix;

- The internal angles of the two SGCs measured using the simulated loading devices, including the DAV with HMS and the RAM; and

- The eccentricities of the gyratory force of the two SGCs measured using the PDA and the simulated loading devices.

The aforesaid test data were screened for outlying observation using the Dixon procedure. In order to investigate the effects of the mix stiffness in terms of the dynamic modulus and eccentricity of the gyratory force on the internal gyration angle measurements using the DAV with mix, the following test data were used:

- The internal gyration angles measured using the DAV with mix;

- The dynamic modulus values of the mixtures used in the internal gyration angle study; and

- The eccentricities of the gyratory force measured using the PDA with mix.

The correlation between the internal angles and the mix stiffness was determined using the simple linear regression. The potential of using the simulated loading devices for the internal gyration angle calibration was evaluated using all of the data listed at the beginning of this section. The evaluation criteria are as follows:

- The internal angles of the simulated loading devices and the HMA mixture should be within the tolerance of $\pm 0.03^{\circ}$

- The eccentricities of the simulated loading devices and the HMA mixtures should be similar.

The conclusions based in the aforesaid analyses are presented in the following section.

8.2 Conclusions

The conclusions drawn from the analyses of the dynamic modulus test results are as follows:

- Among different approaches recommended in the AASHTO TP 62-03 to determine the peak stress and peak strain from the raw data acquired from the dynamic modulus testing, the curve fitting technique using the numerical optimization method was relatively easy to accomplish using a spreadsheet. The DYNMOD program developed in this project using the curve fitting technique was an excellent tool to calculate the dynamic modulus and phase angle values from the raw test data.

- The statistical analyses of the LVDT measurements showed that the differences between the LVDT responses were not significant. In addition, the testing order of the replicates was randomized, so the testing order should not be a sensitive factor in the test variability. Therefore, the dynamic modulus test results obtained in this project have no defects caused by the test measurement errors.

- The variability of the dynamic modulus test results was evaluated using the coefficients of variation, which is capable of normalizing the test variability across the test temperatures and frequencies. Two types of coefficient of variation were determined: (1) the "within" coefficient of variation that measured the variability between the individual LVDT measurements in a specimen; and (2) the "between" coefficient of variation that measured the variability between the average parameters of the replicates. The effects of

mixture properties and test parameters on the variability of the test results
are as follows:

- o The "within" and "between" coefficients of variation were higher with
  increasing nominal maximum aggregate size;

- o The "within" coefficients of variation were higher with increasing air
  void content; and

- o The test variability was higher at higher temperatures or higher
  frequencies. The differences between the lowest and highest coefficients
  of variation for both temperature and frequency sweeps were about 1.5
  percent for "within" values and about 0.6 percent for "between" values.

- The variability of the test results obtained in this study were much lower
  than those in other studies (*73,75,84*). However, it was noted that other
  studies used a different testing program that featured two replicate
  specimens instrumented with two LVDTs per specimen, compared to three
  replicates instrumented with four LVDTs used in this study.

- The confidence interval of the dynamic modulus test results was calculated
  based on the CVs. The average 95-percent confidence interval for the
  dynamic modulus test results obtained in this study was ±13.56 percent,
  which was less than the required value of ±15 percent, as specified in
  AASHTO TP 62-03.

- The dynamic modulus test results can be presented using the master curves.
  The master curves can be used to determine the dynamic modulus in a
  broaden range of frequency and temperature without performing a complex

testing program. The master curves of the test data were constructed using a spreadsheet developed in this project based on the sigmoidal function developed at the University of Maryland (*73*), and the sigmoidal function fits the test data very well.

- The final product of the laboratory dynamic modulus test program was the dynamic modulus and phase angle values measured at five temperatures and six frequencies and the subsequent master curves. The dynamic modulus values were presented in the preset form for level 1 input of the M-E Design Guide.

The laboratory dynamic modulus test results were used to evaluate the Witczak predictive equation, and the analysis results are as follows:

- Overall, the predicted dynamic modulus values agreed quite well with the laboratory measured dynamic modulus values. The evaluation statistics for level 2 $|E^*|$ inputs were even better than the calibrated statistics ($R^2 = 0.886$ and $S_e/S_y = 0.338$ in arithmetic space), and those for level 3 $|E^*|$ inputs compared favorably to the calibrated statistics.

- It was observed that comparing to level 1 inputs, level 2 predicted dynamic modulus values were more accurate than those of level 3, and the dynamic modulus for HMA mixtures was slightly over predicted using level 3 inputs.

- Even though level 2 inputs seemed to predict the dynamic modulus values better than level 3, further investigation showed that both input levels overpredicted the dynamic modulus of the mixtures at high temperatures

(compared to test results). These systematic errors (bias) may influence predicted pavement performance.

The M-E Design Guide 2002 design software (version 0.007) was used to investigate the effects of level 2 and 3 |E*| predictions on predicted pavement performance, and the investigation results are as follows:

- Based on the analyses of predicted pavement performance using the measured and predicted dynamic modulus values, the differences between level 2 and 3 predicted distresses were not significant.

- The pavement distresses predicted using the predicted |E*| inputs were relatively close to those using the measured |E*| inputs.

Since many mixtures used in the future would not be the same as those studied in this project, the sensitivity analysis of the inputs of the Witczak equation was performed to help designers determine the effects of the mixture changes on predicted pavement performance. The sensitivity analysis results are as follows:

- The sensitivity analysis showed that the test temperature is the most sensitive factor to the predicted dynamic modulus. Increasing test temperature from the lowest [-10C (14F)] to the highest [54C (130F)] caused 367 percent change in |E*|.

- Among volumetric properties, air void content is the most sensitive factor, but its variation through its range just causes up to 20 percent change in the predicted |E*|. In contrast, percent retained on No. 4 sieve seems to be a moderately sensitive factor, but its variation through its range can cause up to 50 percent change in the predicted |E*|. Therefore, the influence of a mix

parameter on predicted $|E^*|$ should be determined based on the combination of the parameter variation range and sensitivity. This issue was also addressed by Schwartz (*107*).

- Based on the sensitivity analysis results, the Witczak model exhibits some errors in predicting the dynamic modulus across test temperatures and does not account for the interaction effects between air voids and test temperature. This observation helps partially explain the prediction errors of the Witczak model at high temperatures.

The conclusions based on the internal gyration angle study are as follows:

- The internal angles of gyration had the tendency to be lower when stiffer HMA mixtures, which have higher dynamic modulus, were used for the internal gyration angle calibration.

- The eccentricity of gyratory force and the tilting moment had very poor correlations with the internal angle.

- The DAV with the 22° HMS can be used to calibrate the internal gyration angles for the Pine and Troxler SGCs. The internal gyration angles measured using the DAV with the 22° HMS were within 0.03^o from the values measured using the DAV with mix.

- This study was not able to find the raised contact ring for the RAM to equal the internal angles measured using the RAM to the values measured using the DAV with mix.

8.3 Recommendations

Based on the aforesaid conclusions, the recommendations are as follows:

- A testing program featuring three replicate specimens instrumented with four LVDTs per specimen is recommended for the future dynamic modulus testing.

- Based on the variability analyses of the dynamic modulus test results, it is recommended that the dynamic modulus values obtained in this study be used for level 1 $|E^*|$ inputs in the M-E Design Guide.

- Based on the evaluation of the Witczak predictive equation, level 3 $|E^*|$ input can be used instead of level 1 and 2 $|E^*|$ inputs for initial implementation of the M-E Design Guide. However, the effects of the dynamic modulus predictions on predicted pavement performance should be re-evaluated when the performance data of in-service pavements become available.

- It is recommended that the design software add a new feature that allows the users to input state/regional calibration factors for the Witczak predictive model incorporated in level 3 predicted dynamic modulus inputs. This feature would be useful for many states in which the Witzcak predictive model requires some modifications to reasonably predict the dynamic modulus of local HMA mixtures.

- The potential of using the DAV with the 22° HMS to calibrate the internal angle of gyration should be further studied.

- It is recognized that the dynamic modulus test results obtained in this project were based on the laboratory compacted specimens. A new plant-mixed specimen study is highly recommended.

REFERENCES

1. 2002 Design Guide Draft, "Development of the 2002 Guide for the Design of New and Rehabilitated Pavement Structures." NCHRP Project 1-37A, 2003.

2. Andrei, D., Witczak, M.W., and Mirza, M.W., "Development of a Revised Predictive Model for the Dynamic (Complex) Modulus of Asphalt Mixtures." NCHRP Project 1-37A, Appendix CC-4, 1999.

3. Al-Khateeb, G., Paugh, C., Stuart, K., Harman, T., and D'Angelo, J., "Target and Tolerance Study for Angle of Gyration used in Superpave Gyratory Compactor." *Transportation Research Record 1789*, 2002.

4. Prowell, B.D., Brown, E.R., and Hunter, M.H., "Evaluation of the Internal Angle of Gyration of Superpave Gyratory Compactors in Alabama." *Journal of Association of Asphalt Paving Technologists*, Vol. 72, 2003.

5. Hall, K.D., and Easley, T., "Establishment of the Precision of the Rapid Angle Measurment (RAM) Device for Superpave Gyratory Compactors." *Submitted to the Transportation Research Board*, 2004.

6. Asphalt Institute, *Superpave Mix Design (SP-2)*. Kentucky, 1996.

7. Kandhal, P.S., Cross, S.A., and Brown, E.R., "Heavy Duty Asphalt Pavements in Pennsylvania: Evaluation for Rutting." *Transportation Research Record 1384*, 1993.

8. Brown, E.R., and Cross, S.A., "A National Study of Rutting in Asphalt Pavement." *Journal of Association of Asphalt Paving Technologists*, Vol. 61, 1992.

9. Asphalt Institute, *Performance Graded Asphalt Binder Specification and Testing (SP-1)*. Third Edition, Kentucky, 2003.

10. American Association of State Highway and Transportation Officials (AASHTO), "Standard Specification for Superpave Volumetric Mix Design", AASHTO MP 2-03 (2003).

11. American Association of State Highway and Transportation Officials (AASHTO), "Standard Practice for Superpave Volumetric Design for Hot-Mix Asphalt (HMA)", AASHTO PP 28-00, 2000.

12. *Standard Specifications for Highway Construction*, Arkansas State Highway and Transportation Department, Little Rock, Arkansas, 2003.

13. Kandhal, P.S., and Parker, F., "Aggregate Tests Related to Asphalt Concrete Performance in Pavements." *NCHRP Report 405*, Transportation Research Board, National Research Council, Washington, D.C., 1998.

14. Parker, F., and Brown, E.R., "Effects of Aggregate Properties on Flexible Pavement Rutting in Alabama." *Asphalt Mixture Performance*, Richard C. Meininger, Editor. ASTM STP 1147, 1992.

15. Dukatz, E.L., "Aggregate Properties Related to Pavement Performance." *Journal of Association of Asphalt Paving Technologists*, Vol. 58, 1989.

16. Meier, W.R., Elnicky, E.J., and Schuster B.R., "Fine Aggregate Shape and Surface Texture." *FHWA-A288-229*, Arizona DOT, Lansing, 1979.

17. Kalcheff, I.V., and Tunnicliff, "Effects of Crushed Stone Aggregate Size and Shape on Properties of Asphalt Concrete." *Journal of Association of Asphalt Paving Technologists*, Vol. 51, 1982.

18. Cheung, L.W, and Dawson, A.R., "Effects of Particles and Mix Characteristics on Performance of Some Granular Materials." *Transportation Research Record 1787*, 2002.

19. Moore, R.B., and Welke, R.A. "Effects of Fine Aggregate on Stability of Bituminous Mixes." *Research Report 78 TB-34-79F*, Testing and Research Division, Michigan DOT, 1979.

20. Field, F., "The Importance of Percent Crushed in Coarse Aggregate as Applied to Bituminous Pavements." *Journal of Association of Asphalt Paving Technologists*, Vol. 27, 1958.

21. Purcell, EM, and Cross, S.A., "Effects of Aggregate Angularity on VMA and Rutting of KDOT Superpave Level 1 Mixes." *Research Report K_TRAN: KU-98-5*. Kansas DOT, 2001.

22. Huber, G.A., Jones, J.C., Messersmith, and Jackson, N.M., "Contribution of Fine Aggregate Angularity and Particle Shape to Superpave Mixture Performance." *Transportation Research Record 1609*, 1998.

23. Wedding, P.A., and Gaynor, R.D., "The Effects of Using Crushed Gravel as the Coarse and Fine Aggregate in Dense Graded Bituminous Mixtures." *Journal of Association of Asphalt Paving Technologists*, Vol. 30, 1961.

24. Park, D.W., Chowdhury, A., and Button J., "Effects of Aggregate Gradation and Angularity on VMA and Rutting Resistance." *Research Report 201-3F,* Texas Transportation Institute, Texas A&M University, 2001.

25. Buchanan, S.M., "Evaluation of the Effect of Flat and Elongated Particles on the Performance of Hot-Mix Asphalt Mixes." *NCAT Report 2000-03*, Auburn University, 2000.

26. Schrimsher, T., "Baghouse Dust and its Effect on Asphaltic Mixtures." *Research Report CA-DOT-TL-3140-1-76-50,* California DOT, 1976.

27. Anderson, D.A., Bahia, H.U., and Dongre R., "Rheological Properties of Mineral Filler - Asphalt Mastics and its Importance to Pavement Performance." *American Society for Testing and Materials*, STP 1147, 1992.

28. Anderson, D.A., Dongre, R., Christensen, D.W., and Dukatz, E.L., "Effects of Minus 200 Sized Aggregate in Fracture Behavior of Dense-Graded Hot Mix Asphalt." *American Society for Testing and Materials*, STP 1147, 1992.

29. Kandhal, P.S., and Cross, S.A., "Effects of Aggregate Gradation on Measured Asphalt Content." *Transportation Research Record 1417*, 1993.

30. Roberts, F.L., Kandhal, P.S., Brown, E.R., Lee, D. and Kennedy, T.W., *Hot Mix Asphalt Materials, Mixture Design, and Construction*. Second Edition. NAPA Education Foundation, Maryland, 1996.

31. Kamel, N.I., and Miller, L.J., "Comparative Performance of Pavement Mixes Containing Conventional and Engineered Asphalts." *Transportation Research Record 1454*, 1994.

32. Qi, X., Sebaaly, P.E., Epps, J.A., "Evaluation of Polymer-Modified Asphalt Concrete Mixtures." *Journal of Materials in Civil Engineering*, Vol. 7, Issue 2, 1995.

33. Brown, E.R., Collins, R., and Brownfield, J.R., "Investigation of Segregation of Asphalt Mixtures in State of Georgia." *Transportation Research Record 1217*, 1989.

34. Santucci, L.E., Allen, D.D., and Coats, R.L., "The Effects of Moisture and Compaction on Quality of Asphalt Pavements." *Journal of Association of Asphalt Paving Technologists*, Vol. 54, 1985.

35. Brown, E.R., and Cross, S., "A Study of In-Place Rutting of Asphalt Pavements." *Journal of Association of Asphalt Paving Technologists*, Vol. 58, 1989.

36. Huber, G.A., and Herman, G.H., "Effect of Asphalt Concrete Parameters on Rutting Performance: A Field Investigation." *Journal of Association of Asphalt Paving Technologists*, Vol. 56, 1987

37.   Kandhal, P.S., Foo, K.Y., and Mallick, R.B., "A Critical Review of VMA Requirements in Superpave." *NCAT Report No. 98-1*, National Center for Asphalt Technology, 1998.

38.   Anderson, R.M., and Bentsen, R.A., "Influence of Voids in the Mineral Aggregate (VMA) on the Mechanical Properties of Coarse and Fine Asphalt Mixtures." *Journal of Association of Asphalt Paving Technologists*, Vol. 70, 2001.

39.   Nukunya, B., Roque, R., Tia M., and Birgisson, B., "Evaluation of VMA and Other Volumetric Properties as Criteria for the Design and Acceptance of Superpave Mixtures." *Journal of Association of Asphalt Paving Technologists*, Vol. 70, 2001.

40.   Coree, B.J., and Hislop, W.P., "A Laboratory Investigation into the Effects of Aggregate-Related Factors of Critical VMA in Asphalt Paving Mixtures." *Journal of Association of Asphalt Paving Technologists*, Vol. 70, 2001.

41.   Hinrichsen, J.A., and Heggen, J., "Minimum Voids in Mineral Aggregate in Hot-Mix Asphalt Based on Gradation and Volumetric Properties." *Transportation Research Record 1545*, 1996.

42.   Kandhal, P.S., and Chakraborty, S., "Evaluation of Voids in the Mineral Aggregate for HMA Paving Mixtures." *NCAT Report No. 96-4*, National Center for Asphalt Technology, 1996.

43.   Stiady, J.L., Hand, A.J.T., Noureldin, A.S., Galal, K., Hua, J., and White, T.D., "Validation of SHRP Asphalt Mixture Specifications Using Accelerated Testing." *National Pooled Fund Study No. 176 Final Report*, Indiana DOT, 2003.

44.   Anderson, R.M., Turner, P.A., Peterson, R.L., and Mallick, R.B., "Relationship of Superpave Gyratory Compaction Properties to HMA Rutting Behavior." *NCHRP Report 478*, Transportation Research Board, National Research Council, Washington, D.C., 2002.

45.   D'Angelo, J., Harman, T.P., and Paugh, C.W., "Evaluation of Volumetric Properties and Gyratory Compaction Slope for the Quality Control of Hot-Mix Asphalt Production." *Journal of Association of Asphalt Paving Technologists*, Vol. 70, 2001.

46.   Anderson, R.M., Christensen, D.W., and Bonaquist, R., "Estimating the Rutting Potential of Asphalt Mixtures Using Superpave Gyratory Compaction Properties and Indirect Tensile Strength." *Journal of Association of Asphalt Paving Technologists*, Vol. 72, 2003.

47. Bahia, H.U., Hanson, D.I., Zeng, M., Zhai, H., Khatri, M.A., and Anderson R.M., "Characterization of Modified Asphalt Binders in Superpave Mix Design." *NCHRP Report 459*, Transportation Research Board, National Research Council, Washington, D.C., 2001.

48. American Association of State Highway and Transportation Officials (AASHTO), "Test Method for Determining Rheological Properties of Asphalt Binder Using a Dynamic Shear Rheometer (DSR)", AASHTO TP5.

49. American Association of State Highway and Transportation Officials (AASHTO), "Viscosity Determination of Asphalt Binder Using Rotational Viscometer", AASHTO T316.

50. American Association of State Highway and Transportation Officials (AASHTO), "Test Method for Determining the Flexural Creep Stiffness of Asphalt Binder Using the Bending Beam Rheometer (BBR)", AASHTO TP1.

51. American Association of State Highway and Transportation Officials (AASHTO), "Test Method for Determining the Fracture Properties of Asphalt Binder in Direct Tension (DT)", AASHTO TP3.

52. McGennis, R.B., Shuler, S., and Bahia, H.U., "Background of Superpave Asphalt Binder Test Methods." *Report No. FHWA-SA-94-069*, FHWA, 1994.

53. American Society for Testing and Materials (ASTM), "Viscosity-Temperature Chart for Asphalts," ASTM D2493, *Annual Book of ASTM Standard*, Vol. 0.403, 2002.

54. Uzan, J., "Asphalt Concrete Characterization for Pavement Performance Prediction." *Journal of Association of Asphalt Paving Technologists*, Vol. 65, 1996.

55. Lytton, R.L., Uzan, J., Fernando, E.G., Roque, R., Hiltunen, D., Stoffels, S.M., "Development and Validation of Performance Prediction Models and Specifications for Asphalt Binders and Paving Mixes." *SHRP-A-357*, National Research Council, Washington, D.C., 1993.

56. Goodrich, J.L., "Asphaltic Binder Rheology, Asphalt Concrete Rheology, and Asphalt Concrete Mix Properties." *Journal of Association of Asphalt Paving Technologists*, Vol. 60, 1991.

57. Pellinen, T.K., and Witczak, M.W., "Stress Dependent Master Curve Construction for Dynamic (Complex) Modulus." *Journal of Association of Asphalt Paving Technologists*, Vol. 71, 2002.

58. Christensen, D., "Analysis of Creep Data from Indirect Tension Test on Asphalt Concrete." *Journal of Association of Asphalt Paving Technologists*, Vol. 67, 1998.

59. Huang, Y.H., *Pavement Analysis and Design*. Prentice Hall, New Jersey, 1993.

60. Witczak, M.W., Kaloush, K., Pellinen, T., El-Basyouny, M., and Von Quintus, H., "Simple Performance Test for Superpave Mix Design." *NCHRP Report 465*, Transportation Research Board, National Research Council, Washington, D.C., 2002.

61. Schapery, R.A., "Viscoelastic Behavior and Analysis of Composite Materials." *Mechanics of Composite Materials*, Vol. 2, G. Sedeckyj (Ed.), Academic, New York, 1974.

62. Christensen, R.M., *Theory of Viscoelasticity*, Second Edition. Academic, New York, 1982.

63. Park, S.W., and Kim, Y.R., "Interconversion Between Relaxation Modulus and Creep Compliance for Viscoelastic Solids." *Journal of Materials in Civil Engineering*, Vol. 11, No. 1, 1999.

64. Papazian, H. S., "The Response of Linear Viscoelastic Materials in the Frequency Domain with Emphasis on Asphaltic Concrete." *1st International Conference on the Structural Design of Asphalt Pavement*, 1962.

65. Witczak, M. W., and Root, R. E., "Summary of Complex Modulus Laboratory Test Procedures and Results." *Fatigue and Dynamic Testing of Bituminous Mixtures, ASTM STP 561*, American Society for Testing and Materials, 1974.

66. Bonnaure, F., Gest, G., Grabois, A., and Uge, P., "A New Method of Predicting the Stiffness of Asphalt Paving Mixtures." *Association of Asphalt Paving Technologists*, Vol. 46, 1977.

67. Francken, L., Partl, M., and Technical Committee on Bitumen and Asphalt Testing, "Complex Modulus Testing of Asphalt Concrete: RILEM Interlaboratory Test Program." *Transportation Research Record 1545*, 1996.

68. Zhang, W., Drescher, A., and Newcomb, D. E., "Viscoelastic Behavior of Asphalt Concrete in Diametral Compression." *Journal of Transportation Engineering*, November/December 1997.

69. Drescher, A., Newcomb, D. E., and Zhang, W., "Interpretation of Indirect Tension Test Based on Viscoelasticity." *Transportation Research Record 1590*, 1997.

70. Stroup-Gardiner, M., and Newcomb, D. E., "Investigation of Hot Mix Asphalt Mixtures at MnROAD." *Minnesota Department of Transportation Final Report 97-06*, 1997.

71. Bonaquist, R.F., Christensen, D.W., and Stump, W., "Simple Performance Tester for Superpave Mix Design: First-Article Development and Evaluation." *NCHRP Report 513*, Transportation Research Board, National Research Council, Washington, D.C., 2003.

72. Witczak, M. W., Leahy, R. B., Caves, and Uzan, J., "The Universal Airport Pavement Design System, Report II: Asphaltic Mixture Material Characterization", University of Maryland, May 1989.

73. Witczak, M.W., Bonaquist, R., Von Quintus, H., and Kaloush K., "Specimen Geometry and Aggregate Size Effects in Uniaxial Compression and Constant Height Shear Tests." *Journal of the Association of Asphalt Paving Technologists*, Vol. 69, 2000.

74. American Association of State Highway and Transportation Officials (AASHTO), "Determining Dynamic Modulus of Hot-Mix Asphalt Concrete Mixtures", AASHTO TP 62-03, 2004.

75. Pellinen, T.K., *Investigation of the Use of Dynamic Modulus as an Indicator of Hot-Mix Asphalt Performance*, Ph.D. Dissertation, Arizona State University, 2001.

76. Zhao, Y., and Kim, Y.R., "Time-Temperature Superposition for Asphalt Mixtures with Growing Damage and Permanent Deformation in Compression" *Transportation Research Record 1832*, 2003.

77. Williams, M. L., Landel, R. F., and Ferry, J. D., "The Time Temperature Dependence of Relaxation Mechanism in Amorphous Polymers and Other Glass Liquids", *Journal of American Chemical Society*, Vol. 77, 1955.

78. Witczak, M.W., and Bari, J., "Development of A Master Curve (E*) Database for Lime Modified Asphaltic Mixtures." *Arizona State University Research Project Report*, 2004.

79. Witczak, M. W., and Fonseca, O. A., "Revised Predictive Model for Dynamic (Complex) Modulus of Asphalt Mixtures", *Transportation Research Record 1540*, 1996.

80. Hirsch, T.J., *The Effects of the Elastic Moduli of the Cement Paste Matrix and Aggregate on the Modulus of Elasticity of Concrete*, Ph.D. Dissertation, Texas A&M University, 1991.

81. Christensen, D.W., Pellinen, T., and Bonaquist, R.F., "Hirsch Model for Estimating the Modulus of Asphalt Concrete." *Journal of the Association of Asphalt Paving Technologists*, Vol. 72, 2003.

82. Alavi, S.H., and Monismith, C.L., "Time and Temperature Dependent Properties of Asphalt Concrete Mixes Tested as Hollow Cylinders and Subjected to Dynamic Axial and Shear Loads." *Journal of the Association of Asphalt Paving Technologists*, Vol. 63, 1994.

83. Clyne, T.R., Li, X., Marasteanu, M.O., and Eugene, L., "Dynamic and Resilient Modulus of MnDOT Asphalt Mixtures." *Research Report MN/RC-2003 – 09*, University of Minnesota, Minnesota, 2003.

84. Dongre, R., Myers, L., D'Angelo, J., Paugh, C., and Gudimettla, J., "Field Evaluation of Witczak and Hirsch Models for Predicting Dynamic Modulus of Hot-Mix Asphalt." Paper Presented at 2005 Annual Meeting of Association of Asphalt Paving Technologist, 2005.

85. Witczak, M.W., Pellinen, T.K., and El-Basyouny, M.M., "Pursuit of the Simple Performance Test for Asphalt Concrete Fracture/Cracking." *Journal of the Association of Asphalt Paving Technologists*, Vol. 71, 2002.

86. Pellinen, T. K., and Witczak, M. W., "Use of Stiffness of Hot-Mix Asphalt as a Simple Performance Test." *Transportation Research Record 1789*, 2002.

87. Witczak, M.W., Kaloush, K.E., and Von Quintus, H., "Pursuit of the Simple Performance Test for Asphalt Mixture Rutting." *Journal of the Association of Asphalt Paving Technologists*, Vol. 71, 2002.

88. Zhou, F, and Scullion, T., "Preliminary Field Validation of Simple Performance Tests for Permanent Deformation." *Transportation Research Record 1821*, 2003.

89. El-Basyouny, M.M., *Calibration and Validation of Asphalt Concrete Pavements Distress Models for 2002 Design Guide*, Ph.D. Dissertation, Arizona State University, 2004.

90. Witczak, M.W., Mirza, M.W., and Uzan, J., "Appendix CC-3: Updated Traffic Frequency Calculation for Asphalt Layers." *Development of the 2002 Guide for the Design of New and Rehabilitated Pavement Structures*, NCHRP Project 1-37A, 2003.

91. "Operating Instructions for the Dynamic Angle Validation Kit (DAV) for Superpave Gyratory Compactors." Test Quip Corporation, New Brighton, MN, 2001.

92.   Dalton, F., "Comparison of Two Internal Angle Measurement Devices for Superpave Gyratory Compactors." *Pine Research Report 2003-01*, Revision B, Pine Instrument Company, Grove City, PA, 2003.

93.   Harman, T., Al-Khateeb, G., and Stuart, K., "Evaluation of Mechanical Mixture Simulation in the Measurement of the Dynamic Internal Angle of Gyration." Preprinted CD of the 79th Annual Meeting of the Association of Asphalt Paving Technologists, Baton Rouge, LA, 2004.

94.   Dalton, F., :Superpave Gyratory Compactors-Angle Problems?" *Pine Research Report 1999-05*, Pine Instrument Company, Grove City, PA, 1999.

95.   Hall, K., "Evaluating the Superpave Gyratory Compactor Internal Angle of Gyration Using Simulated Loading." Paper Submitted to the 80th Annual Meeting of the Association of Asphalt Paving Technologists, 2005.

96.   Guler, M, Bahia, H, Bosscher, J, and Plesha, M., "Device for Measuring Shear Resistance of Hot Mix Asphalt in Gyratory Compactor." *Transportation Research Record 1723*, 2000.

97.   Test Quip, Inc. Web Site: http://www.testquip.com/DAV2_Brochure.PDF. Accessed April 2005.

98.   Romero, P., Pradhan, M., Niederhauser, S., and Biel, T., "Control of the Superpave Gyratory Compactor's Internal Angle of Gyration: Utah Department of Transportation Experience." Paper Presented at 2005 *84th TRB Annual Meeting*, 2005.

99.   *Standard Specifications for Highway Construction*, Arkansas State Highway and Transportation Department, Little Rock, Arkansas, 2003.

100.   American Association of State Highway and Transportation Officials (AASHTO), "Practice for Mixture Conditioning of Hot Mix Asphalt (HMA)", AASHTO R30-02, 2004.

101.   Chapra, S.C., and Canale, R.P., *Numerical Methods for Engineers*, 4th Edition, McGraw-Hill, Boston, 2001.

102.   Montgomery, D.C., *Design and Analysis of Experiments*, 5th Edition, John Wiley & Son, New York, 2001.

103.   Lasdon, L.S., Waren, A.D., Jain, A., and Ratner M., "Design and Testing of a Generalized Reduced Gradient Code for Nonlinear Programming." *ACM Transactions on Mathematical Software*, Association for Computing Machinery, Vol. 4, 1978.

104. The World Road Association (PIARC). *A Guide to Calibration and Adaptation of HDM-4*. The International Study of Highway Development and Management (ISOHDM), 2001.

105. R.H. McCuen, *Modeling Hydrologic Change*, CRC Press, Boca Raton, Florida, 2003.

106. Mirza, M.W., and Witczak, M.W., "Development of a Global Aging System for Short and Long Term Aging of Asphalt Cements." *Journal of the Association of Asphalt Paving Technologists*, Vol. 64, 1995.

107. Schwartz, C.W., "Evaluation of the Witczak Dynamic Modulus Prediction Model." Paper Presented at 2005 *84th TRB Annual Meeting*, 2005.

108. Birgisson, B., Sholar, G., and Roque, R., "Evaluation of Predicted Dynamic Modulus for Florida Mixtures." Paper Presented at 2005 *84th TRB Annual Meeting*, 2005.

109. American Society for Testing and Materials (ASTM), "Standard Practice for Dealing With Outlying Observations", ASTM E 178 - 94, 2002.

110. Easley, T.M., *Evaluation of Measurement Techniques for the Internal Angle of Gyration for the Superpave Gyratory Compactor*, Master's Thesis, University of Arkansas, 2004.

APPENDIX A

WHITE PAPER ON STATIC CREEP/FLOW TIME OF ASPHALT MIXTURES IN COMPRESSION

Introduction

The National Cooperative Highway Research Program (NCHRP) Project 9-19 recommends a "Simple Performance Test" be used with the Superpave volumetric mixture design procedure and continues developing advanced material characterization methods for Superpave distress predictive models.

The current Superpave volumetric Level 1 design was based upon volumetric properties of the asphalt mixtures and did not include any test method to evaluate the distress characteristics of the hot mix asphalt (HMA) mixture. Therefore, the current volumetric mix design procedure is not sufficient to ensure mixture performance.

Based on the research results, the NCHRP 9-19 project team *(1)* recommends three test parameters for further field validation for permanent deformation, including the dynamic modulus, $E^*/Sin\phi$, determined from the triaxial dynamic modulus test at high temperatures; the flow time, F_t, determined from the triaxial static creep test; and the flow number, F_n, determined from the triaxial repeated load test. For fatigue cracking, it is the dynamic modulus, E^*, measured at low test temperatures. For low temperature cracking, the team recommends the static creep compliance measured by the indirect tensile creep test.

The purpose of this paper is to present the literature review on the triaxial static creep test to determine the flow time, F_t, of the HMA mixtures.

Background

Theoretical Background

The static creep test, using either one cycle load/unload or simple loading, provides information about the material response characteristics of bituminous mixtures. The interpretation of the strain/time response obtained from a static creep test provides significant parameters, which describe the instantaneous elastic/plastic and viscoelastic/plastic components for evaluating the tested mixture's rutting resistance *(1,2)*.

Strain-Time Response Curve

A load/unload cycle of a typical strain time response of a bituminous mixture, which is obtained from a static creep test, is illustrated in Figure 1. The denotes in this figure are as follows:

L, U	represent superscripts denoting whether the strain response is in the loading (*L*) phase or unloading (*U*) phase
t_1, t_2	represent variable times in the loading and unloading phases,

respectively

T_L, T_{UL}	represent the end of the loading cycle (T_L) and the end of the unloading cycle (T_{UL})

The various train components in Figure 1 are:

$\varepsilon_e^L = \varepsilon_e^U$	instantaneous recoverable (elastic strain)
ε_p^L	instantaneous non-recoverable plastic strain (negligible except at high temperatures)
$\varepsilon_{ve}^L(t_1) = \varepsilon_{ve}^U(t_2 - T_L)$ when $t_1 = t_2 - T_L$	
	this is the time dependent viscoelastic (recoverable) strain
$\varepsilon_{vp}^L(t_1)$	time dependent viscoplastic (non-recoverable) strain (negligible except at high temperatures)
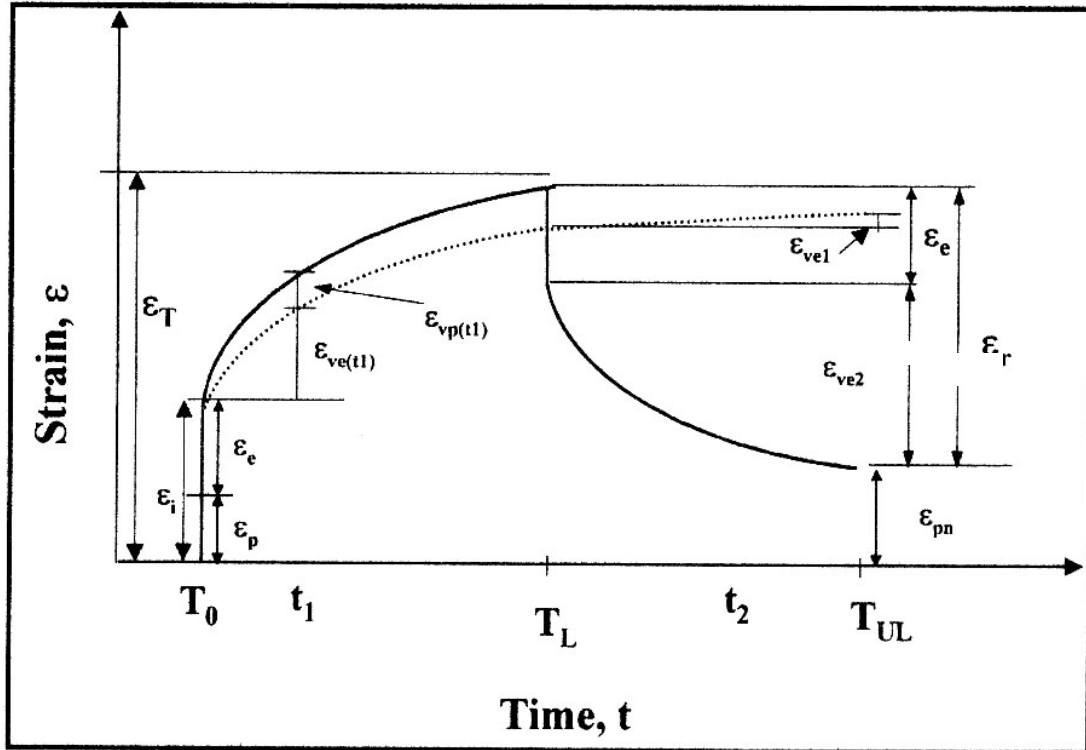
Figure 1. Typical Strain –Time Response for Asphalt Mixture Under Static Creep Test *(1)*

$\varepsilon_{pn}{}^{U}(T_{UL})$ non-recoverable time dependent strain at the end of one load/unload cycle

$\varepsilon_r = \varepsilon_e{}^{U} + \varepsilon_{ve}{}^{U}(t_2 - T_L)$ or $\varepsilon_r = \varepsilon_e{}^{L}(T_L) - \varepsilon_{pn}(T_{UL})$

this is the resilient strain (recoverable) at the end of one load/unload cycle

Modulus/Compliance Components

The following "modulus" values, which are the ratio of stress to strain, are defined dependent upon the particular strain value used. The resilient modulus is:

$$E_R = \frac{\sigma_d}{\varepsilon_r} \tag{1}$$

The pure elastic (instantaneous) modulus is:

$$E_e = \frac{\sigma_d}{\varepsilon_e} \tag{2}$$

313

The creep or time dependent modulus is:

$$E_c = \frac{\sigma_d}{\varepsilon(t)}$$

(3)

Where ε_r, ε_e, $\varepsilon(t)$ are the resilient, elastic, and total strain as shown in Figure 1. The reciprocal of the modulus values is defined as the compliance:

$$D(t) = E(t)^{-1} = \frac{\varepsilon(t)}{\sigma_d}$$

(4)

The use of compliance in viscoelastic-viscoplastic theory is advantageous because it allows for the separation of the time-dependent and time-independent components of the strain response. The total strain, $\varepsilon(t)$, can be expressed in term of its recoverable and irrecoverable components or time-dependent and time-independent components as follows:

$$\varepsilon(t) = \varepsilon_e + \varepsilon_p + \varepsilon_{ve} + \varepsilon_{vp}$$

(5)

$$= \sigma_d \left(D_e + D_p + D_{ve}(t) + D_{vp}(t) \right)$$

$$= \sigma_d * D(t)$$

The deviator stress in Equation (5) is determined using Equation (6).

$$\sigma_d = \sigma_1 - \sigma_3$$

(6)

where

σ_d = deviator stress (psi)

σ_1 = axial stress (psi)

σ_3 = confining stress (psi)

For the unconfined static creep test, $\sigma_d = \sigma_1$ ($\sigma_3 = 0$), while for the triaxial/confined condition, $\sigma_d = \sigma_1 - \sigma_3$. In Equation (6), the axial stress (σ_1) is determined as follows:

$$\sigma_1 = \frac{P}{A}$$

(7)

where

P = axial load applied (lb)

A = area of cross section of specimen (in^2)

Flow Time

A total strain-time relationship is measured in the laboratory using a static compressive creep test under unconfined or confined conditions. As a result, a relationship between the calculated total compliance and loading time is developed, as shown in Figure 2. The total compliance in Figure 2 can be divided into three major zones:

- The primary zone - the portion in which the strain rate decreases with loading time;
- The secondary zone – the portion in which the strain rate is constant with loading time; and
- The tertiary zone – the portion in which the strain rate increases with loading time.
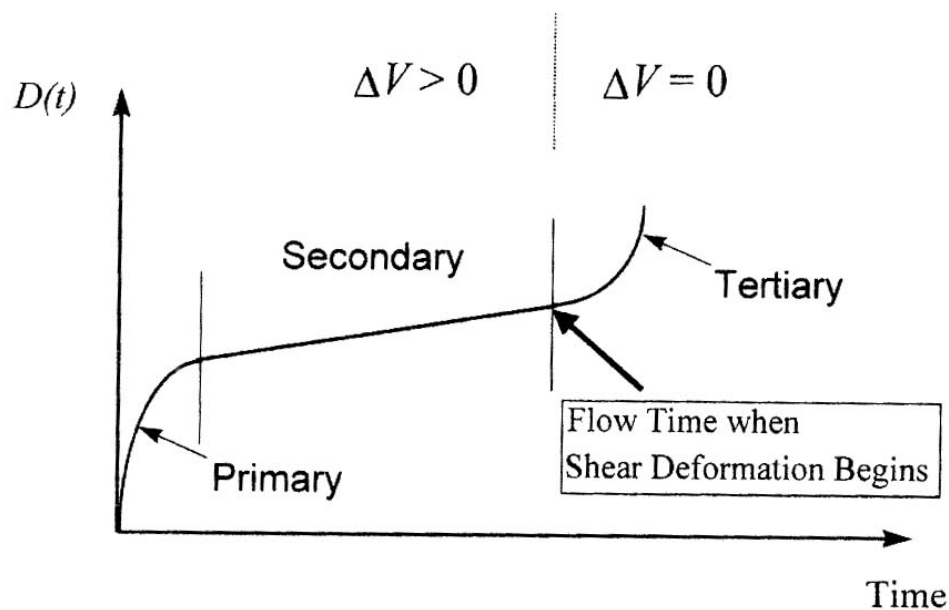
Figure 2. Typical Relationship Between the Calculated Compliance and Time *(3)*

Ideally, the large increase in compliance generally occurs at a constant volume within the tertiary zone. The starting point of tertiary zone is defined as the flow time, F_T. The flow time is the point at which the rate of change of compliance to loading time in the relationship is minimum. Therefore, the flow time is also defined as the time at which the shear deformation under constant volume begins. As reported, the flow time is a significant parameter in evaluating an HMA mixture's rutting resistance *(1,2)*.

315

Compliance Model

The following power model is used to represent the secondary (i.e., linear) phase of the creep compliance curve, as shown in Figure 3.

$$D(t) = at^m \qquad (8a)$$

or
$$\log D(t) = \log a + m \log(t) \qquad (8b)$$

where

        D(t)   = total compliance at any time

        t   = loading time

        a, m   = material regression coefficients

The regression coefficients *a* and *m* are generally referred to as the compliance parameters, which indicate the permanence deformation behavior of the material. The larger the value of *a*, the larger the compliance value, *D(t)*, the smaller the modulus value, *E(t)*, and the larger the permanent deformation. For a constant *a*-value, the larger the value of *m*, the larger the permanent deformation.
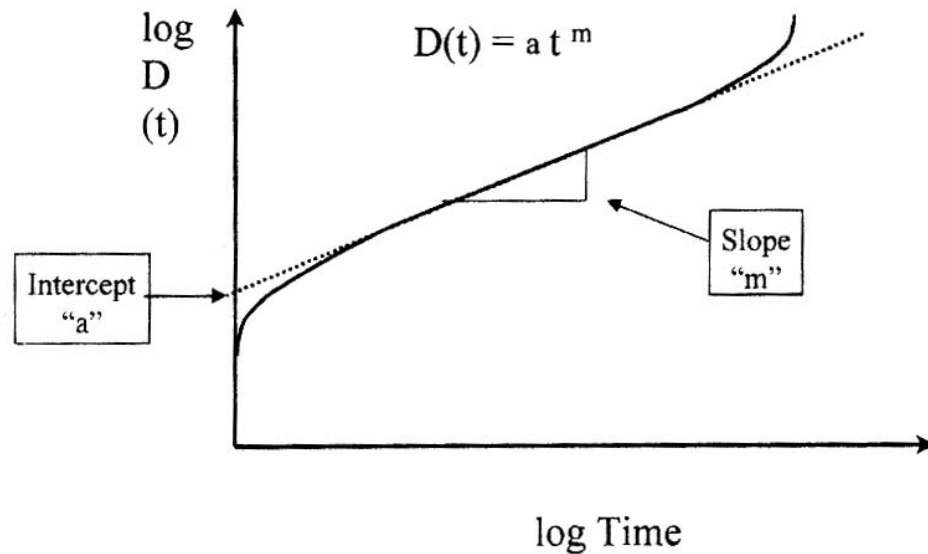
Figure 3. Compliance Model for Secondary Zone of the Log Compliance-Log Time Plot *(1)*

Total Compliance at Failure

Total compliance at failure (D_{tf}) was defined by Hafez *(2)* as the total compliance calculated at the flow time (F_T):

$$D_{tf} = D_0 + D_1 F_T^{m1} \tag{9}$$

where

D_{tf} = total compliance at failure

D_0 = instantaneous elastic and plastic compliance ($= D_e + D_p$)

F_T = flow time (sec)

D_1, m_1 = material regression coefficients

The total compliance at failure and the critical flow time are used to define the safe zone for mix designs, as shown by the hatched area in Figure 4. The horizontal line in Figure 4 represents the value of the total compliance (D_{tf}) at failure at a given reliability value, R, and the vertical line represents the critical flow time, $F_{T\ critical}$. A mix that falls within the safe zone will be accepted *(3)* because (1) the actual flow time of an acceptable mix is larger than the critical flow time; and (2) the total compliance at failure for an acceptable mix occurs at reliability levels equal or larger than the target reliability level for the total compliance at failure (target reliability = 50 percent if the mean total compliance at failure is used as the horizontal limit time).
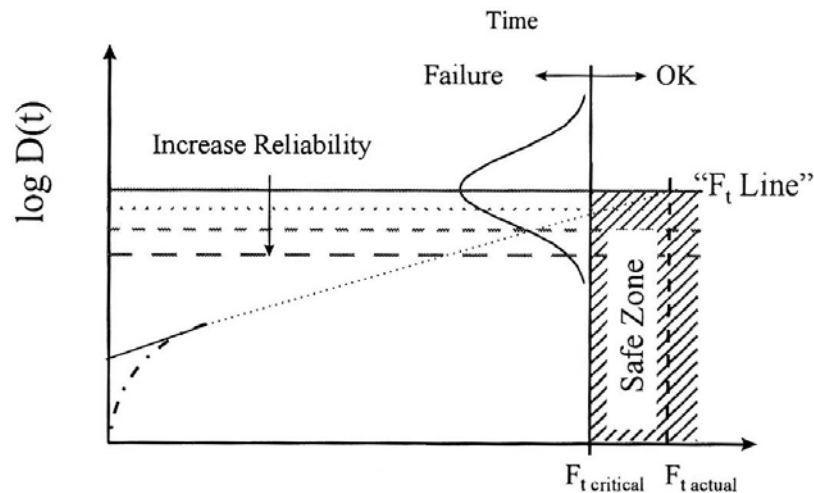
Figure 4. Criteria for the Creep Test Safe Zone *(4)*

Static Creep Test Description

A detailed test method for static creep/flow time of HMA mixtures in compression is presented in *(1)*. The static creep test can be performed under unconfined or confined conditions and using one load-unload cycle provide sufficient information to determined the time independent and time dependent components of the material's response.

Specimen Preparation

The mixture is mixed and compacted to the 150 mm (6 in.) diameter by 170 mm (6.7 in.) high. A 100 mm (4 in.) diameter specimen is cored from the center of the gyratory specimen. The ends of the cored specimen are sawed to obtain a 100 mm (4 in.) diameter by 150 mm (6 in.) high. The geometric properties and air void content of the final test specimen are checked for acceptance. The air voids of the test specimen should not differ by more than 0.5 percent from the target air voids.

The number of replicates required depends on the measurement devices used in the testing and the desired accuracy of the average flow time values. Table 1 presents a guideline for selecting the number of replicates required for testing.

Table 1. Recommended Number of Specimens *(1)*

LVDTs per Specimen (Either Vertical or Horizontal, not Conbined)	Number of Specimen	Estimated Standard Error of the Mean, %, Per Mixture's Nominal Aggregate Size		
		12.5 mm	**19 mm**	**37.5 mm**
2	2	7.6	9.5	18.8
2	3	6.2	7.7	15.3
3	2	6.7	8.9	17.4
3	3	5.5	7.3	14.2
4	2	6.2	8.6	16.6
4	3	5.0	7.0	13.6

Test Procedure

The test specimen is placed in the environmental chamber and allowed to equilibrate to the specified testing temperature. After temperature equilibrium is reached, the test is performed using an electro-hydraulic machine, which is capable of applying static load up to 25 kN (5,600 lbs). Load is measured through the load cell, and the specimen's deformations are measured by axial and radial LVDTs. Figure 5 shows a static creep test setup for an unconfined condition, and Figure 6 shows a test setup for a confined condition.
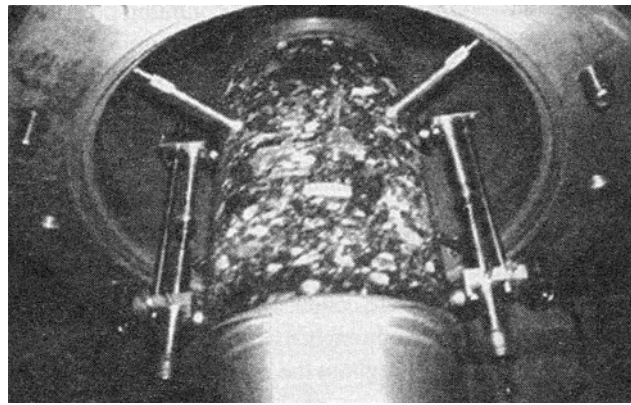
Figure 5. Static Creep Test Setup for Unconfined Condition (1)
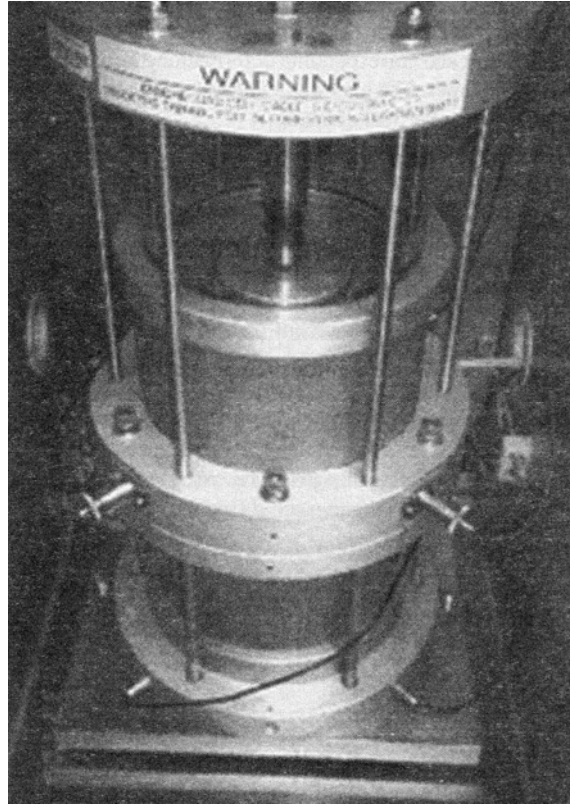
Figure 6. Static Creep Test Setup for Confined Condition *(1)*

The design stress level covers the range between 69 and 207 kPa (10 - 30 psi) for the unconfined tests, and 483 to 966 kPa for the confined tests. Typical confinement stresses range between 35 and 207 kPa (5 - 30 psi). The load is hold constant until tertiary flow occurs or the total axial strain reached approximately 2% for unconfined test and 4-5% for confined tests.

Actual test results and plots from a static creep test are presented in Figures 7 and 8. Figure 7 shows the total axial strain versus time on a log-log scale. The compliance parameters *a* and *m* are estimated by drawing a straight line on the linear portion of the curve. Figure 8 shows a plot of the rate of change in compliance versus time on a log-log scale. The flow time is the time at which the curve in Figure 8 reaches the minimum value.
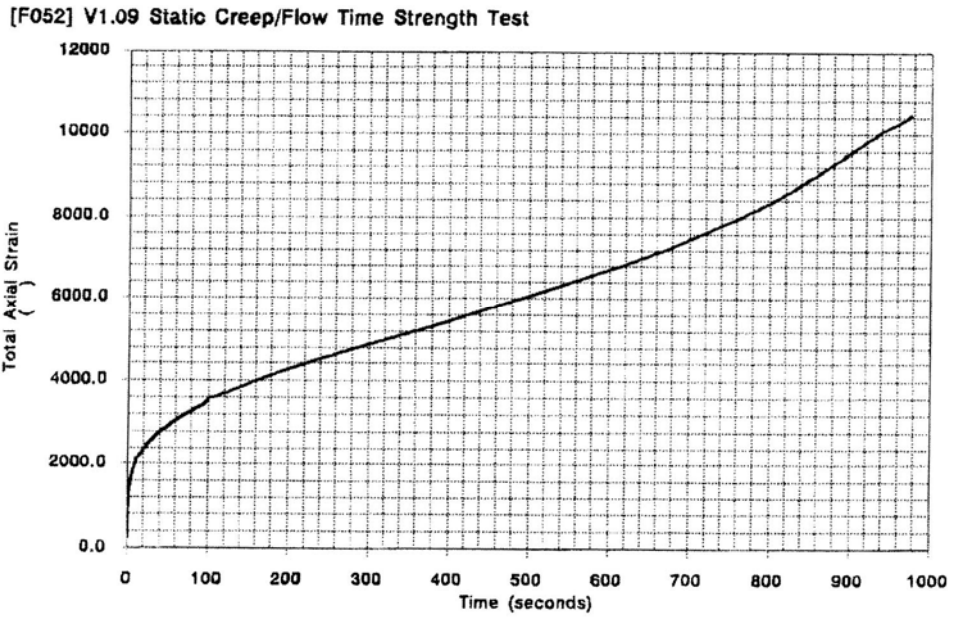
Figure 7. Total Axial Strain versus Time *(1)*
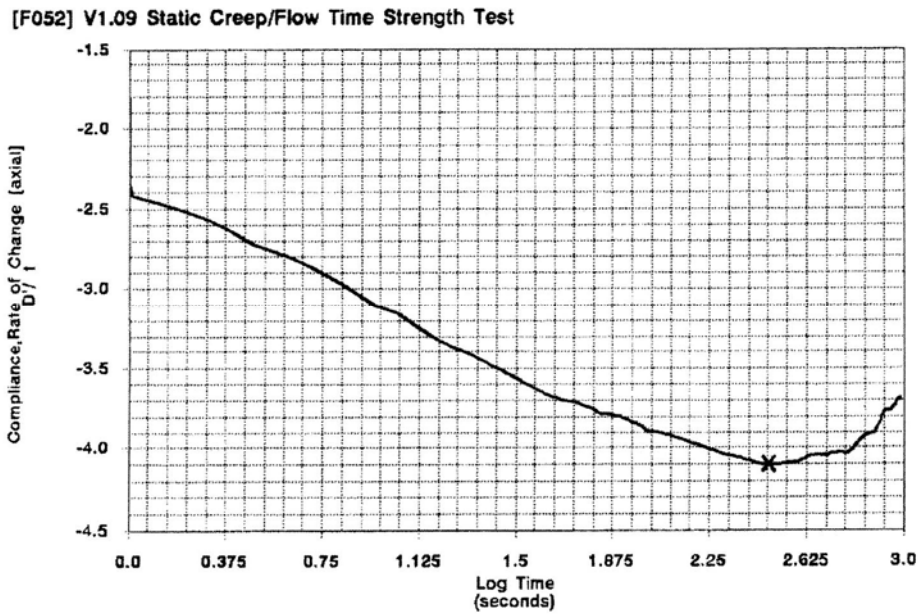
Figure 8. Rate of Change in Compliance versus Loading Time *(1)*

Analyses and comparisons of mixture responses to permanent deformation

Researchers have studied the relationship between the static creep test parameters and the performance deformation behavior of the asphalt material in the field. In one project *(5)*, the test parameters were compared to the Asphalt Pavement Analyzer (APA) and Hamburg Wheel-Tracking Device (HWTD) results. The test parameters investigated include the intercept (*a*), slope (*m*), compliance (*D(t)*) at short time and long time, and flow time (F_T).

Intercept Parameter (*a*)

The intercept for unconfined conditions showed rational relationships with the rut depth, and the statistics obtained for linear models were rated fair to good. However, the intercept for confined conditions had very poor measures of model accuracy, and it was not related to the but-depth measurements *(1)*.

Slope Parameter (*m*)

The slope parameters for both unconfined and confined conditions had positive and rational relationship with the rut-depth. The goodness-of-fit statistics of the linear models were rated fair to good *(1)*.

Bhasin et al. *(5)* reported that among the test parameters investigated, including dynamic modulus (*E**), $E^*/\sin\phi$, flow time (F_T), flow time slope (*m*), flow time intercept (*a*), flow number (F_N), and flow number slope (*b*), the slope parameter of static creep test provided the best correlations with the APA and HWTD rut depth.

Compliance *D(t)* at Short and Long Term

The compliance at short and long term for both unconfined and confined conditions had a good relation with the rut depth. The measure of linear model accuracy was rated fair to good *(1)*.

Flow Time (F_T)

The flow time for both unconfined and confined conditions had a good correlation with field rut depth measurements. The goodness-of-fit statistics obtained from the power models were good to excellent. Figures 9 and 10 present two examples of rut depth versus unconfined and confined flow time. The weighted average statistical measures for the flow time (F_T) were $R^2 = 0.91$ and $S_e/S_y = 0.323$ for unconfined conditions, and $R^2 = 0.87$ and $S_e/S_y = 0.388$ for confined conditions *(1)*.

Overall, the flow time was rated the best among all static creep test parameters to correlate with the rutting behavior in the field. The higher the flow time value, the longer time to failure, the better the mixture performance.
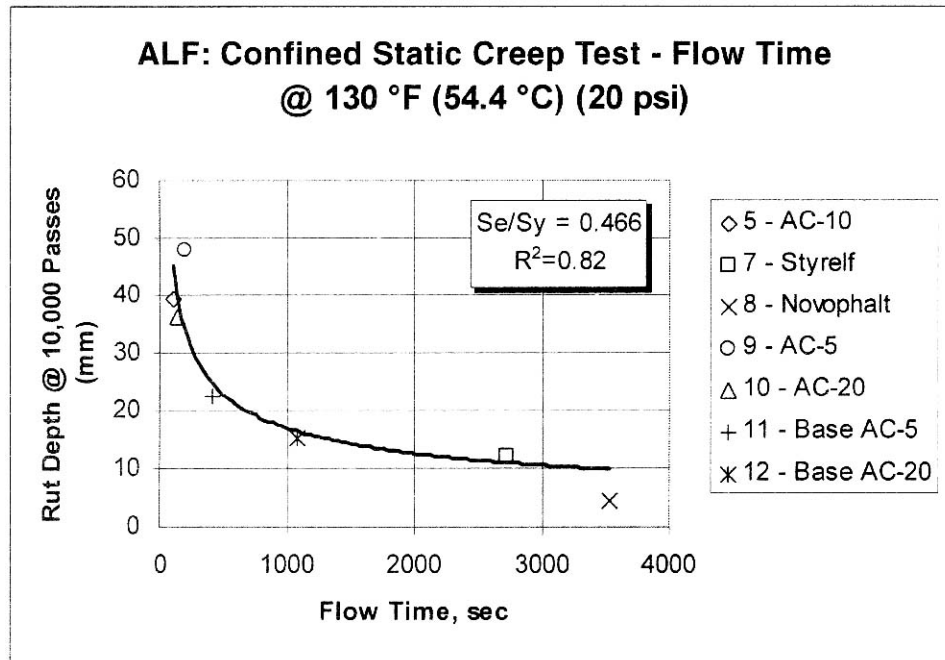
Figure 9. Rut Depth versus Unconfined Flow Time *(1)*
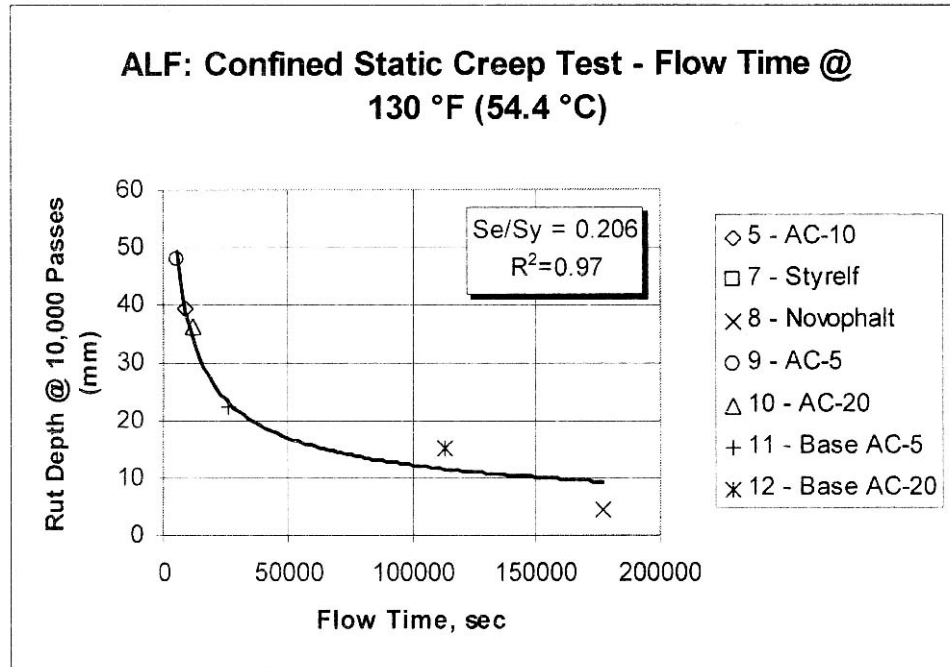
Figure 10. Rut Depth versus Confined Flow Time *(1)*

Flow Time (F_T) versus Flow Number (F_N) and Dynamic Modulus (E^*)

The flow time and flow number, obtained from a repeated permanent deformation load test, showed a better correlation to the rutting behavior of the mixture than the dynamic modulus *(5)*. The flow time showed the best correlation to the mixture permanent deformation in confined conditions. The static creep test for determining the flow time requires simple equipment with static load capability and is inexpensive to operate. However, the test does not simulate the field dynamic loading behavior.

The flow number also showed a good relation to mixture rutting behavior, and the test loading conditions simulate the field dynamic phenomenon. However, the test is more complicated to implement, especially for confining conditions that may be required.

A correlation analysis between the flow time and flow number showed that two parameters are well correlated, and the relationship was $F_N = 1.565*F_T$ with an R^2 of 0.81 *(3)*.

Summary

The static creep test, using either one cycle load/unload or simple loading, provides significant parameters, including flow time, flow time slope, compliance. The test can be implemented in unconfined and confined conditions. Overall, the flow time showed the best correlation to the rut depth in the field over the other test parameters. The goodness-of-fit statistics of the flow time were rated good to excellent for both unconfined and confined conditions. The higher the flow time values, the better the mixture performance.

The flow time and flow number showed a better correlation to rut depth than the dynamic modulus. The flow time also well correlated to the flow number.

REFERENCES

1. Witczak M.W., K. Kaloush, T. Pellinen, and M. El-Basyouny. *Simple Performance Test for Superpave Mix Design*. NCHRP Report 465. Transportation Research Board. National Research Council, Washington, D.C., 2002.

2. Hafez, I. "Development of a Simplified Asphalt Mix Stability Procedure for Use in Superpave Volumetric Mix Design," Ph.D. Dissertation, Civil Engineering Department, University of Maryland, College Park, MD, 1997.

3. Kaloush, K.E., and M.W. Witczak. "Tertiary Flow Characteristics of Asphalt Mixtures," *Journal of Association of Asphalt Paving Technologists*, Vol. 71, 2002.

4. Brown, S.F., and K.E. Cooper. "The Mechanical Properties of Bituminous Materials for Road Bases and Base Courses," *Journal of Association of Asphalt Paving Technologists*, Vol 53, 1984.

5. Bhasin, A., J. Button, and A. Chowdhury. "Evaluation of Simple Performance Tests on HMA Mixtures from the South Central United States," TRB 2004 Annual Meeting, Washington D.C.

APPENDIX B   HMA MIXTURE PROPERTIES

Mix Type: 12.5 mm HMA Surface Course (PG 70-22)

AHTD Lab No.: SP238C-02   Date: 06/03/2002

Plant Name: McClinton Anchor   Location: Lowell

Status: Verified at the Asphalt Lab (University of Arkansas)

Material Gradations (Percent Passing)

Sieve Size	MCA Preston 3/4"	MCA Sharps 1/2"	MCA Flintrock HDS	MCA West Fork Screenings	Job Mix
25.0 - 1"	100	100	100	100	100
19.0 - 3/4"	100	100	100	100	100
12.5 - 1/2"	67	100	100	100	93
9.5 - 3/8"	38	80	100	100	80
4.75 - #4	6	13	97	100	51
2.36 - #8	4	2	78	74	37
1.18 - #16	4	2	50	51	25
0.6 - #30	3	2	28	35	16
0.3 - #50	3	2	14	23	10
0.15 - #100	3	2	6	16	6
0.075 - #200	1.5	1.6	3	13	4.2
Cold Feed %	21	33	26	20	

Mix Design Summary

Asphalt Content %:	5.8	Air Voids (Va):	4.5
Max. Theor. Sp. Gr. (Gmm):	2.403	VMA:	14.9
Asphalt Binder:	PG 70-22	VMA Correction Factor:	-2.7
Mixing Temperature:	335F	Gsb:	2.532
Compaction Temperature:	300F	Gse:	2.624
		Gb:	1.016

Mix Type: 12.5 mm HMA Surface Course (PG 76-22)

AHTD Lab No.: SP238C-02   Date: 06/03/2002

Plant Name: McClinton Anchor   Location: Lowell

Status: Verified at the Asphalt Lab (University of Arkansas)

Material Gradations (Percent Passing)

Sieve Size	MCA Preston 3/4"	MCA Sharps 1/2"	MCA Flintrock HDS	MCA West Fork Screenings	Job Mix
25.0 - 1"	100	100	100	100	100
19.0 - 3/4"	100	100	100	100	100
12.5 - 1/2"	68	100	100	100	90
9.5 - 3/8"	38	80	100	100	75
4.75 - #4	6	13	97	93	43
2.36 - #8	4	2	78	63	30
1.18 - #16	4	2	51	38	19
0.6 - #30	3	2	28	24	12
0.3 - #50	3	2	12	15	7
0.15 - #100	3	2	4	12	5
0.075 - #200	1.7	1.9	1.8	11.8	4.0
Cold Feed %	32	28	18	22	

Mix Design Summary

Asphalt Content %:	6.2	Air Voids (Va):	4
Max. Theor. Sp. Gr. (Gmm):	2.369	VMA:	14.9
Asphalt Binder:	PG 76-22	VMA Correction Factor:	-2.9
Mixing Temperature:	340F	Gsb:	2.51
Compaction Temperature:	300F	Gse:	2.595
		Gb:	1.023

Mix Type: 25 mm HMA Binder Course (PG 70-22)

AHTD Lab No.: SP072A-99   Date: 10/05/1999

Plant Name: McClinton Anchor   Location: Lowell

Status: Verified at the Asphalt Lab (University of Arkansas)

Material Gradations (Percent Passing)

Sieve Size	MCA Preston 1-1/2"	MCA Sharps 1/2"	MCA Flintrock HDS	MCA West Fork Screenings	Job Mix
37.5 - 1-1/2"	100	100	100	100	100
25.0 - 1"	79	100	100	100	94
19.0 - 3/4"	50.1	100	100	100	85
12.5 - 1/2"	12.3	100	100	100	74
9.5 - 3/8"	7.6	80	100	100	64
4.75 - #4	2.1	12.9	97.3	99.9	34
2.36 - #8	2	2.2	77.7	71.9	22
1.18 - #16	1.9	2	50.5	47.5	15
0.6 - #30	1.7	1.9	28.3	31.8	10
0.3 - #50	1.5	1.8	11.5	21.1	7
0.15 - #100	1.4	1.7	3.9	14.7	5
0.075 - #200	1.2	1.6	1.8	10.6	3.6
Cold Feed %	30	42	5	23	

Mix Design Summary

Asphalt Content %:	5.0	Air Voids (Va):	4.5
Max. Theor. Sp. Gr. (Gmm):	2.430	VMA:	13.3
Asphalt Binder:	PG 70-22	Gsb:	2.540
Mixing Temperature:	340F	Gse:	2.622
Compaction Temperature:	300F	Gb:	1.016

Mix Type: 25 mm HMA Binder Course (PG 76-22)

AHTD Lab No.: SP075-98   Date: 05/11/1998

Plant Name: McClinton Anchor   Location: Lowell

Status: Verified at the Asphalt Lab (University of Arkansas)

Material Gradations (Percent Passing)

Sieve Size	MCA Preston 1-1/2"	MCA Sharps 1/2"	MCA Flintrock HDS	MCA West Fork Screenings	Job Mix
37.5 - 1-1/2"	100	100	100	100	100
25.0 - 1"	79	100	100	100	94
19.0 - 3/4"	50.1	100	100	100	85
12.5 - 1/2"	12.3	100	100	100	74
9.5 - 3/8"	7.6	80	100	100	63
4.75 - #4	2.1	12.9	97.3	99.9	32
2.36 - #8	2	2.2	77.7	71.9	21
1.18 - #16	1.9	2	50.5	47.5	14
0.6 - #30	1.7	1.9	28.3	31.8	9
0.3 - #50	1.5	1.8	11.5	21.1	6
0.15 - #100	1.4	1.7	3.9	14.7	4
0.075 - #200	1.2	1.6	1.8	10.6	3.3
Cold Feed %	30	44	6	20	

Mix Design Summary

Asphalt Content %:	5.3	Air Voids (Va):	4.0
Max. Theor. Sp. Gr. (Gmm):	2.404	VMA:	13.9
Asphalt Binder:	PG 76-22	Gsb:	2.538
Mixing Temperature:	340F	Gse:	2.600
Compaction Temperature:	300F	Gb:	1.023

Mix Type: 37.5 mm HMA Base Course (PG 70-22)

AHTD Lab No.: SP030C-01   Date: 02/01/2001

Plant Name: McClinton Anchor   Location: Lowell

Status: Verified at the Asphalt Lab (University of Arkansas)

Material Gradations (Percent Passing)

Sieve Size	MCA Preston 1-1/2"	MCA Sharps 1/2"	MCA Humbel HDS	MCA West Fork Screenings	Job Mix
37.5 - 1-1/2"	100	100	100	100	100
25.0 - 1"	79	100	100	100	89
19.0 - 3/4"	50.1	100	100	100	74
12.5 - 1/2"	12.3	100	100	100	54
9.5 - 3/8"	7.6	80	100	100	48
4.75 - #4	2.1	12.9	97.3	99.9	31
2.36 - #8	2	2.2	77.7	71.9	22
1.18 - #16	1.9	2	50.5	47.5	15
0.6 - #30	1.7	1.9	28.3	31.8	10
0.3 - #50	1.5	1.8	11.5	21.1	6
0.15 - #100	1.4	1.7	3.9	14.7	4
0.075 - #200	1.2	1.6	1.8	10.6	3.1
Cold Feed %	52	20	9	19	100

Mix Design Summary

Asphalt Content %:	4.3	Air Voids (Va):	4.5
Max. Theor. Sp. Gr. (Gmm):	2.457	VMA:	12
Asphalt Binder:	PG 70-22	Gsb:	2.547
Mixing Temperature:	340F	Gse:	2.624
Compaction Temperature:	300F	Gb:	1.016

Mix Type: 37.5 mm HMA Base Course (PG 76-22)

AHTD Lab No.: SP074-98   Date: 1998

Plant Name: McClinton Anchor   Location: Lowell

Status: Verified at the Asphalt Lab (University of Arkansas)

Material Gradations (Percent Passing)

Sieve Size	MCA Preston 1-1/2"	MCA Sharps 1/2"	MCA Humbel HDS	MCA West Fork Screenings	Job Mix
37.5 - 1-1/2"	100	100	100	100	100
25.0 - 1"	79	100	100	100	89
19.0 - 3/4"	50.1	100	100	100	73
12.5 - 1/2"	12.3	100	100	100	53
9.5 - 3/8"	7.6	80	100	100	47
4.75 - #4	2.1	12.9	97.3	99.9	31
2.36 - #8	2	2.2	77.7	71.9	22
1.18 - #16	1.9	2	50.5	47.5	15
0.6 - #30	1.7	1.9	28.3	31.8	10
0.3 - #50	1.5	1.8	11.5	21.1	6
0.15 - #100	1.4	1.7	3.9	14.7	4
0.075 - #200	1.2	1.6	1.8	10.6	3.1
Cold Feed %	54	18	9	19	100

Mix Design Summary

Asphalt Content %:	4.2	Air Voids (Va):	4.0
Max. Theor. Sp. Gr. (Gmm):	2.442	VMA:	11.8
Asphalt Binder:	PG 76-22	Gsb:	2.548
Mixing Temperature:	340F	Gse:	2.600
Compaction Temperature:	300F	Gb:	1.023

Mix Type: 12.5 mm HMA Surface Course (PG 70-22)

AHTD Lab No.: SP248C-02   Date: 07/02/2002

Plant Name: Jet Asphalt   Location: El Dorado

Status: Verified at the Asphalt Lab (University of Arkansas)

Material Gradations (Percent Passing)

Sieve Size	GMQ Granite 3/4"	GMQ Granite 1/2"	GMQ Granite Ind. Sand	AR Lime Batesville Bag House	Job Mix
25.0 - 1"	100	100	100	100	100
19.0 - 3/4"	100	100	100	100	100
12.5 - 1/2"	78	100	100	100	92
9.5 - 3/8"	62	88	100	100	80
4.75 - #4	38	58	84	100	56
2.36 - #8	23	38	53	100	36
1.18 - #16	15	26	34	100	24
0.6 - #30	10	18	22	100	17
0.3 - #50	6	12	12	100	11
0.15 - #100	4	8	6	95	7
0.075 - #200	2.3	4.7	3	78	4.2
Cold Feed %	38	43	18	1	100

Mix Design Summary

Asphalt Content %:	5.3	Air Voids (Va):	4.5
Max. Theor. Sp. Gr. (Gmm):	2.436	VMA:	15.1
Asphalt Binder:	PG 70-22	Gsb:	2.601
Mixing Temperature:	330F	Gse:	2.638
Compaction Temperature:	300F	Gb:	1.028

Mix Type: 12.5 mm HMA Surface Course (PG 76-22)

AHTD Lab No.: SP097-99   Date: 05/06/1999

Plant Name: Cranford   Location: Sweet Home

Status: Verified at the Asphalt Lab (University of Arkansas)

Material Gradations (Percent Passing)

Sieve Size	GMQ Granite 3/4"	GMQ Granite 1/2"	GMQ Granite Ind. Sand	AR Lime Batesville Bag House	Job Mix
25.0 - 1"	100	100	100	100	100
19.0 - 3/4"	100	100	100	100	100
12.5 - 1/2"	85.7	100	100	100	95
9.5 - 3/8"	71	92.5	100	100	86
4.75 - #4	45.1	64.1	89.7	100	62
2.36 - #8	29.9	42.1	60.7	100	41
1.18 - #16	18.8	27.3	38.7	100	27
0.6 - #30	12.4	18.3	24.4	100	18
0.3 - #50	7.3	11.4	13.8	100	11
0.15 - #100	4.8	6.8	7.4	95.2	7
0.075 - #200	2.6	3.8	2.9	78.1	3.9
Cold Feed %	48	42	9	1	100

Mix Design Summary

Asphalt Content %:	5.6	Air Voids (Va):	4.0
Max. Theor. Sp. Gr. (Gmm):	2.420	VMA:	15.9
Asphalt Binder:	PG 76-22	Gsb:	2.602
Mixing Temperature:	340F	Gse:	2.631
Compaction Temperature:	300F	Gb:	1.033

Mix Type: 25 mm HMA Binder Course (PG 70-22)

AHTD Lab No.: HM304-03   Date: 08/14/2003

Plant Name: Cranford   Location: North Little Rock

Status: Verified at the Asphalt Lab (University of Arkansas)

Material Gradations (Percent Passing)

Sieve Size	GMQ Granite 1 1/2"	GMQ Granite 3/4"	GMQ Granite 1/2"	GMQ 3M Corp Donna Fill	Job Mix
37.5 - 1-1/2"	100	100	100	100	100
25.0 - 1"	96	100	100	100	98
19.0 - 3/4"	73	100	100	100	86
12.5 - 1/2"	40	86	100	100	64
9.5 - 3/8"	26	71	88	100	51
4.75 - #4	6	45	58	100	29
2.36 - #8	3	30	38	100	21
1.18 - #16	2	19	26	99	16
0.6 - #30	2	12	18	90	13
0.3 - #50	1	7	12	81	9
0.15 - #100	1	5	8	43	6
0.075 - #200	0.7	2.6	4.7	22	3.1
Cold Feed %	53	32	8	7	100

Mix Design Summary

Asphalt Content %:	4.4	Air Voids (Va):	4.5
Max. Theor. Sp. Gr. (Gmm):	2.472	VMA:	13.4
Asphalt Binder:	PG 70-22	Gsb:	2.602
Mixing Temperature:	340F	Gse:	2.641
Compaction Temperature:	300F	Gb:	1.033

Mix Type: 25 mm HMA Binder Course (PG 76-22)

AHTD Lab No.: HM304-03   Date: 08/14/2003

Plant Name: Cranford   Location: North Little Rock

Status: Verified at the Asphalt Lab (University of Arkansas)

Material Gradations (Percent Passing)

Sieve Size	GMQ Granite 1 1/4"	GMQ Granite 3/4"	GMQ Granite Ind. Sand	GMQ 3M Corp Donna Fill	Job Mix
37.5 - 1-1/2"	100	100	100	100	100
25.0 - 1"	97.5	100	100	100	99
19.0 - 3/4"	68.2	100	100	100	87
12.5 - 1/2"	28.2	65.2	100	100	60
9.5 - 3/8"	20	30.6	100	100	46
4.75 - #4	3.3	2.4	89.7	100	28
2.36 - #8	2	0.8	60.7	99.9	21
1.18 - #16	2	0.5	36.7	99.4	16
0.6 - #30	2	0.5	24.4	90.1	13
0.3 - #50	1	0.3	13.8	65	8
0.15 - #100	1	0.3	7.4	43	5
0.075 - #200	1	0.2	2.9	26.9	3.2
Cold Feed %	40	32	20	8	100

Mix Design Summary

Asphalt Content %:	4.5	Air Voids (Va):	4.0
Max. Theor. Sp. Gr. (Gmm):	2.458	VMA:	13.8
Asphalt Binder:	PG 76-22	Gsb:	2.613
Mixing Temperature:	340F	Gse:	2.629
Compaction Temperature:	300F	Gb:	1.033

Mix Type: 37.5 mm HMA Base Course (PG 70-22)

AHTD Lab No.: SP313C-02   Date: 08/29/2002

Plant Name: Cranford   Location: Little Rock

Status: Verified at the Asphalt Lab (University of Arkansas)

Material Gradations (Percent Passing)

Sieve Size	GMQ Granite ASTM #4	GMQ Granite 3/4"	GMQ Granite Ind. Sand	GMQ 3M Corp Donna Fill	Job Mix
50.0 – 2"	100	100	100	100	100
37.5 - 1-1/2"	93	100	100	100	98
25.0 - 1"	41	100	100	100	81
19.0 - 3/4"	12	100	100	100	71
12.5 - 1/2"	6	85	100	100	64
9.5 - 3/8"	2	75	100	100	59
4.75 - #4	1	49	86	100	46
2.36 - #8	0	31	57	100	33
1.18 - #16	0	21	37	100	24
0.6 - #30	0	12	22	93	17
0.3 - #50	0	7	12	63	10
0.15 - #100	0	5	5	40	6
0.075 - #200	0	2.9	3.1	25.9	3.8
Cold Feed %	33	35	24	8	100

Mix Design Summary

Asphalt Content %:	3.7	Air Voids (Va):	4.5
Max. Theor. Sp. Gr. (Gmm):	2.487	VMA:	12.4
Asphalt Binder:	PG 70-22	Gsb:	2.604
Mixing Temperature:	330F	Gse:	2.630
Compaction Temperature:	300F	Gb:	1.031

Mix Type: 37.5 mm HMA Base Course (PG 76-22)

AHTD Lab No.: HM021-03   Date: 01/31/2003

Plant Name: Cranford   Location: Little Rock

Status: Verified at the Asphalt Lab (University of Arkansas)

Material Gradations (Percent Passing)

Sieve Size	GMQ Granite ASTM #4	GMQ Granite 3/4"	GMQ Granite Ind. Sand	GMQ 3M Corp Donna Fill	Job Mix
50.0 - 2"	100	100	100	100	100
37.5 - 1-1/2"	93	100	100	100	98
25.0 - 1"	41	100	100	100	81
19.0 - 3/4"	12	100	100	100	71
12.5 - 1/2"	6	85	100	100	64
9.5 - 3/8"	2	75	100	100	59
4.75 - #4	1	49	86	100	46
2.36 - #8	0	31	57	100	33
1.18 - #16	0	21	37	100	24
0.6 - #30	0	12	22	93	17
0.3 - #50	0	7	12	63	10
0.15 - #100	0	5	5	40	6
0.075 - #200	0	2.9	3.1	25.9	3.8
Cold Feed %	33	35	24	8	100

Mix Design Summary

Asphalt Content %:	3.6	Air Voids (Va):	4.0
Max. Theor. Sp. Gr. (Gmm):	2.486	VMA:	11.6
Asphalt Binder:	PG 76-22	Gsb:	2.604
Mixing Temperature:	330F	Gse:	2.625
Compaction Temperature:	300F	Gb:	1.031

Mix Type: 12.5 mm HMA Surface Course (PG 70-22)

AHTD Lab No.: SP099C-99   Date: 03/27/2000

Plant Name: Arkhola   Location: Van Buren

Status: Verified at the Asphalt Lab (University of Arkansas)

Material Gradations (Percent Passing)

Sieve Size	ARK Preston 3/4"-#4	ARK Preston 1/2"-Chp	ARK Arkhola 3/8"-Grv	ARK Preston 1/4"-Scr	ARK Preston 1/4"-Wsh	ARK Preston BHFines	Job Mix
25.0 - 1"	100	100	100	100	100	100	100
19.0 - 3/4"	100	100	100	100	100	100	100
12.5 - 1/2"	64.5	100	100	100	100	100	93
9.5 - 3/8"	37.1	88.3	100	100	100	100	85
4.75 - #4	3.5	36.1	62.1	90.2	89.9	100	55
2.36 - #8	2.7	6.5	19.9	63.9	60.1	100	29
1.18 - #16	2.4	4.1	10.3	48.2	41.1	100	20
0.6 - #30	2.3	3.7	6.8	40.4	37.1	100	17
0.3 - #50	2.3	3.6	5	35.2	25.6	99.9	14
0.15 - #100	2.1	3.2	3.7	25.1	15.2	99.6	10
0.075 - #200	1.1	2.1	2.2	14.7	7.2	97.1	5.7
Cold Feed %	20	20	24	14	21	1	100

Mix Design Summary

Asphalt Content %:	6.5	Air Voids (Va):	4.5
Max. Theor. Sp. Gr. (Gmm):	2.358	VMA:	15.4
Asphalt Binder:	PG 70-22	Gsb:	2.486
Mixing Temperature:	340F	Gse:	2.594
Compaction Temperature:	300F	Gb:	1.021

Mix Type: 12.5 mm HMA Surface Course (PG 76-22)

AHTD Lab No.: SP170C-00   Date: 07/10/2000

Plant Name: Arkhola   Location: Van Buren

Status: Verified at the Asphalt Lab (University of Arkansas)

Material Gradations (Percent Passing)

Sieve Size	ARK Preston 3/4"-#4	ARK Preston 1/2"-Chp	ARK Arkhola 3/8"-Grv	ARK Preston 1/4"-Scr	ARK Preston 1/4"-Wsh	ARK Preston BHFines	Job Mix
25.0 - 1"	100	100	100	100	100	100	100
19.0 - 3/4"	100	100	100	100	100	100	100
12.5 - 1/2"	72.3	100	100	100	100	100	94
9.5 - 3/8"	41.3	88.3	100	100	100	100	86
4.75 - #4	2.7	36.1	62.1	90.2	89.9	100	55
2.36 - #8	1.7	6.5	19.9	63.9	60.1	100	29
1.18 - #16	1.6	4.1	10.3	48.2	41.1	100	20
0.6 - #30	1.5	3.7	6.8	40.4	31.7	100	16
0.3 - #50	1.5	3.6	5	35.2	25.6	99.9	14
0.15 - #100	1.3	3.2	3.7	25.1	15.2	99.6	9
0.075 - #200	0.9	2.1	2.2	14.7	7.2	97.1	5.7
Cold Feed %	24	22	16	15	22	1	100

Mix Design Summary

Asphalt Content %:	6.0	Air Voids (Va):	4.0
Max. Theor. Sp. Gr. (Gmm):	2.368	VMA:	14.5
Asphalt Binder:	PG 76-22	Gsb:	2.496
Mixing Temperature:	340F	Gse:	2.581
Compaction Temperature:	300F	Gb:	1.033

Mix Type: 25 mm HMA Binder Course (PG 70-22)

AHTD Lab No.: SP257C-02   Date: 07/09/2002

Plant Name: Arkhola   Location: Van Buren

Status: Verified at the Asphalt Lab (University of Arkansas)

Material Gradations (Percent Passing)

Sieve Size	ARK Preston 1-1/4"	ARK Preston 3/4"	ARK Preston 1/2"-Chp	ARK Arkhola 3/8"-Grv	ARK Preston 1/4"-Scr	ARK Preston 1/4"-Wsh	ARK Preston BHFines	Job Mix
37.5-1-1/2"	100	100	100	100	100	100	100	100
25.0 - 1"	76.3	100	100	100	100	100	100	94
19.0 - 3/4"	25.8	100	100	100	100	100	100	82
12.5 - 1/2"	2.7	64.5	100	100	100	100	100	67
9.5 - 3/8"	2	37.1	88.3	100	100	100	100	59
4.75 - #4	1.8	3.5	36.1	62.1	90.2	92	100	39
2.36 - #8	1.8	2.7	6.5	19.9	63.9	61	100	22
1.18 - #16	1.7	2.4	4.1	10.3	48.2	42	100	16
0.6 - #30	1.7	2.3	3.7	6.8	40.4	33	100	13
0.3 - #50	1.7	2.3	3.6	5	35.2	27	99.9	11
0.15 - #100	1.6	2.1	3.2	3.7	25.1	16	99.6	8
0.075 - #200	0.8	1.1	2.1	2.2	14.7	7.4	96.4	4.7
Cold Feed %	25	23	10	13	10	18	1	

Mix Design Summary

Asphalt Content %:	5.3	Air Voids (Va):	4.5
Max. Theor. Sp. Gr. (Gmm):	2.398	VMA:	13.1
Asphalt Binder:	PG 70-22	Gsb:	2.492
Mixing Temperature:	335F	Gse:	2.594
Compaction Temperature:	300F	Gb:	1.021

Mix Type: 25 mm HMA Binder Course (PG 76-22)

AHTD Lab No.: SP181C-00   Date: 07/25/2000

Plant Name: Arkhola   Location: Van Buren

Status: Verified at the Asphalt Lab (University of Arkansas)

Material Gradations (Percent Passing)

Sieve Size	ARK Preston 1-1/4"	ARK Preston 3/4"	ARK Preston 1/2"-Chp	ARK Arkhola 3/8"-Grv	ARK Preston 1/4"-Scr	ARK Preston 1/4"-Wsh	ARK Preston BHFines	Job Mix
37.5-1-1/2"	100	100	100	100	100	100	100	100
25.0 - 1"	76.3	100	100	100	100	100	100	93
19.0 - 3/4"	25.8	100	100	100	100	100	100	79
12.5 - 1/2"	2.7	72.3	100	100	100	100	100	66
9.5 - 3/8"	2	41.3	86	100	100	100	100	58
4.75 - #4	1.8	2.7	31.8	54.1	89.1	89.6	100	36
2.36 - #8	1.8	1.7	4.7	14.7	64	60.1	100	21
1.18 - #16	1.7	1.6	3.3	5.8	48.6	40.6	100	15
0.6 - #30	1.7	1.5	3	3.2	41.2	31.8	100	12
0.3 - #50	1.7	1.5	2.9	1.8	35.9	25.5	99.9	10
0.15 - #100	1.6	1.3	2.5	1.2	25	14.9	99.6	7
0.075 - #200	0.8	0.9	1.6	0.7	14.3	7	96.4	4.3
Cold Feed %	28	23	10	10	10	18	1	100

Mix Design Summary

Asphalt Content %:	4.9	Air Voids (Va):	4.0
Max. Theor. Sp. Gr. (Gmm):	2.401	VMA:	12.7
Asphalt Binder:	PG 76-22	Gsb:	2.505
Mixing Temperature:	340F	Gse:	2.577
Compaction Temperature:	300F	Gb:	1.033

Mix Type: 37.5 mm HMA Base Course (PG 70-22)

AHTD Lab No.: SP268C-02   Date: 06/28/2002

Plant Name: Arkhola   Location: Van Buren

Status: Verified at the Asphalt Lab (University of Arkansas)

Material Gradations (Percent Passing)

Sieve Size	ARK Preston 1-1/2"	ARK Preston 3/4"	ARK Preston 1/2"-Chp	ARK Preston 1/4"-Scr	ARK Preston 1/4"-Wsh	ARK Preston BHFines	Job Mix
37.5 - 1-1/2"	100	100	100	100	100	100	100
25.0 - 1"	52	100	100	100	100	100	82
19.0 - 3/4"	18	100	100	100	100	100	70
12.5 - 1/2"	2	73	100	100	100	100	56
9.5 - 3/8"	2	44	85	100	100	100	46
4.75 - #4	1	4	32	92	89	100	26
2.36 - #8	1	3	6	66	57	100	16
1.18 - #16	1	2	4	50	37	100	12
0.6 - #30	1	2	4	43	28	100	11
0.3 - #50	1	2	3	37	22	99.9	9
0.15 - #100	1	2	3	26	13	99.6	7
0.075 - #200	0.8	1.3	1.8	14.5	6.6	97.4	5.0
Cold Feed %	37	28	13	10	10	2	100

Mix Design Summary

Asphalt Content %:	4.6	Air Voids (Va):	4.5
Max. Theor. Sp. Gr. (Gmm):	2.413	VMA:	12.4
Asphalt Binder:	PG 70-22	Gsb:	2.512
Mixing Temperature:	335F	Gse:	2.578
Compaction Temperature:	300F	Gb:	1.038

Mix Type: 37.5 mm HMA Base Course (PG 76-22)

AHTD Lab No.: SP182C-00   Date: 07/25/2000

Plant Name: Arkhola   Location: Van Buren

Status: Verified at the Asphalt Lab (University of Arkansas)

Material Gradations (Percent Passing)

Sieve Size	ARK Preston 1-1/2"	ARK Preston 3/4"	ARK Preston 1/2"-Chp	ARK Preston 1/4"-Scr	ARK Preston 1/4"-Wsh	ARK Preston BHFines	Job Mix
37.5 - 1-1/2"	100	100	100	100	100	100	100
25.0 - 1"	66.9	100	100	100	100	100	88
19.0 - 3/4"	25.3	100	100	100	100	100	72
12.5 - 1/2"	2.2	72.3	100	100	100	100	56
9.5 - 3/8"	1.8	41.3	86	100	100	100	46
4.75 - #4	1.6	2.7	31.8	89.1	89.6	100	26
2.36 - #8	1.6	1.7	4.7	64	60.1	100	16
1.18 - #16	1.6	1.6	3.3	48.6	40.6	100	12
0.6 - #30	1.6	1.5	3	41.2	31.8	100	10
0.3 - #50	1.5	1.5	2.9	35.9	25.5	99.9	9
0.15 - #100	1.4	1.3	2.5	25	14.9	99.6	7
0.075 - #200	1.2	0.9	1.6	14.3	7	97.1	4.3
Cold Feed %	37	28	12	12	10	1	100

Mix Design Summary

Asphalt Content %:	4.5	Air Voids (Va):	4.0
Max. Theor. Sp. Gr. (Gmm):	2.418	VMA:	11.7
Asphalt Binder:	PG 76-22	Gsb:	2.507
Mixing Temperature:	340F	Gse:	2.581
Compaction Temperature:	300F	Gb:	1.033

Mix Type: 12.5 mm HMA Surface Course (PG 70-22)

AHTD Lab No.: SP174C-01   Date: 06/06/2000

Plant Name: Jet Asphalt   Location: El Dorado

Status: Verified at the Asphalt Lab (University of Arkansas)

Material Gradations (Percent Passing)

Sieve Size	JET Gravel C	JET Gravel D	JET Gravel Screenings	JET 3M Corp Donna Fill	Job Mix
25.0 - 1"	100	100	100	100	100
19.0 - 3/4"	100	100	100	100	100
12.5 - 1/2"	35.7	100	100	100	94
9.5 - 3/8"	9.2	92	100	100	86
4.75 - #4	1.6	39	98.3	100	56
2.36 - #8	1	12	71.2	99.9	34
1.18 - #16	0.7	5	42.8	95.6	23
0.6 - #30	0.4	2	25.1	90.1	17
0.3 - #50	0.4	1	11	65	10
0.15 - #100	0.3	0.2	3.7	43	6
0.075 - #200	0.3	0.2	1.7	26.9	3.5
Cold Feed %	10	56	23	11	100

Mix Design Summary

Asphalt Content %:	5.5	Air Voids (Va):	4.5
Max. Theor. Sp. Gr. (Gmm):	2.407	VMA:	14.9
Asphalt Binder:	PG 70-22	Gsb:	2.558
Mixing Temperature:	320F	Gse:	2.609
Compaction Temperature:	295F	Gb:	1.033

Mix Type: 25 mm HMA Binder Course (PG 70-22)

AHTD Lab No.: SP101C-02   Date: 04/01/2002

Plant Name: Jet Asphalt   Location: El Dorado

Status: Verified at the Asphalt Lab (University of Arkansas)

Material Gradations (Percent Passing)

Sieve Size	JET Gravel A	JET Gravel C	JET Gravel D	JET Gravel Screenings	JET 3M Corp Donna Fill	Job Mix
37.5 - 1-1/2"	100	100	100	100	100	100
25.0 - 1"	92	100	100	100	100	97
19.0 - 3/4"	73.9	97.9	100	100	100	90
12.5 - 1/2"	27.1	38.5	99.4	100	100	66
9.5 - 3/8"	12.6	11.3	88.1	99.8	100	54
4.75 - #4	4.8	4.2	40.3	97.5	100	37
2.36 - #8	1.8	2.2	14.3	74.7	100	24
1.18 - #16	1.3	1.6	6	46.3	99.9	17
0.6 - #30	1.1	1.3	3.3	28.1	93.5	13
0.3 - #50	1	1.2	2.1	13.5	63.2	8
0.15 - #100	0.9	1.1	1.5	5.5	40.2	5
0.075 - #200	0.8	1	1.3	3.3	26.9	3.2
Cold Feed %	38	10	29	16	7	

Mix Design Summary

Asphalt Content %:	4.6	Air Voids (Va):	4.5
Max. Theor. Sp. Gr. (Gmm):	2.436	VMA:	13.0
Asphalt Binder:	PG 70-22	Gsb:	2.565
Mixing Temperature:	325F	Gse:	2.608
Compaction Temperature:	295F	Gb:	1.028

Mix Type: 37.5 mm HMA Base Course (PG 70-22)

AHTD Lab No.: SP102C-02   Date: 04/01/2002

Plant Name: Jet Asphalt   Location: El Dorado

Status: Verified at the Asphalt Lab (University of Arkansas)

Material Gradations (Percent Passing)

Sieve Size	GMQ Granite ASTM #4	JET Gravel C	JET Gravel D	JET Gravel Screenings	JET 3M Corp Donna Fill	Job Mix
50.0 - 2"	100	100	100	100	100	100
37.5 - 1-1/2"	95	100	100	100	100	98
25.0 - 1"	35	100	100	100	100	77
19.0 - 3/4"	11	97.9	100	100	100	69
12.5 - 1/2"	2	38.5	99.4	100	100	56
9.5 - 3/8"	1.5	11.3	88.1	99.8	100	48
4.75 - #4	1.2	4.2	40.3	97.5	100	31
2.36 - #8	1	2.2	14.3	74.7	100	20
1.18 - #16	0.9	1.6	6.0	46.3	99.9	14
0.6 - #30	0.9	1.3	3.3	28.1	93.5	11
0.3 - #50	0.9	1.2	2.1	13.5	63.2	7
0.15 - #100	0.8	1.1	1.5	5.5	40.2	4
0.075 - #200	0.7	1.0	1.3	3.3	26.9	3.0
Cold Feed %	35	15	33	10	7	100

Mix Design Summary

Asphalt Content %: 4.2		Air Voids (Va): 4.5
Max. Theor. Sp. Gr. (Gmm): 2.461		VMA: 12.6
Asphalt Binder: PG 70-22		Gsb: 2.585
Mixing Temperature: 325F		Gse: 2.621
Compaction Temperature: 295F		Gb: 1.028

APPENDIX C   INTERNAL GYRATION ANGLE (DAV WITH MIX)

Internal Angles (DAV with Mix)

SGC	Agg.	Size	Binder	Rep.	Ht (mm)		Angle (Deg)		DIA
					Top	Bott	Top	Bott	(deg)
PINE	MCA	12.5	70-22	1	117	116	1.194	1.150	
125X				2	118	117	1.199	1.146	
				3	118	118	1.196	1.156	
				Ave.			1.196	1.151	1.174
				Sdev			0.003	0.005	0.003
			76-22	1	118	119	1.197	1.141	
				2	119	119	1.201	1.143	
				3	118	118	1.200	1.153	
				Ave.			1.199	1.146	1.173
				Sdev			0.002	0.006	0.003
		25	70-22	1	119	119	1.194	1.156	
				2	120	121	1.195	1.159	
				3	120	120	1.192	1.165	
				Ave.			1.194	1.160	1.177
				Sdev			0.002	0.005	0.002
			76-22	1	121	120	1.184	1.134	
				2	121	120	1.182	1.140	
				3	121	120	1.187	1.146	
				Ave.			1.184	1.140	1.162
				Sdev			0.003	0.006	0.003

Internal Angles (DAV with Mix)

SGC	Agg.	Size	Binder	Rep.	Ht (mm)		Angle (Deg)		DIA
					Top	Bott	Top	Bott	(deg)
PINE	ARK	12.5	70-22	1	119	120	1.192	1.167	
125X				2	119	120	1.201	1.168	
				3	120	120	1.201	1.173	
				Ave.			1.198	1.169	1.184
				Sdev			0.005	0.003	0.003
			76-22	1	120	121	1.190	1.161	
				2	120	120	1.194	1.161	
				3	121	121	1.197	1.160	
				Ave.			1.194	1.161	1.177
				Sdev			0.004	0.001	0.002
		25	70-22	1	120	119	1.190	1.151	
				2	121	120	1.191	1.158	
				3	119	119	1.194	1.156	
				Ave.			1.192	1.155	1.173
				Sdev			0.002	0.004	0.002
			76-22	1	121	122	1.171	1.157	
				2	121	120	1.183	1.147	
				3	121	121	1.186	1.156	
				Ave.			1.180	1.153	1.167
				Sdev			0.008	0.006	0.005

Internal Angles (DAV with Mix)

SGC	Agg.	Size	Binder	Rep.	Ht (mm)		Angle (Deg)		DIA
					Top	Bott	Top	Bott	(deg)
TROX 4141	MCA	12.5	70-22	1	37	37	1.278	1.279	
				2	37	37	1.273	1.286	
				3	37	37	1.278	1.283	
				Ave.	37	37	1.276	1.283	
				Sdev			0.003	0.004	
				1	68	67	1.188	1.190	
				2	69	67	1.196	1.193	
				3	68	67	1.198	1.197	
				Ave.	68	67	1.194	1.193	
				Sdev			0.005	0.004	
				Ave.	115	115	1.068	1.051	1.060
				Sdev			0.014	0.011	0.009
			76-22	1	39	38	1.247	1.296	
				2	39	39	1.246	1.299	
				3	39	38	1.254	1.303	
				Ave.	39	38	1.249	1.299	
				Sdev			0.004	0.004	
				1	69	68	1.181	1.198	
				2	69	68	1.181	1.205	
				3	69	69	1.189	1.206	
				Ave.	69	68	1.184	1.203	
				Sdev			0.005	0.004	
				Ave.	115	115	1.085	1.053	1.069
				Sdev			0.013	0.012	0.009

Internal Angles (DAV with Mix)

SGC	Agg.	Size	Binder	Rep.	Ht (mm)		Angle (Deg)		DIA
					Top	Bott	Top	Bott	(deg)
TROX	MCA	25	70-22	1	40	39	1.257	1.296	
4141				2	39	39	1.247	1.307	
				3	39	39	1.252	1.303	
				Ave.	39	39	1.252	1.302	
				Sdev			0.005	0.006	
				1	71	71	1.183	1.199	
				2	71	71	1.178	1.212	
				3	70	70	1.178	1.213	
				Ave.	70	71	1.180	1.208	
				Sdev			0.003	0.008	
				Ave.	115	115	1.075	1.074	1.074
				Sdev			0.010	0.021	0.011
			76-22	1	40	41	1.248	1.273	
				2	40	40	1.246	1.288	
				3	40	39	1.246	1.299	
				Ave.	40	40	1.247	1.287	
				Sdev			0.001	0.013	
				1	70	69	1.181	1.203	
				2	70	69	1.191	1.201	
				3	70	70	1.183	1.212	
				Ave.	70	69	1.185	1.205	
				Sdev			0.005	0.006	
				Ave.	115	115	1.092	1.079	1.086
				Sdev			0.013	0.025	0.014

Internal Angles (DAV with Mix)

SGC	Agg.	Size	Binder	Rep.	Ht (mm)		Angle (Deg)		DIA
					Top	Bott	Top	Bott	(deg)
TROX 4141	ARK	12.5	70-22	1	37	38	1.264	1.292	
				2	38	38	1.285	1.272	
				3	38	38	1.256	1.303	
				Ave.	38	38	1.268	1.289	
				Sdev			0.015	0.016	
				1	68	68	1.171	1.198	
				2	69	70	1.171	1.204	
				3	69	68	1.181	1.205	
				Ave.	69	68	1.174	1.202	
				Sdev			0.006	0.004	
				Ave.	115	115	1.033	1.071	1.052
				Sdev			0.027	0.026	0.019
			76-22	1	39	38	1.268	1.290	
				2	39	39	1.278	1.285	
				3	38	38	1.269	1.297	
				Ave.	39	39	1.272	1.291	
				Sdev			0.006	0.006	
				1	69	69	1.169	1.188	
				2	69	68	1.163	1.195	
				3	69	70	1.166	1.196	
				Ave.	69	69	1.166	1.193	
				Sdev			0.003	0.004	
				Ave.	115	115	1.007	1.046	1.027
				Sdev			0.011	0.014	0.009

Internal Angles (DAV with Mix)

SGC	Agg.	Size	Binder	Rep.	Ht (mm)		Angle (Deg)		DIA
					Top	Bott	Top	Bott	(deg)
TROX 4141	ARK	25	70-22	1	38	38	1.245	1.288	
				2	39	39	1.244	1.300	
				3	39	38	1.254	1.294	
				Ave.	39	38	1.248	1.294	
				Sdev			0.006	0.006	
				1	68	67	1.168	1.191	
				2	69	68	1.184	1.190	
				3	70	69	1.178	1.197	
				Ave.	69	68	1.177	1.193	
				Sdev			0.008	0.004	
				Ave.	115	115	1.068	1.034	1.051
				Sdev			0.022	0.014	0.013
			76-22	1	41	39	1.250	1.295	
				2	39	39	1.247	1.298	
				3	39	39	1.249	1.303	
				Ave.	40	39	1.249	1.299	
				Sdev			0.002	0.004	
				1	70	69	1.170	1.191	
				2	69	70	1.166	1.196	
				3	71	71	1.177	1.195	
				Ave.	70	70	1.171	1.194	
				Sdev			0.006	0.003	
				Ave.	115	115	1.054	1.043	1.049
				Sdev			0.014	0.009	0.008

Note: DAV = 71.78 mm, DAV Plate = 9.56 mm

354

APPENDIX D   ECCENTRICITY TEST RESULTS (PDA WITH MIX)

Eccentricity (PDA with Mix)

SGC	Agg.	Size	Bind.	Rep.	Load (N)			Ecc. (mm)			T-Mo
					Top	Bott	Ave.	Top	Bott	Ave.	(N-m)
PINE	MCA	12.5	70-22	1	10587	11095		28.54	27.40		
125X				2	10725	11004		29.15	28.08		
				3	10413	10564		30.55	29.44		
				Ave.	10575	10888	10731	29.41	28.31	28.86	310
				Sdev	156	284	162	1.031	1.039	0.732	
			76-22	1	10436	10969		30.01	28.90		
				2	10511	10572		30.16	29.04		
				3	10320	10537		31.23	30.18		
				Ave.	10422	10692	10557	30.47	29.37	29.92	316
				Sdev	96	240	129	0.665	0.702	0.484	
		25	70-22	1	10084	11536		28.87	27.74		
				2	10547	11048		29.30	28.24		
				3	9822	10647		30.81	29.68		
				Ave.	10151	11077	10614	29.66	28.55	29.11	309
				Sdev	367	445	288	1.019	1.007	0.716	
			76-22	1	10778	11176		28.66	27.56		
				2	9915	10534		30.13	29.05		
				3	10284	10723		30.57	29.47		
				Ave.	10326	10811	10568	29.79	28.69	29.24	309
				Sdev	433	330	272	1.000	1.004	0.708	

Eccentricity (PDA with Mix)

SGC	Agg.	Size	Bind.	Rep.	Load (N)			Ecc. (mm)			T-Mo
					Top	Bott	Ave.	Top	Bott	Ave.	(N-m)
PINE	ARK	12.5	70-22	1	10725	11163		29.00	27.95		
125X				2	9844	10698		30.15	29.07		
				3	9679	10415		31.28	30.15		
				Ave.	10083	10759	10421	30.14	29.06	29.60	308
				Sdev	562	378	339	1.140	1.100	0.792	
			76-22	1	10547	11018		29.76	28.68		
				2	10191	10270		30.68	29.60		
				3	10253	10360		30.80	29.73		
				Ave.	10330	10549	10440	30.41	29.34	29.88	312
				Sdev	190	408	225	0.569	0.572	0.404	
		25	70-22	1	10484	11174		29.44	28.37		
				2	10249	11111		29.76	28.71		
				3	10017	10930		29.87	28.82		
				Ave.	10250	11072	10661	29.69	28.63	29.16	311
				Sdev	234	127	133	0.223	0.235	0.162	
			76-22	1	10938	11633		27.89	26.82		
				2	10089	10401		30.06	28.94		
				3	10422	10344		31.61	30.55		
				Ave.	10483	10793	10638	29.85	28.77	29.31	312
				Sdev	428	729	422	1.869	1.871	1.322	

Eccentricity (PDA with Mix)

SGC	Agg.	Size	Bind.	Rep.	Load (N)			Ecc. (mm)			T-Mo
					Top	Bott	Ave.	Top	Bott	Ave.	(N-m)
TROX 4141	MCA	12.5	70-22	1	10694	11343		26.93	25.74		
				2	10203	9719		29.99	28.76		
				3	9433	10004		30.32	29.09		
				Ave.	10110	10355	10233	29.08	27.86	28.47	291
				Sdev	636	867	538	1.869	1.846	1.314	
			76-22	1	10657	11512		27.40	26.21		
				2	9838	10569		28.46	27.23		
				3	9661	9928		31.57	30.40		
				Ave.	10052	10670	10361	29.14	27.95	28.55	296
				Sdev	531	797	479	2.167	2.185	1.539	
		25	70-22	1	10821	10938		26.80	25.63		
				2	11234	11169		27.06	25.84		
				3	10478	10885		27.20	25.96		
				Ave.	10844	10997	10921	27.02	25.81	26.42	288
				Sdev	379	151	204	0.203	0.167	0.131	
			76-22	1	9778	10066		30.68	29.47		
				2	9522	10178		30.77	29.58		
				3	9704	10142		31.12	29.90		
				Ave.	9668	10129	9898	30.86	29.65	30.25	299
				Sdev	132	57	72	0.232	0.223	0.161	

Eccentricity (PDA with Mix)

SGC	Agg.	Size	Bind.	Rep.	Load (N)			Ecc. (mm)			T-Mo
					Top	**Bott**	**Ave.**	**Top**	**Bott**	**Ave.**	**(N-m)**
TROX 4141	ARK	12.5	70-22	1	11317	11450		25.36	24.17		
				2	11528	11352		25.85	24.60		
				3	10856	10978		26.99	25.75		
				Ave.	11234	11260	11247	26.07	24.84	25.45	286
				Sdev	344	249	212	0.836	0.817	0.585	
			76-22	1	9583	10427		29.53	28.32		
				2	9144	10671		30.84	29.65		
				3	9739	10182		31.42	30.20		
				Ave.	9489	10427	9958	30.60	29.39	29.99	299
				Sdev	309	245	197	0.968	0.967	0.684	
		25	70-22	1	11321	11468		27.03	25.81		
				2	9589	10440		29.93	28.76		
				3	9643	10378		31.63	30.44		
				Ave.	10184	10762	10473	29.53	28.34	28.93	303
				Sdev	985	612	580	2.326	2.344	1.651	
			76-22	1	10042	11054		28.28	27.13		
				2	9517	11094		29.63	28.40		
				3	9552	10871		29.94	28.78		
				Ave.	9704	11006	10355	29.28	28.10	28.69	297
				Sdev	294	119	158	0.883	0.864	0.618	

APPENDIX E   **INTERNAL ANGLE TEST RESULTS (HMS AND RAM)**

Internal Angles (HMS with DAV and RAM)

SGC	Device	Angle/Dia	Rep.	Ht (mm)	Angle (Deg) Top	Angle (Deg) Bottom	DIA (deg)
PINE 125X	DAV 106	18 Deg	1	115.0	1.175	1.146	
			2	115.0	1.169	1.157	
			3	115.0	1.175	1.159	
			Ave.		1.173	1.154	1.164
			Sdev		0.003	0.007	0.004
		21 Deg	1	115.0	1.169	1.121	
			2	115.0	1.168	1.134	
			3	115.0	1.170	1.136	
			Ave.		1.169	1.130	1.150
			Sdev		0.001	0.008	0.004
		24 Deg	1	115.0	1.138	1.090	
			2	115.0	1.152	1.107	
			3	115.0	1.153	1.106	
			Ave.		1.148	1.101	1.124
			Sdev		0.008	0.010	0.006
	DAV 110	18 Deg	1	115.0	1.160	1.141	
			2	115.0	1.169	1.144	
			3	115.0	1.174	1.147	
			Ave.		1.168	1.144	1.156
			Sdev		0.007	0.003	0.004
		21 Deg	1	115.0	1.145	1.126	
			2	115.0	1.159	1.130	
			3	115.0	1.163	1.128	
			Ave.		1.156	1.128	1.142
			Sdev		0.009	0.002	0.005
		24 Deg	1	115.0	1.145	1.098	
			2	115.0	1.147	1.110	
			3	115.0	1.151	1.109	
			Ave.		1.148	1.106	1.127
			Sdev		0.003	0.007	0.004

Internal Angles (HMS with DAV and RAM)

SGC	Device	Angle/Dia	Rep.	Ht	Angle (Deg)		DIA
				(mm)	Top	Bottom	(deg)
PINE	RAM 29	44 mm	1	125.0	1.14	1.16	
125X			2	125.0	1.15	1.16	
			3	125.0	1.15	1.16	
			Ave.		1.147	1.160	1.153
			Sdev		0.006	0.000	0.003
		64 mm	1	125.0	1.06	1.12	
			2	125.0	1.08	1.12	
			3	125.0	1.07	1.13	
			Ave.		1.070	1.123	1.097
			Sdev		0.010	0.006	0.006
	RAM 12	44 mm	1	125.0	1.12	1.16	
			2	125.0	1.13	1.16	
			3	125.0	1.13	1.16	
			Ave.		1.127	1.160	1.143
			Sdev		0.006	0.000	0.003
		64 mm	1	125.0	1.06	1.13	
			2	125.0	1.07	1.13	
			3	125.0	1.08	1.13	
			Ave.		1.070	1.130	1.100
			Sdev		0.010	0.000	0.005

Internal Angles (HMS with DAV and RAM)

SGC	Device	Angle/Dia	Rep.	Ht	Angle (Deg)		DIA
				(mm)	Top	Bottom	(deg)
TROX	DAV 106	18 Deg	1	115.0	1.069	1.138	
4141			2	115.0	1.079	1.130	
			3	115.0	1.062	1.168	
			Ave.		1.070	1.145	1.108
			Sdev		0.009	0.020	0.011
		21 Deg	1	115.0	1.046	1.121	
			2	115.0	1.040	1.131	
			3	115.0	1.040	1.134	
			Ave.		1.042	1.129	1.085
			Sdev		0.003	0.007	0.004
		24 Deg	1	115.0	0.992	1.112	
			2	115.0	0.987	1.119	
			3	115.0	1.007	1.120	
			Ave.		0.995	1.117	1.056
			Sdev		0.010	0.004	0.006
	DAV 110	18 Deg	1	115.0	1.083	1.173	
			2	115.0	1.080	1.182	
			3	115.0	1.131	1.173	
			Ave.		1.098	1.176	1.137
			Sdev		0.029	0.005	0.015
		21 Deg	1	115.0	1.074	1.141	
			2	115.0	1.057	1.161	
			3	115.0	1.070	1.153	
			Ave.		1.067	1.152	1.109
			Sdev		0.009	0.010	0.007
		24 Deg	1	115.0	1.014	1.109	
			2	115.0	1.023	1.116	
			3	115.0	1.047	1.116	
			Ave.		1.028	1.114	1.071
			Sdev		0.017	0.004	0.009

Internal Angles (HMS with DAV and RAM)

SGC	Device	Angle/Dia	Rep.	Ht	Angle (Deg)		DIA
				(mm)	Top	Bottom	(deg)
TROX 4141	RAM 29	44 mm	1	125.0	1.14	1.11	
			2	125.0	1.17	1.14	
			3	125.0	1.17	1.16	
			Ave.		1.160	1.137	1.148
			Sdev		0.017	0.025	0.015
		64 mm	1	125.0	1.15	0.99	
			2	125.0	1.16	0.99	
			3	125.0	1.15	1.00	
			Ave.		1.153	0.993	1.073
			Sdev		0.006	0.006	0.004
	RAM 12	44 mm	1	125.0	1.15	1.10	
			2	125.0	1.16	1.10	
			3	125.0	1.18	1.13	
			Ave.		1.163	1.110	1.137
			Sdev		0.015	0.017	0.012
		64 mm	1	125.0	1.12	1.00	
			2	125.0	1.14	1.01	
			3	125.0	1.12	1.05	
			Ave.		1.127	1.020	1.073
			Sdev		0.012	0.026	0.014

APPENDIX F   ECCENTRICITY (PDA WITH HMS OR RAM)

Eccentricities (PDA with HMS or RAM)

SGC	Device	Ang/Dia	Rep.	Load (N)			e (mm)			T-Mo
				Top	Bott	Ave.	Top	Bott	Ave.	(N-m)
PINE 125X	DAV 110	18 Deg	1	10565	10230		22.22	27.98		
			2	10529	10220		22.15	27.38		
			3	10520	10300		22.12	27.88		
			Ave.	10538	10250	10394	22.16	27.75	24.96	259
			Sdev	24	44	25	0.051	0.321	0.163	
		21 Deg	1	10355	10146		23.97	31.02		
			2	10667	10156		24.09	29.25		
			3	10511	10166		24.03	30.88		
			Ave.	10511	10156	10334	24.03	30.38	27.21	281
			Sdev	156	10	78	0.060	0.984	0.493	
		24 Deg	1	10627	10230		27.76	32.09		
			2	10605	10210		27.91	32.07		
			3	11146	10090		27.90	32.01		
			Ave.	10793	10177	10485	27.86	32.06	29.96	314
			Sdev	307	76	158	0.084	0.042	0.047	
	RAM 29	44 mm	1	10680	10458		22.95	22.08		
			2	10680	10467		22.97	22.10		
			3	11214	10985		23.00	22.10		
			Ave.	10858	10637	10747	22.97	22.09	22.53	242
			Sdev	308	302	216	0.025	0.012	0.014	
		64 mm	1	10533	10258		32.08	31.97		
			2	10538	10222		32.16	31.97		
			3	11062	10752		32.20	31.90		
			Ave.	10711	10410	10561	32.15	31.95	32.05	338
			Sdev	304	296	212	0.061	0.040	0.037	

Eccentricities (PDA with HMS or RAM)

SGC	Device	Ang/Dia	Rep.	Load (N)			e (mm)			T-Mo
				Top	Bott	Ave.	Top	Bott	Ave.	(N-m)
TROX 4141	DAV 110	18 Deg	1	10529	10947		22.12	27.88		
			2	10538	10974		22.08	27.98		
			3	10315	10578		22.32	27.95		
			Ave.	10461	10833	10647	22.17	27.94	25.06	267
			Sdev	126	221	127	0.129	0.051	0.069	
		21 Deg	1	10529	10947		23.64	30.98		
			2	10538	10974		23.81	30.55		
			3	11060	11508		23.70	30.67		
			Ave.	10709	11143	10926	23.72	30.73	27.23	297
			Sdev	304	317	220	0.086	0.222	0.119	
		24 Deg	1	10378	10689		27.57	32.09		
			2	10315	10578		27.15	32.05		
			3	10864	11165		27.40	31.99		
			Ave.	10519	10811	10665	27.37	32.04	29.71	317
			Sdev	300	312	216	0.211	0.050	0.109	
	RAM 29	44 mm	1	10885	10943		21.94	23.06		
			2	10854	10863		21.97	23.08		
			3	11413	11448		22.00	23.00		
			Ave.	11050	11084	11067	21.97	23.05	22.51	249
			Sdev	314	317	223	0.030	0.042	0.026	
		64 mm	1	10622	10524		31.62	32.13		
			2	10542	10524		31.64	32.14		
			3	11111	11051		31.70	32.10		
			Ave.	10759	10700	10729	31.65	32.12	31.89	342
			Sdev	308	304	216	0.042	0.021	0.023	